Non-equilibrium dynamics in two-dimensional quantum systems

Shinichi Sunami

St. Hilda's College

University of Oxford

A thesis submitted for the degree of

Doctor of Philosophy

Michaelmas 2021

Non-equilibrium dynamics in two-dimensional quantum systems

Shinichi Sunami

St. Hilda's College
University of Oxford

A thesis submitted for the degree of Doctor of Philosophy

The understanding and precise prediction of non-equilibrium quantum many-body dynamics, in particular across a critical point, remains a difficult task due to the relevance of all length scales near the critical point. Furthermore, the number of parameters required to characterise the state of the system increases exponentially with the number of particles, making the numerical investigation of such a system extremely difficult.

In this thesis, we use ultracold ^{87}Rb atoms prepared in a bilayer two-dimensional (2D) trap to probe the Berezinskii-Kosterlitz-Thouless (BKT) phase transition in detail, both in and out of equilibrium. These experiments use a multiple-radiofrequency dressed trap, which allows dynamical control of the trapped atoms as well as the precise determination of the many-body wavefunction. For the characterisation of the 2D Bose gases using matter-wave interferometry, a novel technique was developed to obtain high contrast fringes by selective imaging of slices of the atomic cloud. This allow the observation of local fluctuations, such as phase correlation function, local vortex density and coherence full counting statistics. Utilising these observables, we have identified the BKT critical point and characterised microscopic features of harmonically-trapped 2D Bose gases in equilibrium. With this information about the system, we probe the non-equilibrium dynamics of 2D Bose gases following a quench across the BKT critical point. The system is quenched by a coherent splitting, which introduces a sudden reduction of density resulting in the quench from the superfluid to thermal phase. We monitor the dynamics towards the vortex-proliferated state and find that the vortex-unbinding dynamics is well described by the real-time renormalisation group theory. Finally, we show preliminary results for a tunnel-coupled bilayer 2D gas, in which we probe the oscillations of the relative phase of the two layers of superfluid.

The results presented in this thesis demonstrate that the multiple-RF dressing technique is a very powerful tool for investigating quantum many-body phenomena. This paves the way for future studies of non-equilibrium critical dynamics and their description with renormalisation-group theory.

Acknowledgements

I am immensely grateful for the support I received while working towards this thesis.

I would firstly thank my supervisor Professor Christopher Foot for accepting me into the ultracold quantum matter group, and the guidance and independence he offered throughout.
I have been extremely fortunate to work with great people at the research group. A huge thank you to Dr Elliot Bentine who has guided me through the learning of experiment. His continuous encouragement and experimental ideas were important for my work, and I enjoyed weekend sport kiting and VR games. I thank all the members who shared time in the basement lab, from debugging misbehaving electronics to discussing physics. In particular, Dr Kathrin Luksch and Dr Adam Barker for introducing me to the BEC experiment and RF-dressed trap. I have been supported throughout by many other members, especially David Garrick, Abel Beregi and Oscar Chang, and I am sure that the experimental apparatus will continue to be very productive in their capable hands. I also thank Sean, Leo, Abigail and all other Foot group members for making the life in the basement lab an enjoyable one.
Outside the research group in Oxford, I would like to express sincere gratitude to all theory collaborators: Dr. Vijay Singh, Dr. Junichi Okamoto and Professor Ludwig Mathey in Germany for numerous and very productive discussions on BKT physics over zoom. It has also been a pleasure to work with Dr. Ebubechukwu Ilo-Okeke and Professor Tim Byrnes, based in Shanghai, in which we developed ideas on spin squeezing into a joint publication.
My time in Oxford was enjoyable thanks to my friends. I would like to thank Suguru, Takahiro and Martin for many physics, mahjong and other discussions. I learned many ideas in quantum physics from them, and I was luckly to be able to share time in Oxford. I would also thank everyone who joined me for mahjong games.
Thanks to my father, mother and sister, Michio, Keiko and Ayaka, who have been extremely supportive throughout the doctorate and I could not have achieved this without your encouragement. Thanks also to my parents-in-law, Mihoko and Masahiro, for their support during the time of childcare and remote working.
Last but by no means least, I would like to express my deepest gratitude to my wife, Lena for her unwavering support. And finally, *arigato* to our newborn child Haru!

The following publications have arisen from work discussed in this thesis:

- **S. Sunami**, V. Singh, D. Garrick, A. Beregi, A.J. Barker, K. Luksch, E. Bentine, L. Mathey, C. J. Foot. *Observation of the BKT Transition in a 2D Bose Gas via Matter-Wave Interferometry*, *arXiv:2108.08840* (2021)

- E. O. Ilo-Okeke, **S. Sunami**, C. J. Foot, T. Byrnes. *Faraday imaging induced squeezing of a double-well Bose-Einstein condensate*, Physical Review A 104, 053324 (2021)

- A. J. Barker, **S. Sunami**, D. Garrick, A. Beregi, K. Luksch, E. Bentine, C. J. Foot. *Coherent splitting of two-dimensional Bose gases in magnetic potentials*, New Journal of Physics 22, 103040 (2020)

- A. J. Barker, **S. Sunami**, D. Garrick, A. Beregi, K. Luksch, E. Bentine and C. J. Foot. *Realising a species-selective double-well using multiple-radiofrequency-dressed potentials*, J. Phys. B: At. Mol. Opt. Phys. 53 155001 (2020)

- A. J. Barker, H. Style, K. Luksch, **S. Sunami**, D. Garrick, F. Hill, C. J. Foot and E. Bentine. *Applying machine learning optimization methods to the production of a quantum gas*, Machine Learning: Science and Technology 1, 015007 (2020)

- E. Bentine, A. J. Barker, K. Luksch, **S. Sunami**, T. L. Harte, B. Yuen, D. J. Owens, J. M. Hutson and C. J. Foot. *Inelastic collisions in radiofrequency-dressed mixtures*, Physical Review Research 2, 033163 (2020)

- K. Luksch, E. Bentine, A. J. Barker, **S. Sunami**, T.L. Harte, B. Yuen and C. J. Foot. *Probing multiple-frequency atom-photon interactions with ultracold atoms*, New Journal of Physics 21, 073067 (2019)

Publication in preparation:

- **S. Sunami**, V. Singh, D. Garrick, A. Beregi, A.J. Barker, K. Luksch, J. Okamoto, E. Bentine, L. Mathey and C. J. Foot. *Dynamical vortex unbinding in a quenched 2D superfluid.*

Publications planned using the data from this thesis:

- **S. Sunami**, V. Singh, D. Garrick, A. Beregi, E. Bentine, L. Mathey and C. J. Foot. *Density-noise correlation in 2D Bose gases across the BKT critical point.*

- **S. Sunami**, V. Singh, D. Garrick, A. Beregi, E. Bentine, L. Mathey and C. J. Foot. *Full counting statistics of 2D Bose gases across the BKT phase transition.*

Contents

List of Figures

1 Introduction

Contents

The *universal* nature of a phase transition connects a wide range of physical systems falling under the same *universality class*, and allows a unified description close to the critical point regardless of microscopic details of individual models. This remarkable feature is also expected to hold for some dynamical critical behaviours, with an astonishing consequence of connecting the results from tabletop experiments to cosmological phenomena [1–3]. As such, it is of great interest to build a versatile physical system that allows detailed investigation of universal critical phenomena both in and out of equilibrium.

One of these universality classes in two spatial dimensions has a unique feature: while the true long-range order (LRO) is precluded in systems at nonzero temperatures according to Mermin-Wagner theorem [4, 5], a *quasi*-order develops through the Berezinskii-Kosterlitz-Thouless (BKT) mechanism [6, 7]. The BKT transition is driven by unbinding of vortex-antivortex pairs, underscoring the topological

nature of the transition. The importance of this phase transition is highlighted by the Nobel Prize in Physics in 2016 for Kosterlitz and Thouless. This transition is characterized by the first-order correlation function $g_1(\boldsymbol{r}, \boldsymbol{r'}) = \langle \Psi^\dagger(\boldsymbol{r})\Psi(\boldsymbol{r'})\rangle$, where $\Psi(\boldsymbol{r})$ is the bosonic field operator at location $\boldsymbol{r}$, which changes from algebraic scaling $\sim r^{-\eta}$ in the superfluid phase, to exponential scaling in the thermal phase, with universal exponent $\eta_c = 0.25$ at the transition.

In the past few decades, ultracold quantum gases have emerged as clean and highly controllable quantum simulators for the study of quantum many-body phenomena which are often out of reach using existing numerical simulation techniques [8, 9]. The exceptional controllability of these systems make them an ideal platform to probe universal critical phenomena of a variety of phase transitions [2, 10–13]. The BKT transition is no exception, and the first observation was reported in 2006 by a pioneering work by Hadzibabic *et al.* [14]. A wealth of BKT physics has been investigated since then, as introduced in the next section.

In this thesis, we present a new experimental approach for probing the BKT transition in 2D quantum gases, both in and out of equilibrium. Firstly, we probe in equilibrium local phase fluctuation of the system, which reveals the phase correlation function and local vortex density. This allows a comprehensive investigation of the BKT transition in inhomogeneous 2D systems, with a precise observation of critical point. Furthermore, our experimental approach allows the investigation of the BKT dynamical critical phenomena, by the coherent splitting of 2D Bose gases. With this, we observe the relaxation dynamics of 2D system quenched out of a quasi-ordered phase into a vortex-proliferated disordered phase. We identify novel dynamical phases of a 2D system, especially the *superheated* superfluid phase that survives for up to a few hundred milliseconds.

In the following sections of this chapter, we give a brief introduction to three important aspects of the research presented in thesis and refer to subsequent chapters for detailed discussion: 1) the two-dimensional quantum gases, 2) the matter-wave interferometry technique for the investigation of 2D system, and 3) an introduction to general relaxation dynamics in cold-atom systems, as well as the description

of a particular dynamics that we study in this thesis, the *reverse* Kibble-Zurek mechanism which is expected in the BKT critical regime.

1.1 Quantum gases in two dimensions and the critical point

Ultracold atoms are usually trapped in a harmonic confinement created by either optical or magnetic methods with potential $V(x,y,z) = m\omega_x^2 x^2/2 + m\omega_y^2 y^2/2 + m\omega_z^2 z^2/2$ where m is the atomic mass and the angular frequencies ω_i characterise the strength of confinement in $i = x, y, z$ directions. The characteristic energy scales of many-body systems are the thermal energy scale $k_B T$ and the chemical potential μ which are usually comparable to, or larger than, $\hbar\omega_i$ for typical cold-atom experiments, where $\hbar$ is the reduced Planck constant and k_B is the Boltzmann constant. To observe 2D phenomena, we require tight confiement in one direction such that

$$k_B T, \mu \ll \hbar\omega_z. \tag{1.1.1}$$

This restricts the kinetic motion of atoms to the $x-y$ plane, since almost all atoms are in the ground state of the harmonic potential along z. This *freezing out* of transverse kinetic motion is a consequence of quantum mechanical nature of the system, which discretises the energy levels. Fig. 1.1 illustrates the realisation of a 2D system. A more detailed description, including the crossover to three-dimensional behaviour when $\hbar\omega_z \lesssim k_B T$, is given in Chapter 2.

The investigation of 2D systems using ultracold gases, especially the investigation of critical points, has a rather long history. Early experimental and theoretical works emerged back in the early 2000s [15–18], soon after the first realisation of Bose-Einstein condensation (BEC) in dilute Bose gases [19, 20]. In 2006, first direct observation of the BKT critical point was reported using a matter-wave interferometric technique [14]. The direct evidence of thermally activated vortices were reported. Dynamical features such as the scissors mode [21], critical velocity [22] and sound modes [23] provide further evidence of superfluid behaviour in 2D Bose gases. Despite the lack of LRO in the thermodynamic limit, the

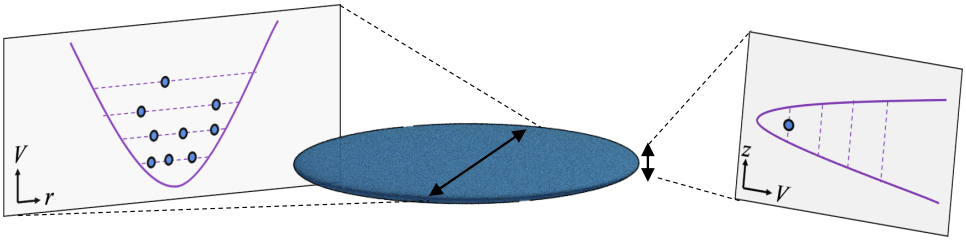

Figure 1.1: Creating 2D systems using trapped ultracold atoms. A pancake-shaped, oblate trapped cloud (blue plane) is shown with an illustration of cylindrically-symmetric trapping potentials (gray panels) in the axial (right, panel, z) and radial (left panel, r) directions. In the z direction, the confinement is tight, resulting in large energy level spacing in the harmonic trap. For the condition $k_B T, \mu \ll \hbar\omega_z$, the atoms cannot acquire enough thermal or interaction energy to populate excited states, and the dynamics is *frozen* in the z direction.

experimentally relevant, finite-sized 2D Bose gas is expected to support two distinct phase transitions, the BEC and BKT transitions. The intricate connection of these was studied in Ref. [24], where the critical point was measured with a wide range of interaction strengths and it was found that at finite interaction strength, the emergence of coherence is due to the BKT mechanism. Only recently the first-order correlation function was observed by measuring the momentum distribution [25]; however the reported algebraic exponent at the critical point was a factor of six larger than the universal theoretical value due to inhomogeneity and thermal components [26]. Even after two decades of investigations into 2D Bose gases, questions remain such as the correct treatment of inhomogeneity for the correlation properties and quantitative comparison to the theoretical model, including the temperature dependence of vortex density and algebraic exponent. These are the objectives of our experimental investigation into the BKT transition in equilibrium, presented in Chapter 5.

1.2 Matter-wave interferometry

A useful feature of the ultracold atoms is the possibility of observing matter-wave interference [27]. This is a direct consequence of ultralow temperatures, such that the thermal de Broglie wavelengths λ_{th} is larger than typical interparticle distances. Intuitively, particles act coherently as a single wave, and matter-wave interference fringes of tens of thousands massive particles can be observed when two of such ultracold clouds are spatially overlapped, in analogy to the Young's two-slit experiment using light. This is illustrated in Fig. 1.2.

The matter-wave analogue of interferometric measurement is an extremely powerful technique for metrology purposes such as searching for gravitational waves [28, 29]. This tool has also led to the enormous success of research into the spatial phase fluctuation of low-dimensional quantum systems both in and out of equilibrium [30–33]; as low-dimensional systems cannot maintain true long-range order, their order parameter possesses spatially fluctuating phase at any non-zero temperature. Cold atomic systems offer an window into the phase structure through spatial interference patterns, as illustrated in Fig. 1.2. These patterns allow us to extract the correlation function of the system [31, 32, 34][1]. Detailed theoretical and experimental tools for analysing such complex patterns are presented in Chapters 2 and 4.

1.3 Non-equilibrium dynamics in reduced dimensions

Ultracold atoms are ideal systems to probe the non-equilibrium (NEQ) dynamics of many-body systems. Atoms are levitated in ultrahigh vacuum of $\sim 10^{-11}$ mbar and the systems experience almost no interaction with the outside world over the duration of typical experiments. This allows us to consider the system as isolated and undergoing unitary evolution, in contrast to an open quantum system connected to a thermal bath characterised by infinite degrees of freedom.

[1] In continuous system, other techniques to extract correlation function exists, such as spatial spin correlations [35, 36].

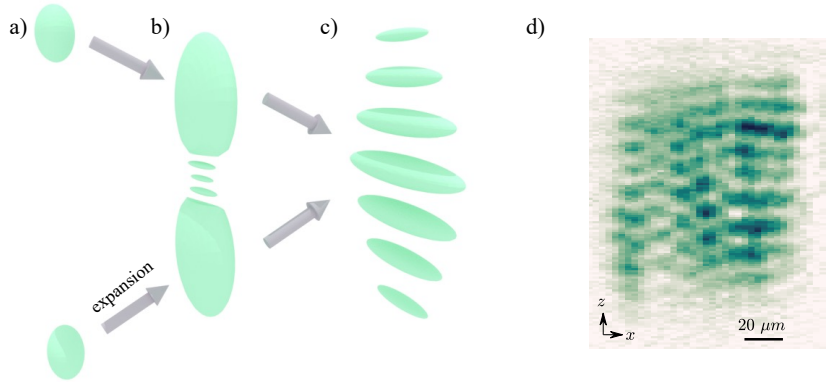

Figure 1.2: Illustration of matter-wave interference. (a-c) Illustration of matter-wave interference analogous to Young's double-slit experiment. (a) Two phase-coherent gases are released from two separate traps. (b) As the clouds expand and spatially overlap, they start to show interference fringes. (c) The two condensates overlap completely, showing a modulation of density with high contrast. (d) Example matter-wave interference pattern: experimentally measured density distribution of interfering 2D clouds showing interference patterns along z, with phase fluctuation along x.

Additionally, the interactions are usually weak, thus providing a timescale of dynamics that is experimentally accessible without extreme effort. These features make the non-equilibrium dynamics of this many-body system tractable both theoretically and experimentally. As such, systems of ultracold atoms have been a testbed of numerous novel dynamical phenomena.

In continuous systems, the dimensionality plays a significant role in the relaxation dynamics. The most intriguing example is the 1D quantum gas, which remains out of equilibrium indefinitely [31, 37]. Intrinsic fluctuation of the order parameter in such systems provide a wide variety of observables for the investigation into these NEQ states, such as full-counting statistics [31] and higher-order correlation [38].

In 3D systems, the effect of criticality on NEQ dynamics has been and is an active field of research [2, 11, 39, 40]. As pointed out at the start of this chapter, the dynamics near the critical point often exhibit an universal behaviour; an example of which is the non-equilibrium energy distribution, which shows a universal, self-similar scaling [11, 40, 41]. A notable theoretical framework to understand such behaviour is the Kibble-Zurek mechanism [1, 42], originally proposed for the investigation of cosmological phenomena in superfluid helium.

The physics of 2D systems has marginal features of 1D and 3D systems. A wealth of interesting behaviours exist thanks to intrinsic thermal fluctuation of the system at finite temperature, in a similar manner to 1D systems. Additionally, the BKT critical point is expected to modify the dynamics significantly and whether the universality holds out of equilibrium in this universality class still remains elusive. This is the main topic of this thesis, and the description of the specific dynamics that we probe is given in the next section.

1.4 The reverse Kibble-Zurek mechanism

In physical sciences, states or processes with *topological* features are often discussed in the context of being protected from perturbation [43, 44]. This relies on the robustness of topology that characterises the system, which therefore remains invariant under smooth perturbations.

In the context of BKT phases in 2D ultracold gases, the topological nature of the transition raise a question: what happens when the system is quenched into a topologically different phase? One particular experimental realisation of this idea, the dynamics after quench from quasi-ordered to thermal phase, was proposed by Mathey *et al.* [45, 46]. The dynamics of such a 2D system towards the thermal equilibrium with abundant vortices is predicted to be slowed down even in the presence of interaction[2]. Mathey coined the phrase *reverse*-Kibble-Zurek mechanism; the Kibble Zurek mechanism describes the dynamics after quenched into ordered phase, with topological defects (vortices) originating from local emergence of order parameters. In the *reverse* process, topological excitations are created from thermal fluctuations and there is relaxation into a thermal phase with abundant vortices. Fig. 1.3 illustrates these ideas.

In this thesis, we probe such phenomena in 2D quantum gases. We prepare a 2D Bose gas in the superfluid regime, and quench the system into the thermal regime by splitting an initial single cloud into two. We observe the time evolution of

[2]In 3D, such a slow thermalisation behaviour following a quench from the BEC phase was observed, with precise control of interactions [47, 48].

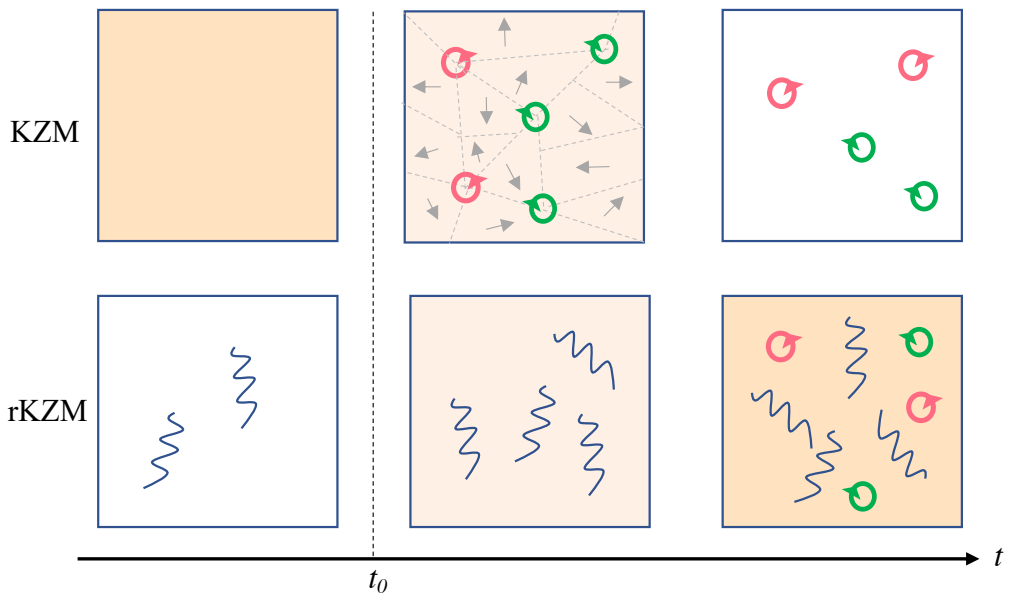

Figure 1.3: Illustration of the Kibble-Zurek mechanism (KZM) and the reverse Kibble-Zurek mechanism (rKZM). The colours of the panels indicate the state of the system, from (quasi-) ordered (white) to disordered (orange). (Top row) As the temperature of the system is rapidly ramped across the critical point towards the ordered phase, the so-called 'freeze-out' occurs when the growth of correlation length does not follow the quench rate; the spontaneous breaking of symmetry occurs locally, creating patches of well-defined phases (indicated by gray arrows with boundaries). At the intersection of patches, topological defects appear depending on the circulation of phases around the intersection (red and blue circulating arrows). The system equilibrates to a ordered phase but with topological defects depending on the quench speed. (bottom row) The rKZM starts with a quasi-ordered phase in the 2D system, quenched into a disordered phase with phonon and vortex excitations. The ordered phase in 2D supports phonon excitations, illustrated as small number of wavy lines. After the quench, phonon excitations rapidly equilibrate and only at longer times are thermally activated vortices expected.

the system towards the vortex-proliferated state using matter-wave interferometry technique, which provides the insight into the transient states in great detail. The experimental implementation of the splitting quench and the experimental results are presented in Chapter 6.

1.5 Overview of this thesis

In Chapter 2, we develop the theoretical basis for the remaining part of this thesis. We give a detailed description of interacting 2D Bose gases both in and out of equilibrium. In Chapter 3, we describe the experimental platform used to study the

BKT transition. The central technique is the multiple-RF dressed potential, and detailed technical considerations are given. In Chapter 4, we describe the analysis technique of matter-wave interference patterns to extract statistical properties of 2D gases, as well as other calibration methods to correctly characterise the 2D system. Chapter 5 is devoted to reporting our experimental observation of the BKT transition in equilibrium. Chapter 6 describes the dynamics of a 2D system quenched out of the BKT superfluid phase. In Chapter 7, we consider quantum tunneling between a pair of 2D gases, and report our work towards the realisation of bilayer 2D gases with controlled coupling. Finally, chapter 8 summarises the work and gives an overview of experimental prospects.

2

Theoretical Background

Contents

In this chapter, we review the theoretical description of the system of interest, namely weakly-interacting 2D Bose gases in harmonic traps. A phase transition

unique to 2D systems is the BKT transition, and this is described for a discrete system in the first section of this chapter. We then move on to a specific physical model of dilute Bose gases in 2D. We begin our analysis with a description of an ideal gas in a 2D harmonic trap, which exhibits saturation-driven Bose-Einstein condensation. Furthermore, we consider the crossover to the 3D regime as a function of temperature and axial confinement of the gas. Next, we introduce contact interaction between particles and examine various treatments of their effect. We consider the density and phase fluctuations separately, which prevail at different temperature regimes. We find that the phase fluctuation is the dominant contribution at low temperatures, and that the effective Hamiltonian in this regime can be mapped to the 2D XY model in which BKT transition occurs. We give detailed description of the phase fluctuation in 2D Bose gases including bilayer system consisting of two 2D gases with variable coupling. Finally, we remark on the non-equilibrium dynamics of 2D Bose gases quenched out of the BKT superfluid phase. We identify the connection of dynamical critical phenomena to equilibrium scaling and introduce renormalisation-group treatment of such physical phenomena.

2.1 The BKT transition

The microscopic theory of phase transition in 2D systems was first introduced by Berezinskii, Kosterlitz and Thouless [6, 7]. Detailed theoretical derivation is outside of the scope of this thesis, and we use a simplified argument to introduce the central concept of the theory.

The characteristic model of BKT theory is the so-called 2D XY model onto which, with certain conditions, many physical realisations of 2D systems can be mapped [49]. Consider a 2D square lattice of classical fixed-length spins $\mathbf{s}$ in 2D, with nearest-neighbour interactions of the form

$$H = -K \sum_{\langle i,j \rangle} \mathbf{s}_i \cdot \mathbf{s}_j = -K \sum_{\langle i,j \rangle} \cos(\theta_i - \theta_j), \tag{2.1.1}$$

where θ is the angle of the spin. In the continuous limit, and at low temperature where all spins are approximately aligned, expansion of Eq. (2.1.1) gives

$$H = K' \int (\nabla\theta(\boldsymbol{r}))^2 d^2r, \tag{2.1.2}$$

where K' generally differs from K. Two distinct types of excitations can be considered in 2D systems: phonons and vortices. Phonons are smooth deformations of phase field θ with wavevector k and the significant effect of the low-dimensional system is that phonons exist at any finite temperatures. On the other hand, the vortex excitations have integer multiples of 2π phase winding around a point, a *vortex core*. The main mechanism underlying the transition in 2D systems was identified by BKT to be vortex excitations [50]. While phonons are present in 2D systems at low temperature they are not strong enough to break the superfluidity; but vortex excitations destroy the quasi-order.

The presence of such a vortex-induced critical point can be identified in a simple argument in terms of the single vortex free energy $F_v = E_v - TS_v$, presented by Kosterlitz in Ref. [50]. We first consider the energy of a vortex placed at the centre of the system with circular geometry of radius R. The energy of such excitation is

$$E_v = K' \int_{\xi}^{R} \frac{1}{r^2} d^2r = 2\pi K' \ln\left(\frac{R}{\xi}\right), \tag{2.1.3}$$

where we introduce a short-range cutoff ξ; this is the lattice constant for discrete systems and for an atomic system the natural choice is the healing length that we introduce later.

The entropy associated with a vortex with area of its core $\pi\xi^2$ is related to the logarithm of the number of possibilities of spatial configurations. For a single vortex, this is given by $S_v = 2k_B \ln\left(\frac{R}{\xi}\right)$, which comes from the number of possible arrangements $\pi R^2/\pi\xi^2$: the area of the system divided by that of a single vortex. Finally, the free energy associated with a vortex is

$$F_v = E_v - TS_v = 2\pi(K' - \frac{k_B T}{\pi}) \ln\left(\frac{R}{\xi}\right) \tag{2.1.4}$$

We notice that this changes sign at $T_c = \pi K'/k_B$. At high temperature $T_c < T$, the vortex excitations are favoured while $T < T_c$ indicates stability against vortices; thus there is a sudden qualitative change in the behaviour of vortex excitations. Furthermore, while the vortex-proliferated system exhibits short-range coherence with exponential decay of correlation, the phonon-dominated low-temperature system has only algebraic decay of correlation [50]. The algebraic decay is extremely slow compared to the exponential decay (in fact the correlation length is divergent), and this change in the behaviour of correlation function constitutes a phase transition.

The illustration of the BKT transition in Fig 2.1 shows the discretised phase fields below (a) and above (b) the BKT transition, obtained by Monte Carlo simulation[1]. The long-distance behaviours of phases (angles of small arrows) is quasi-uniform in (a) while clear phase disruptions are evident in (b). The phase disruption is clearest around the vortices which are marked with black circles or squares, with different marker indicating a different winding direction of the phase around the vortex core. BKT theory predicts that vortices appear even in the quasi-ordered phase; however vortices of opposing signs of circulations are bound together and screen each other's effect at long distance, as illustrated in the left panel by locally disturbed phase field only around the pair of vortices. Such short-distance excitations are called bound vortex pairs, and short-distance physics in the proximity of the phase transition is strongly affected by these pairs. While the analytical treatment of such pairs is difficult, the renormalisation-group technique can correctly incorporate them through a series of renormalisations of the short-distance effects. This led to the precise derivation of the critical point in 2D system by BKT [6, 7], which was first confirmed experimentally by Bishop and Reppy [51], in 2D liquid helium.

The disruption of phase by vortices, in panels (a) and (b) can be clearly seen in phase profiles along a line, as plotted in (c) and (d). A more quantitative argument can be made using the correlation function $g_1(r) = \langle \boldsymbol{s}_i \cdot \boldsymbol{s}_j \rangle$ where the mean is taken over pairs of spins (i, j) with equal distance r, as well as over many

[1] using a python implementation in https://github.com/Shiling42/XY-MODEL

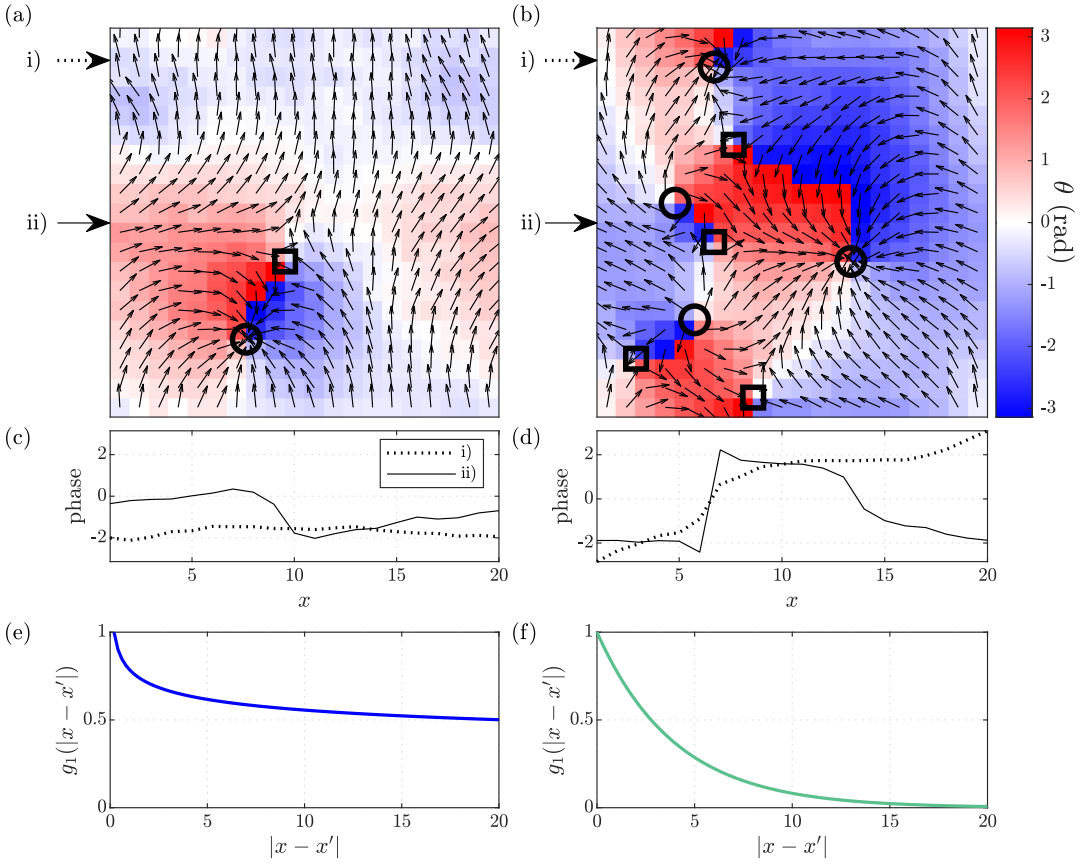

Figure 2.1: The illustration of phase fluctuations in the 2D XY model. Illustrations of the phase field on 2D lattice at low (a) and high (b) vortex density. (c,d) show the phase profile along lines indicated by arrows in upper panels. (e,f) plot the corresponding scaled correlation functions.

realisations of phase fields. The theoretically predicted correlation functions in superfluid and normal phases are plotted in Fig. 2.1 (e) and (f). There is a qualitative difference in these functions, with the low-temperature phase having maintained correlation at long distance. This is the result of quasi-long-range order with diverging correlation length. The correct functional form in the SF regime was derived by BKT [6, 50] to be an algebraic form $g_1(r) \propto r^{-\eta}$ with temperature-dependent exponent $\eta = T/4T_{\mathrm{BKT}}$. At higher temperature, the decay of correlations is much faster, following an exponential function [50]. From this, we see that the correlations decay to zero at infinite distance $r \to \infty$ in both phases, in accordance with Mermin-Wagner theorem [4, 5]. The temperature dependence

of η implies the value of η at the critical point,

$$\eta_c = 0.25. \tag{2.1.5}$$

This value is universal, meaning that this relation holds regardless of microscopic details of the physical system. However, the critical value is expected to be different for finite-size systems, with logarithmic dependence on the system size L [52],

$$\eta(L) = \frac{\eta(\infty)}{\left(1 + \frac{1}{2}\frac{1}{\ln(L)+C}\right)}, \tag{2.1.6}$$

with non-universal constant $C \sim 0.5$ [53]. For the square-lattice 2D XY model, the size L is defined by the size of the systetm in the number of lattice sites along one direction; in continuous systems, L is well approximated by the system size divided by the smallest length scale for the system dynamics, for example, the healing length for Bose gases.

The BKT transition occurs in a wide range of physical systems such as liquid helium [51], superconducting films [54], Josephson junction arrays [55], ultracold atoms [14] and polariton condensates [56], which all lie in the XY universality class. We will take a detailed look at the case of a dilute Bose gas in 2D harmonic trap in the rest of this chapter.

2.2 Ideal Bose gases in a 2D harmonic trap

We begin our analysis with a non-interacting gas in a 3D cylindrically-symmetric harmonic confinement with large anisotropy $\omega_r \ll \omega_z$. In contrast to the uniform 2D Bose gases in the thermodynamic limit where long-range order is precluded, this trapped system undergoes a BEC transition even in the strict quasi-2D case, as we see below.

2.2.1 Equation of state

We consider a harmonic trap with weak in-plane and tight axial confinement $V(r,z) = \frac{1}{2}m\omega_r^2 r^2 + \frac{1}{2}m\omega_z^2 z^2$ with large anisotropy $\omega_r \ll \omega_z$. For temperatures $\hbar\omega_r \ll k_B T \lesssim \hbar\omega_z$, we can treat the z degree of freedom quantum-mechanically while

radial kinetics is treated semiclassically. For this nonuniform system, we employ the local density approximation (LDA), in which we replace global chemical potential μ by $\mu - V(r)$. This gives a local density by integration over the Bose distribution [57]

$$\begin{aligned} n(r) &= \sum_{\nu=0}^{\infty} \int_0^{\infty} \frac{d(k^2)}{4\pi} \left\{ \exp\left[\beta \left(\frac{\hbar^2 k^2}{2m} + V(r) + \nu\hbar\omega_z - \mu \right) \right] - 1 \right\}^{-1} \\ &= -\frac{1}{\lambda_{\mathrm{th}}^2} \sum_{\nu=0}^{\infty} \ln\left(1 - e^{\beta\mu - \beta V(r) - \beta\nu\hbar\omega_z}\right), \end{aligned} \tag{2.2.1}$$

where $\beta = 1/k_B T$. An illustration of this density distribution is shown in Fig. 2.3. Firstly, we consider a situation where the 2D approximation is good $k_B T \ll \hbar\omega_z$, such that the population of axial excited states are negligible and only $\nu = 0$ contributes to Eq. (2.2.1). The total number of atoms are

$$N(T) = -\int d^2 r \frac{1}{\lambda_{\mathrm{th}}^2} \ln\left(1 - e^{\beta\mu - \beta V(r)}\right), \tag{2.2.2}$$

The critical atom number for the ideal-gas BEC transition is found by setting μ to zero. Eq. (2.2.2) can then be solved and gives

$$N_{\mathrm{c,2d}} = \frac{\pi^2}{6} \left(\frac{k_B T}{\hbar\omega_r} \right)^2, \tag{2.2.3}$$

or equivalently,

$$T_{\mathrm{c,2d}} = \frac{\sqrt{6N}\hbar\omega_r}{\pi k_B}. \tag{2.2.4}$$

This number coincides with the one obtained by a quantum-mechanical treatment of ideal Bose gases in a purely 2D harmonic trap in the thermodynamic limit; the maximum number of atoms that can be placed in excited states of a harmonic oscillator $V(r)$ is $N_{\mathrm{c,2d}}$, and atom number exceeding this value results in the macroscopic occupation of the ground state. It follows from Eq. (2.2.1) that the central phase-space density (PSD) $\mathcal{D} = n\lambda_{\mathrm{th}}^2$ at the critical point is divergent for a non-interacting gas.

2.2.2 Effect of the third dimension

When the temperature is higher than the harmonic-oscillator level spacing in axial potential $\hbar\omega_z < k_B T$, the system is allowed to explore the excited states in z direction, and it is expected that the condensation phenomena will smoothly converge towards conventional 3D BEC transition. This can be seen by incorporating $\nu > 0$ levels in Eq. (2.2.1), and the T_c can be found by numerically solving the implicit equation for given ω_z and N [57]

$$T_c = \alpha(N)/F(T_c), \tag{2.2.5}$$

where $\alpha(N) = Nh^2/(2\pi m k_B)$ and

$$F(T_c) = -\int d^2r \sum_{\nu=0}^{\infty} \ln\left[1 - \exp\left(\frac{-V(r) - \nu\hbar\omega_z}{k_B T_c}\right)\right]. \tag{2.2.6}$$

We plot the resulting critical temperatures, rescaled with the purely 2D result $T_{\mathrm{c,2d}}$ as a function of $\hbar\omega_z/k_B T_{\mathrm{c,2d}}$ in Fig. 2.2. We find that the critical temperature smoothly crosses over from 3D to 2D scaling at around $\hbar\omega_z/k_B T \sim 0.5$ where the quasi-2D scaling is defined as $T_c/T_{c,2d} = 1 - \exp(-\hbar\omega_z/k_B T_{c,2d})/2\zeta(2)^{3/2}$ [57]. For our typical experimental parameters the ratio $\hbar\omega_z/k_B T \gtrsim 1$ is comfortably in the 2D regime.

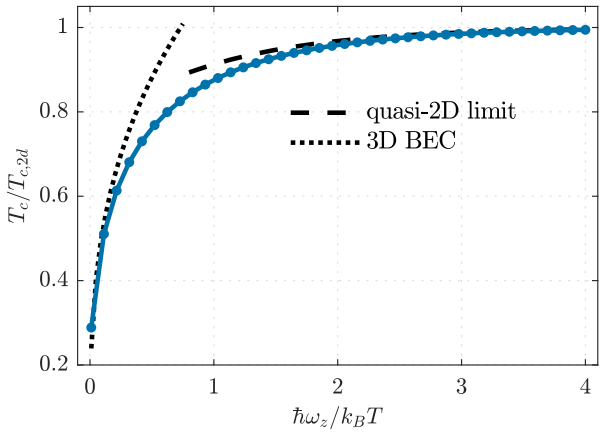

Figure 2.2: The condensation temperature in the 2D-3D crossover regime around $\hbar\omega_z \sim k_B T$. The dotted line is the scaling of the 3D BEC critical temperature in a 3D harmonic trap and the dashed line is the scaling for a 2D BEC.

2.3 Interacting Bose gases in 2D

We now introduce contact interactions between constituent particles. This changes the nature of the system fundamentally, beyond the change in equation of state caused by the addition of a mean-field potential. As we will see, it is found that the critical point that we reach in experiments with finite interaction is the interaction-driven BKT transition, instead of the saturation-driven BEC transition.

2.3.1 Interaction in quasi-2D Bose gases

To consider the interaction of 2D Bose gases, we first notice that the quasi-2D limit typically realised in the lab is insufficient for the scattering problem to be truly 2D [16, 49]. This is most easily seen by the comparison of the length scale of the system along the z direction, given by the Gaussian ground-state wavepacket with its characteristic size $\ell_0 = \sqrt{\hbar/m\omega_z} \sim 1\,\mu\text{m}$ to the 3D s-wave scattering length of ^{87}Rb atoms, $a_s \sim 5.3\,\text{nm}$ [58]. This means the scattering is still 3D, while the motion of atoms is constrained to 2D. As such, the a_s determines the interaction strength following [59]

$$g = \frac{4\pi\hbar^2 a_s}{m} \int dz\ \rho(z) \sim \frac{\sqrt{8\pi}a_s}{\ell_0}\frac{\hbar^2}{m}, \tag{2.3.1}$$

where $\rho(z)$ is the density distribution along the z direction and the last part is satisfied for quasi-2D limit, which is a good approximation for the range of parameters used in experiments reported in this thesis. For typical experimental parameters, we have dimensionless interaction strength $\tilde{g} = mg/\hbar^2 = \sqrt{8\pi}a_s/\ell_0 = 0.076$. We notice that the interaction strength $\tilde{g}$ possesses no intrinsic length scale associated with the in-plane physics. This is in contrast to the 3D case, where a_s is always relevant for the 3D dynamics. This leads to the scale-invariance of the system, which will be elucidated in Section 2.3.5. The effect of the third dimension, as discussed in Section 2.2.2, adds a correction to the interaction strength of the gas through the broadening of the wavefunction along the z direction. This effect can be incorporated into Eq. (2.3.1) and renormalises the interaction strength to $g_{\text{eff}} = g\sqrt{\tanh(\hbar\omega_z/2k_BT)}$ [57, 59].

2.3.2 Mean-field approach

We now approach the equation of state of 2D Bose gases using the mean-field treatment, which replaces the external potential $V(r)$ with $V_{\text{eff}}(r) = V(r) + 2gn(r)$. The significant effect of this is that the integration Eq. (2.2.2) can now be made arbitrarily large by setting appropriate μ. This means that the condensation phenomena is absent in an interacting system, at least in the mean-field picture. The critical point, if present, is then the interaction-mediated one, and we find that the BKT transition is the mechanism behind it as we see in the following sections.

Using the mean-field approach, we can make a prediction of the density distribution in a harmonic trap, at sufficiently high temperatures. For this, we revisit the expression for the local density Eq. (2.2.1) with the addition of a mean-field potential. To reach a self-consistent solution, we use an iterative approach given in Ref. [57]. The result is shown in Fig. 2.3, together with the ideal gas limit Eq. (2.2.1). We observe significant broadening of the density distribution as the interaction is increased, which is a direct consequence of additional mean-field potential around the centre of the trap.

For interacting gases, the effect of a third dimension has a known effect on the density distribution. We plot the radial density distribution for the weak quasi-2D limit $\tilde{\omega_z} = \hbar\omega_z/k_BT \lesssim 1$ in Fig. 2.3 on the right. The slope of the lines in Fig. 2.3 right panel represents the Gaussian width, which converges to the quasi-2D limit as we increase the value of $\tilde{\omega_z}$. By comparison of curves at different $\tilde{\omega_z}$, we find that $\tilde{\omega_z} \gtrsim 1$ is already a good approximation of the quasi-2D limit $\tilde{\omega_z} \gg 1$.

2.3.3 Suppression of density fluctuations

We now consider the fluctuation properties of 2D Bose gases. The full Hamiltonian of 2D Bose gases with contact interaction is

$$\hat{H} = \int d^2\boldsymbol{r}[\hat{\Psi}^\dagger(\boldsymbol{r})\frac{\hbar^2}{2m}\nabla^2\hat{\Psi}(\boldsymbol{r}) + \frac{g}{2}\hat{\Psi}^\dagger(\boldsymbol{r})\hat{\Psi}^\dagger(\boldsymbol{r})\hat{\Psi}(\boldsymbol{r})\hat{\Psi}(\boldsymbol{r})], \tag{2.3.2}$$

where $\hat{\Psi}(\boldsymbol{r})$ is the bosonic field operator at location $\boldsymbol{r}$. This neglects the harmonic potential, which will be incorporated using LDA later in this chapter. In Eq. (2.3.2),

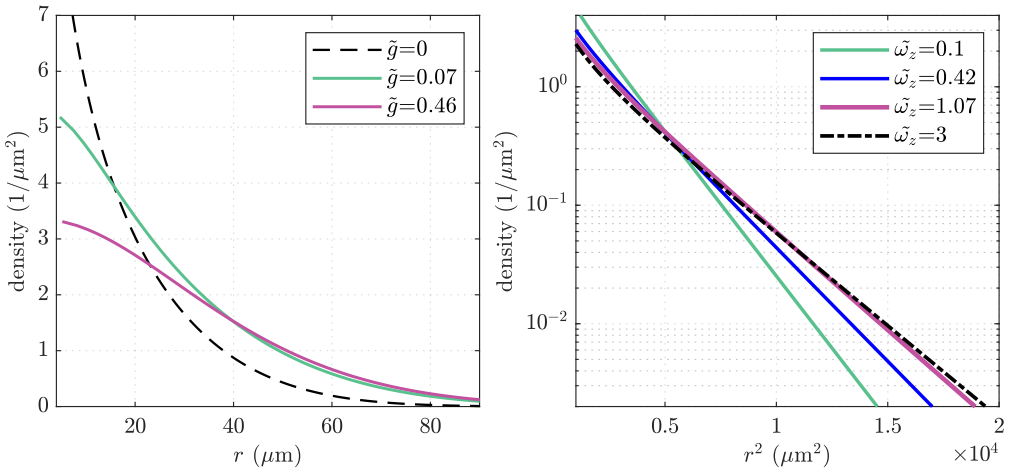

Figure 2.3: Mean-field density distribution in the harmonic trap. The temperature is set so that the system is deep in the thermal regime. (left) Density distribution from MF theory at varying interaction strength, calculated using (2.2.1) with peak chemical potential $\mu = 10^{-4}$. The black dashed line is the ideal gas prediction. (right) Density distribution at varying axial trapping frequency: $\tilde{\omega_z} = 0.1$ is close to 3D limit and $\tilde{\omega_z} = 3$ is deep in the 2D regime. The density distributions are shown in log-linear plot as a function of squared distance r^2, such that a Gaussian density distribution leads to a straight line.

the mean interaction energy is given by the $g\langle n^2\rangle/2$. So at sufficiently low temperature, if we keep the mean density fixed the energy is minimized by reducing the density fluctuations. The temperature regime for suppressed density fluctuation is thus found by comparing the thermal and interaction energies, $k_B T \ll g\langle n\rangle$ or

$$\mathcal{D} \gg \frac{2\pi}{\tilde{g}}, \tag{2.3.3}$$

where $\mathcal{D} = \langle n\rangle\lambda_{\text{th}}^2$ is the PSD of the system. As we will see in Section 2.3.5, $\mathcal{D} \gg 1$ is already a sufficient criteria for suppressed density fluctuation. This criteria is almost always satisfied for the range of parameters used in the experimental work of this thesis, except for the far edges of density distributions in harmonic trap which we only consider for thermometry of the gas. With the suppression of density fluctuations the kinetic term of Eq. (2.3.2) reduces to only having a contribution from phase fluctuation and we can approximate Eq. (2.3.2) to

$$H_{\text{eff}} = n\frac{\hbar^2}{2m}\int d^2\boldsymbol{r}(\nabla\varphi(\boldsymbol{r}))^2, \tag{2.3.4}$$

where we approximate the Bosonic field operator in terms of the density and phase, $\hat{\Psi}(\boldsymbol{r}) \sim \sqrt{n}e^{i\varphi(\boldsymbol{r})}$ and neglect the interaction term which is only an additive constant for the suppressed density fluctuation. We find from Eq. (2.3.4) that the 2D Bose gas at low temperature exhibits 'stiffness' against phase modulations. While this is a good approximation at $T \ll T_c$, as the temperature is increased close to the critical point the short-distance physics such as vortex pairs start to take effect and the population of thermal components without 'stiffness' becomes large. In such a case, we obtain an effective Hamiltonian describing the long-range behaviour of the system by replacing the total density n by the superfluid density $n_s < n$ [60].

Importantly, the effective Hamiltonian Eq. (2.3.4) is equivalent to the low-temperature (spin-wave) effective Hamiltonian of 2D XY model Eq. (2.1.1). Assuming that Eq. (2.3.4) is a good approximation near the critical point (as indeed it is, see Sec. 2.3.5), the critical point from the simplified argument in Section 2.1 can now be expressed for atomic systems as $T_c = \pi n_s \hbar^2/2mk_B$ by which we recover the well-known expression for the universal superfluid density at the critical point [60],

$$n_s \lambda_{\mathrm{th}}^2 = 4. \tag{2.3.5}$$

2.3.4 Classical-field approximation

While the mean-field approach works well in the normal regime, an alternative approach is needed at lower temperature in the fluctuation region. This is because near the critical point, the perturbative approach to the ideal-gas theory does not work well, as discussed in Ref. [17]. To better characterise the system in the fluctuation region, the field operators in Hamiltonian Eq. (2.3.2) can be treated as a classical field[2], which amounts to replacing $\hat{\Psi}(\boldsymbol{r})$ with a complex number $\psi(\boldsymbol{r})$. The resulting Hamiltonian is

$$H = \int d^2\boldsymbol{r} \left[\frac{\hbar^2}{2m} |\nabla\psi|^2 + V(\boldsymbol{r})|\psi|^2 + \frac{g}{2}|\psi|^4 \right]. \tag{2.3.6}$$

This approach has wide applicability, from the prediction of the critical point [17] to the detailed understanding of equation of state in the fluctuation region [18]. We will

[2]The temperature needs to be high enough that the quantum effects are not important; this is almost always satisfied for typical experiment with 2D Bose gases.

also use the classical-field Monte-Carlo simulation of our specific experimental system using this method to benchmark our experimental results, as presented in chapter 4.

Based on the classical-field simulation, the BKT critical point in weakly-interacting 2D Bose gases was predicted back in 2001 by Prokof'ev *et al.* [17]. The authors used the finite-size scaling of an uniform system to identify the superfluid critical point in 2D gas and obtained the critical total PSD for the BKT transition

$$\mathcal{D}_c = n_{\mathrm{tot}}\lambda_{\mathrm{th}}^2 = \ln\left(\frac{\xi}{\tilde{g}}\right), \tag{2.3.7}$$

with $\xi = 380(3)$ [17]. For our experimental parameters, we thus predict the critical PSD to be $\mathcal{D}_c = \ln(\xi/0.076) = 8.5$. Furthermore, the authors of Ref. [17] predicted the scaling of quasicondensate, defined by

$$Q = 2\langle|\psi^2|\rangle^2 - \langle|\psi|^4\rangle. \tag{2.3.8}$$

In terms of density we can define the quasicondensate density n_{qc} by $n_{\mathrm{qc}}^2 = 2\langle n\rangle^2 - \langle n^2\rangle$, which is zero for thermal gas with Gausssian fluctuation $\langle n^2\rangle = 2\langle n\rangle^2$ while the low-temperature gas with suppressed density fluctuation has $\langle n^2\rangle = \langle n\rangle^2$ and n_{qc} is equal to total density. The temperature scaling of the quasicondensates are given later in this chapter, in Fig. 2.4 and Fig. 2.5.

2.3.5 Universal, scale-invariant equation of state

As we have already seen in Section 2.3.1, the quasi-2D Bose gas possesses intrinsic scale-invariance, which is closely connected to the symmetry of the Hamiltonian [61]. As the interaction energy cannot provide an absolute energy scale, the only relevant scales are the chemical potential and temperature [62]; this means that the equation of state of the gas is expected to be only dependent on the ratio of chemical potential to temperature μ/k_BT for a given interaction strength $\tilde{g}$. This fact was confirmed in experiments using 2D Bose gases in harmonic traps [62, 63]. Furthermore, the authors of Ref. [17] pointed out that the interaction dependence can be absorbed by referencing the chemical potential to the value at critical point, using

$$X = \frac{\tilde{\mu} - \tilde{\mu}_c}{\tilde{g}}, \tag{2.3.9}$$

where $\tilde{\mu} = \mu/k_BT$ and $\tilde{\mu_c}$ is the rescaled critical chemical potential $\tilde{\mu_c} = \frac{\tilde{g}}{\pi}\ln\left(\frac{13.2}{\tilde{g}}\right)$. This leaves the equation of state only dependent on X, realising a universal description in the fluctuation region. This remarkable feature was confirmed experimentally with harmonically-trapped 2D Bose gases using LDA in Ref. [62–64]. Fig. 2.4 shows a universal curve of total, quasicondensate and superfluid density, based on the calculation in [18].

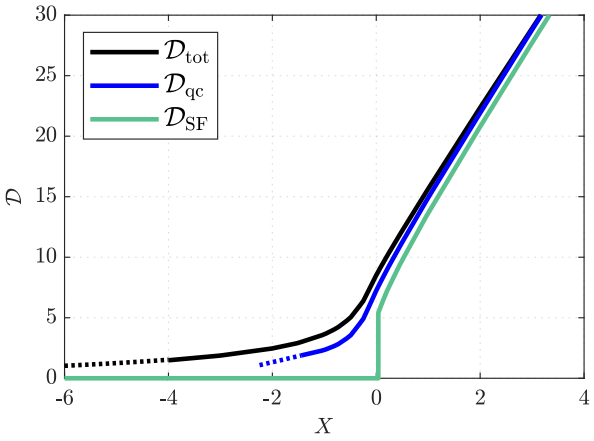

Figure 2.4: Universal equation of state around the critical point in 2D Bose gases, data obtained from [18]. The PSD of total, quasicondensate and superfluid components are plotted against the unitless parameter X. The dotted black line is the Hartree-Fock mean-field (HFMF) prediction of the total density distribution [65], which smoothly connects to the results of [18].

2.3.6 Application of the universal EOS to trapped gases

While the universal description of 2D Bose gas above was derived for an uniform system, the predictions in Fig. 2.4 can be applied to harmonically-trapped 2D Bose gases by invoking the LDA[3] which amounts to replacing the chemical potential with a local effective quantity,

$$\mu_{\rm loc}(r) = \mu - \frac{m\omega_r^2 r^2}{2}. \tag{2.3.10}$$

[3]The applicability of the LDA in an interacting 2D gases in a harmonic trap was discussed in Ref. [66] in which the authors demand the condition $\hbar\omega_r < \tilde{g}k_BT$ for LDA to be reasonable; this is always satisfied for the range of parameters used in this thesis.

Using this, we show in Fig. 2.5 the predicted density profiles in a harmonic trap for three different values of peak chemical potentials. The universal description is only applicable in the fluctuation region $|X| \lesssim 4$ and we have observed that the extension of the description to normal regime $X < -4$ often results in negative density. To correctly characterise the low-density region at the far edges of trap, we use mean-field prediction shown in 2.3.1 with quasi-2D limit ($\tilde{\omega_z} \to \infty$). The obtained MF density distribution smoothly connects to the universal description at $X \sim -2$.

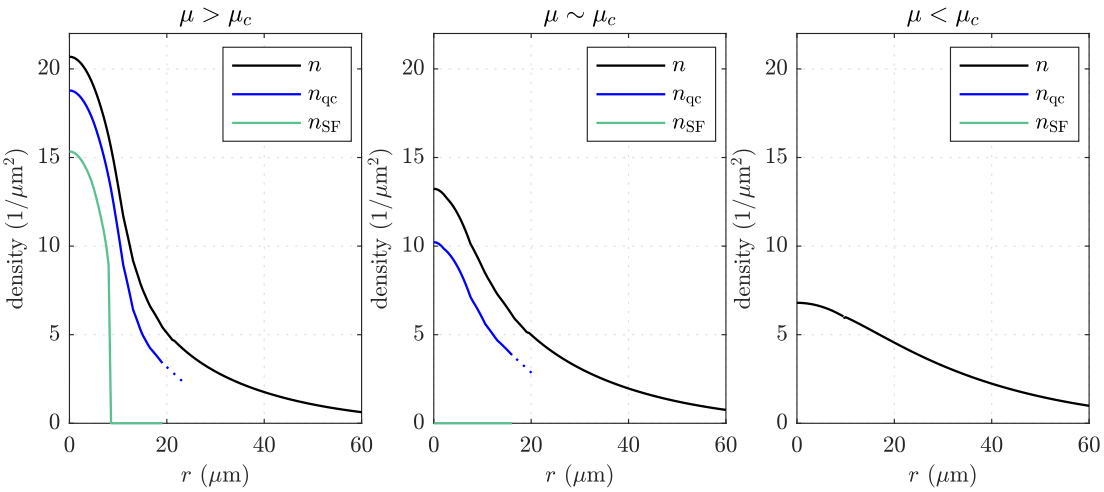

Figure 2.5: Density profiles of total (black), quasicondensate (red) and superfluid (blue) components. Central chemical potentials are $\mu/\mu_c = 1.2, 0.9$ and 0.4. from left to right, interaction strength $\tilde{g} = 0.076$ and the radial trap frequency is $\omega_r/2\pi = 11$ Hz. The temperature of the gases are 65, 71 and 84 nK, chosen such that total atom number is 5×10^4.

From Fig. 2.5, the qualitative difference in the density distribution is evident between different peak chemical potentials, below $\mu < \mu_c$ and above the critical point $\mu_c \lesssim \mu$; a narrow central peak consisting of large fraction of quasicondensate appears above the critical chemical potential.

To fully characterise the emergence of bimodal distribution, we plotted the total density distributions over a wider range of peak chemical potentials in Fig. 2.6 (left panel). We observe the gradual emergence of a central peak around $r^2 \lesssim 500$, on top of a broader Gaussian distribution.

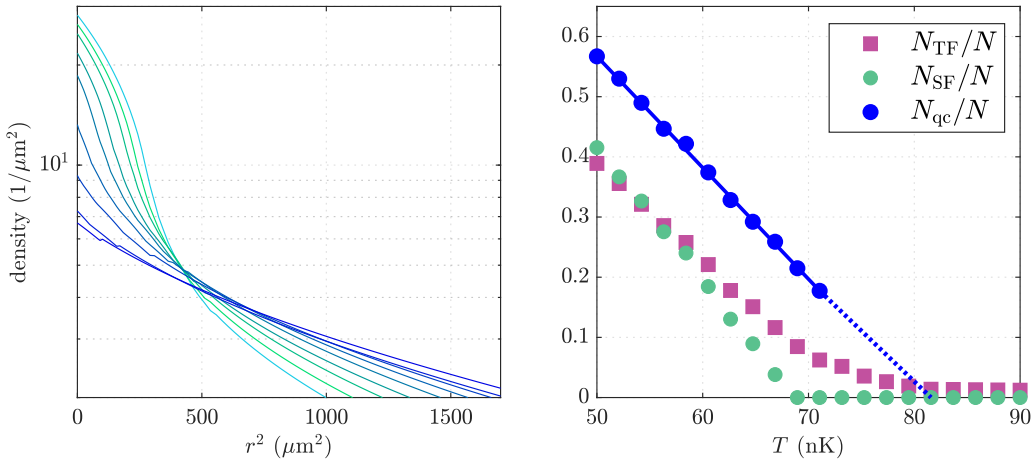

Figure 2.6: Emergence of a bimodal density distribution and two-step transition. (left) Density distribution of a harmonically-trapped 2D Bose gas, with peak chemical potentials from $\mu/\mu_c = 0.13$ (blue) to $\mu/\mu_c = 3.7$ (green). The temperature of the gas was chosen such that total atom number is around 5×10^4. (right) The fraction of atoms in the Thomas-Fermi peak (purple, square), superfluid component (green, circle) and quasicondensate component (blue, triangle) in a harmonic trap. The blue dotted line is the linear extrapolation of the quasicondensate fraction data.

For more quantitative comparison, we have fitted the density distribution with a bimodal model,

$$f(r) = ae^{-x^2/2\sigma_r^2} + b\max(1 - x^2/R^2, 0), \tag{2.3.11}$$

where the first term is responsible for the broad Gaussian of normal gas and the second term arise from the Thomas-Fermi density profile of low-momentum modes in a harmonic trap [67]. The Fig. 2.6 right panel shows the fraction of atoms in the inverted parabola (Thomas-Fermi peak), along with the fraction of atoms in the superfluid and quasicondensate components. The superfluid component shows a sharp onset at around $T_{\mathrm{SF}} \sim 70\,\mathrm{nK}$ as a result of finite jump in its density at the transition, and increases linearly. The Thomas-Fermi component however emerges smoothly below $T_{\mathrm{TF}} \sim 80\,\mathrm{nK}$. The emergence of bimodality, often referred to as the superfluid transition, is more accurately attributed to the emergence of significant quasicondensate fraction for the range of interaction and trap configurations that is typically used in our experiment. The middle panel of Fig. 2.5 illustrates this situation well; the total density shows a clear bimodal shape, with central peak

consisting of large fraction of quasicondensate and no superfluid. As such, we treat the critical point T_{TF} separately from the superfluid critical point, and refer to it as the quasicondensate critical point.

2.3.7 Critical point in a harmonic trap

So far, we have seen that the superfluid transition in a 2D Bose gas occurs at a critical total PSD Eq. (2.3.7), as well as reviewed the theoretical prediction of the density distribution in harmonic trap. Combining both, we can make a prediction of the superfluid critical point in a harmonic trap, as a function of total atom number and temperature which is a more straightforward guide for our experimental work. According to Ref. [68], the analytical expression for such a critical point is

$$T_{\mathrm{BKT}} \simeq T_{\mathrm{c,2d}} \left[1 + \frac{3\tilde{g}}{\pi^3} \ln^2\left(\frac{\tilde{g}}{16}\right) + \frac{6\tilde{g}}{16\pi^2}\left(15 + \ln\frac{\tilde{g}}{16}\right)\right]^{-1/2}. \tag{2.3.12}$$

In Fig. 2.7, we show the phase diagram of 2D Bose gases in a harmonic trap. The superfluid phase boundary obtained from Eq. (2.3.12) agrees with the classical-field result of Ref. [18] with LDA.

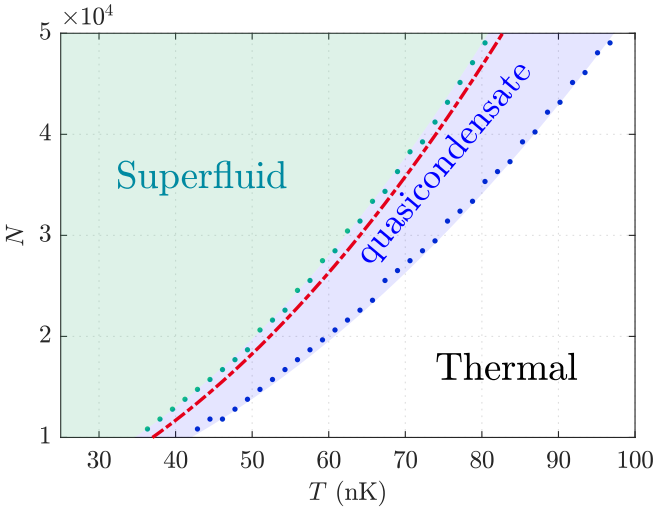

Figure 2.7: Phase diagram of harmonically-trapped 2D Bose gases, obtained by the application of classical-field results in Ref. [18] to a harmonic trap with $\omega_r/2\pi = 11$ Hz using the LDA as described in Section 2.3.6. The green points indicate the onset of finite superfluid fraction and blue points are the atom number where 10 % quasicondensate fraction is observed when increasing the atom number at fixed temperature. The red dashed line is the analytical expression for the superfluid transition in harmonic trap, Eq. (2.3.12).

2.4 Phase fluctuation in 2D Bose gases

As already pointed out with Eq. (2.3.4), interacting 2D Bose gases at low temperature are dominated by phase fluctuations, characterised by the phase stiffness Hamiltonian in Eq. (2.3.4). As described in Section 2.1, the equivalent model of the 2D XY model possess a superfluid critical point while being dominated by fluctuations at any nonzero temperature. We give a detailed description of the properties of phase fluctuations in 2D Bose gases and extend the theory to harmonically-trapped and bilayer 2D Bose gases which are of interest in order to understand the experimental results.

2.4.1 Phase correlation function

In a uniform quasi-2D Bose gas in the vicinity of BKT critical point, density fluctuations are strongly suppressed and excitations are limited to phase modes. As a result, the long-distance behaviour of the first-order correlation function reduces to a *phase* correlation function,

$$g_1(\boldsymbol{r}, \boldsymbol{r}') = \langle \Psi^\dagger(\boldsymbol{r})\Psi(\boldsymbol{r}')\rangle \sim n\langle e^{i(\phi(\boldsymbol{r})-\phi(\boldsymbol{r}'))}\rangle. \tag{2.4.1}$$

Since the BKT critical point is below the quasicondensate critical point, we expect the BKT transition to be observed through an investigation of phase correlation functions.

So far, several experimental attempts have been made to characterise the phase fluctuation of trapped 2D Bose gas. The first attempt used the matter-wave interference contrast [14] of a stack of several 2D gases. This quantity is related to the average phase coherence of the system [69]. Another method used the density noise of a single 2D cloud after free expansion, as a result of interference between separate parts of the cloud during the expansion [70]; the power spectrum of this density noise is related to the phase coherence of the system [71].

As we describe in Chapter 3, we performed experiments to locally probe the phase fluctuation of a 2D system by a matter-wave interferometry technique, with an addition of a density slicing method. This allows us to directly compute the phase

correlation function in Eq. (2.4.1) from the experimental data as described in detail in Chapter 5.

2.4.2 Phase fluctuation in an inhomogeneous system

The LDA treats the inhomogeneity of trapped Bose gases by replacing the global chemical potential with a local one defined by $\mu - V(r)$. The assumption for LDA is that within a length scale shorter than any significant change in $V(r)$, *local* equilibration is established. In this spirit, the phase fluctuation properties can be treated to obtain the approximate form of correlation decay in an inhomogeneous system. The authors of Ref. [26] proposed applying LDA to the correlation properties of the 2D gas by comparing the LDA treatment of phase fluctuation to spin-wave theory in the presence of a harmonic trap. This procedure of LDA for phase fluctuations is called *local correlation approximation* (LCA); the essence of the procedure is the replacement of the algebraic exponent η by a local one $\eta(\boldsymbol{r}, \boldsymbol{r}')$,

$$\eta(\boldsymbol{r}, \boldsymbol{r}') = \eta_0 \frac{n_0}{\sqrt{n(\boldsymbol{r}) n(\boldsymbol{r}')}}, \tag{2.4.2}$$

where η_0 is the local algebraic exponent at the centre of the trap and n_0 is the peak density. We compare the correlation function for inhomogeneous and uniform systems in Fig. 2.8.

2.4.3 Density fluctuation after free expansion

An intriguing consequence of the phase fluctuation in 1D and 2D quasicondensates is the appearance of characteristic density fluctuation after free expansion, due to the interference of separate parts of the same cloud during the TOF. In 1D, the phase fluctuations translate into strong density fluctuations along the transverse direction and such an effect was extensively studied in both single-well and double-well cases [72]. In a double-well configuration, the density correlation analysis gave the effective temperature of the common phase degrees of freedom, providing a complementary observable to the relative phase measurements based on matter-wave interference [73]. In 2D, some theoretical and experimental results [70–72, 74]

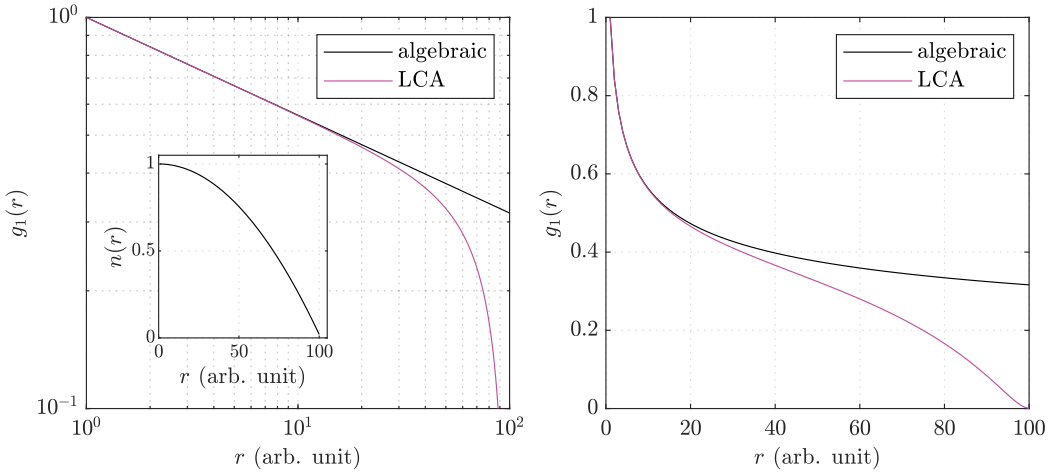

Figure 2.8: Local correlation approximation for the correlation function. Normalised correlation function in a uniform (black) and inhomogeneous (purple) systems are shown, on both panels with different axes scaling. The inset shows the Thomas-Fermi density distribution used to calculate the correlation function with LCA.

confirm the appearance of a characteristic density power spectrum. The density correlation function is defined by

$$g_2(\boldsymbol{r}_1, \boldsymbol{r}_2) = \frac{\langle n(\boldsymbol{r}_1) n(\boldsymbol{r}_2) \rangle}{\langle n(\boldsymbol{r}_1) \rangle \langle n(\boldsymbol{r}_2) \rangle}, \tag{2.4.3}$$

where the expectation is taken over an ensemble of realisations. The density correlation function can be probed by the experimental technique that was employed in this thesis (see Section 5.4.2); the two-point correlation function of the sliced density corresponds to Eq. (2.4.3) with correction due to the finite thickness L_y and finite imaging resolution.

2.5 Bilayer 2D gases

Motivated by our specific experimental system of double-well 2D Bose gases, we now consider coupled bilayer 2D systems. The effective low-temperature Hamiltonian Eq. (2.1.2) becomes [75]

$$\begin{aligned} H =& K_1 \int (\nabla \phi_1(\boldsymbol{r}))^2 d^2\boldsymbol{r} + K_2 \int (\nabla \phi_2(\boldsymbol{r}))^2 d^2\boldsymbol{r} \\ &+ J \int \cos(\phi_1(\boldsymbol{r}) - \phi_2(\boldsymbol{r})) d^2\boldsymbol{r}, \end{aligned} \tag{2.5.1}$$

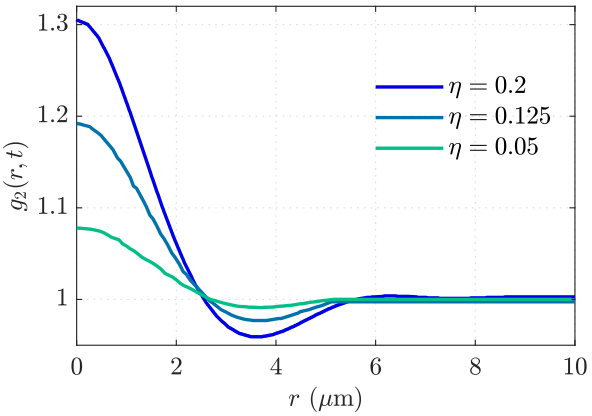

Figure 2.9: Theoretical prediction of the correlation function after 3 ms TOF in the superfluid regime, obtained from Ref. [71]. Calculation was performed for an uniform system and assuming no *in situ* density fluctuations.

where $\phi_i(\boldsymbol{r})$ with $i = 1, 2$ are the phases of layers 1 and 2, respectively. The linear coupling of the two layers is characterised by energy scale J [76]. Usually, such a situation is studied via symmetric and antisymmetric superpositions of the phases in each layer,

$$\theta(\boldsymbol{r}) = \phi_1(\boldsymbol{r}) - \phi_2(\boldsymbol{r}),$$
$$\varphi(\boldsymbol{r}) = \phi_1(\boldsymbol{r}) + \phi_2(\boldsymbol{r}).$$

The Hamiltonian Eq. (2.3.4) can now be expressed in terms of $\theta(\boldsymbol{r})$ and $\varphi(\boldsymbol{r})$,

$$H_{\text{tot}} = H_{\text{a}} + H_{\text{s}} + H_{\text{m}}, \tag{2.5.2}$$
$$H_a = (K_1 + K_2) \int (\nabla\theta(\boldsymbol{r}))^2 d^2\boldsymbol{r} + J \int \cos(\theta(\boldsymbol{r})) d^2\boldsymbol{r}, \tag{2.5.3}$$
$$H_s = (K_1 + K_2) \int (\nabla\varphi(\boldsymbol{r}))^2 d^2\boldsymbol{r}, \tag{2.5.4}$$
$$H_m = (K_1 - K_2) \int \nabla\theta(\boldsymbol{r}) \nabla\varphi(\boldsymbol{r}) d^2\boldsymbol{r}. \tag{2.5.5}$$

We thus see that with $K_1 = K_2$, the mixing Hamiltonian becomes zero, $H_m = 0$, and the symmetric and antisymmetric degrees of freedom decouple.

In atomic systems, the condition for decoupling of symmetric and antisymmetric modes is the same density in the two layers $n_1 = n_2$. Such decoupling should be treated with care in 2D atomic systems; while the density fluctuations are suppressed in each of the layers at sufficiently low temperature, careful treatment of their effect

in a bilayer system is needed to confirm the decoupling of phases $\theta(\boldsymbol{r})$ and $\varphi(\boldsymbol{r})$. In the special case of a pair of 1D gases, the symmetric and antisymmetric modes decouple and stay out of equilibrium for an extended period of time following a quench [31]. In the following, we look at equilibrium properties of bilayer 2D Bose gases for the two separate cases of zero coupling $J = 0$ and finite coupling $J > 0$.

2.5.1 Decoupled layers

We first take a look at the case of $J = 0$, a pair of independent 2D Bose gases. In atomic systems, this can be realised by a sufficient spatial separation of the two layers and most of our experimental investigation focuses on such a scenario, as detailed in Chapters 5 and 6. As we briefly described in Chapter 1, our main experimental observables for the 2D Bose gases are the relative phases $\theta(\boldsymbol{r})$. In this section, we describe the connection of relative phase fluctuation properties and the physics of a single 2D system, such as the BKT transition.

In the following, we show that spatial correlation of the relative phases $\theta(\boldsymbol{r})$ is related to the one-body correlation function $g_1(\boldsymbol{r}, \boldsymbol{r}')$ of individual layers in the absence of the coupling J. We start by considering the two-point correlation of relative phases of two independent clouds:

$$C(\boldsymbol{r}, \boldsymbol{r}') := \frac{\langle \Psi_1(\boldsymbol{r})\Psi_2^\dagger(\boldsymbol{r})\Psi_1^\dagger(\boldsymbol{r}')\Psi_2(\boldsymbol{r}')\rangle}{\langle|\Psi_1(\boldsymbol{r})|^2\rangle\langle|\Psi_2(\boldsymbol{r}')|^2\rangle}, \tag{2.5.6}$$

where $\Psi_j(\boldsymbol{r})$ are the bosonic field operators at location $\boldsymbol{r}$ of clouds ($j = 1, 2$). We describe $\Psi_j(\boldsymbol{r})$ in terms of the density-phase representation as $\Psi_j(\boldsymbol{r}) = \sqrt{n_j(\boldsymbol{r})}e^{i\phi_j(\boldsymbol{r})}$. Assuming uniform and equal density $n_j(\boldsymbol{r}) \sim n_{2\mathrm{D}}$ for each cloud and small density fluctuations we can simplify the expression to $\Psi_j(\boldsymbol{r}) \sim \sqrt{n_{2\mathrm{D}}}e^{i\phi_j(\boldsymbol{r})}$. Writing the relative phase of the two fields $\theta(\boldsymbol{r}) = \phi_1(\boldsymbol{r}) - \phi_2(\boldsymbol{r})$ gives

$$C(\boldsymbol{r}, \boldsymbol{r}') = \langle e^{i(\theta(\boldsymbol{r})-\theta(\boldsymbol{r}'))}\rangle, \tag{2.5.7}$$

which is the phase correlation function of relative phases $\theta(\boldsymbol{r})$ that we probe experimentally throughout this thesis. If the two clouds in the double-well are decoupled, the fields $\Psi_1(\boldsymbol{r})$ and $\Psi_2(\boldsymbol{r})$ are fluctuating independently. Furthermore,

assuming that the two clouds are identical and have the same correlation function $g_1(\boldsymbol{r}, \boldsymbol{r}')$, we find

$$C(\boldsymbol{r}, \boldsymbol{r}') \simeq \frac{\langle \Psi^\dagger(\boldsymbol{r})\Psi(\boldsymbol{r}')\rangle^2}{\langle|\Psi(\boldsymbol{r})|^2\rangle\langle|\Psi(\boldsymbol{r}')|^2\rangle} = \frac{g_1(\boldsymbol{r}, \boldsymbol{r}')^2}{n_{2\mathrm{D}}^2}. \tag{2.5.8}$$

As such, we find that the phase correlation function $C(\boldsymbol{r}, \boldsymbol{r}')$ is closely related to the first-order correlation function.

2.5.2 The effect of finite coupling strength

We now take a look at the effect of coupling $J > 0$. In the limiting case of infinite coupling $J \to \infty$, the phases in two layers ϕ_1, ϕ_2 are forced to align $\phi_1(\boldsymbol{r}) = \phi_2(\boldsymbol{r})$. If $K_1 = K_2$, we arrive at a simple effective Hamiltonian [76]

$$H_{tot} = 2K_1 \int (\nabla\phi_1(\boldsymbol{r}))^2 d^2r. \tag{2.5.9}$$

This is the same as the single-layer case but with twice the coefficient K because of the presence of second layer. We thus expect that in the presence of strong coupling, the BKT critical temperature will be doubled, $T_{c,\mathrm{bilayer}} = 2T_c$.

At intermediate strength of the coupling J with identical layers $K_1 = K_2$, the effective Hamiltonian for the antisymmetric degree of freedom Eq.(2.5.3) is

$$H_a = 2K \int (\nabla\theta(\boldsymbol{r}))^2 d^2r + J \int \cos(\theta(\boldsymbol{r}))d^2r. \tag{2.5.10}$$

From the two limiting cases $J = 0$ and $J = \infty$, we expect the BKT critical temperature to smoothly change from T_c to $2T_c$ as the coupling strength is increased. Furthermore, it is found that the competition of thermal, interaction and phase-locking energy scales in such a system results in a rich variety of novel phases, as predicted in theoretical works [75–77]. In addition, many intriguing NEQ phenomena can be probed by dynamically modulating the coupling strength J. One example is a sudden quench of the J from zero to a finite value, with phase-imbalanced initial state. The relaxation towards the phase-locked equilibrium state and its relation to the sine-Gordon model is a subject of theoretical interest [78–80]. An opposite quench can be considered, in which a phase-locked state is prepared and the J is

suddenly turned to zero. The relaxation dynamics towards equilibrium, as well as the relation to BKT critical phenomena, has been studied theoretically [45, 81]. We have performed experiments where the time evolution is investigated after quenching the bilayer coupling to a finite value from close to zero as described in Chapter 7.

2.6 Non-equilibrium dynamics across a critical point

Non-equilibrium critical dynamics are ubiquitous, including the boiling of water, rapid financial market crashes [82] and the emergence of structure in early universe [42]. Their intriguing connection to universal equilibrium critical scaling is an active field of study [2]. In a typical experimental setting, the Hamiltonian of the system is quenched or ramped to a different one which (in equilibrium) corresponds to a different phase; the system is then expected to evolve towards the new equilibrium characteristic of the new phase. This is schematically illustrated in Fig. 2.10.

The relaxation dynamics is generally affected by the presence of a critical point even in the simplest case of dynamics with a single timescale. For example, the emergence of a global order parameter after a dynamical second-order phase transition is related to the equilibrium universality class, through the Kibble-Zurek mechanism [2]. More complex relaxation dynamics may occur, which has multiple timescales with nontrivial transient states often surviving for an extended period of time. An example of this is the critical slowing down as a precursor of sudden dynamical transition [82].

2.6.1 Renormalisation group theory

Universal critical phenomena, both in and out of equilibrium, are often closely related to renormalisation group (RG) theory. Intuitively, RG theory treats a given system characterised by a small set of parameters $\{s_i\}$ in successively coarse-grained spatial scales. With an appropriate choice of rescaling protocol, each coarse-graining step can be constructed so that it only changes the set of parameters $\{s_i\} \to \{\tilde{s}_i\}$ while keeping the equation of motion unchanged. The set of parameters $\{s_i\}$

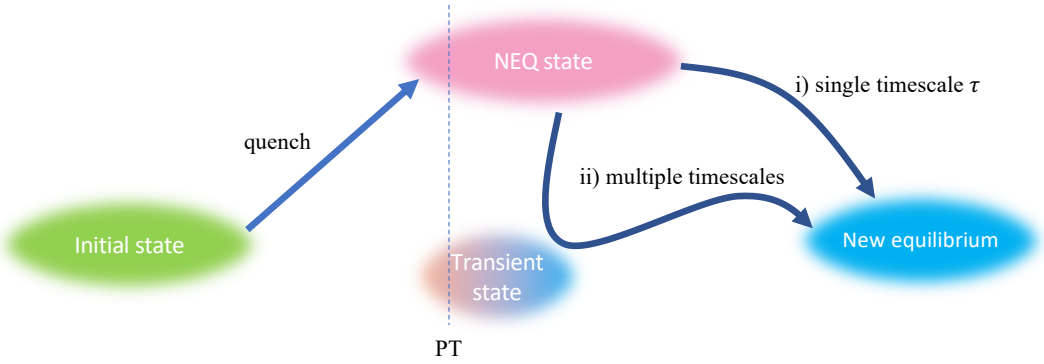

Figure 2.10: Emergence of an equilibrium distribution following a quench across phase transition (PT). A quench is a sudden (non-adiabatic) change that takes an initial equilibrium system (green, left) to the other side of the PT with a non-equilibrium (NEQ) distribution (purple, top). Since the NEQ state often cannot be rigorously attributed to either side of phase transition, the NEQ state is distributed across the phase boundary (dotted line). From the NEQ state, various distinct relaxation dynamics towards the equilibrium state (blue, right) are expected, of which two cases are shown. i) The simplest case of single timescale towards the equilibrium. ii) Generally, more complex dynamics occurs with multiple timescales, e.g. when there are multiple excitations involved at the interface of distinct phases, or when the presence of critical point significantly alters the rate of equilibration.

that stay relevant under the coarse-graining are the fundamental properties of the phase transition relevant at all length scales, and these are the important quantities characterising the universality class of the phase transition [83]. For infinitesimal coarse-graining steps, for example of the length scale $r \to r(1 + dl)$, the change in the parameters is often expressed in terms of differential equations, which are called RG flow equations.

As an example, we briefly introduce the BKT renormalisation group which was used to formally prove the BKT transition in 2D XY model [50]. System parameters of interest are the vortex fugacity $g_v = e^{-\epsilon_c}$, where ϵ_c is the vortex core energy, and the coupling strength K/T, and the renormalisation of length scale integrates out the short-range physics such as paired vortices, to obtain new parameters $\{g_v, K/T\}$. As the short-range physics is successively integrated out, we are left only with long-distance physics such as free vortices and spin-waves. The

BKT RG procedures can be expressed by coupled differential equations [50]

$$\begin{aligned}\frac{dx}{dl} &= -\frac{(x+2)^3 y^2}{8l}, \\ \frac{dy}{dl} &= \frac{xy}{l},\end{aligned} \tag{2.6.1}$$

where $x = \pi K/T - 2$ and $y = be^{-\beta\epsilon_c}$; here b is a model-specific nonuniversal constant and ϵ_c denotes the vortex core energy. In Fig. 2.11, we show the RG *flow* diagram of Eq. (2.6.1). We notice $x = 0$ separates two distinct regimes under the evolution of l. At high temperature $x > 0$, the y goes to infinity at the long-l limit; this indicates that the vortex energy is close to zero, and vortex excitations can occur at effectively no cost, whereas $x < 0$ means $y \to 0$ so that the vortex excitations are suppressed, and we expect quasi-order in the system. Indeed, a critical point can be identified by nontrivial fixed points of an RG flow, i.e. $\frac{dx}{dl} = \frac{dy}{dl} = 0$ and $T \neq 0, \infty$ [84]. This gives $T_c = \pi K/2$, in agreement with the single-vortex argument in Sec. 2.1 [50].

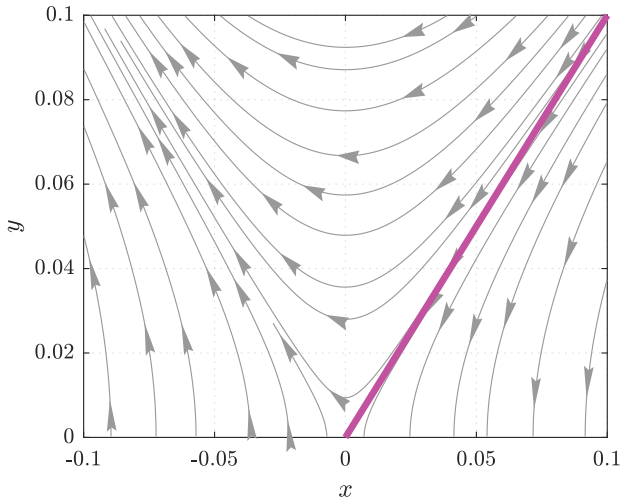

Figure 2.11: Plot of BKT RG flow, Eq. (2.6.1) near $x = y = 0$. The arrows indicate increasing l. The purple thick line separates two regimes with different $l \to \infty$ asymptote, $y \to 0$ (below the line) or $y \to \infty$ (above the line or $x < 0$), separating the two BKT phases.

2.6.2 Real-time RG

Even for a well-understood equilibrium phase transition, its non-equilibrium counterpart is generally very difficult to treat analytically. Therefore, a wide variety of theoretical tools have been imported from theories of equilibrium phase transition to tackle non-equilibrium dynamics across a critical point, e.g. real-time RG treatments have been used to predict various dynamical critical phenomena [85, 86]. For the non-equilibrium BKT critical dynamics, an RG-based treatment was proposed in Refs. [45, 46]; the situation considered in these works is the *dynamical vortex unbinding*, which occurs after quenching the system from superfluid to thermal phase.

After suddenly increasing the effective temperature of a 2D system above T_c, the unbinding of vortex pairs into free vortices is expected to be slow because of their energy barriers [45]. The goal of the real-time RG treatment of the non-equilibrium BKT transition is to precisely predict the vortex unbinding dynamics, from a non-equilibrium initial condition of 2D system after a sudden quench. In the following, we treat a system prepared in a non-equilibrium initial state characterised by algebraic exponent η and vortex fugacity g_v at time t_0. We then aim to study its long-time, long-distance behaviour towards equilibrium by coarse-graining the time and space simultaneously, in a similar manner to the spatial coarse-graining of equilibrium RG treatment. Formally, one step of rescaling is done for spatial and temporal coordinates r and t, by $r \to r(1+dl)$ and $t \to t(1+dl)$. The resulting RG equations are then given in terms of 'flow' parameter l. For simplicity, we use time instead of the flow parameter by $t = t_0 e^l$ [46], which gives

$$\begin{aligned} \frac{dg_v}{dt} &= \left(2 - \frac{1}{2\eta}\right)\frac{g_v}{t}, \\ \frac{d\eta}{dt} &= \frac{4\pi^2 g_v^2}{\eta t}. \end{aligned} \tag{2.6.2}$$

From the time evolution obtained from Eq. (2.6.2), the dynamics of vortex density in non-equilibrium system can be obtained by the mean-field relation of vortex density n_v and g_v, η [87],

$$n_v(t) \propto \exp\left[-\frac{2\ln\left(\frac{g_v(t)}{2}\right)}{\frac{1}{2\eta(t)} - 2}\right]. \tag{2.6.3}$$

We plot the time evolution of η and n_v with selected initial conditions in Fig. 2.12. With the initial conditions used in Fig. 2.12, the η flows to infinity and indicates the transition into thermal state; this is due to relatively high $g_v(t_0)$ values. The temporal growth of η is linear at long time, while n_v scales exponentially in time with varying time for the onset of sharp increase in vortex density.

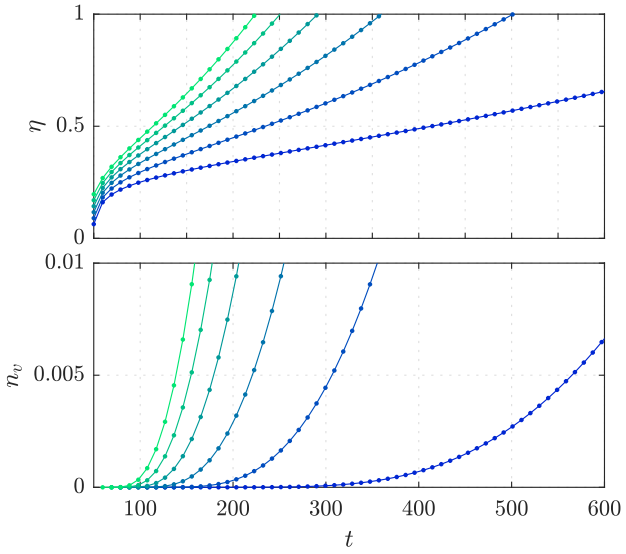

Figure 2.12: The numerical solution of the real-time RG equation Eq. (2.6.2). The initial condition at $t_0 = 50$ was $g_v(t_0) = 0.05$ and $\eta(t_0)$ ranges from 0.04 (blue) to 0.22 (green).

Furthermore, we have fitted the numerical solution of RG equations in Fig. 2.12 to obtain the dependence of these dynamics to the initial temperature $T = 4\eta_0 T_{\mathrm{BKT}}$. We use a linear function $f(t) = \kappa t + b$ for the time evolution of η and exponential model $f(t) = n_c e^{(t-t_0)/\gamma}$ for the vortex density, as shown in Fig. 2.13 left panels. We find that the κ scale exponentially as a function of the inverse of initial temperature, $\kappa(T) \propto e^{-\zeta/T}$ from the linear dependence on log-linear plot in Fig. 2.13 top right panel. The characteristic timescale of vortex unbinding t_0 depends linearly on the initial temperature where the initial temperature is close to the critical point, while the γ shows only slow dependence on the initial temperature.

Remarkably, with transformation $x = 1/2\eta - 2$ and $y = \sqrt{2\pi} g_v$, we recover the

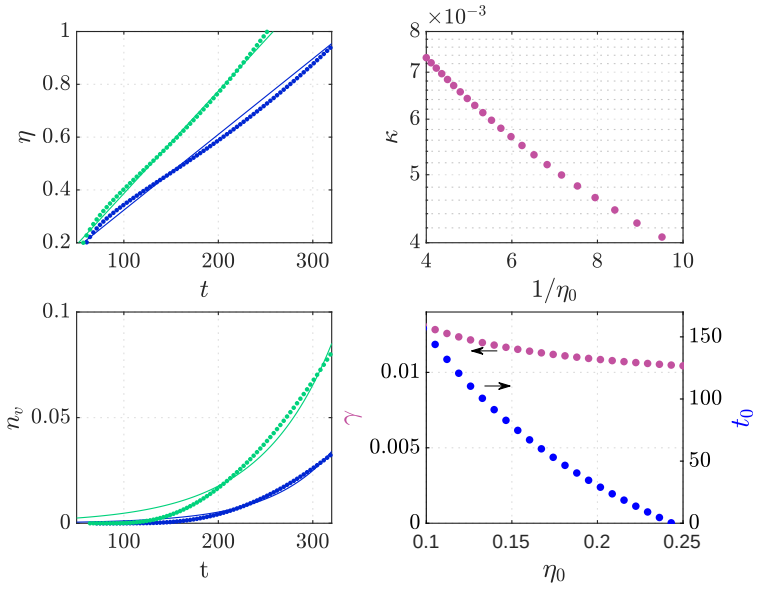

Figure 2.13: The numerical solution of the real-time RG equation Eq. (2.6.2) and their fit. Left panels show the time evolution of η and n_v under the RG flow equation Eq. (2.6.2), for two selected initial conditions at $t_0 = 50$ chosen to be $g_v(t_0) = 0.06$, and $\eta(t_0) = 0.06$ (blue) and 0.1 (green). The η was fitted with the linear function $f(t) = \kappa t + b$ and κ against $1/\eta$ is shown in the top right panel. The vortex density was fitted with an exponential $f(t) = n_c e^{(t-t_0)/\gamma}$ where n_c was fixed to $n_c = 0.01$; the fit results are shown in the bottom right panel, where the arrows indicate the corresponding axes for γ and t_0.

same form as the equilibrium flow equations Eq. (2.6.1),

$$\begin{aligned} \frac{dx}{dt} &= -\frac{(x+2)^3 y^2}{8t}, \\ \frac{dy}{dt} &= \frac{xy}{t}. \end{aligned} \tag{2.6.4}$$

We then find that the non-equilibrium scaling in time (and space) can be cast into the equilibrium scaling by an appropriate transformation. This indicates the universality out of equilibrium, where the scaling parameters for an equilibrium phase transition matches that of critical dynamics out of equilibrium.

In Chapter 6, we compare the real-time RG predictions to the experimentally observed non-equilibrium dynamics in a 2D system quenched across the BKT transition.

3

Experimental realisation of a 2D double-well potential

Contents

To experimentally prepare a 2D system with ultracold atoms, one must confine atoms in highly oblate geometries such that the quasi-2D condition Eq. (1.1.1)

is met. To achieve this, we use RF-dressed potentials to create an oblate trap geometry for the atoms with advantages over optical trapping methods, such as low heating rates and being defect-free. The robustness of the RF dressing technique allows a wide range of applications, such as the cold-atom experiments in space performed by NASA [88, 89] and the atom-chip technologies including compact atom interferometers [90, 91]. Here, we extend the RF dressing technique and create a double-well potential using a multiple-RF dressing [34, 92–96]. In addition to the detailed description of the final trapping technique, we give an account of the experimental procedures to cool an atomic vapour from room temperature to degeneracy. We further address the requirements of experimental parameters to probe the BKT critical phenomena, including the stability and repeatability of the experiments which are essential to obtain the large amount of data required for the measurement of statistical properties of 2D gases.

3.1 RF-dressed Quadrupole potentials

We first review the theory of RF-dressed potentials and their characteristics which are essential for the design of the apparatus of the BKT experiments.

3.1.1 Atoms in a DC magnetic field

Atoms with total angular momentum $\boldsymbol{F}$ have magnetic moment $\boldsymbol{\mu} = -g_F \mu_B \boldsymbol{F}$ where g_F is the Landé g-factor and μ_B is the Bohr magneton. In the presence of a weak DC magnetic field, $B = |\boldsymbol{B}|$, the interaction Hamiltonian is

$$H = -\boldsymbol{\mu} \cdot \boldsymbol{B}. \tag{3.1.1}$$

The eigenstates are the Zeeman states $|m_F\rangle$ with eigenenergy[1] $E_m = m_F g_F \mu_B B$, i.e.

$$H|m_F\rangle = E_m|m_F\rangle. \tag{3.1.2}$$

The quantum number m_F takes integer or half-integer values. For ^{87}Rb atoms in $F = 1$ in the lowest hyperfine level the states are $m_F = -1, 0, 1$. In the presence of a

[1] We have neglected the effect of quadratic Zeeman effect, which is not significant in the range of magnetic field that we use throughout this thesis.

magnetic field gradient e.g. $|B| \propto x$, the atoms are either attracted to the high-field (positive x) or low-field (negative x) directions depending on the sign of $m_F g_F$. This makes confinement of atoms possible by creating a quadrupole magnetic field, for example an anti-Helmholz configuration of two circular coils, which has the form

$$\boldsymbol{B} = b(\boldsymbol{e}_x + \boldsymbol{e}_y - 2\boldsymbol{e}_z). \tag{3.1.3}$$

where b is the magnetic field gradient (units of G/m). We use this trapping technique in an early stage of our experimental sequence. In the quadrupole trap, we perform evaporative cooling by forced ejection of atoms with higher than average energy. This is achieved by applying weak RF field at a frequency ω_{rf} corresponding to potential energy in the trap $E_{\mathrm{rf}} = \hbar\omega_{\mathrm{rf}}$. The RF field induces transitions between magnetic states including states with quantum numbers such that $g_F m_F \leq 0$ which are untrapped, and atoms in these states leave the trap. Since transitions occur in an energy-selective manner, the mean kinetic energy of the atoms can be reduced and rethermalisation by atomic collisions results in lower temperature of the gas. The procedure is illustrated in Fig. 3.1.

While the quadrupole trap is conceptually and experimentally simple, it has a major shortcoming that prevents the production of quantum gases. The issue arises when atoms congregate around the centre of the trap where the magnetic field is zero and so different m_F states become degenerate. Initially trapped atoms traversing the central region can thus change their internal state into one with different m_F, causing them to leave the trap. This is called Majorana loss, and there are various techniques to overcome it. One example is the additional blue-detuned optical dipole trap propagating at the centre of the trap ('plug beam'), such that atoms are repelled from the point where the loss occurs. Another technique involves addition of a strong RF magnetic field, to form a trap with a minimum shifted from the centre, as we describe in the next section.

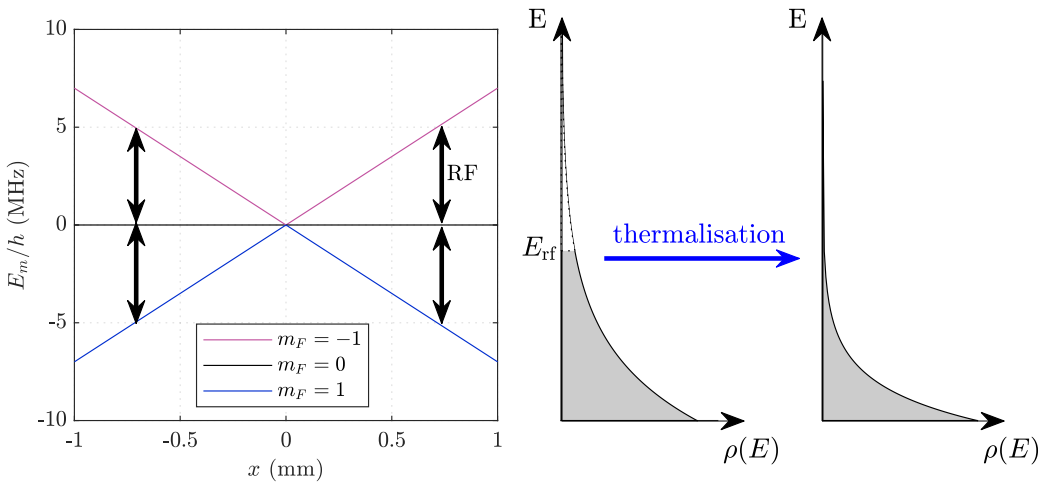

Figure 3.1: Quadrupole magnetic trap and evaporative cooling. (left) Energies of Zeeman states $m_F = -1, 0$ and 1 with $g_F = -1/2$ in a quadrupole magnetic field with gradient $b = 100$ G/cm. Atoms in the $m_F = -1$ state (purple) are trapped. Black arrows indicate the magnetic resonance conditions for atoms in the quadrupole trap with an additional weak RF field at frequency $\omega/2\pi = 5$ MHz. Atoms that reach the resonance become untrapped and leave. (right) Illustration of evaporative cooling. We apply an RF to remove atoms from the initial energy distribution. As atomic collisions rethermalise the system, we recover Boltzmann distribution but with a lower temperature.

3.1.2 Dressed-atom formalism

Applying a strong RF field to the atoms in a static magnetic field gives a composite system of RF photons and atoms in the magnetic field with Hamiltonian

$$H_{\rm tot} = H_{\rm rf} \otimes H. \tag{3.1.4}$$

In the absence of atom-photon interactions, the eigenstates of this Hamiltonian are tensor products of the Zeeman states and Fock states,

$$H_{\rm tot}|N_{\rm rf}\rangle \otimes |m_F\rangle = (N_{\rm rf}\hbar\omega_{\rm rf} + m_F g_F \mu_B B)|N_{\rm rf}\rangle \otimes |m_F\rangle, \tag{3.1.5}$$

where $N_{\rm rf}$ is the RF photon number. These eigenstates form a ladder of states with different photon number $N_{\rm rf}$, which are generally macroscopic for strong RF fields. Now let us consider atom-photon interaction $H_{\rm int}$ that couples the RF field and atomic states. The treatment of atom-photon interaction can be simplified by several steps of approximations. Firstly, for a strong RF field, the semiclassical approximation can be made such that the RF field is a classical,

oscillating magnetic field

$$\boldsymbol{B}_{\rm tot} = \boldsymbol{B}_{\rm DC}(\boldsymbol{r}) + \boldsymbol{B}_{\rm rf}(t). \tag{3.1.6}$$

In our experimental context, the DC field is in z direction while the RF fields are in $x-y$ plane, $\boldsymbol{B}_{\rm DC}(\boldsymbol{r}) = b_z(z)\boldsymbol{e}_z$ with $b_z(z) = -2bz$ and $\boldsymbol{B}_{\rm rf}(t) = b_x\boldsymbol{e}_x \sin(\omega_{\rm rf}t) + b_y\boldsymbol{e}_y \sin(\omega_{\rm rf}t + \phi)$. RF field can be configured to have either linear ($b_y = 0$) or circular ($b_x = b_y, \phi = \pi/2$) polarisations[2]. The amplitude of AC magnetic field is often expressed in terms of the Rabi frequency, defined by $\Omega = |g_F|\mu_B b_x/2\hbar$ for a linear RF polarisation and $\Omega = |g_F|\mu_B b_x/\hbar$ for a circular field. We define the angular frequency detuning from magnetic resonance, $\delta(z) = \omega_0(z) - \omega_{\rm rf}$ where $\omega_0(z) = |g_F|\mu_B b_z(z)/\hbar$ is the magnetic resonance condition.

Within the semiclassical approximation, the Hamiltonian is $H_{\rm sc} = g_F\mu_B \boldsymbol{F}\cdot\boldsymbol{B}_{\rm tot}$. The detailed treatment of $H_{\rm sc}$ can be found in Ref. [97], where it is shown that the rotating wave approximation (RWA) further simplifies the Hamiltonian to a diagonalised expression in rotating frame

$$H_{\rm RWA} = \Omega_g F', \tag{3.1.7}$$

where $\Omega_g(z) = \sqrt{\delta(z)^2 + \Omega^2}$ is the generalised Rabi coupling and F' is relative to the effective direction of the static field in the rotating frame. Eigenstates of Hamiltonian Eq. (3.1.7) are given by $H_{\rm RWA}|\tilde{m}\rangle = \tilde{m}\hbar\Omega_g|\tilde{m}\rangle$. The resulting dependence of energies to the spatial position forms a confining potential. The potential shape is given by the dependence of the generalised Rabi coupling to the position through $\delta(z)$,

$$V(z) = \tilde{m}\hbar\sqrt{\left(\omega_{\rm rf} - \frac{|g_F|\mu_B b_z(z)}{\hbar}\right)^2 - \Omega^2}, \tag{3.1.8}$$

for atoms in state $\tilde{m}$. Fig. 3.2 (a) shows the potential $V(z)$ for $\tilde{m} = -1, 0, 1$ states; $V(z)$ confines atoms with $\tilde{m} > 0$ in a potential well centred at the location where $\delta = 0$. There is a condition for the atoms to remain trapped as they traverse the region of magnetic resonance [97, 98]. Depending on the velocity of

[2]The atom-photon coupling depends the polarisation and g_F. This fact was exploited to realise a g_F-dependent species-selective potential of atoms in Ref. [93] by the use of elliptical polarisations $b_x \neq b_y, \phi = \pi/2$.

the particle, the internal state may fail to follow the $\tilde{m}_F > 0$ dressed eigenstate, resulting in a nonadiabatic transition into untrapped states by a Landau-Zener transition [97]. For atoms to be trapped, the Landau-Zener loss rate Γ must be small, i.e. the loss rate must obey [98]

$$\Gamma \sim \frac{2\omega_z}{\pi} \exp\left(-\frac{\pi\hbar\Omega^2}{2|g_F|\mu_B b}\sqrt{\frac{m}{2k_B T}}\right) \ll 1. \tag{3.1.9}$$

This adiabaticity condition for atoms to be trapped leads the RF-dressed potential often being called an adiabatic potential. Dressed atoms in a static quadrupole field (Eq. (3.1.3)) are confined close to an isomagnetic surface which satisfies

$$\sqrt{x^2 + y^2 + 4z^2} = \frac{\hbar\omega_{\mathrm{rf}}}{|g_F|\mu_B b}. \tag{3.1.10}$$

Fig. 3.2 (b) illustrates an isomagnetic surface. We often refer to the RF-dressed quadrupole trap as a 'shell trap' because of its geometry. In the laboratory, gravitational force pulls the atoms to the bottom of the shell (indicated by yellow region in Figure. 3.2 (b)), where the axial confinement along z is tight compared to the radial direction x, y with typical anisotropy $\omega_z/\omega_r \sim 100$. Atoms are trapped at a distance R below the quadrupole node, with

$$R = \frac{\hbar\omega_{\mathrm{rf}}}{2|g_F|\mu_B b}\left(1 + \frac{\varepsilon}{\sqrt{1-\varepsilon^2}}\frac{\Omega}{\omega}\right), \tag{3.1.11}$$

where $\varepsilon = \frac{mg}{2m_F|g_F|\mu_B b}$; the term with ε comes from the gravitational sag of potential minimum below the position of the magnetic resonance. The radial confinement is analogous to a pendulum motion of the atoms as they follow the isomagnetic surface in the presence of gravity[3]. On the other hand, the axial confinement is dominantly determined by the dressed potential Eq. (3.1.8). The oscillation frequencies in the trap that characterises the confinement, are given by [99]

$$\omega_z = \frac{2|g_F|\mu_B b}{\hbar}\sqrt{\frac{m_F\hbar}{m\Omega}}(1-\varepsilon^2)^{3/4}, \tag{3.1.12}$$

$$\omega_r = \sqrt{\frac{g}{4R}}\sqrt{1 - \frac{\hbar m_F\Omega}{mgR}\sqrt{1-\varepsilon^2}}, \tag{3.1.13}$$

for a cylidrically-symmetric circularly-polarised dressing RF field.

[3]We have neglected the effect of spatially-varying atom-light coupling strength. This is a good approximation in the parameter regime used in this thesis where the spheroid size $R \sim 600\,\mu\mathrm{m}$ is large compared to the size of the trapped atomic cloud $\sim 30\,\mu\mathrm{m}$.

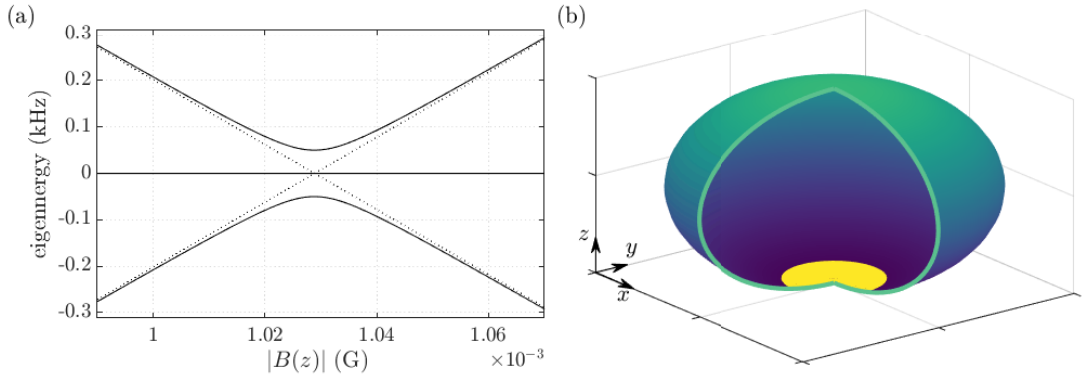

Figure 3.2: The RF-dressed 'shell' potential. (a) The eigenenergies of uncoupled (Eq. (3.1.2), dotted lines) and coupled (Eq. (3.1.7), solid lines) systems. (b) The 3D illustration of the RF-dressed potential minimum in the quadrupole magnetic field Eq. (3.1.3). In the presence of gravity along the $-\boldsymbol{e}_z$ direction, atoms are trapped at the bottom of the shell indicated by yellow. Part of the shell structure is cut away for clarity.

3.1.3 MRF-dressed potentials

By applying multiple frequency components, we can create a much wider variety of trapping geometries such as a double-well potential [93, 94, 96, 100] and lattice [101]. Using this method, we have demonstrated coherent splitting of a BEC and the observation of matter-wave interference in our lab [94]. The Hamiltonian in the semiclassical approximation is

$$\mathcal{H}_{\mathrm{MRF}} = g_F \mu_B \boldsymbol{F} \cdot \left[\boldsymbol{B}_{\mathrm{DC}} + \sum_j b_j \boldsymbol{e}_x \sin(\omega_j t + \phi_j) \right], \tag{3.1.14}$$

for RF fields linearly polarised along x. An analytical treatment of multi-frequency atom-photon coupling is challenging, requiring special care to treat the complex degeneracy of the states [102]. Nevertheless, simplified techniques to treat such effect exist thanks to the commensurate frequency combinations $\{\omega_j\}$ that we use. We typically use commensurate frequencies with fundamental frequency ω_f in order to avoid dense RF transition spectrum mediated by higher-order combinations of incommensurate frequencies, which leads to a wideband atom loss channel. With Hamiltonian periodic in time with period $2\pi/\omega_f$, we can resort to Floquet theory to numerically calculate the eigenenergies [103]. The result of a numerical simulation with three-component RF double-well potential is displayed in Fig. 3.3. The amplitudes of the frequency components can be individually controlled to form

different potential shapes such as single-well, flat bottom potential and asymmetric double-well. Fig. 3.3 (c) and (d) shows the eigenenergies of MRF-dressed atoms, illustrating the controllability of the potential by the manipulation of the RF amplitudes. Similarly to the single-RF case, we express RF field amplitudes by Rabi frequencies for each frequency components $\Omega_j = |g_F|\mu_B b_j/2\hbar$.

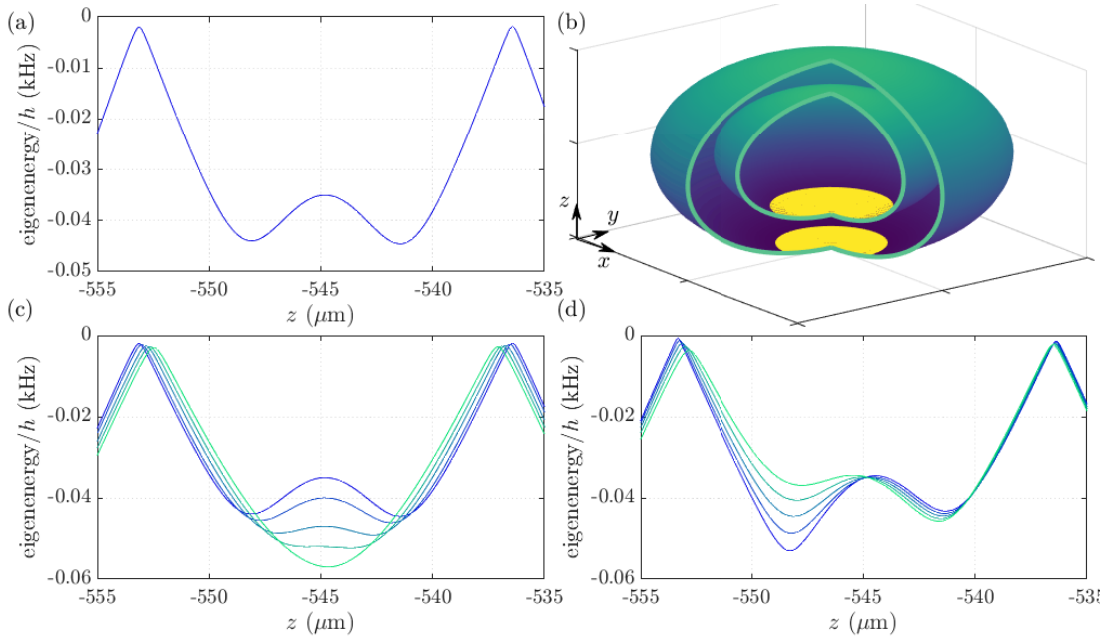

Figure 3.3: The multiple-RF dressed potential and their controllability. (a) The MRF-dressed potential with RF frequencies 7.14, 7.2 and 7.26 MHz with amplitudes $[\Omega_{7.14}, \Omega_{7.2}, \Omega_{7.26}]/2\pi = [20, 35, 20]$ kHz. z is the distance from the quadrupole node with a quadrupole gradient $b = 95$ G/cm. (b) The trapping surfaces for the MRF-dressed potential configured to be a double-well as shown in (a). Two spheroidal traps with same origin and different size are created. The difference in the size of spheroids are exaggerated for clarity. (c) The transformation of the potential from a single-well to a double-well is accomplished by changing the $\Omega_{7.2}/2\pi$ from 57 kHz (green) to 35 kHz (blue). (d) Controllability of the double-well asymmetry by the change in $\Omega_{7.26}/2\pi$, from 10 kHz (blue) to 30 kHz (green).

3.1.4 Parameter regime for the BKT transition in a MRF-dressed potential

In this part, we discuss the characteristics of MRF-dressed potentials to identify the parameter regime where we are able to observe the BKT critical phenomena. The condition for the observation of critical phenomena, the 2D condition (1.1.1) and

the expected critical point (2.3.12), as well as the experimental capability determine the parameter regime where observation is plausible.

2D condition and criteria for observing BKT transition

The condition for 2D confinement of atoms is determined by the axial trapping frequency and temperature[4], $k_B T < \hbar\omega_z$. The lowest temperature routinely achieved in the experiment is in the range[5] $30 - 50$ nK, where a measurable fraction of thermal atoms are present to extract the temperature. This requires a certain trapping frequency ω_z to achieve a 2D system, 1 kHz $\lesssim \omega_z/2\pi$. Moreover, the atom number needs to be large enough around the critical point to be above the current experimental detection threshold, namely $10^4 \lesssim N_c$ for the range of trap frequencies, expansion time and cloud temperatures used in this thesis.

The 2D condition can be cast into experimental control parameters such as RF frequency f_{RF}, amplitude of the RF field (in terms of Rabi frequency) Ω, and quadrupole gradient b from Eqs. (2.3.12), (3.1.12) and (3.1.13). Fig. 3.4 (a) shows ω_z as a function of RF amplitude Ω and static field gradient b. As expected from Eq. (3.1.12), we find that with higher b and lower Ω, the confinement is tighter along z and the 2D condition is better satisfied. However, as we describe later, higher ω_z leads to intrinsic loss from the trap and lower Ω increasing the coupling of atoms to the noise present in the experiment, leading to shorter lifetime of the gas. We thus need to find an optimal point to maximize the lifetime of atoms while satisfying the 2D condition.

Fig. 3.4 (b) shows the BKT critical atom number N_{BKT} from Eq. (2.3.12) at the temperature $T = \hbar\omega_z/k_B$ with the dressing RF frequency $f_{\mathrm{RF}} = 7.2$ MHz that we typically use in the experiment. To satisfy the 2D condition across the BKT critical temperature (at a constant atom number), the total atom number of the system needs to be kept well below the atom numbers shown in Fig. 3.4 (b); the inset

[4]The chemical potential μ is usually small, $\mu/k_B \sim 10nK$ and we almost always satisfy $\mu < \hbar\omega_z$ with the operational parameter regime of RF-dressed potentials in our apparatus.

[5]While we can achieve much lower temperature, our straightforward thermometry method using the thermal component fails to work reliably at temperatures below around 20 nK, see Section 4.1.3.

shows the same quantity with a different RF frequency $f_{\mathrm{RF}} = 2$ MHz which was used previously in our lab. The main difference arising from this change of the f_{RF} is the radial trap frequency, which determines the critical atom number for a given temperature in harmonic trap. The critical atom number is significantly reduced with $f_{\mathrm{RF}} = 2$ MHz such that the signal-to-noise (S/N) ratio becomes low around the critical point and it becomes difficult to probe the BKT critical phenomena.

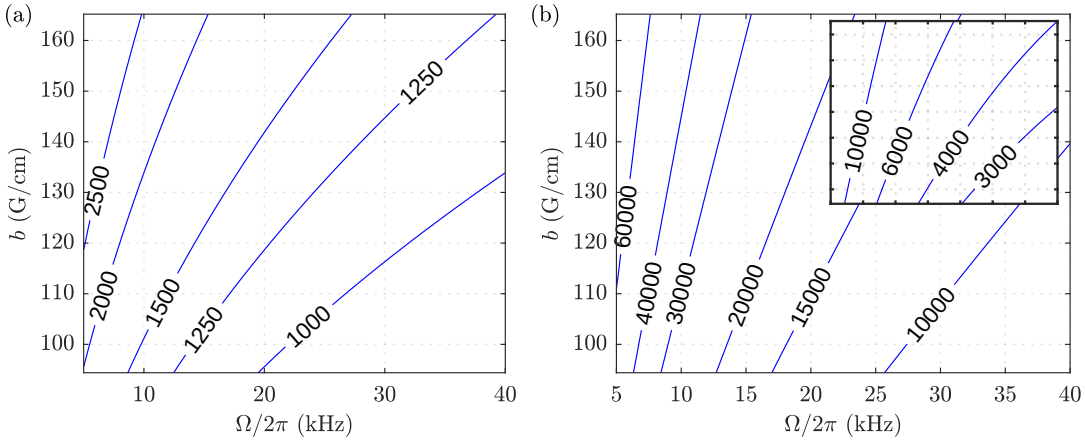

Figure 3.4: Experimental parameter regime to observe the BKT critical phenomena. (a) Vertical trapping frequency $\omega_z/2\pi$ in a single-RF dressed potential in Hz, as a function of RF amplitude Ω and the quadrupole magnetic field gradient b. (b) The BKT critical atom number for the temperature at the limit of 2D condition $T = \hbar\omega_z/k_B$, using Eq. (2.3.12) for the dressing RF frequency 7.2 MHz. Inset shows the same quantity with same axes scale, but for a different dressing RF frequency of 2 MHz.

Non-adiabatic loss

At low RF amplitude $\Omega/2\pi \sim 10$ kHz and high static field gradient b, the Landau-Zener losses become important because of the exponential increase as in Eq. (3.1.9). This sets the fundamental limit of ω_z that can be achieved for dressed atoms, thus the temperature range that can be probed while keeping the 2D condition. Fig. 3.5 (a) shows the rate of atom loss Γ at the expected BKT critical point. The timescale of our experiment with the 2D gas is usually ~ 1 s which requires $\Gamma \ll 1\ \mathrm{s}^{-1}$. The non-adiabatic losses thus bound the RF amplitudes to be $\Omega/2\pi \gtrsim 10\,\mathrm{kHz}$. Combining the results with Fig. 3.4, we show in Fig. 3.6 the parameter regime to observe 2D phenomena in a RF-dressed potential. Additionally, even above

10 kHz $\sim \Omega/\hbar$ experimental imperfections limit the lifetime of atoms in the dressed trap, as we describe below.

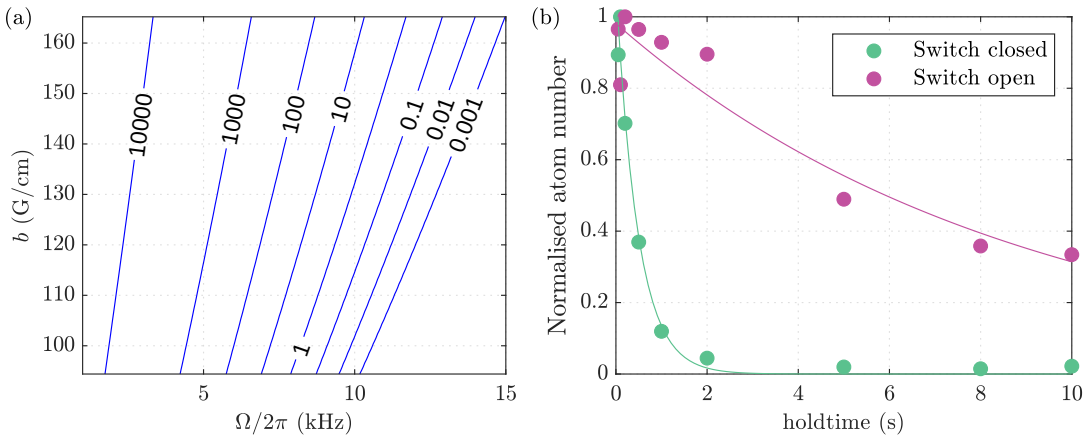

Figure 3.5: The Landau-Zener losses and the effect of noise on the experiment. (a) The Landau-Zener loss rate (s^{-1}) for atoms trapped in a single-RF dressed trap with temperature at predicted BKT critical temperature Eq. (2.3.12). (b) The effect of low-frequency noise to the atom loss rate. The time evolution of trapped atom number in a linearly-polarised trap with $\Omega/2\pi = 20$ kHz and $b = 140$ G/cm. An RF switch decouples an electric circuit that produces undesired noise from the experiment, thus protecting the trapped atoms. The obtained lifetime of the atoms are 0.48 s (switch closed) and 8.8 s (switch open). A jump in the RF phase caused by an error in the RF generator resulted in a sudden reduction of observed atom number in one of the measurements at holdtime ~ 0 s, for the 'switch open' dataset.

Effect of electrical noise

The MRF-dressed potential has a number of loss channels for the trapped atoms, as previously investigated in Ref. [92]. This limits the lifetime of the atoms in the trap even when Landau-Zener losses are not significant. There are many frequencies for which external noise can couple atoms in a trapped state to untrapped states; these transitions arise from the higher-order terms involving a complex combinations of dressing RFs. Furthermore, noise near the dressing RF frequency causes vibration of the trap, resulting in heating by parametric or dipolar excitation [104]. As such, it is crucial to eliminate electric and magnetic noise in the lab as much as possible. During the work towards this thesis, we have significantly reduced the noise coupled to the experiment by bias field electronics, and increased the lifetime of single-RF dressed potential by a factor of 20. Measurement at 20 kHz Rabi frequency, close to

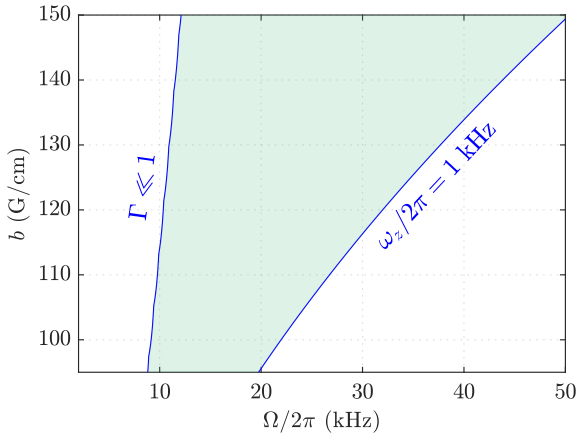

Figure 3.6: The parameter regime to observe 2D phenomena in a RF-dressed potential. Shaded area corresponds to high vertical trap frequency $f_z > 1$ s^{-1} to ensure 2D confinement and low nonadiabatic loss $\Gamma \ll 1$ Hz. As described in the main text, noise in the experiment and the efficiency of loading into MRF-dressed potential further limit the available region in this plot.

the value routinely used for the experiment, is shown in Fig. 3.5 (b) before and after the experimental improvements. Unidentified low-frequency noise from other circuits still affect the atoms, at a few particular frequencies [104]. The current lifetime is sufficient for the measurements reported in this thesis. Further improvement would be possible however a new apparatus is being constructed with completely redesigned coils which should be more stable and have less cross-coupling [105, 106]

Spin-flip losses

Another source of atom loss is a mechanism similar to that of Majorana transitions in a quadrupole trap. When two, or more, different $|\tilde{m}_F\rangle$ states have the same energy, then spin flip into different $|\tilde{m}_F\rangle$ state may occur. One such mechanism in a MRF-dressed potential occur when the Rabi frequency equals the frequency separation of the multiple dressing RFs $\Omega = \omega_f$. This is illustrated in Fig. 3.7 (a). Another case where the Majorana-like losses are observed is when the states with different $\tilde{m}_F$ as well as the Fock state of fundamental RF photon field, namely $|\tilde{m}_F, N\rangle$ and $|\tilde{m}'_F, N-1\rangle$, have the same energy

$$N\hbar\omega_f + V_{\tilde{m}_F}(z) = (N-1)\hbar\omega_f + V_{\tilde{m}'_F}(z). \tag{3.1.15}$$

While we have not fully understood the origin of loss mechanism in such case, avoiding this situation usually leads to more efficient and stable loading of the atoms into a double-well. An example of potentials where we observed such loss is illustrated in Fig. 3.7 (b). Our experimental procedures, such as the coherent splitting shown in Fig. 3.15, are carefully designed to avoid these losses.

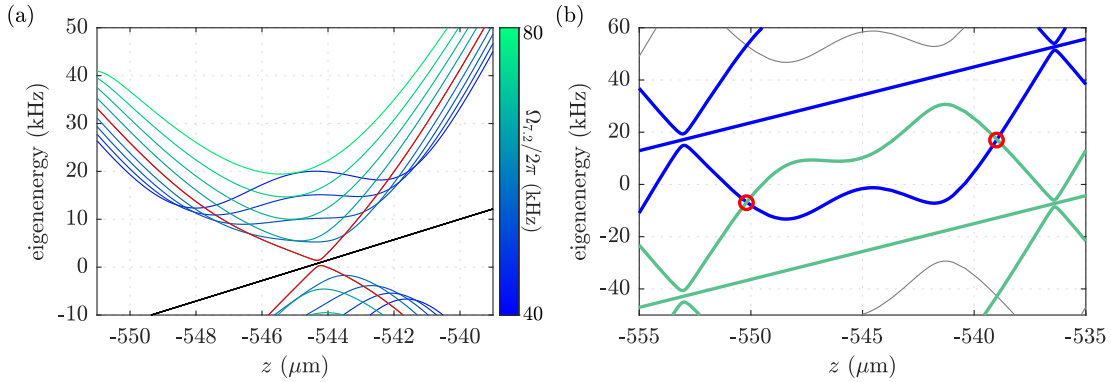

Figure 3.7: Additional loss mechanism in MRF-dressed potentials. (a) The Majorana-like loss mechanism that occurs when the Rabi frequency of one of the RF frequency components are exactly at the fundamental RF frequency ω_f. The dressed eigenenergies with dressing RFs 7.14, 7.2 and 7.26 MHz are shown, with their field amplitudes $[\Omega_{7.14}, \Omega_{7.26}]/2\pi = [20, 27]$ kHz and $\Omega_{7.2}/2\pi$ ranges from 40 (blue) to 80 (green) kHz with 5 kHz increment. The eigenenergy with $\Omega_{7.2} = \omega_f = 2\pi \times 60$ kHz is shown in red, with which the loss is expected. (b) The illustration of the observed loss mechanism between dressed eigenstates with different RF photon number, $|N, \tilde{m}_F\rangle$ (blue) and $|N-1, \tilde{m}_F\rangle$ (green). Atoms are initially trapped in the $|N, \tilde{m}_F = 1\rangle$ state (blue, lowest). The potentials for $|\tilde{m}_F = 1, N\rangle$ (blue) and $|\tilde{m}_F = -1, N-1\rangle$ intersect at $z = -540$ μm and -550 μm as indicated by red markers. The intersection at $z = -550$ μm is close to the potential minimum, and causes atom loss from the well centred at $z = -548$ μm. The energies shown include gravitational potential.

Relative phases

For multiple RFs that have common fundamental frequency, the relative phases are important as the exact shape of waveform depend on the phases. Appropriate choices of the relative phases of multiple RFs are thus crucial for the stability of loading into a MRF-dressed double-well potential. The relative phase of the RFs affect the potential through the difference in the alignment of RF fields. This effect is most clearly seen when the MRF-dressed potential is configured to be a single-well potential, as illustrated in Fig. 3.8 (a). Since the loading of atoms into a double-well

necessarily involves an initial step of MRF-dressed potential configured to be a single-well, the relative phases of RFs, and their stability, significantly affect the splitting of the cloud of atoms as the potential evolves into a double-well. Fig. 3.8 (c) shows the strength of confinement as a function of relative phases of three RFs. As expected, we see that the potential shape is only dependent on a single parameter, $\phi_{7.14} + \phi_{7.26}$.

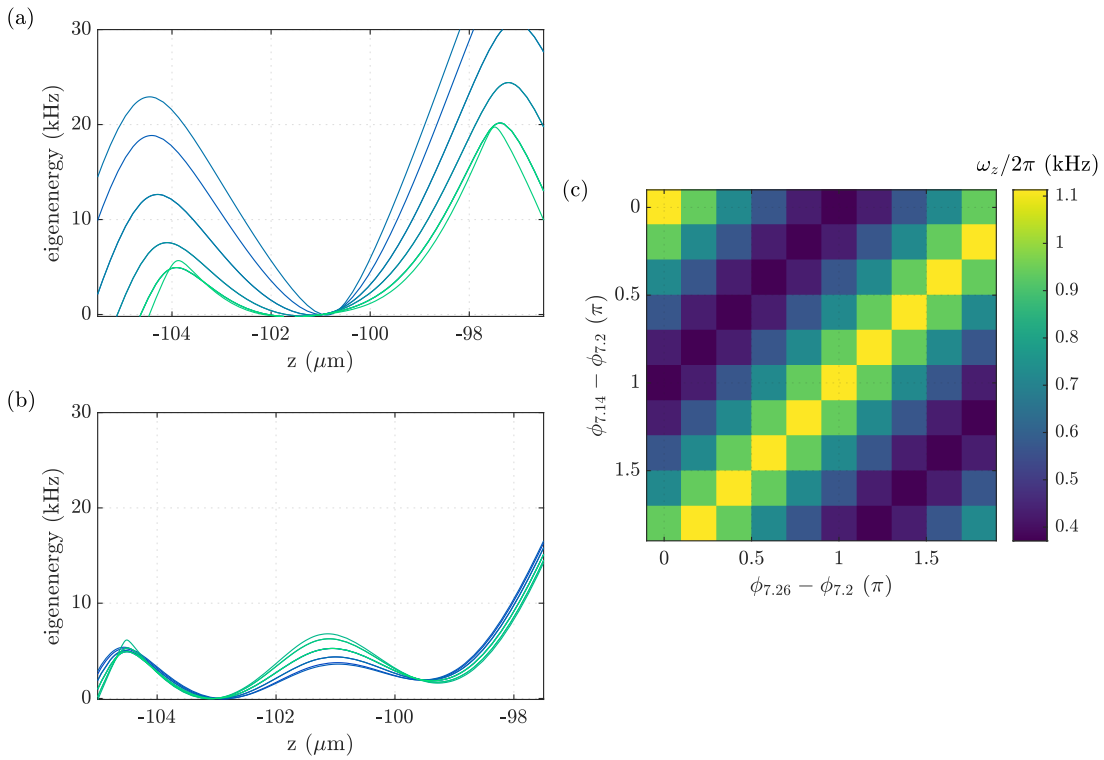

Figure 3.8: The effect of RF relative phases on MRF-dressed potentials. (a) MRF-dressed potential with RF frequencies 1.95, 2 and 2.05 MHz with amplitudes $\Omega/2\pi$ for respective frequencies 35, 44 and 42 kHz. Colours of lines indicate the phase difference of 1.95 and 2 MHz components, from 0(blue) to π (green) radians. (b) The same plot as (a) with different amplitudes $\Omega/2\pi$ for each frequencies 35, 15 and 42 kHz, configured to create a double-well potential. (c) The trap frequencies measured with the configurations in (a) as a function of phase difference of RFs.

Amplitude stability

In the experiment, the final evaporative cooling sequence is performed in a single-RF dressed potential by forced evaporation using an additional weak RF field (see Section 3.4.1). The RF transition of atoms in the RF-dressed potential resembles that in the quadrupole trap, with major difference being the existence of transitions

that are assisted by dressing RF photons. In particular, we use the transition at angular frequency $\omega_{\mathrm{rf}} + \Omega$ for the evaporation sequence with detuning $\delta_{\mathrm{evap}} = \omega_{\mathrm{probe}} - \omega_{\mathrm{rf}} - \Omega$. Since the frequency detuning depends on RF field amplitude Ω, the energy threshold for the atoms to leave the trap depends linearly on the RF amplitude. Thus the stability of RF amplitudes is important to consistently perform the evaporation sequence.

Furthermore, the amplitudes of the multiple RFs affect the loading into the double-well potential, especially the population imbalance between the wells. We typically require less than 1% fluctuation of the RF amplitudes to avoid these problems.

3.2 RF field generation

The RF-dressing technique described above requires strong and very stable RF fields to be applied to the atoms. Furthermore, the use of *multiple* RF introduces the intricacy of controlling relative phases of RF components. We have implemented the RF signal generator using Artiq[6] software and hardware package that addresses the phase stability issue that plagued our previous RF generator. Furthermore, the RF signal chain was improved to meet the stringent stability requirement for the investigation of BKT critical phenomena.

3.2.1 Impedance matching

A major challenge in implementing RF-dressed potentials in the lab is the generation of sufficiently strong RF fields using macroscopic coils of dimensions of a few centimetres. AC signals propagating in the signal chain experience a fraction of their power reflected at the interface of components with different impedance; not only does this cause power loss, the standing wave formed by input and reflected signals can damage the amplifier and other RF components. Thus we use the *impedance matching* techniques to transform the input impedance of the macroscopic coil to match the output impedance of the standard RF components, typically 50 Ohm.

[6]https://m-labs.hk/experiment-control/artiq/.

Wire-wound coils have a self-resonance frequency (SRF) determined by the inductive and capacitive contributions of the solenoid. The coil has a complex impedance, $Z_{\text{coil}}(\omega) = Z_r(\omega) + iZ_i(\omega)$ where $Z_r(\omega), Z_i(\omega) \in \mathbb{R}$. The imaginary part of the complex impedance is positive $Z_i(\omega) > 0$ in the inductive regime at frequencies below the SRF, and $Z_i(\omega) < 0$ in the capacitive regime above the SRF. We had implemented a simple capacitive matching at 2MHz below the SRF of 4 MHz, by cancelling the imaginary impedance of the coil with a series capacitor [105], but this was not adequate for the experimental work reported in this thesis.

To observe the BKT transition in the RF-dressed potential, we found that, as described in Section 3.1.4, that much higher dressing frequency around 10 MHz is required. This makes it necessary to impedance-match well above the SRF, which is not common practice and the literature on this is scarce. While it is conceptually simple to match above the SRF by using a series inductance to cancel the imaginary part of the impedance, difficulty arises because the inductive components such as wire-wound coils have intrinsic capacitance as well as resistance. Additionally, since commercially available inductor components with the high current rating have only limited selection of their values, the impedance matching above the SRF thus becomes a trial and error[7]. We found that for an inductive impedance matching, components with low DC resistance and high SRF generally worked better to match at higher frequencies. The final matching network is shown in Figure. 3.9 (a) blue shaded region. The series capacitance was added to suppress the propagation of low-frequency noise to the coils.

3.2.2 Stability of the RF amplitudes and phases

As discussed in Section 3.1.4, very stable RF amplitudes and phases are essential for the reproducible manipulation of quantum gases. Both amplitudes and phases of RFs are critical because the double-well potential and their population balance sensitively depend on these parameters. Fluctuations of less than 1% in amplitude, as well as 0.1π radian in phase are required, for extremely large datasets that take

[7]For mechanical rigidity of the circuit we only used surface-mount components; this further limited the selection of component values.

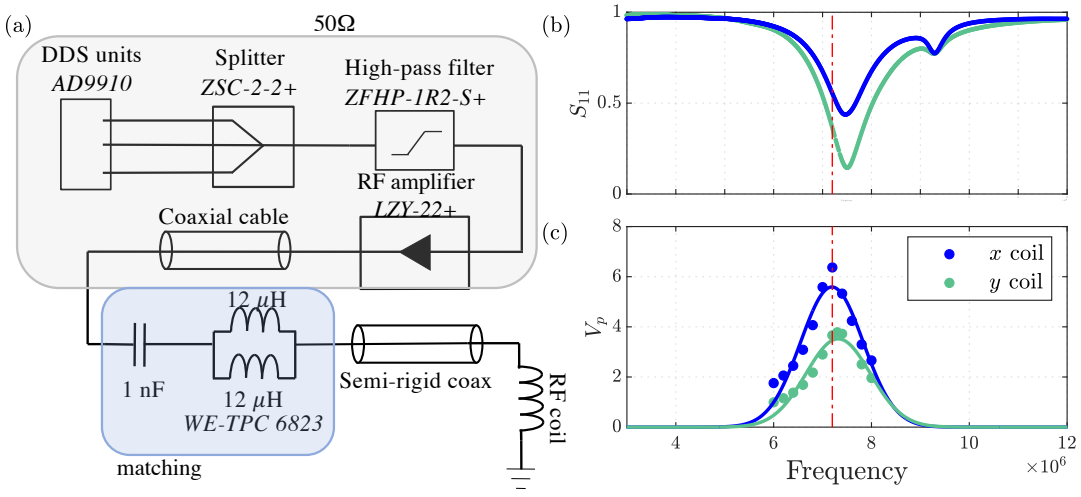

Figure 3.9: RF signal chain and impedance matching. (a) The RF signal chain to apply RF magnetic field to the atoms using a macroscopic RF coil near the glass cell. Gray shaded area indicates industrial standard 50 Ω components. The impedance matching circuits is marked by blue shaded region, which matches the impedance of RF coil and semi-rigid coax to 50 Ω at the desired frequency 7.2 MHz. (b) The reflection coefficient S_{11}, in linear scale (not dB scale), measured at the input of impedance matching circuit using a vector-network analyser (Bode 100, OMICRON lab). Colours indicate the two different circuits (individual coils and matching circuits) responsible for creating RF field in x and y directions. Red dash-dotted line indicates the frequency used for the experiment, 7.2 MHz. (c) The pickup voltage V_p at different RF output frequencies (markers) which serves as a measure of the magnetic field amplitude. Solid lines are a Gaussian fit to the data.

a period of several weeks to acquire, in order to explore statistical properties of 2D gases. A significant part of the improvement in the stability of RF amplitudes was achieved by the replacement of the twisted-pair signal cables with semi-rigid coaxial cables, as well as the appropriate choice of RF frequency in the impedance matching characteristics. Even with these improvements to the apparatus, it was necessary to operate the experiment continuously in order to keep long-term drifts to a minimum. Continuous operation for many days allows the temperature of the whole experimental apparatus including the RF components to reach a stable thermal equilibrium, thus stabilising the amplitude of the RF field. Fig. 3.10 shows the amplitudes of three different RF components, as probed by co-wound pickup wires, plotted over the duration of 12 days while the dataset for Chapter 6 was taken. We have excluded a very small number of outliers up to 100 points out

of more than 12000 points in total, in which no RF was measured because of a temporary error of the DDS. These outliers affect the atom loading significantly and are easy to post-select by the anomalously low atom number.

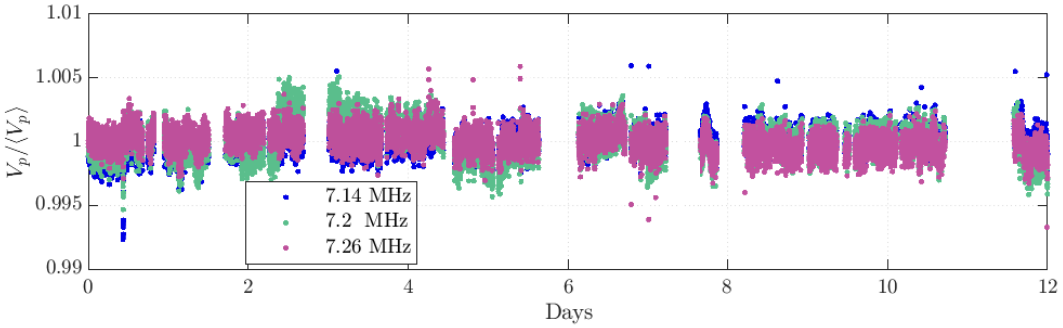

Figure 3.10: RF amplitude stability over a 12-day period during a long continuous data-taking. One multiple-RF waveform from the pickup coil is recorded and analysed to extract the mean amplitude of the three RF components for each experimental realisation. One experimental run contributes one data point for each frequency component in the graph.

The relative phase stability of multiple RFs is also essential, as discussed in Section 3.1.4. The control of relative phases of different RF signals to the level of 0.01π radian is usually challenging: for our RF frequency of 7.2 MHz, a timing difference of 2 ns already results in 0.01π radian difference of the phase. Thus, a slight signal delay or logic-clock synchronisation error would lead to a sudden jump of phase difference, as is discussed previously by Bentine [107]. The previous implementation of the RF signal generator failed to satisfy these requirements especially for the higher RF frequency 7.2 MHz, and we have upgraded our DDS controller using an FPGA control system Artiq[8] and the open-source software package developed for it. These RF generators are the Urukul[9] units, RF generators which house four direct digital synthesis chips (DDS, *Analog Devices* AD9910). This open-source hardware has been developed as part of the Artiq project (the hardware family Sinara[10]); this project was primarily motivated by the requirements for quantum information processing with trapped ions but meets our requirements

[8]https://m-labs.hk/experiment-control/artiq/
[9]https://github.com/sinara-hw/Urukul/wiki
[10]https://sinara-hw.github.io/

very well, i.e. complex and precise timing sequences and the multiple controllable RFs. An essential improvement over the previous system of RF generators is the synchronisation of clock of the FPGA system and the clocks of the multiple AD9910 DDS chips that it controls. The effect of this clock synchronisation is shown in Fig. 3.11 (a) and (b), where the sudden jumps of the relative phases are eliminated. We have also plotted the long-term stability of the relative phases of the multiple RFs in Fig. 3.11 (c) which shows excellent consistency over the two week period shown in the graph. The finite fluctuation of phase differences are due to the slow drift of impedance matching characteristics.

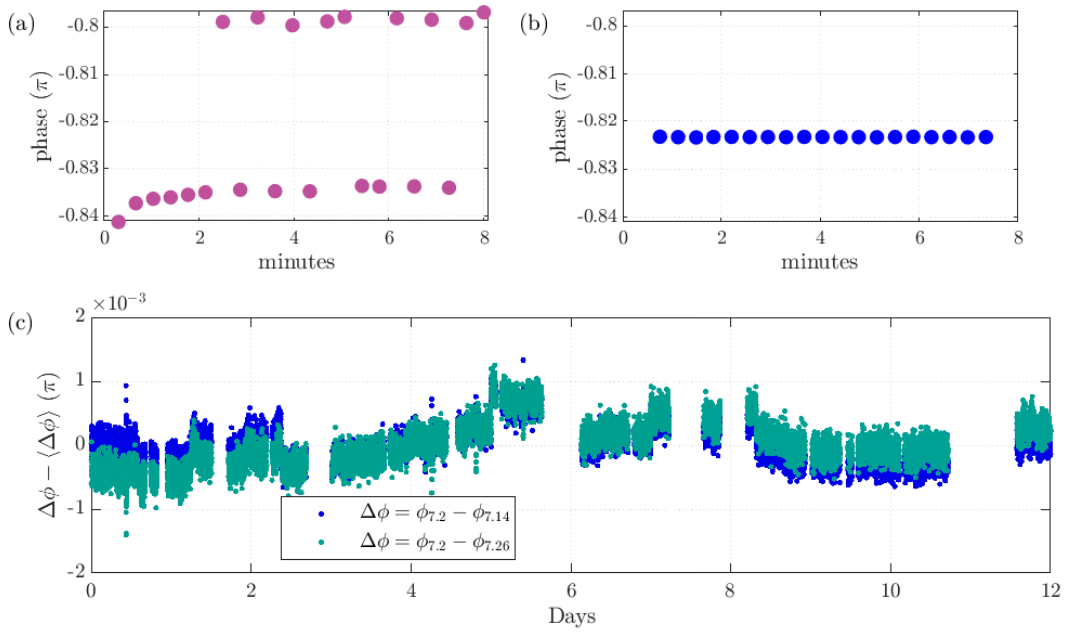

Figure 3.11: Phase jumps and long-term phase stability. (a) The relative phases of the 7.2 MHz sinusoidal output signals from two different DDS chips on an Urukul card, triggered simultaneously using our old DDS control system. The lack of synchronisation of the FPGA and DDS clocks causes the sudden jumps of the RF phases that are observed. (b) The same measurement as (a) but with the DDS chips controlled and triggered using the Artiq control system, achieving clock synchronisation for every run. (c) Long-term relative phase stability of the MRF signal frequency components, referenced to the mean phase difference $\langle\Delta\phi\rangle$. The three frequency component is derived from different DDS chips.

3.2.3 Turn-off of the RF signals

Another improvement from our previous implementation of RF sources is the ability to stop the RFs at a specified phase, using the conditional sequencing functionality of Artiq. The spin $\boldsymbol{F}$ of atoms undergoes complex oscillation in the RF-dressed potential, precessing around an effective B-field in the rotating frame, which is also oscillating in the lab frame. As we describe later, we project atoms into bare Zeeman states from a dressed state and let the atoms undergo time-of-flight (TOF) expansion in the presence of a residual magnetic field. Since the Zeeman state with $m_F = 0$ is insensitive to the residual magnetic field, the analysis of this state after a projection is thus preferable. It is thus important to maximise the fraction of atoms projected into $m_F = 0$. The overlap of the RF-dressed atomic states with the $m_F = 0$ depends on the RF phases at the time of projection into bare Zeeman states. Fig. 3.12 illustrates the procedure used to control the RF phase to maximize the fraction of atoms projected onto $m_F = 0$. For experiments with MRF-dressed potentials, we sweep the phase of the fundamental frequency ω_f at turn-off to maximize the detected fraction. We found that in the double-well configuration, maximizing the fraction of $m_F = 0$ population for one of the wells usually results in a maximum (and same) fraction for the other well as shown in Fig. 3.12 (b) and (c).

3.3 The laser system

The detail of our laser system is described in past theses, Refs. [107–109]. Our laser system consists of three Toptica DL Pro external-cavity diode lasers (ECDL). The first ECDL is the reference laser, which is locked to ^{87}Rb D2 line $F = 2 \rightarrow F' = 3$ 'cooling' transition using modulation transfer spectroscopy [110]. The other two lasers provide 'repumping' and 'cooling' light, both offset-locked to the first laser. The repumping light is resonant for $F = 1 \rightarrow F' = 2$ transition.

For the laser cooling stage which requires hundreds of mW of laser power, we amplify the laser intensity in two stages. The first stage is the additional injection-locked diode laser which increases the power of cooling light to around 100 mW.

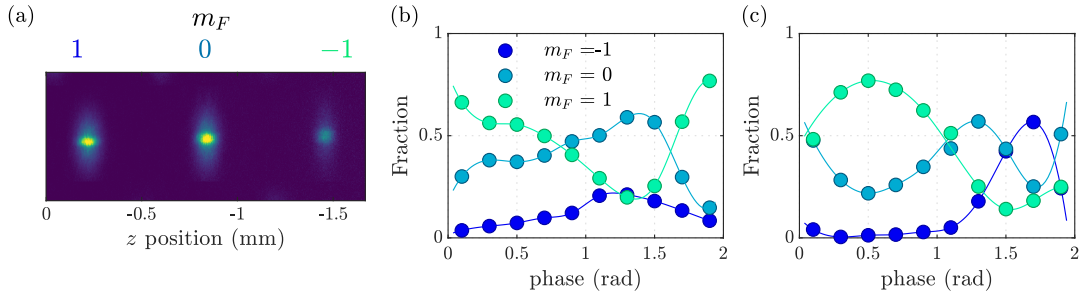

Figure 3.12: The control of the RF phase for the projection into Zeeman states. (a) A single image of atomic density taken after the TOF sequence involving the projection of dressed states into Zeeman states. When the RFs are turned off, the atoms in different Zeeman states experience different forces along the z direction in the residual quadrupole magnetic field. The population of each Zeeman substate can be inferred by the atom numbers of three localised clouds as we see in the image. (b) and (c) The fraction of atoms projected onto each Zeeman state, as a function of the phase of the fundamental RF, ω_f, at the time of RF turn-off. The MRF-dressed potential was configured to be a double-well as shown in Fig. 3.3 and (b) is measured with atoms localised in the well near the resonance at 7.14 MHz, while (c) is for atom trapped in the other well. Solid lines are a guide to the eye.

The cooling light is combined with repumping light, and both frequencies are amplified using a tapered amplifier[11] to obtain around 400 mW of light of which the cooling light has the dominant power.

The light for the detection of atoms is also derived from the cooling and repumper ECDLs. For stability of the detection, the cooling light used for the absorption imaging is intensity-stabilised using a photodetector and a PID controller (*Stanford Research Systems* SIM960).

3.4 Experimental procedure

Here we describe the complete procedure of the experimental sequence to cool atoms from room temperature to tens of nanokelvin. Greater detail of each of the steps can be found in past theses [102, 107–109] by graduate students who have contributed to this work. Fig. 3.13 illustrates our experimental apparatus, as well as the overview of the experimental sequence.

[11] Eagleyard EYP-TPA-0780-01000

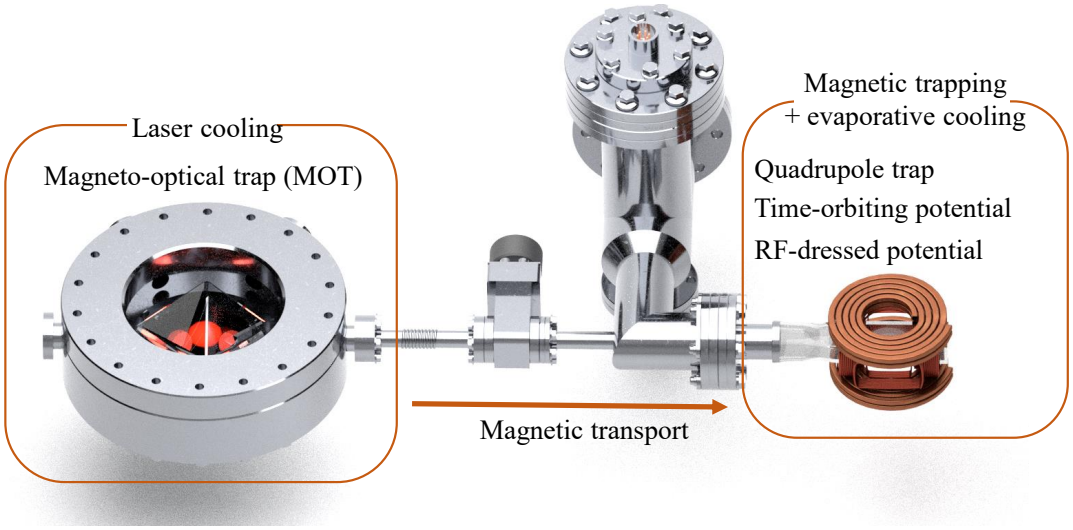

Figure 3.13: Overview of the experiment. We first laser cool atoms in the pyramidal MOT (left) and magnetically transport them to a UHV glass cell (right), where we perform a series of evaporative cooling sequences in different confinements, as listed in the figure. The UHV glass cell is surrounded by coils to produce DC and AC magnetic fields, which are described in detail in Fig. 3.14. This figure and Fig. 3.14 are based on the 3D model of the experiment made by Elliot Bentine.

Our vacuum chamber consists of two parts. The first part is the laser cooling stage, where ^{87}Rb atoms are captured from a room-temperature vapour and cooled in a magneto-optical trap (MOT) [111]. During the MOT loading, we typically apply UV light (using LEDs) onto the vacuum glass window, such that the pressure of Rb is increased because of light-induced atom desorption (LIAD) giving faster loading of the MOT. The typical MOT loading time with LIAD is around 10 seconds, during which around 2×10^9 atoms accumulate in the MOT. The atoms are then magnetically transported [108] over a distance of $\sim$80 centimetres to the ultra-high vacuum glass cell, where magnetic trapping and further cooling is performed. The transport causes the atoms to be heated up and therefore afterwards atoms are evaporatively cooled down in a quadrupole trap, from hundreds of μK to tens of μK. Since the Majorana loss rate increases at a lower temperature, we stop the cooling in the quadrupole trap at a relatively high temperature compared to the Bose-condensation point. Subsequently, we turn on the rotating bias field at 7 kHz to realise a time-orbiting potential (TOP) trap, which shifts the quadrupole node away from the centre of time-averaged potential and avoids Majorana losses.

After further cooling in the TOP trap, RF dressing fields are turned on to load atoms into a time-averaged adiabatic trap (TAAP) while the TOP bias fields are kept on. The final evaporation sequence is performed in the TAAP trap, where a partially-condensed 3D cloud is obtained. The bias fields ensure that the atoms are initially trapped outside of the resonant spheroid, such that the sudden turn-on of RF fields do not heat up the trapped atoms. Since the oscillation of the TOP field is circularly symmetric in the $x-y$ plane, we must ensure the cylindrical symmetry of the dressed trap to avoid heating and we choose circularly-polarised RF along the z axis in this stage. In the TAAP trap, we perform the final evaporative cooling sequence to reach a final desired temperature. After the evaporative cooling and rethermalisation, we ramp down the TOP bias field to slowly transfer atoms from a TAAP to the RF-dressed potential[12].

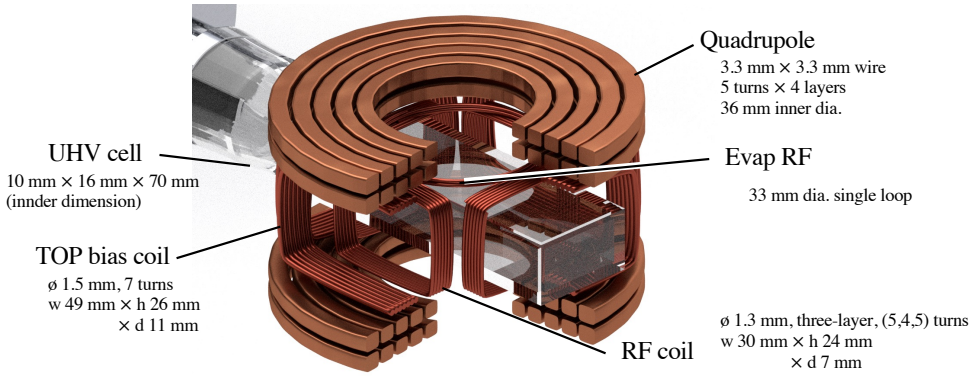

Figure 3.14: Close-up view of the coils used to generate magnetic fields. RF and TOP coils are installed along two directions x and y to create circulary-polarised field around the z axis. The Evap. RF coil creates a weak RF field along the z direction to perform forced evaporative cooling. The TOP and quadrupole coils are cut away for clarity. The ultrahigh vacuum (UHV) glass cell has glass thickness of 2 mm.

3.4.1 Double-well loading

Following the loading of a BEC into the circularly-polarised single-RF shell trap, we further manipulate the RF fields to load atoms into 2D double-well potential by splitting a single condensate into two. Since we only work with linearly-polarised

[12]The detail of the loading from TOP, TAAP and then the RF-dressed potential can be found in thesis by Bentine [107]

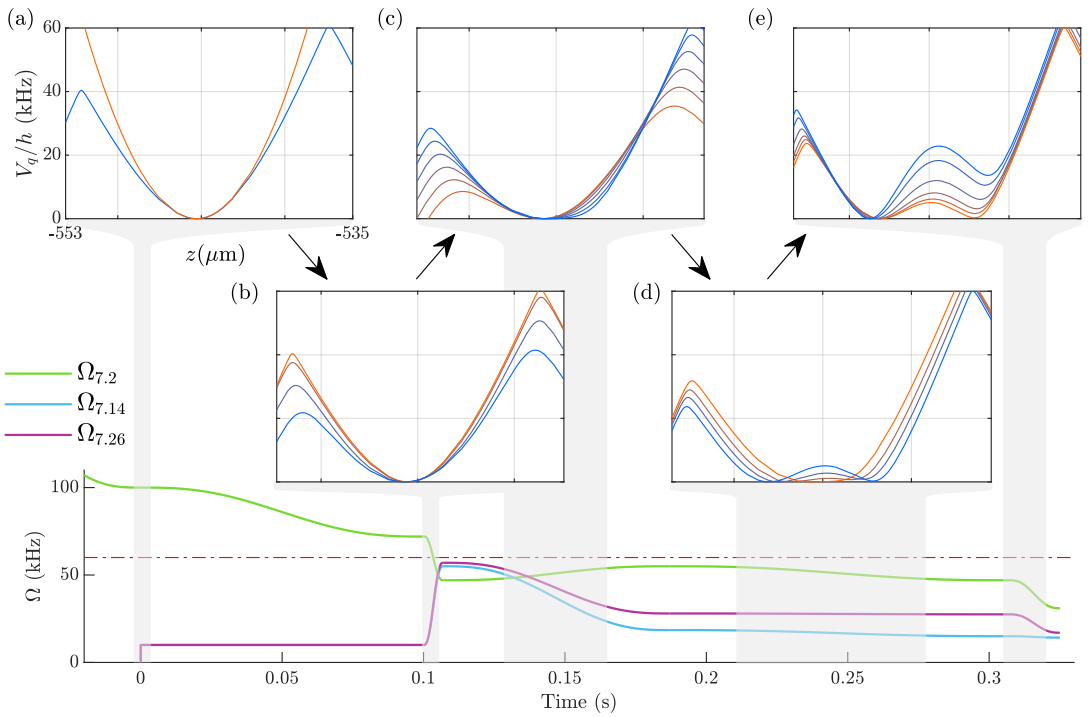

Figure 3.15: The slow loading and splitting procedure for the MRF double-well potential. The RF amplitude ramp (bottom) is shown with the corresponding trapping potentials (MRF-dressed eigenenergies, V_q), whose time evolution is indicated by the colours of the plots from orange (initial) to blue (final). The shading (grey) links the five snapshots of the potential to the time axis. (a) The two additional RFs, $\Omega_{7.14}$ and $\Omega_{7.26}$, are turned on while the amplitude of the central RF, $\Omega_{7.2}$, is kept high such that the turn-on does not perturb the clouds. The effect is negligible near the potential minima while the geometry of the trap far from the trap centre is modified significantly by the emergence of higher-order avoided crossing. (b) For the realisation of a 2D double-well the RF amplitudes satisfy $\Omega < \omega_f$ (indicated by red dash-dotted line; see Fig. 3.7), $\Omega_{7.2}$ must be turned down below ω_f before the splitting ramp. To minimise the loss of atoms occurring at $\Omega_{7.2} = \omega_f$, the amplitudes are ramped quickly through this range in 7 ms (this is the steep amplitude ramp starting at 0.1s in the above). $\Omega_{7.14}$ and $\Omega_{7.26}$ are ramped simultaneously to keep the change in the potential geometry to a minimum during this process. (c) To prepare for the splitting of trapped atoms, the potential is transformed into a flat-bottom geometry. (d) Coherent splitting is performed slowly to avoid collective excitations. It is also important to split symmetrically to minimize excitations. Since the splitting process is very sensitive to the initial and final potential geometry, this particular section of the ramp is completed soon after the cloud is split and reasonably decoupled. This allows the final potential geometry to be changed without affecting the population balance of the two wells. (e) Finally, the double-well potential is modified to satisfy quasi-2D conditions as well as to ensure complete decoupling of wells. Due to the effect of gravity, it is necessary to slightly imbalance the wells to achieve the same axial trapping frequencies for the two wells; see Figure. 3.20 for trap calibration.

RF fields when creating MRF-dressed potentials, we first need to slowly change the RF from circular to linear polarisation. This is achieved by ramping down the output from the y coil so that the final field is only along x. To avoid the excitation of collective modes such as sloshing during this process, we perform the ramp adiabatically over 1s. Once linear polarisation is achieved, we commence the loading into MRF-dressed potentials. The combination of RF frequencies used for the experiments in this thesis is typically $7.14, 7.2$, and 7.26 MHz.

Depending on the nature of the experiment, the purpose of the double-well loading is different. For the investigation of equilibrium BKT transition shown in Chapter 5, the loading is performed as slowly as possible to avoid the excitation of collective modes and atom loss. On the other hand, for the investigation of quench dynamics across the BKT critical point (Chapter 6), we need to split the cloud more quickly than the in-plane dynamics of the system on a timescale $\sim 2\pi/\omega_r \sim 100$ ms. The elimination of the collective mode is achieved by an additional stage of the experiment, specifically for the fast splitting within timescale ~ 10 ms (see Chapter 6).

In both cases, the transformation from the single- to multiple-RF dressing is a challenging task. The main challenge is the atom loss during the RF amplitude ramps as described in Sec. 3.1.4. The RF amplitudes cannot simply be ramped up to final value, since a smooth change in the Rabi frequencies results in the effective Rabi frequency being ramped over a wide range of the low-frequency regime, where the electric noise is prevalent. The RFs on the other hand cannot be jumped straight to a final desired value, since the frequency separation of 60 kHz corresponds to a small spatial separation of 4.5 µm in our typical magnetic field gradient of $b = 94$ G/cm and sudden perturbation of the trap near the locations of atoms would unavoidably cause collective motion.

To circumvent the aforementioned issues, the loading into MRF potentials needed to be performed in five separate stages as detailed in Fig. 3.15. Essentially, we prepare atoms in a single-RF potential with $\omega_{\mathrm{rf}}/2\pi = 7.2$ MHz at $\Omega_{7.2}/2\pi > 100$ kHz, and first turn on the other two RFs at around $\Omega/2\pi \sim 10$ kHz to avoid the

coupling to low-frequency noise as well as keeping the perturbation to the atoms to a minimum by the large amplitude difference $\Omega_{7.14}, \Omega_{7.26} \ll \Omega_{7.2}$ of original and the other RF components. To avoid the Majorana-like loss illustrated in Fig. 3.7 (a), we then quickly ramp the $\Omega_{7.2}/2\pi$ from 100 kHz to $\sim$ 50 kHz. We modify the other two RF components at the same time, such that the potential shape does not change over this short amplitude ramp over the duration of 7 ms. The splitting of atoms is performed adiabatically after these two stages, which serves to avoid loss mechanisms.

3.5 Detection of 2D gases

To characterise the state of 2D gases, we image the density distribution of atoms either *in situ*, or after TOF expansion, using absorption imaging. Observation is performed in either vertical or horizontal directions in the lab, i.e. either parallel or perpendicular to the direction of gravity.

The imaging is carried out by sending a resonant laser pulse onto the atom, to drive $F = 2 \rightarrow F' = 3$ cyclic transition. While the imaging is performed on atoms in $F = 2$ state, the preferred hyperfine state to carry out the experiment with atoms is the $F = 1$ hyperfine level since it has longer lifetime in the trap. We transfer atoms into $F = 2$ by means of optical pumping and a separate optical path was prepared to send in the repumping light.

Resonant light is absorbed by the atomic cloud leaving a region of 'shadow' in the transmitted laser beam where the light intensity is lower than for an unattenuated incident beam. We send the light onto a charge-coupled device (CCD) to measure the intensity distribution $I(x_p, y_p)$ where coordinates x_p and y_p are the pixel location of the CCD. As well as the 'absorption image' of the laser beam after passing through the cloud, $I_a(x_p, y_p)$, we capture an auxiliary image of the incident beam after the atoms have been dispersed, $I_i(x_p, y_p)$. We then obtain the spatial distribution of optical density according to Beer's law with the effect of saturation taken into account [112]: $OD(x_p, y_p) = \log(I_a/I_i) + (I_i - I_a)/I_{\rm sat}$, where $I_{\rm sat} = 1.67$ mW/cm^2 is the saturation intensity for circularly polarised light [113]. The calibration of optical

density to the actual atomic density is performed using knowledge of the conditions for the BEC critical point in a 3D trap [114], as discussed in Section 3.5.4.

The optical system makes the absorption image extracted from $OD(x_p, y_p)$ a convolution of the actual density distribution and the point spread function (PSF) of the imaging system that can be well-approximated by a Gaussian:

$$f_{\mathrm{PSF}}(r) \propto \exp\left(-\frac{r^2}{2\sigma_{\mathrm{PSF}}^2}\right). \tag{3.5.1}$$

We refer to σ_{PSF} as the imaging resolution throughout this thesis. The standard imaging resolution (the radius of the first zero of the Airy disc) is related to this by $r_{\mathrm{Airy}} = 2.9\sigma_{\mathrm{PSF}}$. Fig. 3.16 shows the optical setup around the glass cell, designed to probe and manipulate the atoms. We give further information on each imaging setup in the following sections.

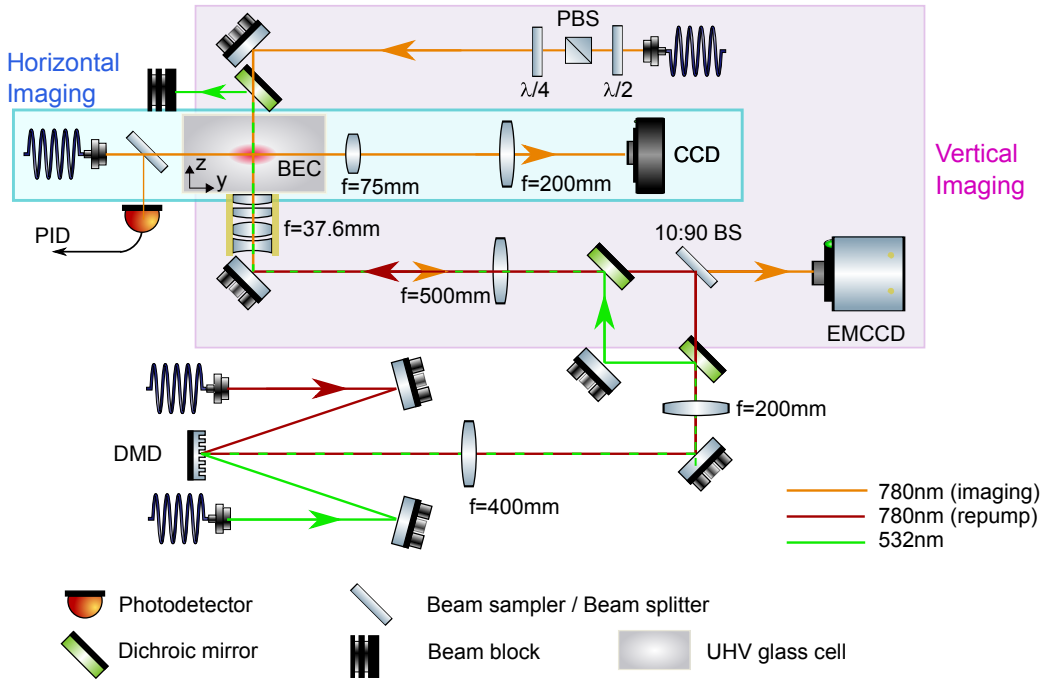

Figure 3.16: The apparatus used to probe and manipulate atoms. This illustration of the optical setup around the ultra high-vacuum (UHV) glass cell shows the arrangement of the optical components which are used to detect (Horizontal and Vertical imaging) and manipulate (DMD) the atoms. Polarisation cleaning and waveplates for polarisation control are not shown for the horizontal imaging and DMD optics for clarity of the illustration.

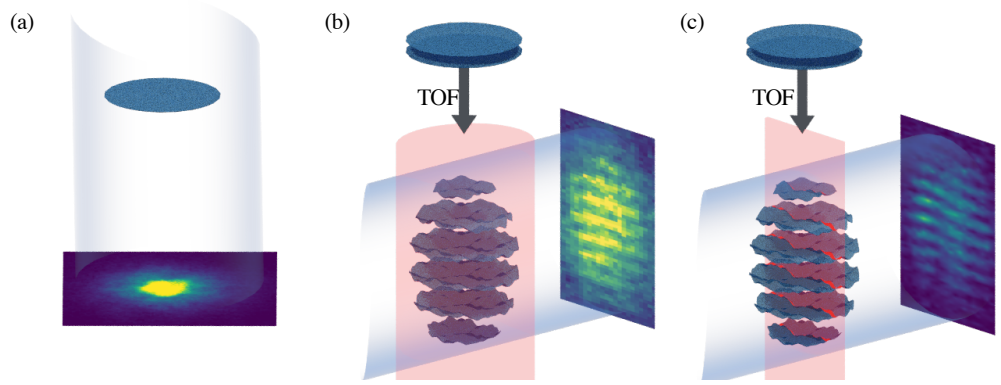

Figure 3.17: Three different types of imaging setups to probe 2D gases. (a) Vertical imaging records the 2D density distribution of atoms by sending the probe light (grey) along the direction of gravity. Repumping light (not shown) is applied to the entire cloud. (b) Horizontal imaging with full repumping of the cloud. The repumping beam (red) transfers all atoms into $F = 2$ state, thereby allowing the total atom number as well as far wings of the density distribution to be recorded for thermometry. The double-well situation is shown for illustration; the integration of the density along the imaging axis means that the observed contrast of interference fringe is low. (c) Density slicing method using spatially-modulated repumping light, to image only a thin slice of density distribution along the imaging axis. The matter-wave interference pattern is clearer than the case in (b), since integration of the fluctuating fringe pattern is avoided. The position and thickness of the sheet of repumping light can be chosen arbitrarily by changing the pattern displayed on the DMD.

3.5.1 Vertical imaging

The vertical imaging records the in-plane density distribution of 2D gases. The optical system consists of a custom-made objective lens with high numerical aperture (NA) [108], a $f = 500$ mm achromat eyepiece lens and an electron-multiplying CCD (EMCCD, *Andor* iKon-M). The NA of the objective lens is 0.27, resulting in resolution of $\sigma_{\mathrm{PSF}} = 0.5\,\mu\mathrm{m}$ at the wavelength of 780 nm that we use for detection. This optical path is shared with the light reflected from a digital micromirror device (DMD) which is propagating in an opposite direction to the imaging beam, as shown in Fig. 3.16. As we describe later in Section 3.5.3, the light from DMD creates an arbitrary spatial pattern of light for selective repumping and potential shaping and utilises the high NA of the objective lens.

3.5.2 Horizontal imaging

The horizontal imaging detects the density distribution along the radial direction and is the main detection method throughout this thesis since the matter-wave interference patterns can be observed. The imaging system consist of two lenses, a doublet lens with $f = 75$ mm as an objective lens and a $f = 200$ mm eyepiece lens, resulting in image-plane pixel size of $\ell_p = 1.67\,\mu\text{m}$. The optical resolution of this imaging setup was measured using a USAF resolution target[13] to be $\sigma_{\text{PSF}} = 2.1\,\mu\text{m}$.

3.5.3 Beam shaping with a DMD and selective imaging

The standard absorption imaging of cold atoms entails the integration of density along the imaging axis. This integration is problematic for the investigation of interfering 2D Bose gases, since the fluctuation of the interference patterns along the imaging axis causes the loss of information. To mitigate the effect, we implemented a method of spatially-selective imaging of the atoms by spatially-selective repumping of atoms into the $F = 2$ state. Fig. 3.18 (b) shows absorption images obtained by using a laser light with a complex shape to selectively repump a partially condensed cloud of atoms and detect them using imaging along the vertical axis. Thanks to the high resolution of the vertical imaging, a small-scale structure can be painted onto the atom, as shown in Fig. 3.18. For the selective imaging, we shape the repumping light into a thin sheet with variable thickness L_y as illustrated in Fig. 3.17 (c). The programmability of the DMD allows us to arbitrarily choose the position and the thickness of this sheet.

The DMD can also be used to shape the confining potential of the atoms using far-detuned intense light, in this way we will be able to implement a wide variety of potential shapes such as a box trap [13], disordered potential [115] and an 'entropy reservoir' [116] to realise complex Hamiltonian, allowing us to probe novel physics. We have installed the 532 nm laser system required for the potential shaping with far-detuned light, shown as a part of Fig. 3.16. However, there has not been sufficient

[13] 1951 USAF resolution chart, defined by U.S. Air Force MIL-STD-150A standard of 1951

experimental time for the precise alignment and characterisation of such arbitrary potential, and this remains an exciting prospect for future work with this apparatus.

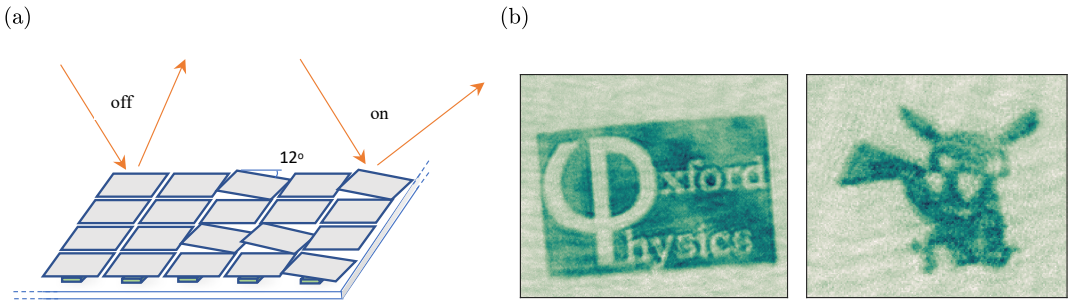

Figure 3.18: Illustration of the DMD. (a) The DMD consists of an array of small square-shaped mirrors, which can be individually tilted to a certain angle by a force applied from the complementary metal-oxide-semiconductor (CMOS) substrate. (b) An application of DMD light shaping to the spatially-selective repumping of atoms in a 2D confinement. The image was taken vertically, to directly image the repumped atoms *in situ*.

3.5.4 Imaging detectivity calibration

To calibrate our imaging detectivity, we observe the 3D BEC critical point in a cylindrically symmetric time-averaged adiabatic potential [117] with trap frequencies: $\omega_r/2\pi = 54\,\text{Hz}$ and $\omega_z/2\pi = 300\,\text{Hz}$, resulting in geometric mean $\overline{\omega}/2\pi = (\omega_r\omega_r\omega_z)^{1/3}/2\pi = 96\,\text{Hz}$. We use this method because it is insensitive to experimental imperfections such as imperfect polarisation of the probing light and it provides absolute calibration of atom number. For the range of temperatures and atom numbers used in this process, the system is three-dimensional (not quasi-2D). We calibrate the atom number by comparing the critical atom number to the theoretical value:

$$N_c = \zeta(3)\left(\frac{k_B T}{\hbar\overline{\omega}}\right)^3\left(\frac{1}{1-3.426(a_s/\lambda)}\right)^3 + \delta N, \tag{3.5.2}$$

where ζ is the Riemann zeta function. δN is the finite-size correction [118] that result in 3 % higher critical atom number for the parameters used in this procedure. Another correction term $(1-3.426(a_s/\lambda))^{-3}$ in Eq. (3.5.2) is the mean-field

correction [114] where a_s is the s-wave scattering length and $\lambda = h/\sqrt{2\pi m k_B T}$ is the thermal de Broglie wavelength. We chose the range of atom numbers used for this calibration such that the average optical density after TOF is close to the values for data shown in the main text.

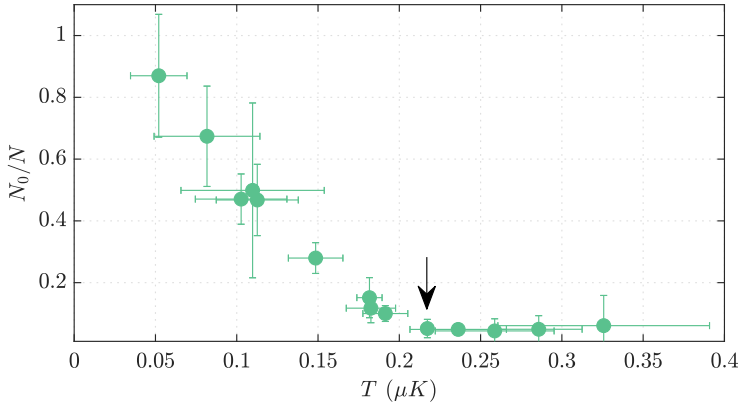

Figure 3.19: The determination of the 3D BEC critical point in a TAAP trap for the calibration of imaging. The fraction of atoms in the central Thomas-Fermi peak N_0/N is shown as a function of the temperature of the cloud in the trap with the total atom number varying from 5×10^4 to 1.2×10^5. The critical point was identified by the temperature at the onset of N_0/N, indicated by the black arrow. The calibration was done by comparing the measured atom number and temperature at the critical point to the expression Eq. (3.5.2).

3.6 Trap characterisation

While we can accurately predict the potential geometry given the combination of RF amplitudes using the Floquet numerical procedure, however, precise experimental determination of the actual RF amplitudes is difficult, mainly because of the small separation of the commensurate RF frequencies. Therefore, we measure a few important characteristics of the double-well by alternative methods. Determination of the confinement is achieved by observing the collective oscillation of atoms in the trap. We apply a momentum kick to the atoms by a sudden change in the quadrupole field strength (for the vertical trap calibration) or by a sudden addition of a horizontal bias field (to produce a kick in x and y). For the vertical trap frequency calibration in a double-well, we slightly modified the usual double-well loading scheme shown in Fig. 3.15, such that atoms are localised in one of the wells,

before we performed the measurement. The results are presented in Fig. 3.20 (a) and (b) for the measurements in the vertical and x directions.

The calibration in the y direction is not straightforward since we do not have sufficient optical access to observe the motions of atoms along the y direction. Instead of building another imaging apparatus, we use the density slicing method to detect the oscillation of the atomic cloud along the imaging axis; to determine the position of atoms, we perform multiple experimental sequences with different positions of the repumping light sheet and reconstruct the density distribution, as shown in Fig. 3.20 (c). We repeat the procedure at variable times after the impulse is applied to the atoms and obtain the oscillation frequency in the trap, see Fig. 3.20 (d). We further characterise the spatial separation of the two wells using the matter-wave interference wavenumbers, which is discussed in the next chapter.

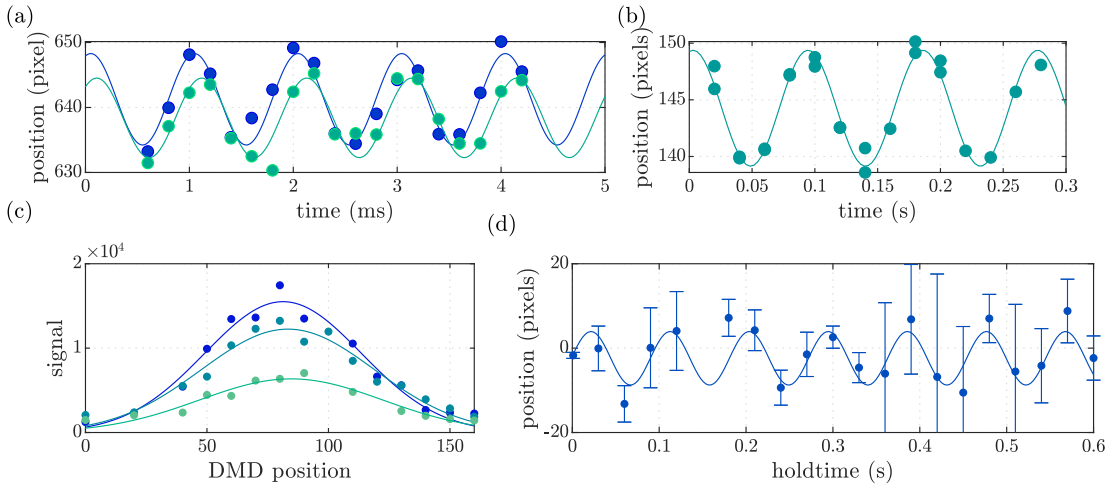

Figure 3.20: Trap characterisation. (a) Measurement of vertical trap oscillations in left (blue) and right (green) wells. Position of atoms after 16 ms TOF is plotted against the time elapsed after a vertical kick. The two measurements were performed separately with slightly different double-well loading parameters which ensure loading of Bose-condensed atoms into only one well. The measured frequencies are 1.01(3) kHz and 0.99(4) kHz. (b) Measurement of the radial trap oscillation (in x direction), perpendicular to imaging axis. The measured frequency is 10.9(2) Hz. (c) Measurement of density distribution along the imaging (y) axis using the density slicing method. The DMD position is in the unit of pixels, corresponding to a real-space length of 0.5 μm. Different colours indicate different times after the kick and solid lines are Gaussian fit. (d) Measurement of trap oscillation along the imaging axis y. Each point represent the centre of the fitted Gaussian at each time. The trap oscillation frequency is 11.0(5) Hz, in good agreement with the result of the measurement along x, as in (b). A datapoint at 0.15 s is missing due to a fit failure.

4

Characterising 2D quantum gases

Contents

Observation of the BKT transition in 2D Bose gases has so far relied on a variety of observables. The most straightforward way to characterise the system is the *in situ* density distribution [62–64] and the density distribution after free expansion [70, 119, 120]. Furthermore, the cold atomic system offers observables to be probed that are not accessible in other experimental systems such as the spatial phase fluctuations [14, 32, 94]. In this section, we describe the analysis methods used to extract properties of 2D systems along with examples of our relevant experimental results. A more detailed discussion of the BKT critical

phenomena can be found in Chapters 5 and 6. We further discuss the practical considerations to be made when investigating the 2D system in the presence of finite imaging resolution and inhomogeneity.

4.1 Density distribution

We rely on the measurement of the density distribution using absorption imaging techniques to infer various properties of 2D gases. The density distribution of harmonically-trapped, weakly-interacting 2D Bose gases was described theoretically in detail in Chapter 2. In this section, we show the method of analysing the experimental data that we use in the following sections, such as fitting and thermometry procedures.

4.1.1 The in situ density distribution

The *in situ* density distribution can be measured by using the vertical imaging system introduced in Section 3.5.1. As described in Section 2.3.6, within the LDA the measurement of the density distribution in a harmonic trap provides a single-shot determination of the equation of state for a range of local chemical potentials [63]. However, our current experimental setting has a problem for the precise measurements near the critical point. This is because at high atom density, the calculation of the optical density via the simple Beer's law is not accurate. As described in Ref. [64], at a small inter-atom distance shorter than the wavelength of the laser $n^{-1/2} \lesssim 780$ nm, collective phenomena take place and modify the atom-light interaction. To circumvent the problem, short high-intensity imaging may be used [64]. Since we have not implemented high-intensity imaging yet, we have limited ourselves to thermal and crossover regime of the BKT critical point for the *in situ* density measurement, where the collective phenomena is not important.

The density distribution of atoms obtained with the vertical imaging system, of atoms with temperature around 100 nK in a single-RF dressed potential with $\omega_r = 25$ Hz, is shown in Fig. 4.1 (a), and Fig. 4.1 (b) shows their azimuthally averaged density distribution.

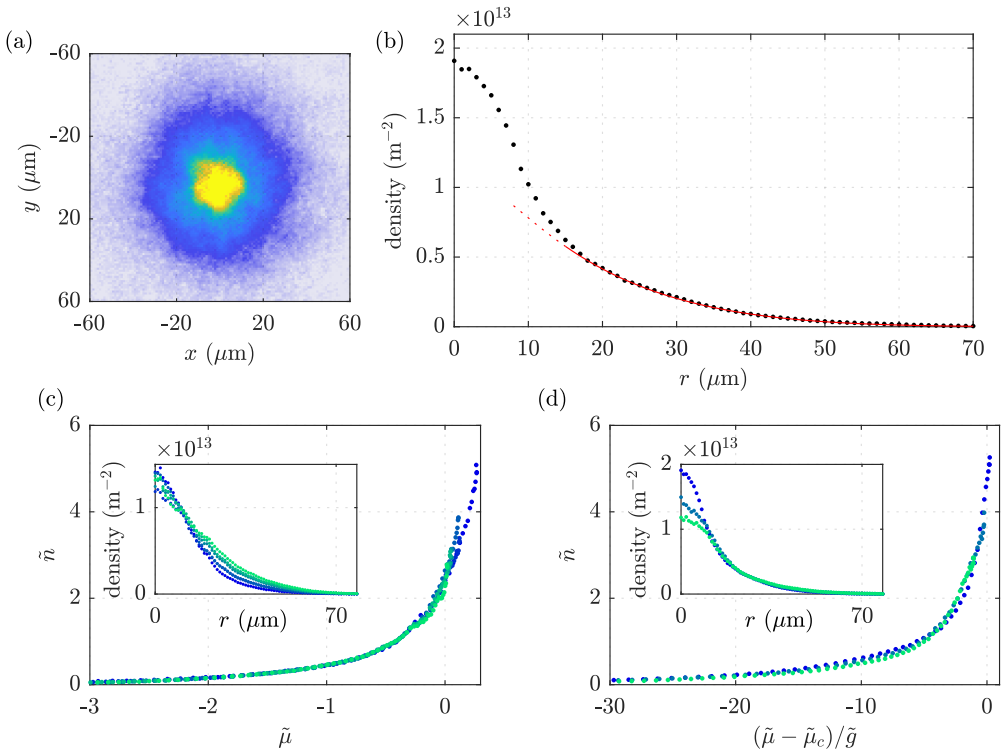

Figure 4.1: *in situ* density distribution, scale invariance and universality. (a) The averaged density distribution of a 2D Bose gas trapped in a single-RF dressed harmonic trap with $\omega_r/2\pi = 25$ Hz and $\omega_z/2\pi = 1.8$ kHz, at temperature 100 nK. (b) Azimuthal average of the density distribution shown in (a). The red line is the Hartree-Fock fit result of the far wing of the density distribution, obtained by fitting the solution of implicit equation $\mathcal{D}(r) = -\ln(1 - \exp(\mu/k_BT - \tilde{g}\mathcal{D}(r)/\pi - V(r)/k_BT))$ to the density distribution in the low-density region, with free parameters μ and T. (c) The demonstration of scale invariance of 2D Bose gases. Rescaled density distribution $\tilde{n} = n\lambda_{\mathrm{th}}^2$ is plotted against rescaled local chemical potential $\tilde{\mu}(r) = (\mu - V(r))/k_BT$ of data taken with temperatures 100 nK (blue) to 170 nK (green), in the thermal regime. Inset shows the same data with the original scales. (d) The universality of the 2D Bose gas near the BKT critical point. The rescaled density distribution is plotted against $(\tilde{\mu} - \tilde{\mu}_c)/\tilde{g} = (\mu - V(r) - \mu_c)/k_BT\tilde{g}$ for three different effective interaction strengths $\tilde{g} = 0.078, 0.084$ and 0.093. In a similar manner to (c), the data collapse onto a single line; this is the demonstration of universality close to the critical point predicted in Ref. [18].

Furthermore, the *in situ* density distribution can be used to confirm the scale invariance and universality of 2D Bose gases that we discussed in Section 2.3.5. Within the LDA, the *in situ* density distribution is a direct measurement of the equation of state across a range of local chemical potential. As such, by taking images using vertical imaging at different temperatures or interaction strengths, we can readily observe the temperature and interaction dependence of the equation

of state, as shown in the following.

Fig. 4.1 (c) shows the azimuthally averaged density distributions $\tilde{n} = n\lambda_{\mathrm{th}}^2$ as a function of rescaled local chemical potential, $\tilde{\mu}(r) = (\mu - V(r))/k_B T$. The data shown are at different temperatures ranging from 100 nK to 170 nK, as measured using the fit of the Hartree-Fock prediction to the wings of the density distribution [65]. All the curves collapse onto a single line, which is a manifestation of the scale invariance of the system. This can be seen by comparison to the density distributions with the original scales for r and n, shown in the inset of Fig. 4.1 (c) which are clearly distinct.

Fig. 4.1 (d) shows the density distribution taken at the same temperature but with different effective 2D interaction strength; this interaction can be varied because of its dependence on the vertical oscillation frequency ω_z, as implicit in Eq. (2.3.1). As discussed in Sec. 2.3.5, the data collapse onto a single line by subtracting the local chemical potential by μ_c and dividing it by the interaction strength. Since the behaviour of the system is not dependent on the microscopic detail of the system, i.e. interaction strength, this indicates the universal behaviour of 2D Bose gas close to a critical point, as previously reported [62].

4.1.2 TOF expansion of quasi-2D Bose gases

The TOF expansion is a method routinely used to extract the momentum distribution of cold atomic gases. For the quasi-2D gases, the expansion dynamics is simplified compared to that of 3D gases because the tight confinement in z direction results in a rapid expansion of the gas at the start of the TOF expansion, making the effect of interactions during TOF negligible. The expansion along the radial direction r and the axial direction z are thus separable, and we focus on the radial expansion dynamics to extract the thermodynamic quantities of the 2D gas. The expansion of cloud along the tightly-confined z direction is simplified since only the ground state is populated when the quasi-2D condition is met. The size of the cloud increases linearly with expansion time at a sufficiently long time [121],

$$l_z(t) = l_z(0)\sqrt{1 + \omega_z^2 t^2} \simeq l_z(0)\omega_z t. \tag{4.1.1}$$

On the other hand, the radial expansion is more complex since harmonic oscillator excited states are thermally occupied.

Fig. 4.2 shows the expansion dynamics of quasi-2D gases initially trapped in RF-dressed potential. Fig. 4.2 (a) illustrates the expansion dynamics after projecting the dressed states into bare Zeeman states; three daughter clouds appear by Stern-Gerlach-like spatial separation of the states in the residual quadrupole magnetic field after the RF fields are turned off. Even with instantaneous turn-off of the current source, the quadrupole field dies away in a finite duration of around 3 ms after the RF turn-off. After the quadrupole field is completely removed, all the clouds undergo free expansion. The red line indicates the free-fall trajectory $z(t) = z(0) - g_{\mathrm{E}}t^2/2$ where g_{E} is the gravitational acceleration at the surface of earth; the magnetically insensitive $m_F = 0$ cloud in the middle follows this curve after its projection into this Zeeman state. We focus on $m_F = 0$ states for analysis, and use the other clouds only to count the total number of atoms.

To visualise the expansion dynamics of 2D clouds in the radial direction, we plot the integrated density distribution in Fig. 4.2 (b) for TOF durations from 3 ms (orange) to 21 ms (blue). The temperature of the gas was around 40 nK and the system is in the superfluid regime. The density profile shows a bimodal distribution as expected from classical-field theory in Sec. 2.3.6. During the TOF, while the central peak shows negligible change in its shape, the wider Gaussian wing shows clear expansion (see Fig. 4.2 (b-d)). For quantitative analysis, we have fitted the density distributions with a bimodal distribution defined by

$$n(x) = n_g e^{-\frac{x^2}{2\sigma_g^2}} + n_{\mathrm{TF}} \max\left(0, 1 - \frac{x^2}{R^2}\right). \tag{4.1.2}$$

The expansion dynamics in the radial direction has two limiting cases. The first case is the Gaussian wing of the density distribution, where the local chemical potential is very small and thermal-gas approximation can be made. For such a low-density part of the gas, a ballistic expansion of thermal gas is expected. This is seen in the fit results of Gaussian width σ_g, plotted in Fig. 4.2 (c) for four different

temperatures. The expansion is fitted well by the form for a thermal gas [67],

$$\sigma_g^2 = \frac{2k_BT}{m} \cdot \frac{1+\omega_r^2 t^2}{\omega_r^2}. \tag{4.1.3}$$

From the fits in Fig. 4.2, we extract temperatures 40(2), 45(2), 58(6) and 83(5) nK from the blue to green data points.

The second case is the analysis of the central peak of the density distribution, which is attributed to zero-momentum modes in a 3D BEC. Similarly, we find that this central peak is associated with low-momentum modes in quasi-2D Bose gases, as we see in Fig. 4.2 (d) which shows the time evolution of the Thomas-Fermi radius R during the expansion. We also plot the vertical extent of the cloud in Fig. 4.2 (e), which shows a linear increase with TOF as expected [121].

4.1.3 Analysing images at fixed TOF duration

As shown in the last section, we can determine the temperature of the system from the standard, integrated absorption image after TOF. Assuming the radial symmetry of the system and the known expansion dynamics, we can estimate various other quantities of interest as we describe below. The following relations are used throughout this thesis to characterise the 2D gases.

Firstly, as we have derived in the last section, the temperature of the gas can be obtained by the expansion of the component that is a thermal gas,

$$k_BT = \frac{1}{2}m\left(\frac{\omega_r^2}{1+\omega_r^2 t^2}\sigma_g\right). \tag{4.1.4}$$

We note that a finite population of excited levels in the axial harmonic oscillator may affect this method of thermometry as pointed out in Refs. [57, 65]. Nevertheless, our experimental parameters are well within the quasi-2D regime, as the mean-field and thermal energy scales are smaller than $\hbar\omega_z$, and so the population of excited levels is negligible. The observed agreement of the experimentally measured density distribution and strictly 2D Monte Carlo simulation presented in Chapter 5 (see Fig. 5.5 (b), Fig. 5.11 and Fig. 5.10) further confirms the reliability of the thermometry method described above.

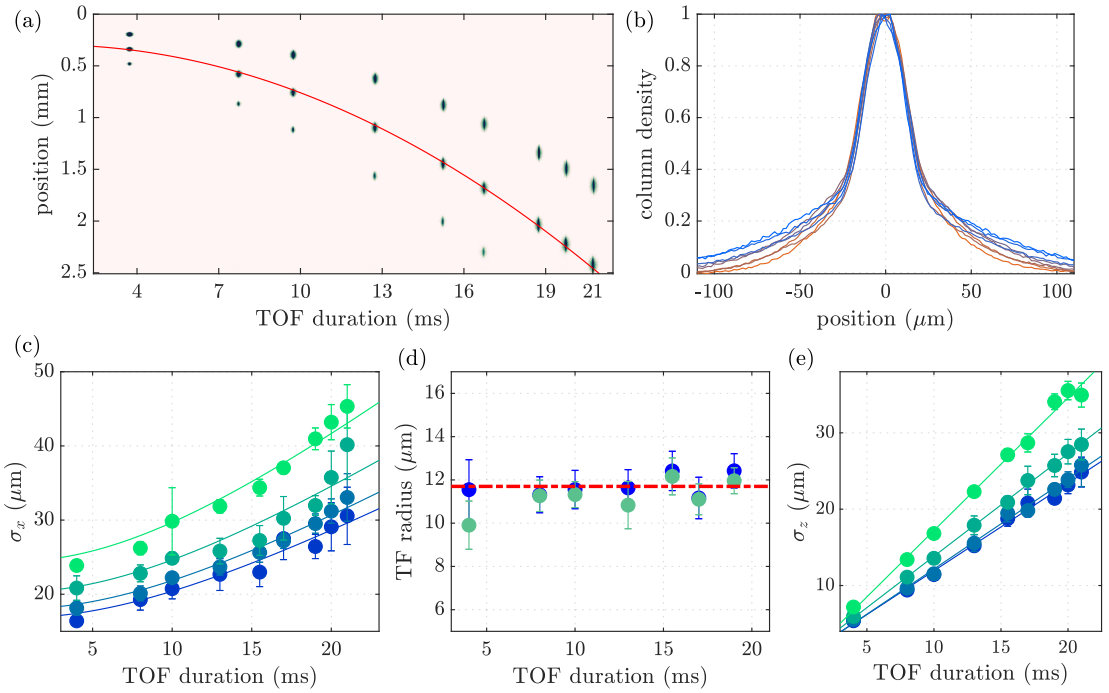

Figure 4.2: TOF expansion of quasi-2D Bose gases. (a) The combined images of atoms released from a MRF-dressed potential at variable TOF durations. The red line indicates the free-fall trajectory. (b) Integrated radial density distributions of 2D Bose gases for TOF durations ranging from 3 ms (orange) to 21 ms (blue). (c) The size of the wide Gaussian part of the density distributions, shown in (b), as a function of TOF duration. Different colour indicates different temperatures of the gas, from 37 nK (blue) to 78 nK (green). Solid lines are the fit with Eq. (4.1.3). (d) Thomas-Fermi radius R of the central peak at 37 nK (blue) and 43 nK (green). The red line is a guide to the eye. (e) The vertical extent (Gaussian standard deviation) of the gas as a function of TOF durations. Solid lines are linear fits, as in Eq. (4.1.1).

Furthermore, the one-to-one mapping of the Gaussian size after TOF to *in situ* size, together with the extracted atom number associated with TF and Gaussian profiles, allows determination of the *in situ* density distribution; from fit results of TOF images using Eq. (4.1.2), we calculate the populations in the Gaussian and Thomas-Fermi parts N_g and N_{TF} and obtain the estimated *in situ* density distribution as

$$n(r) = n_{g,0} e^{-\frac{r^2}{2\sigma^2\alpha^2}} + n_{\mathrm{TF},0} \max\left(0, 1 - \frac{r^2}{R^2}\right), \tag{4.1.5}$$

where $\alpha = (1 + \omega_r^2 t^2)^{-1}$; the peak 2D densities $n_{g,0}$ and $n_{\mathrm{TF},0}$ are chosen such that the populations of each component in the *in situ* distribution Eq. (4.1.5) match to that obtained in TOF images. We found good agreement of the estimated *in situ*

density distribution to that obtained from the Monte Carlo simulation performed for our particular experimental parameters (see Chapter 5).

4.2 Matter-wave interference patterns

We investigate the fluctuation properties of 2D Bose gases using matter-wave interference (MWI). The MWI patterns reveal the intrinsic fluctuation of the 2D system from which we obtain the correlation functions. In this section, we give a description of the matter-wave interference analysis methods, as well as the effect of finite imaging resolution. An important consideration is the method of accounting for the inhomogeneity of the system in our analysis leading to the correlation function.

4.2.1 Matter-wave interference

We calculate the density distribution of quasi-2D Bose gases which are initially trapped in a double-well potential and released for a TOF expansion. The wavefunction in the z direction consists of two Gaussian wavepackets in the two wells $j = 1, 2$ with initial spatial separation d, and the total wavefunction is $\varphi(z,t) = \varphi_1(z,t) + \varphi_2(r,t)$. The expansion of the individual wavepacket is described by [67]

$$\varphi_j(z,t) \propto \exp\left[i\phi_j(\boldsymbol{r}) - \frac{(z \pm d/2)^2(1 + iht/ml_0^2)}{2l_t^2}\right], \tag{4.2.1}$$

where the $\phi_j(\boldsymbol{r})$ is the *in situ* phase of each cloud, $l_t^2 = l_0^2 + (ht/ml_0)^2$ and l_0 is the initial wavepacket size. The corresponding density distribution after TOF is

$$n(z,t) = |\varphi(z,t)|^2 = |\varphi_1(r,t)|^2 + |\varphi_2(r,t)|^2 + 2\,\mathrm{Re}[\varphi_1(r,t)^*\varphi_2(r,t)], \tag{4.2.2}$$

$$\propto \exp\left(-\frac{r^2}{2l_t^2}\right)\left[1 + \cos\left(\frac{md}{\hbar t}z + \phi_1 - \phi_2\right)\right], \tag{4.2.3}$$

where we have used $\exp\left(-\frac{(z\pm d/2)^2}{2l_t^2}\right) \simeq \exp\left(-\frac{z^2}{2l_t^2}\right)$ and $l_t \simeq ht/ml_0$ for sufficiently long TOF duration such that $l_t \gg l_0, d$. The density distribution of 2D gases released from a double-well trap thus shows a sinusoidal modulation of density with a Gaussian envelope. The periodicity of the modulation is $\Delta z \sim 2\pi\frac{\hbar t}{md}$. Additionally, the phase profile of the interference pattern along r depends on the

phase difference of the initial gases $\phi_1 - \phi_2$ and this allows us to infer the spatial distribution of the *in situ* relative phase.

As described in Sec. 3.5.3, we image slices of the density distribution with thickness L_y to reveal the local fluctuation of the phases. This technique works if the L_y is shorter than the characteristic length scale for the change in phase, i.e. the phase correlation length r_0. Thus, when investigating the BKT critical phenomena, we only take data in the superfluid and crossover regime where the detection of the phase profile is feasible, i.e. $L_y \lesssim r_0$. The thickness of the slice needs to be large enough to give a good signal-to-noise ratio in the absorption imaging; typically, we use a thickness $L_y = 5\,\mu\text{m}$ which is a compromise between the two constraints and is short enough to probe the phase correlation function across the BKT critical point.

4.2.2 Extracting phases

To extract the phases from the observed interference pattern, we fit the column density distribution $n_x(z)$ with the fit function

$$n_x(z) = n_p \exp\left(-\frac{(z-z_0)^2}{2\sigma_z^2}\right)\Big[1 + c_0\cos(kz + \theta(x))\Big], \tag{4.2.4}$$

where $n_p, z_0, \sigma_z, c_0, k$ and $\theta(x)$ are the fit parameters. With the density slicing method, the extracted phase $\theta(x)$ encodes a specific realisation of the fluctuations of the *in situ* local relative phase along the line $\boldsymbol{r} = (x, y = 0)$ between the pair of 2D gases. Fig. 4.3 (a) illustrates the fitting.

For small well separations, where $d \sim l_t(t = 0)$, the fit becomes increasingly difficult as the interference fringe spacing becomes comparable to the extent of the cloud $\Delta z \sim l_t(t_{\text{TOF}})$. In such cases, the Fourier transform is a better method to extract the phases by taking the argument of complex fast Fourier transform (FFT) amplitude at the fringe wavenumber $k = \hbar t_{\text{TOF}}/md$. We thus used the FFT for the results reported in Chapter 7, where the well separation is made small, $d \sim 2\,\mu\text{m}$ to induce coupling between the two wells. We compare the two phase extraction methods in Fig. 4.3. Fig. 4.3(b) shows that for a fringe wavelength longer than $0.2\sigma_z$, the FFT method is more reliable.

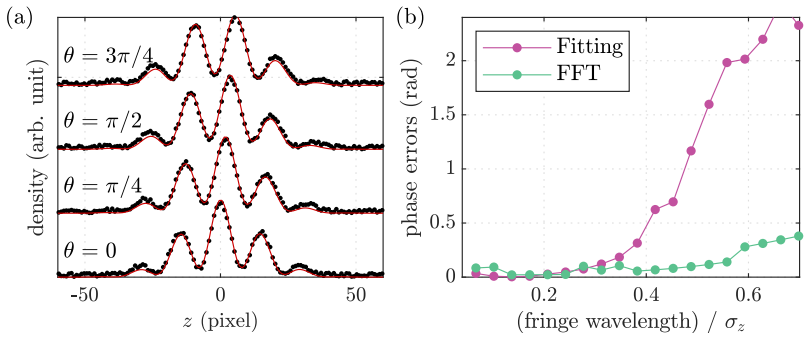

Figure 4.3: Phase extraction from interference patterns. (a) artificially generated density profiles along z using Eq. (4.2.4) at different θ with the added white noise of amplitude at 10 % of the peak value. Red lines are fit with Eq. (4.2.4). (b) Comparison of two methods to extract the phases. For a range of fringe wavelengths from $0.02\sigma_z$ to $0.7\sigma_z$, we generated 20 images with different phases θ in the same way as (a) and extracted the phases using two methods. The root-mean-squared errors of true and measured phases are shown as a function of fringe wavelength divided by the extent of the Gaussian envelope σ_z.

4.2.3 Postselection of fit results

Even at a small fringe wavelength where the fitting with Eq. (4.2.4) is expected to work well, noise and imperfections in the experiment lead to cases where the fit fails to converge and returns unrealistic parameters. Anomalous jumps of phases from failed fit attempts significantly affect the correlation analysis, therefore we postselect fit results that can be considered a reasonable fit and exclude those that can be considered a fit error or absence of interference signal. This selection is based on the fact that the double-well separation is fixed for any temperature of the gas and thus the k must be fixed. Therefore we use anomalous values of k as an indication of fit failure, and exclude these datapoints from further analysis. Specifically, we discard datapoints where the fitted value of k is outside the region of the peak of its histogram, as illustrated in Fig. 4.4 for the datasets shown in Chapter 5.

4.2.4 Obtaining the phase-correlation function

As we have discussed in Sec. 2.5.1, the correlation function of the relative phases of two decoupled 2D gases is related to the first-order correlation function of each layer, thus providing a direct probe of the BKT transition. In this section, we describe the specific method used to obtain the phase correlation function of the 2D system.

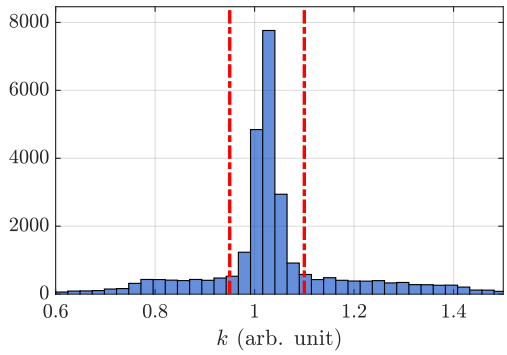

Figure 4.4: Histogram of the fringe wavenumber k from fits with Eq. (4.2.4), performed on the experimental data shown in Chapter 5. The red dashed lines indicate the range of k that we use for postselection.

For each experimental run, we obtain the relative phase profile $\theta(x)$ as described previously. From $\theta(x)$, we first calculate the two-point phase correlation function $e^{i[\theta(x)-\theta(x')]}$ for all combinations of locations x and x' within the interfering part of the cloud. We then determine the averaged correlation function

$$C_{\mathrm{exp}}(x,x') = \frac{1}{N_r}\sum_j e^{i\theta(x)-i\theta(x')}, \tag{4.2.5}$$

where the index j runs over N_r individual experimental realisations. Typically N_r is on the order of 100. The real part of the correlation function $C^r(x,x') = \mathrm{Re}\,[C_{\mathrm{exp}}(x,x')]$, equals 1 for perfect correlation between pairs of points and 0 for uncorrelated pairs of points.

Fig. 4.5(b) shows an example of this correlation $C^r(x,x')$, using the data of an equilibrium system in crossover regime at $T \sim 40$ nK, from Chapter 5. The range of spatial correlations around the diagonal $x = x'$ indicates the coherence of the system. $C^r(x,x')$ is related to the one-body correlation function $g_1(\boldsymbol{r},\boldsymbol{r'})$ by

$$C(\boldsymbol{r},\boldsymbol{r'}) \simeq \frac{\langle\Psi^\dagger(\boldsymbol{r})\Psi(\boldsymbol{r'})\rangle^2}{\langle|\Psi(\boldsymbol{r})|^2\rangle\langle|\Psi(\boldsymbol{r'})|^2\rangle} = \frac{g_1(\boldsymbol{r},\boldsymbol{r'})^2}{n^2}. \tag{4.2.6}$$

To quantify the decay of correlations, we calculate $C(\overline{x})$ by averaging $C^r(x,x')$ over the set of points with the same spatial separation $\overline{x} = x - x'$. This averaging was performed over antidiagonal and their adjacent and second adjacent elements of $C^r(x,x')$, corresponding to the points that are distanced $\overline{x}/2$, $\overline{x}/2 \pm 1$ and

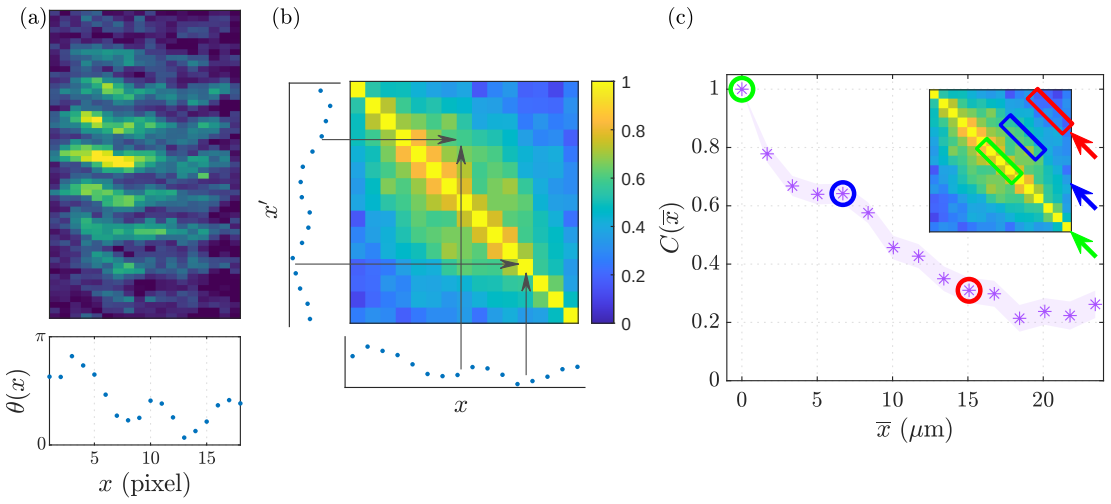

Figure 4.5: Extraction of the phase correlation function $C(\overline{x})$. (a) An example phase profile extracted from an interference pattern using the fit function Eq. (4.2.4). The bottom panel shows the phase profile in radians. (b) From the phase profiles $\theta(x)$ extracted from large number of images, we calculate the two-point phase correlation Eq. (4.2.5). Diagonal elements $C^r(x,x) = 1$ by definition. (c) From $C^r(x,x')$, the correlation function $C(\overline{x})$ at distance $\overline{x}$ (in number of pixels) is calculated by taking the mean of $\overline{x}$-th diagonal elements of $C^r(x,x')$ according to Eq. (4.2.7). The shaded region is the uncertainties obtained by the bootstrapping method. The elements of the $C^r(x,x')$ included in the averaging are indicated by the rectangles (red, blue and green), corresponding to $C(\overline{x})$ data points marked by circles in matching colours.

$\overline{x}/2 \pm 2$ pixels from the centre of the cloud (see Fig. 4.5(c) inset). The averaged correlation function $C(\overline{x})$ is defined as

$$C(\overline{x}) = \frac{1}{N_{\overline{x}}} \sum_{x=-\overline{x}/2-2}^{-\overline{x}/2+2} \mathrm{Re}\left[C(x, x+\overline{x})\right], \tag{4.2.7}$$

where $N_{\overline{x}} = 5$ is the number of pixels used for the averaging. This procedure is illustrated in Fig. 4.5 (c).

4.3 Effect of finite imaging resolution

The imaging system in our apparatus has finite imaging resolution with point-spread function (PSF) approximated by Gaussian with a standard deviation of $\sigma_{\mathrm{PSF}} = 2.1\,\mu\mathrm{m}$. The observed images involve a density distribution convolved with the PSF of the imaging system. Specifically, this is expected to affect the short-range correlations $\overline{x} \sim \sigma_{\mathrm{PSF}}$. The change in short-range correlation is not expected to

affect our determination of the BKT critical point significantly because we are only interested in the long-distance behaviour of the correlation functions to probe BKT critical phenomena. However, it is important to quantitatively estimate the effect.

Superfluid regime

To model the effect of imaging resolution to the correlation analysis within the superfluid regime, we assume the equilibrium phonon mode population [122] and the effect of imaging resolution can be straightforwardly modelled by multiplying the phonon mode populations with the Fourier transform of the PSF, $\exp(-\sigma_{\mathrm{PSF}}^2 k^2/2)$. We plot the normalised correlation function with true exponent $\eta = 0.2$ and imaging resolution σ_{SF} =0,0.5,...,2.5 in Figure 4.6 (a), along with fitting with a power-law function $f(x) = ax^{-\eta}$. As expected, the long-distance decay of the correlation function is unchanged by having finite imaging resolution. In Figure 4.6 (b), we present the results of fitting which show that a finite imaging resolution of $\sigma_{\mathrm{PSF}} = 2.1\,\mu\mathrm{m}$ has negligible effect on the extracted value of η within the superfluid regime.

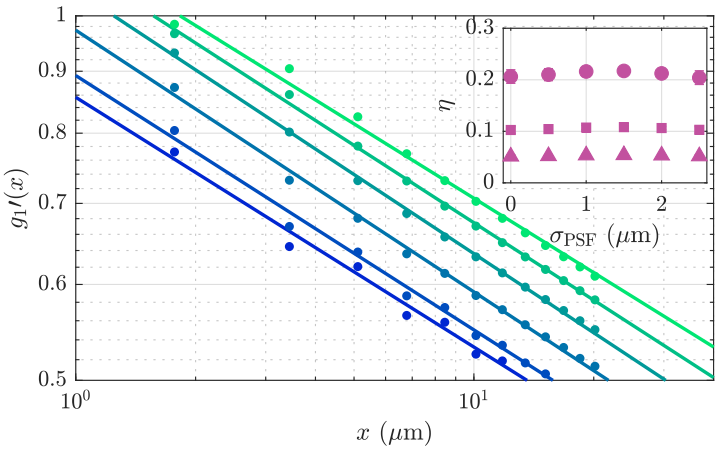

Figure 4.6: Effect of imaging resolution on the measurement of the algebraic exponent η. Points represent normalised one-body correlation functions $g_1'(x) = g_1(x)/n$ in the superfluid regime, simulated with the effect of imaging in real-space with σ_{PSD}=0,0.5,...,2.5 μm from bottom to top (blue to green). σ_{PSF}=0 corresponds to the absence of any imaging effect. Lines in corresponding colours are fitted curves with $f(x) = ax^{-\eta}$. (inset) Fitted values of η as a function of imaging resolution with $\eta_0 = 0.2$ (circle), 0.1 (square) and 0.05 (triangle).

Thermal regime

To estimate the effect of finite imaging resolution on the correlation function in the thermal regime, we have simulated the fluctuations of the system using the Ornstein-Uhlenbeck stochastic process [123] with the time axis replaced by the real-space axis along a direction perpendicular to the imaging direction. This process gives fluctuating phase profiles with exponentially decaying two-point phase correlation with a given correlation length ξ_0 and was used in the analysis of experiments elsewhere to simulate the fluctuating phase profiles of 1D gases [32]. The effect of imaging resolution was incorporated by convolving the interference pattern arising from the ballistic expansion of a pair of phase-fluctuating clouds along z direction [67] with a Gaussian PSF. We generate $N = 200$ images at each set of parameters and apply the image analysis procedure as described in Section 4.2.4 to obtain the correlation functions. In Fig. 4.7 (b) the correlation functions in the presence of finite imaging effect are plotted. The inset of Fig. 4.7 (b) shows the correlation length r_0 extracted by fitting the correlation functions obtained with $\sigma_{PSF} = 2.1\,\mu\text{m}$. The plot shows the measured correlation length against the true correlation function used to generate the data, ξ_0. From this, we find that the imaging effect systematically shifts the observed correlation length up to around σ_{PSF}.

4.4 Effect of inhomogeneity on correlation functions

Power-law model

In harmonically trapped 2D Bose gases, the spatially varying density of the gas modulates the local thermodynamic quantities. For the analysis based on correlation properties of 2D gases, the inhomogeneity introduces deviation from the BKT picture derived for uniform systems. It is thus necessary to properly account for the inhomogeneity when analysing the correlation functions.

Recently, a spin-wave theory in trapped 2D systems was derived in Ref. [26], focusing on the effect of the harmonic trap on the correlation function. It was

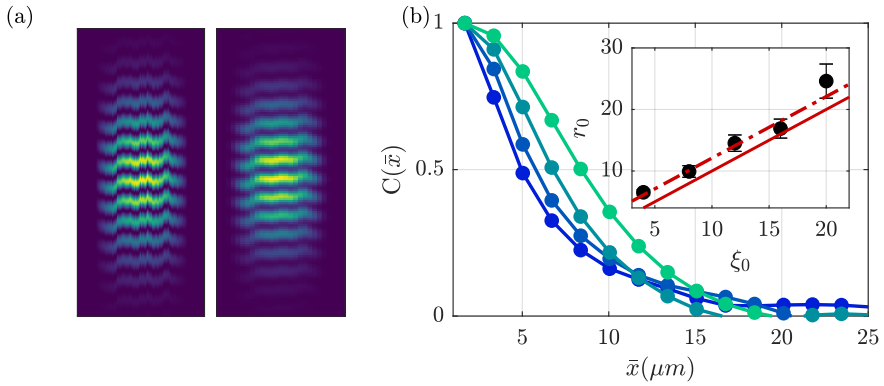

Figure 4.7: Effect of imaging resolution in the thermal regime. (a) Simulated density distribution after TOF with phase correlation length $\xi_0 = 10\,\mu$m. The left image is the simulated distribution without any imaging effect and that on the right figure is the output of the simulated imaging process, including the finite imaging resolution and pixel size. (b) Phase correlation functions obtained from simulated images, with imaging resolution 0,1,2,3 µm (blue to green) and $\xi_0 = 8\,\mu$m. (inset) Fitted correlation length from the correlation functions, with $\sigma_{PSF} = 2.1\,\mu$m. Error bars are 95% confidence intervals. The red solid line is $r_0 = \xi_0$ and red dash-dotted line is $r_0 = \xi_0 + 2.1\,\mu$m.

found that the density-dependent modulation of the exponent η from local density $n(\boldsymbol{r})$ according to

$$g_1(\boldsymbol{r}, \boldsymbol{r}') \propto |\boldsymbol{r} - \boldsymbol{r}'|^{-\eta \frac{n_0}{\sqrt{n(\boldsymbol{r})n(\boldsymbol{r}')}}}, \tag{4.4.1}$$

reproduces the result of trapped spin-wave theory well [26], where n_0 is the peak density. This procedure was named the *local correlation approximation* (LCA). We use the procedure with the minor modification described below to derive a model which we used to fit the correlation function $f_{\mathrm{SF}}(\overline{x})$ and to extract the algebraic exponent η for all the correlation measurements reported in this thesis.

Since the data points in the correlation function $C(\overline{x})$ are averaged over multiple locations, we replace $n(r)$ of Eq. (4.4.1) with $n(\overline{x})$ defined by

$$n(\overline{x}) = \frac{1}{N_{\overline{x}}} \sum_{x=-\overline{x}/2-2}^{-\overline{x}/2+2} \sqrt{n(x)n(x+\overline{x})}, \tag{4.4.2}$$

where $N_{\overline{x}} = 5$, same as Eq. (4.2.7). For $n(x)$, we used estimated *in situ* density distributions as described in Section 4.1.3. We then use the model function

$$f_{\mathrm{SF}} = a\overline{x}^{-2\eta_0\alpha(\overline{x})}, \tag{4.4.3}$$

where $\alpha(\overline{x}) = \frac{\max(n(\overline{x}))}{n(\overline{x})}$ with fit parameters a and η and the factor of two in the exponent stems from the fact that the fluctuation from two clouds contribute to the measured correlation function (see Eq. (4.2.6)). This model gives a good description of the long-range behaviour of the measured correlation decay in the superfluid regime, as shown in Fig. 4.8 and the obtained value of η corresponds to the mean value within the region of interest, 80% of the Thomas-Fermi diameter.

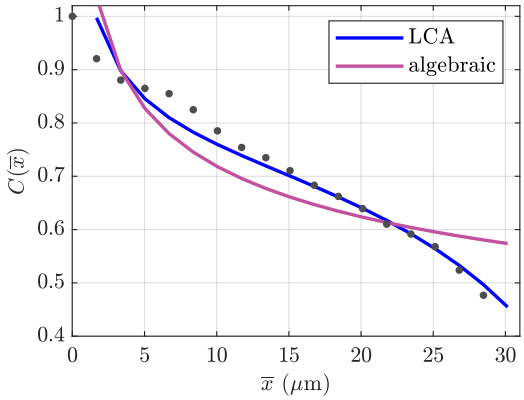

Figure 4.8: The effect of inhomogeneity to the correlation function. The experimental measurement of the correlation function in the superfluid regime (black points) is plotted, taken from results shown in Chapter 5. The correlation function was fitted with a power-law model (purple) and power-law model within the LCA (blue).

Exponential model

In an inhomogeneous trapping potential the density varies over a characteristic length scale that is relatively long compared to the short-ranged correlation function in the thermal regime. This smooth density variation is expected to have only a small effect on the correlations in this regime, however we have not found a suitable theoretical treatment in the literature and have developed the approach described here. As above, we simulate the exponentially decaying correlation function using the Ornstein-Uhlenbeck stochastic process [123], this time with spatially varying correlation length $\xi(x)$ depending on the location within the trap. We assume that the local correlation length $\xi(x)$ decays exponentially as a function of distance from the centre of the cloud, $\xi(x) \propto \exp(-x/b)$ and fix the correlation length at the

centre of the trap ξ_0. Fig. 4.9 shows correlation function obtained from homogeneous (black) and inhomogeneous (red) model which overlap within uncertainties. The close agreement of two correlation functions is reflected in the exponential fit of these functions, which gives correlation lengths in agreement with each other within their confidence intervals. We found the same results regardless of the scaling factor b, and even with small b such that $\xi(x) \sim 0$ at the edge of the analysis region.

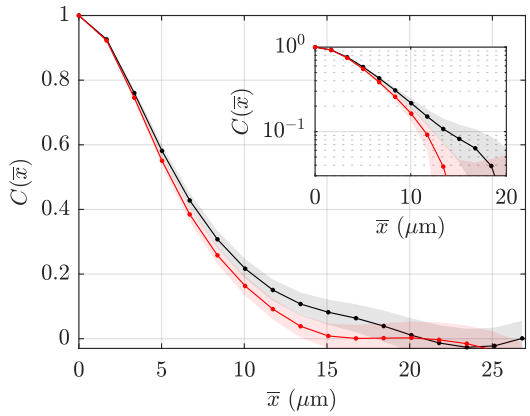

Figure 4.9: The effect of inhomogeneity on the correlation function in the thermal regime. Exponentially-decaying correlation functions, as expected in the thermal regime, are obtained from an Ornstein-Uhlenbeck simulation. The black line is corresponds to constant local correlation length $\xi_0 = 8\,\mu$m across the system while the red line is for a non-uniform local correlation length, decaying to close to zero at the edges of the cloud. The shaded region denoting the 1σ uncertainty was obtained by the bootstrapping method from the realisations of the Ornstein-Uhlenbeck process and the inset shows the same quantities on log-linear scale.

Although the above arguments hold within each distinct phase, further theoretical investigation is needed to determine the effect of inhomogeneity within the crossover regime, where the BKT transition is crossed at a certain radius of the cloud r_{BKT}.

4.5 Vortex detection

The extracted phase profiles also provide a way to detect vortices in the 2D Bose gases by looking for sharp disruptions of the phase $\theta(x)$. As shown in Fig. 2.1 (c) and (d), the phase profile along a line cutting through a vortex core has a sharp dislocation of phase.

The methodology that we use to find vortices is similar to that in Ref. [14], in which the criterion for a vortex at location x was taken to be a phase difference greater than $2\pi/3$ between adjacent pixels. To avoid false counting, we make the following improvements to the vortex detection method described in Ref. [14]. Firstly, since our imaging resolution is comparable to the expected size of a vortex core $\sim 1\,\mu$m and, furthermore, a single pixel corresponds to an equivalent size in the image plane, the vortex detection is performed by evaluating the phase difference at second adjacent pixels (next-nearest neighbours). Secondly, to avoid the local phases returned from failed fitting being counted as a vortex, we only consider positions where the postselection criteria shown in Fig. 4.4 is satisfied for the pair pixel locations. Fig. 4.10 illustrates the vortex detection. The vortex detection was performed within 90% of the TF region; we analyse a wider region than for the correlation analysis, to obtain better statistics.

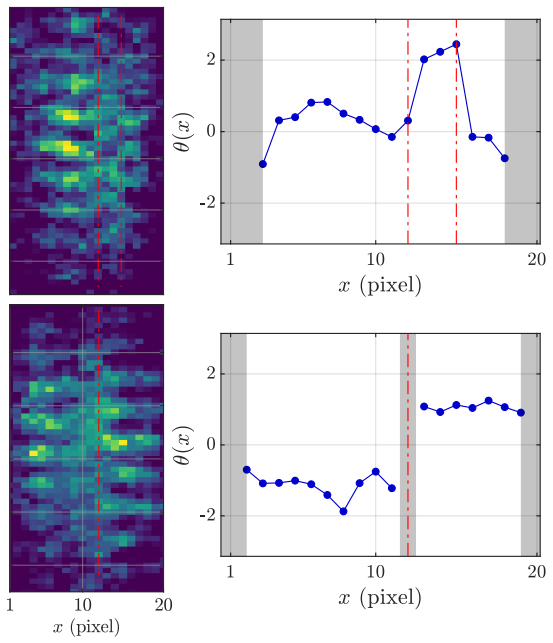

Figure 4.10: Vortex detection. Example images with vortices are shown, with corresponding phase profiles $\theta(x)$ obtained by fitting with Eq. (4.2.4). The disruption of the relative phases at certain positions x is evident by comparison with Fig. 4.5. In the phase profiles on the right panel, grey shaded regions indicate either outside of the Thomas-Fermi region or a failed fit at the pixel column (e.g. bottom right panel at $x = 12$). The vortex detected in the bottom panel coincides with a grey shaded area; this suggests the presence of a vortex core where the phase cannot be defined.

With the density slicing method, we can extract the local vortex density because the location of vortex in image x_v can be mapped onto a small region[1] in the 2D plane centred at $\boldsymbol{r}_v = (x_v, 0)$. This would not be possible without the density slicing method, as the position along the y axis cannot be determined with standard absorption images that integrate along y. To obtain the vortex density distribution, we first calculate the local vortex probability $P_v(x)$ which is defined by the ratio of the number of detected vortices to the number of phase difference evaluations at each location x. Here, datapoints that are rejected by the postselection criteria are not counted towards the number of phase evaluations. Then, we define the local vortex density as the $P_v(x)$ divided by the 2D area of detection region for a single pixel $\ell_p L_y = 8.4\,\mu\text{m}^2$,

$$n_v(x) = \frac{P_v(x)}{\ell_p L_y} = \frac{(\text{vortex count})}{(\text{number of phase evaluations})} \cdot \frac{1}{8.4\,\mu\text{m}^2}. \tag{4.5.1}$$

We relate the local vortex density to the local PSD at the corresponding position, as described in Chapter 5. The local density along the slice is obtained from a one-to-one mapping of the TOF density distribution to the *in situ* density distribution as discussed in Section 4.1.3.

[1]The finite thickness of the slice $L_y = 5\,\mu\text{m}$ and image-plane pixel size $\ell_p = 1.67\,\mu\text{m}$ mean that a vortex detected at pixel location x_v is located in a small region $x \in [x_v - \ell_p/2, x_v + \ell_p/2]$ and $y \in [-L_y/2, L_y/2]$.

5

BKT transition in equilibrium 2D systems

Contents

In this chapter, we present our experimental results on the BKT transition in equilibrium 2D Bose gases using matter-wave interferometry to probe local phase fluctuations of trapped 2D systems. This enables us to measure the phase correlation function changing from an algebraic to an exponential decay when the system crosses the BKT transition. We identify the transition temperature T_c by the change in functional form of the correlation functions, from algebraic to exponential. From the critical temperature, we identify the critical exponent η_c. Furthermore, we measure the local vortex density as a function of the local phase-space density, which shows a temperature-independent behaviour following an exponential growth

across the transition. Our experimental investigation is supported by Monte Carlo simulations to provide a comprehensive understanding of the BKT transition in a trapped system. Furthermore, we present the full counting statistics of the interference contrast as well as the density-noise correlation of double-well 2D gases after expansion, which provide deeper insight into the properties of 2D systems in equilibrium across the BKT critical point.

5.1 Preparation of the 2D cloud

We prepare 2D gases in equilibrium by a slow splitting into a double-well potential and a subsequent equilibration time of 500 ms. We initially prepare atoms in a single-RF dressed 3D trap as described in Section 3.4, and turn on the other two RF components to form the MRF-dressed potential. The initial parameters for the MRF-dressed potential are chosen to spatially overlap with the single-RF dressed potential, which minimises heating and atom loss. Subsequently, the RF amplitudes are ramped over 220 ms to transform the MRF potential from a single well to a double-well potential, and to increase the confinement along the z direction to $\omega_z/2\pi = 1\,\mathrm{kHz}$ while radial trapping frequency remains at $\omega_r/2\pi = 11\,\mathrm{Hz}$, thus realising 2D clouds. The characteristic dimensionless 2D interaction strength is $\tilde{g} = \sqrt{8\pi}a_s/\ell_0 = 0.076$ and there are $N \approx 3.5 \times 10^4$ atoms in each well. The detail of the multi-stage ramp used to transform into a double-well is given in Section 3.4.1. The gas has a final temperature in the range $31-47\,\mathrm{nK}$, which is controlled by forced evaporation in the TAAP stage.

After equilibrating the gases for 500 ms, the MRF-dressed potential is turned off by first switching off the RF fields and subsequently the quadrupole magnetic field. As described in Chapter 4, when the RF field turns off, the internal state of the atoms is projected into Zeeman substates labelled by quantum numbers m_F. Only atoms with $m_F = 0$ are used for the analysis of matter-wave interference and temperature measurements [94] but the populations in $m_F = \pm 1$ states are included in the count when determining the total atom number N. We choose the phase of the RF at the turn-off to ensure equal proportions of atoms are projected to $m_F = 0$

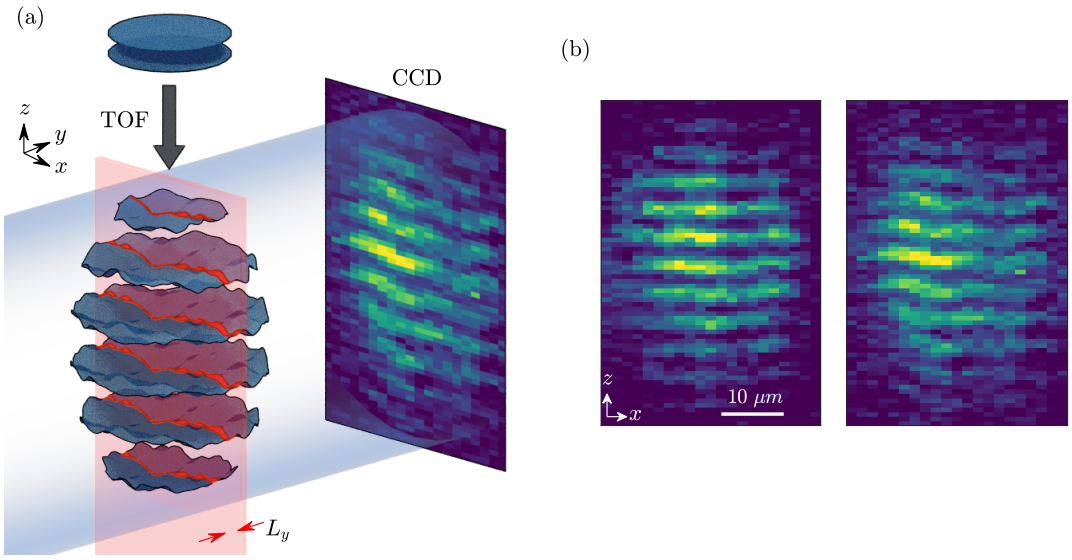

Figure 5.1: Probing local phase fluctuations using matter-wave interference. (a) Schematic of the experimental procedure. We begin with quasi-2D Bose gases trapped in a double-well potential (blue discs, top). The clouds fall and undergo time-of-flight (TOF) expansion, such that they spatially overlap and produce interference fringes with fluctuating phases (blue wavy planes). The red sheet of thickness L_y denotes the thin laser beam that repumps a slice of the atoms. We image repumped atoms using resonant light (depicted as a blue beam propagating along the y direction), producing an absorption image captured by a CCD camera. (b) Matter-wave interference images with weak (left) and strong (right) phase fluctuations, both at $\tilde{T} = 0.52$.

from each well, such that the density profile of atoms in the $m_F = 0$ state after TOF gives complete information of the system up to a global rescaling of density. The separation of the wells is 7 µm which is large compared to the characteristic length scale of the cloud along the z direction $\ell_0 \sim 1$ µm and the two clouds are decoupled. We ensure the populations in the two wells are equal by maximizing the observed matter-wave interference contrast as described in our recent publication Ref. [94]. The density scaling factor can be obtained by counting the number of atoms in $m_F = \pm 1$ components. Throughout this chapter, we set the temperature scale for our system using the condensation temperature of an ideal 2D Bose gas in a harmonic trap, $T_0 = \sqrt{6N}(\hbar\omega_r/\pi k_B) \approx 75$ nK and use rescaled temperatures $\tilde{T} = T/T_0$.

Finally, to locally probe the fluctuating matter-wave interference patterns after TOF expansion with duration $t_{\mathrm{TOF}} = 16.2$ ms, we apply a sheet of repumping light that propagates vertically (in z direction) with thickness $L_y = 5$ µm and width

much larger than the extent of the cloud of atoms before absorption imaging. All atoms are initially in a state with $F = 1$ and are then selectively pumped to $F = 2$ by the sheet of repumping light, which we image using light resonant for the atoms in the $F = 2$ state. The selective imaging method is illustrated in Fig. 5.1 (a). We ensure the repumping light passes through the centre of the cloud by moving the pattern along the y direction, in parallel to the propagation of imaging light, to the position where the total absorption signal is maximum.

Fig. 5.1 (b) shows examples of interference patterns obtained from two independent measurements at the temperature $\tilde{T} = 0.52$. The wavenumber of the interference fringes along the z direction is consistent with $k = md/\hbar t_{\mathrm{TOF}}$ [67], where $d = 7\,\mu\mathrm{m}$ is the spatial separation between the double-well minima. The interference pattern is only visible in the narrow Thomas-Fermi peak of the density distribution, in agreement with the results reported in Ref. [119].

5.2 Numerical Simulation of an equilibrium system

We complement our experimental observations with a numerical simulation performed for our specific parameters by Dr. V. Singh (Hamburg University). Here, the classical Monte-Carlo simulation is used to study the BKT transition in a trapped 2D Bose gas of ^{87}Rb atoms. The system is described by the many-body Hamiltonian

$$\hat{H} = \int \mathrm{d}\mathbf{r}\Big[\frac{\hbar^2}{2m}\nabla\hat{\psi}^\dagger(\mathbf{r})\cdot\nabla\hat{\psi}(\mathbf{r}) + \frac{g}{2}\hat{\psi}^\dagger(\mathbf{r})\hat{\psi}^\dagger(\mathbf{r})\hat{\psi}(\mathbf{r})\hat{\psi}(\mathbf{r}) + V(\mathbf{r})\hat{\psi}^\dagger(\mathbf{r})\hat{\psi}(\mathbf{r})\Big], \tag{5.2.1}$$

where $\hat{\psi}$ ($\hat{\psi}^\dagger$) is the bosonic annihilation (creation) operator and the 2D interaction strength is $\tilde{g} = 0.076$ as in the experiments. The simulation maps the system onto a lattice system of size $N_x \times N_y$, which introduces a discretization length l. For the continuum limit, l is chosen such that it is smaller than or comparable to the healing length $\xi = \hbar/\sqrt{2mgn}$ and the de Broglie wavelength [122].

The simulation method involves a classical-field approximation, i.e., replacing the operators $\hat{\psi}$ by complex numbers ψ [124] and the initial states are generated in a

grand-canonical ensemble of temperature T and chemical potential μ via a classical Metropolis algorithm. The lattice size used in the simulation is $N_x \times N_y = 200 \times 200$ and $l = 0.5\,\mu\text{m}$. μ is chosen such that the cloud consists of about 3.5×10^4 atoms, corresponding to the atom number in each well of the experiment. T in the range $10 - 62\,\text{nK}$, which covers a wide range of temperatures across the BKT transition. The simulated cloud corresponds to the equilibrium system that the experiment reaches after a slow splitting and 500 ms of equilibration time. For each sample, $\psi(x)$ is used to determine the phase $\phi(x)$ and density of the central line along the x direction.

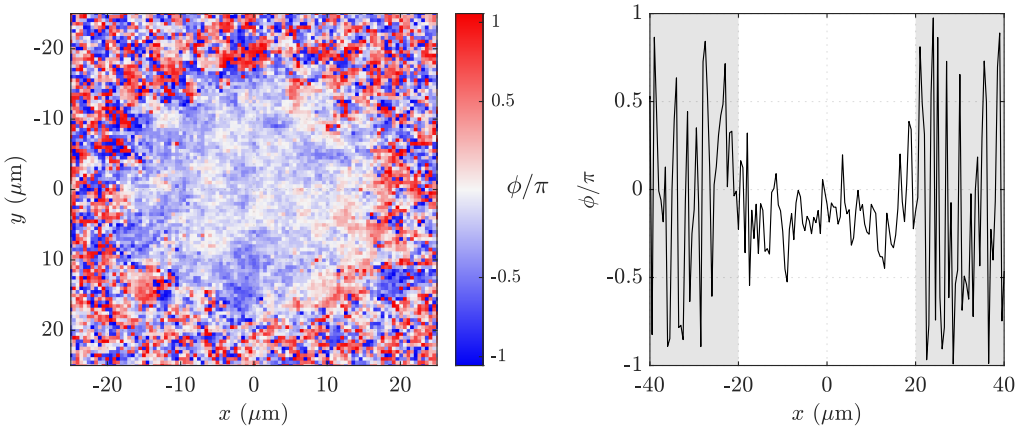

Figure 5.2: Illustration of the correlation analysis from the Monte-Carlo simulation result. The MC simulation was performed by Dr. V. Singh (Hamburg University). (Left) The spatial distribution of the phase $\phi(\boldsymbol{r})$, obtained from the MC simulation. The temperature of the gas was 47 nK, resulting in an TF radius of $\sim 20\,\mu\text{m}$. (Right) The phases ϕ in the left panel along a line going through the centre of the cloud. Such one-dimensional data was used for the phase correlation analysis of MC results reported in this thesis, which uses the exact same code used for the analysis of experimental data and thus reproduces the experimental situation well. Gray shaded regions are outside of 80% of the TF region, which are not used for the correlation analysis.

Using the phase data $\phi(x)$ from the simulation, we calculate the phase correlation function $C'_{sim}(\overline{x})$ in the same way as described in Section 4.2.4 with 500 realisations at each temperature. To compare with experimental results, we use $C_{sim}(\overline{x}) = C'^2_{sim}(\overline{x})$ since the fluctuation of two clouds are contributing to the relative phase fluctuation that we observe in the experiment while the simulation is done in a single 2D system. We calculate the phase correlation function within the 80% region of

the Thomas-Fermi diameter obtained from the simulation results, similarly to the analysis of experimental data.

Vortices are identified by calculating the phase winding around the lattice plaquette of size $l \times l$ using $\sum \delta\phi(x,y) = \delta_x\phi(x,y) + \delta_y\phi(x+l,y) + \delta_x\phi(x+l,y+l) + \delta_y\phi(x,y+l)$, where the phase differences between sites are taken to be $\delta_{x/y}\phi(x,y) \in (-\pi,\pi]$. A Vortex and an antivortex are identified by a phase winding of 2π and -2π, respectively. We determine the density profile $n(x)$ and the vortex distribution $n_v(x)$ by averaging them over the region $L_y = 5\,\mu\text{m}$ and the ensemble, where n_v counts both a vortex and an antivortex. The correspondence between $n(x)$ and $n_v(x)$ allows us to determine n_v as a function of the local PSD as we show in the following sections.

5.3 Correlation properties across the BKT transition

The local fluctuations of the interference fringes contain the phase information of the *in situ* clouds. At each location x, we fit the interference pattern with the function Eq. (4.2.4). The extracted phase $\theta(x)$ encodes a specific realisation of the fluctuations of the *in situ* local relative phase along the line $\boldsymbol{r} = (x, y = 0)$ between the pair of 2D gases. From $\theta(x)$, we calculate the two-point phase correlation Eq. (4.2.5). Fig. 5.3 shows $C^r(x,x')$ determined at the temperatures ranging from $\tilde{T} = 0.41$ to 0.61. We have $N_r = 220$ experimental realisations at each temperature. The range of spatial correlations around the diagonal $x = x'$ is broad at low temperature, as compared to the measurement at higher temperature.

To quantify the decay of correlations, we calculate $C(\overline{x})$ by averaging $C^r(x,x')$ over points with the same spatial separation $\overline{x} = x - x'$, as described in Section 4.2.4. This averaging was performed over a central region corresponding to 80% of the TF diameter, to limit the analysis to where clear interference fringes are observed.

Fig. 5.4 shows the measurements of $C(\overline{x})$ for various temperatures. $C(\overline{x})$ decays slowly at short and intermediate distances for a low-temperature system. However, at higher temperatures, $C(\overline{x})$ decays rapidly with increasing distance $\overline{x}$. This

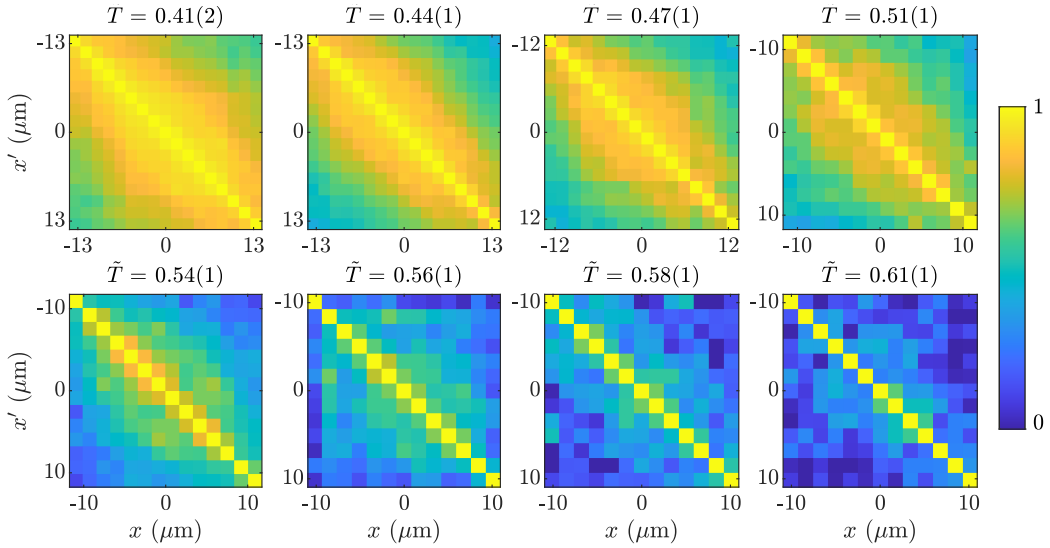

Figure 5.3: Phase correlation functions. Two-point phase correlation functions $C^r(x, x')$ in the 2D gases, obtained from 220 images from the experiment at temperatures indicated above each panel.

qualitative change of the correlation decay with temperature indicates the crossover to the thermal phase across the BKT transition.

At low temperatures, we observe a large deviation between simulation and experiment; this is due to the small length scale structure that can be analysed in the simulation with 0.5 µm grid size compared to the experiment which is limited by the imaging resolution $\sigma_{\mathrm{PSF}} = 2.1\,\mu\mathrm{m}$; short-range physics affects the correlation at short length in the simulation while in the experiment such an effect is masked by the imaging resolution. However, the long-range behaviour of the correlation functions are similar (see also Section 4.3) and since we are only interested in the long-range physics, the deviation has only a small effect to the identification of BKT physics, as we see in the following chapters. Furthermore, the coarse-graining procedure of the simulation data (such as one shown in Fig. 5.2) via convolution of the phasor distribution $e^{i\psi(x)}$ with a Gaussian kernel results in a reasonable agreement with the measurements.

We fit the correlation functions with the algebraic model function with spatial modulation of exponent $f_{\mathrm{SF}}(\overline{x}) = a\overline{x}^{-2\eta_0\alpha(\overline{x})}$ according to LCA, as described in Section 4.4. We further fit the correlation functions with exponential models $f_{\mathrm{th}}(\overline{x}) = be^{-2\overline{x}/r_0}$ where b and correlation length r_0 are fit parameters. The factor

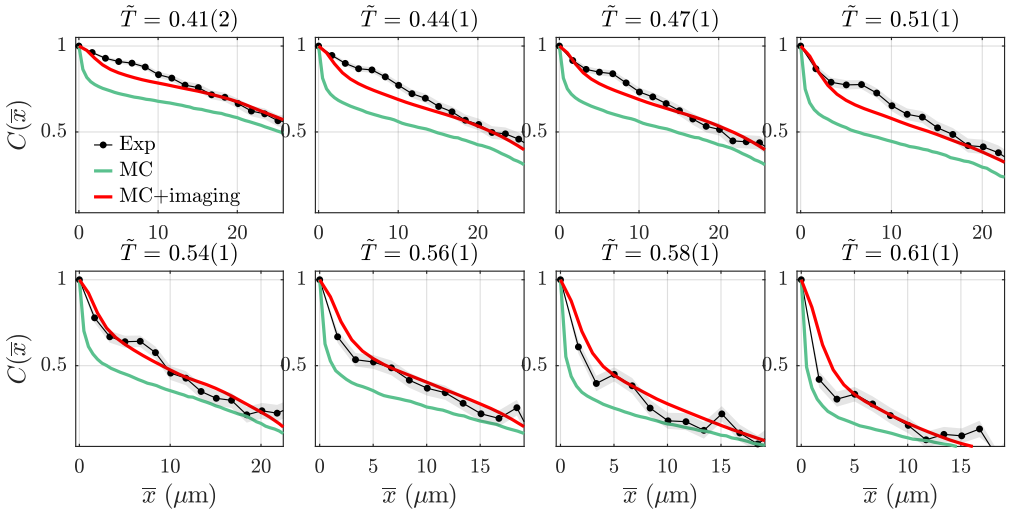

Figure 5.4: Phase correlation functions. Phase correlation functions $C(\overline{x})$ from experimental data (black connected points) at temperatures indicated above graphs. Uncertainties were obtained by a bootstrapping resampling method (grey shaded areas) [125]. The green line is the correlation function from simulation $C_{\rm sim}(\overline{x})$ at corresponding temperatures, $\tilde{T}$ =0.42, 0.46, 0.49, 0.53, 0.53, 0.56, 0.59, 0.6 from left top to right bottom subfigures. The red lines are the correlation function from the simulation, with the effect of imaging resolution taken into account by the coarse-graining of phase profiles obtained from the simulation (such as one shown in Fig. 5.2).

of two in the exponent of both $f_{\rm th}(\overline{x})$ and $f_{\rm SF}(\overline{x})$ are due to the fact that the fluctuations of two 2D clouds are contributing to the correlation function that we observe, as discussed in Section 2.5.1.

To quantify the temperature dependence of the phase fluctuation across the BKT transition we analyse the temperature dependence of $\eta(T)$ and $r_0(T)$, determined from our data. In Fig. 5.5 (a), we show $\eta(T)$ for various values of $\tilde{T}$. By definition, $\eta(T)$ should scale linearly as $\eta \equiv T/(4T_{\rm BKT})$ in the superfluid phase, where $T_{\rm BKT}$ is the BKT critical temperature [60]. Indeed, our measurement of $\eta(T)$ follows a linear dependence for $T/T_0 \lesssim 0.52$, where the system is deep in the superfluid regime. We show in Fig. 5.5 (a) the linear fit to the first four data points showing the linear scaling.

However, as the system approaches the crossover regime, $\eta(T)$ deviates from the linear behaviour and increases more rapidly. To compare with the measurements, we performed Monte-Carlo (MC) simulations of a cloud at equilibrium having the same parameters as in the experiment as described in Section 5.2. We show the

simulation results of $\eta(T)$ in Fig. 5.5 (a), which agree with the experimental results. At higher temperatures, the value of η diverges rapidly, as the system crosses over to the thermal phase, as we describe below.

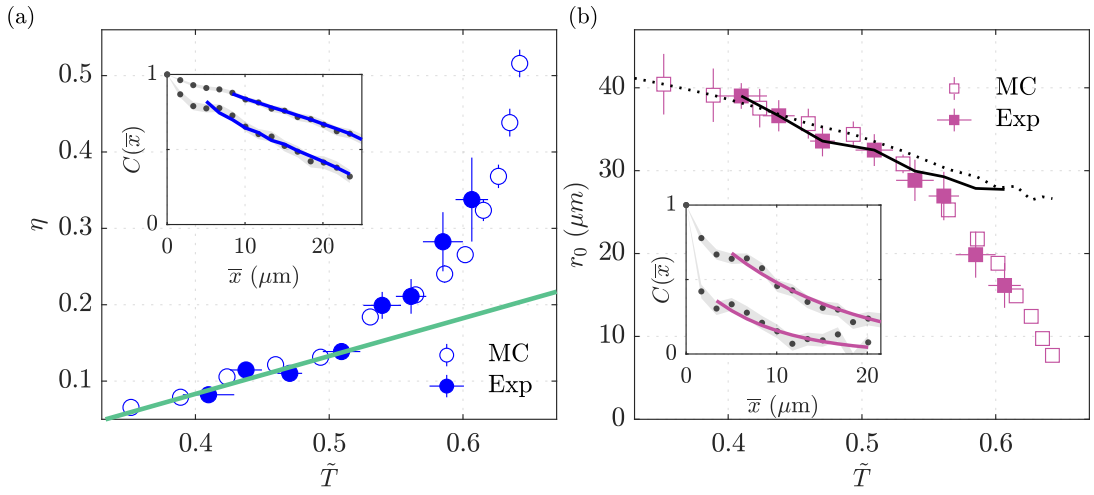

Figure 5.5: Characterising the BKT transition in a 2D Bose gas. (a) Measurements of the algebraic exponent η (filled circles) are compared with the results of Monte-Carlo simulations (open circles) as a function of the scaled temperature $\tilde{T}$. η is determined by fitting the correlation function with an algebraic model f_{SF}. The solid line is the linear fit to the data points at $\tilde{T} < 0.52$ which returns the slope 0.24(3). (b) Measurements of the correlation length r_0 (filled squares) are compared with the simulation results (open squares), where r_0 is determined by fitting the correlation function with an exponential model f_{th}. The values of the temperature-dependent Thomas-Fermi diameter are shown for the experiment (continuous line) and the simulation (dotted line). The error bars in η and r_0 denote standard fit errors, while the error bars in temperature are statistical errors.

In Fig. 5.5 (b), we show the correlation length $r_0(T)$ and the temperature-dependent TF diameter. Since r_0 cannot be well-defined above the system size, the value of r_0 is bounded by the TF diameter. We considered here the TF region as the effective system size; this is motivated by the fact that the quasicondensation is required to observe BKT phenomena since the suppression of density fluctuation results in the mapping of effective Hamiltonian of 2D Bose gases to the 2D XY model (see Section 2.3.3). As we have observed in Section 2.3.6, the Thomas-Fermi peak of the system corresponds to the region of the cloud where a significant fraction of quasicondensate is present. As such, we treat the TF region as the system in which the BKT physics can take place.

In a finite-size system, as the transition temperature is crossed, r_0 becomes smaller than the system size. We observe the deviation of r_0 from the effective system size (TF diameter, solid black line), which we identify as a signature of phase transition from the (quasi-)LRO to short-range order which occurs at $\tilde{T} \sim 0.55$. In Fig. 5.5 (b) we present the simulation results for $r_0(T)$ and the TF diameter, which show consistent behaviour in agreement with the measurements.

The BKT critical point is identified by the sudden change in the functional form of the first-order correlation function. In Fig. 5.6, we plot the χ^2 statistic of the algebraic and the exponential fits. The χ^2_{alg} shows a clear transition between two values while the χ^2_{exp} increases sharply below $\tilde{T} \sim 0.55$. At low temperature $\tilde{T} \lesssim 0.53$, χ^2-test of the best fit model at the 5 % significance level reject the exponential model while accepting the algebraic model with LCA. At $\tilde{T} \gtrsim 0.53$, while the exponential model is preferred with about 20 % lower χ^2 values, the model selection is marginal; the χ^2_{alg} value is close to the critical χ^2 value and we cannot confidently reject the algebraic model. Nevertheless, the corresponding p values are 0.2 and 0.5 for the algebraic and exponential models, allowing us to confidently choose the exponential model as the preferred model at higher temperatures.

To find the critical temperature, we fitted the χ^2_{alg} with a arctangent function, and χ^2_{exp} with a piecewise function which is constant above $\tilde{T}_{c,\mathrm{exp}}$ and linear below $\tilde{T}_{c,\mathrm{exp}}$. The fitted functions are plotted in Fig. 5.6 as dotted lines. From the two fitted values $\tilde{T}_{c,\mathrm{exp}}$ and $\tilde{T}_{c,\mathrm{alg}}$, we find the critical temperature $T_c = (\tilde{T}_{c,\mathrm{exp}} + \tilde{T}_{c,\mathrm{alg}})/2 = 0.53(1)$. The obtained critical temperature is in good agreement with the temperature at which the correlation length r_0 deviates from the system size (TF diameter), which is the signature of critical point in finite-size system. To obtain the critical algebraic exponent, we interpolate the result in Fig. 5.5 (a) with polynomial function and find $\eta(\tilde{T}_c) = 0.17(3)$ which is 30% lower than the universal critical exponent η_{BKT}=0.25. The lower critical exponent is attributed to the finite-size effect with expression Eq. (2.1.6); for a system with linear size $L \sim 30$, one expects $\eta_c = 0.21$. The choice of parameter L is motivated by our specific experiment, the TF radius $\sim 30\,\mu\mathrm{m}$ divided by the healing length $\xi \sim 1\,\mu\mathrm{m}$.

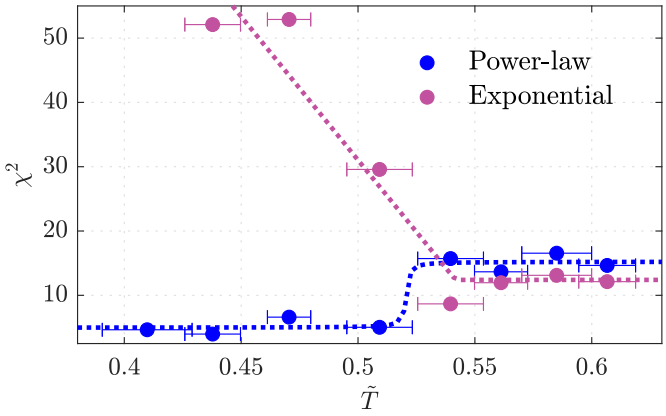

Figure 5.6: χ^2 statistic of the exponential model (purple ,f_{exp}) and algebraic model with LCA (blue, f_{SF}). Dotted lines are the fit to the temperature dependence of χ^2; see text.

While the critical temperature obtained in this work requires a significant fraction of atoms within the detection region (80% of the TF region) to be superfluid, this definition differs from the usual one which requires only the centre of the trap to become superfluid. The deviation of the observed critical temperature to the theoretical prediction, such as the quasi-2D prediction $T_c/T_0 = 0.74$ [57], can be described by these differences; indeed, for narrower correlation analysis region we found increasing critical temperature which gives the expected zero-region critical temperature at the centre of the trap at $T_c/T_0 = 0.68(4)$ with the corresponding critical PSD $\mathcal{D}_c = 9(1)$, in agreement with the theoretical prediction $\mathcal{D}_c = 8.5$ [17] for the interaction strength $\tilde{g} = 0.076$ used in this thesis.

5.3.1 Interference contrast analysis

Previous work on the interferometric observation of the BKT transition [14] relied on the method proposed in Ref. [69], namely the decay of integrated contrast as a function of integration area is used to determine the correlation property of the system characterising the BKT transition. In essence, the decay of interference contrast as a function of integration area $\mathcal{A}_{\mathrm{I}}$ scales algebraically, and the exponent γ approximates η deep in the SF regime while $\gamma \simeq 0.5$ in the thermal regime. With the selective repumping method used in this work, the product of the image integration length L_x and the thickness of the slice L_y equals the integration area, $\mathcal{A}_{\mathrm{I}} = L_x L_y$.

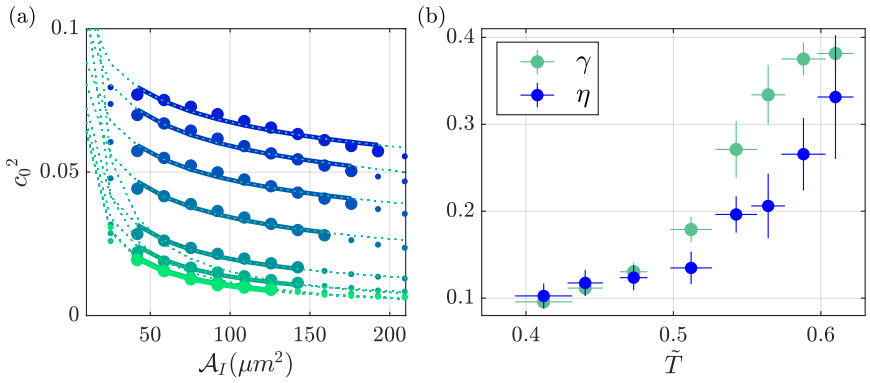

Figure 5.7: The comparison of the phase correlation analysis method to the previously used contrast-based analysis method proposed in Ref. [69]. (a) The decay of squared contrast as a function of integration area $\mathcal{A}_I$ at temperatures 31 nK (blue, top) to 47 nK (bottom, green). Power-law fitting of ${c_0}^2$ (solid lines) is performed where $L_y \ll I_x <$ (80% of TF diameter) is satisfied, indicated by larger markers. (b) The comparison of exponent γ obtained from the fits in (a) and the η obtained from power-law fits of phase correlation function described in the main text. The two quantities are expected to agree in the superfluid regime according to Ref. [69]. Errors in γ are standard errors of the fit.

For a comparison of our method to the one used in Ref. [14], we performed the contrast-based analysis and the result is presented in Fig. 5.7 (b). While the two methods return similar results at low temperatures that are deep in the superfluid regime, deviation is apparent even within the superfluid regime. This shows that the presence of a larger fraction of thermal atoms affects the contrast-based analysis within the crossover regime.

5.3.2 Local correlation and critical radius

Instead of the global fluctuation properties of the gas, the density slicing method allows us to locally probe phase fluctuations. This allows us to test the applicability of LDA on the phase fluctuation properties. In Fig. 5.8 (a), we show the histogram of phase fluctuations between points separated by two pixels, $2\ell_p \sim 3.5\,\mu$m. The fluctuations are approximately Gaussian at low temperature, with much wider width at higher temperature. Using the variance of the phase difference, we obtain the local algebraic exponent η using [26]

$$\eta(x) \simeq \frac{\langle \Delta\theta(x, x+2\ell_p)^2 \rangle}{2\ln\left(4\ell_p^2/\lambda_{\rm th}^2\right)}. \tag{5.3.1}$$

In Fig. 5.8 (b), we plot the local η against local PSD $\mathcal{D}_{loc}$. The points approximately collapse on the theoretical prediction of η from Ref. [18] (as described in Section 2.3.5) independent of temperature, supporting the applicability of the LDA on phase correlation properties.

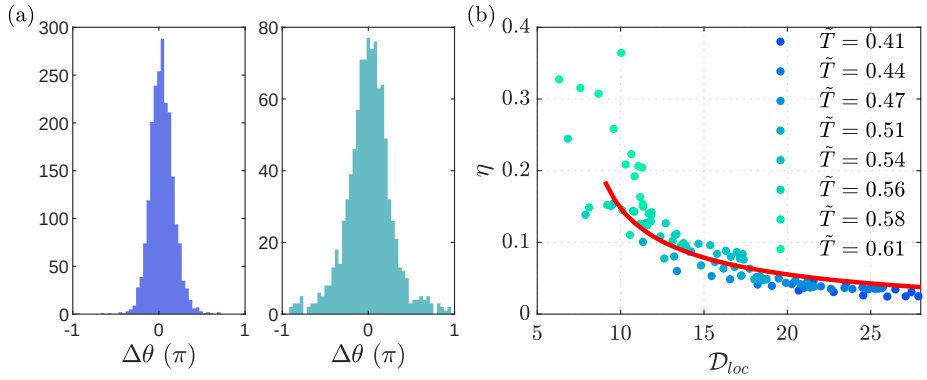

Figure 5.8: Observation of the local phase fluctuation and local η. (a) histogram of phase fluctuation at distance $\Delta x = 2$(pixel) $\sim 3.4\,\mu$m , at temperatures $\tilde{T} = 0.41$ (left) and 0.54 (right). (b) Local algebraic exponent obtained by the magnitude of local phase fluctuation, Eq. (5.3.1). The colours of the points indicate eight different dataset with temperatures ranging from $\tilde{T} = 0.41$ (blue) to 0.61 (green). Red solid line is the classical-field theory prediction of η [18].

Furthermore, we probe the full distribution of local η in the system by repeating the measurement for different locations y of the slicing region. In Fig. 5.9, we probe the reconstructed distribution of density and local algebraic exponent. The slight asymmetry of the density distribution is due to the long-term drift of the experiment which slightly changes the position of atoms along x between the separate measurements of individual y slices. We identify the approximate critical radius by the critical value $\eta_c = 0.17$ and plot it in Fig. 5.9 (b).

5.4 Density distributions

The density distribution of 2D gases in a harmonic trap is another source of information about the system properties, as discussed in Section 2.3.6. Importantly, the bimodality of the density distribution indicates the suppression of density fluctuation which is important to observe the BKT critical phenomena. Fig. 5.10 (a) shows the mean density profile at temperatures ranging from $\tilde{T} = 0.41$ to $\tilde{T} = 0.81$,

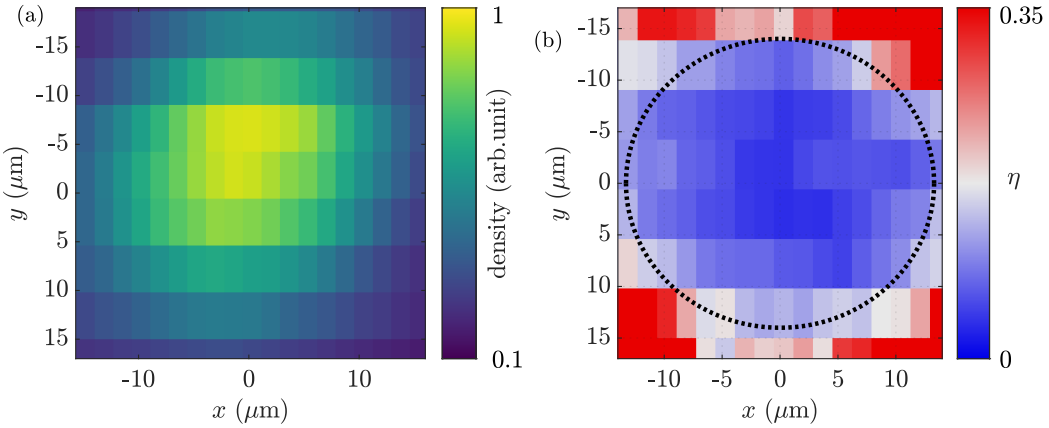

Figure 5.9: Tomographic reconstruction of the density profile and local phase fluctuations at $\tilde{T} = 0.47$. (a) The density distribution of the 2D Bose gases reconstructed from density slicing method at different slice location y. (b) The local algebraic exponent η obtained from the interference measurement at varying slice position y. The black dotted circle is the approximate critical radius $r_c \sim 14\,\mu$m obtained from the measured local η.

obtained with the density slicing method. The observed density distribution fits well with the bimodal distribution and we plot the fraction of atoms in the TF peak in Fig. 5.10 (c). We plot in Fig. 5.10 (b) the estimated *in situ* density distribution, from the one-to-one mapping of TOF and *in situ* density distribution as discussed in Section 4.1.3. We find good agreement of the distributions between the experiment and simulation.

5.4.1 Phase-space density

The theoretical prediction of the critical PSD at the BKT transition in 2D Bose gases is $\mathcal{D}_c = \ln(380/\tilde{g}) = 8.5$ [17]. We find the mean PSD for our trapped system by averaging the 2D density within 80% of the TF diameter, where we performed the correlation analysis. In Fig. 5.11, we show these measurements together with the corresponding simulation results of the mean PSD for various values of $\tilde{T}$. We find good agreement of the total PSD between the experiment and simulation. The observed PSD at T_c in the experiment $\mathcal{D}_{c,\mathrm{exp}} \sim 10$ is in close agreement with the theoretical prediction. We further plot the results of the superfluid PSD $\mathcal{D}_s = n_s\lambda^2$, where n_s is the 2D superfluid density. We obtain $\mathcal{D}_s$ using the measurement of $\eta(T)$ via $\mathcal{D}_s = 1/\eta(T)$ [60]. In Fig. 5.11 we also

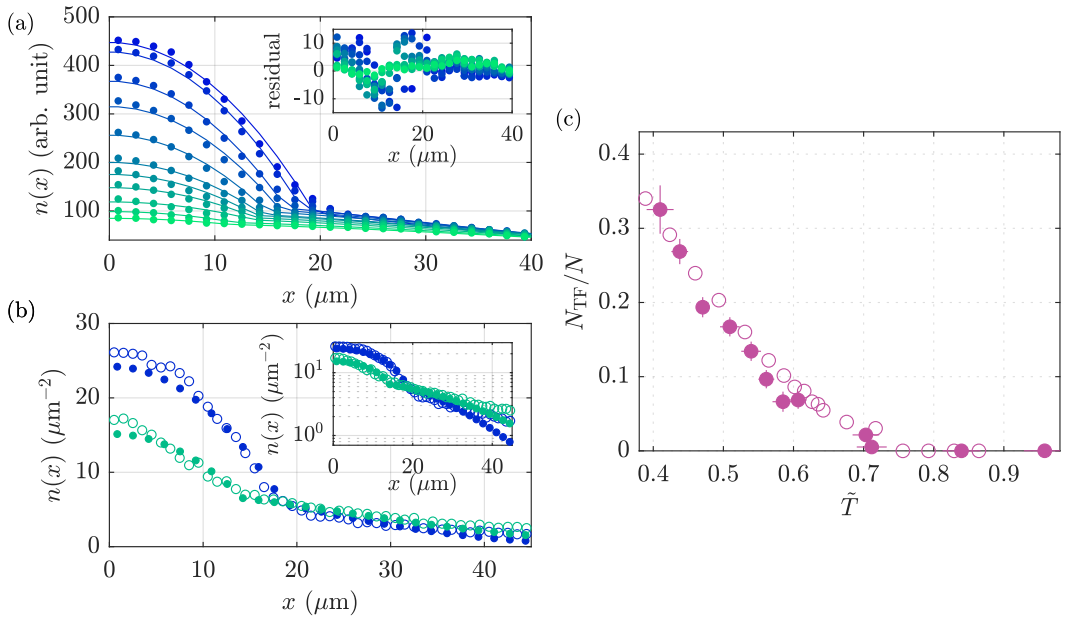

Figure 5.10: Mean density profile across the BKT transition. (a) Measurements of the sliced density distribution after TOF from $\tilde{T} = 0.41$ (blue) to $\tilde{T} = 0.81$ (green). The solid lines are the bimodal fit with Eq. (4.1.2). (b) The comparison of the estimated *in situ* density distribution in the experiment (filled markers) and the simulated distribution (open markers). The range of colours indicates the temperature and is the same scheme as (a). (c) The fraction of atoms in the TF peak, obtained from the bimodal fits of experimental data (filled markers) and mean density from the simulation (open markers). Error bars are standard errors.

show the measurements of the quasicondensate PSD $\mathcal{D}_0 = n_0\lambda^2$, where n_0 is the mean density of the TF peak of the density distribution. The results of $\mathcal{D}_0$ show similar behaviour to the results of $\mathcal{D}_s$ below the transition, which suggest that n_s is close to n_0 in our trapped system. This is in good agreement with the result of the classical-field theory presented in Fig. 2.6, where the TF fraction and the SF fraction agree and scale linearly below the superfluid transition. However, we could not observe the finite 'superfluid jump' of SF density as seen in Fig. 2.6; the inhomogeneity and finite-size of the system broadens the phase transition. We note that the quasicondensation critical temperature, defined by the emergence of a narrow TF peak in the density distribution, is at a higher temperature of $T/T_0 \sim 0.7$ than the superfluid transition temperature. This suggests that the BKT critical point is below the quasicondensation threshold as we have seen in Fig. 2.6, as well as previously reported elsewhere in [66, 126].

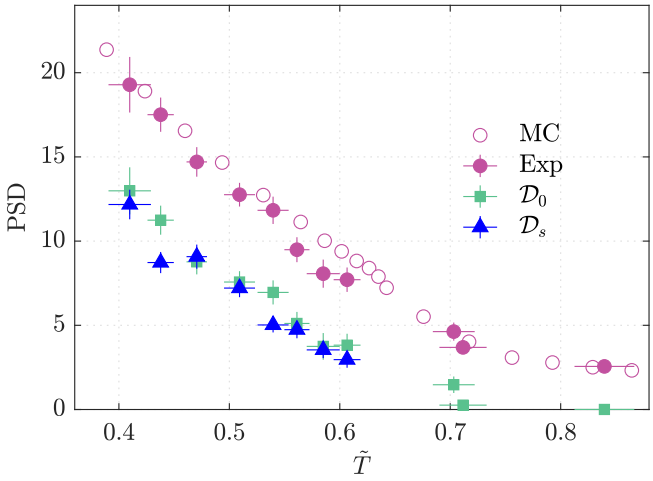

Figure 5.11: Phase-space density (PSD) across the BKT transition. Measurements of the mean PSD within the central TF region of the cloud (filled circles) are compared with the corresponding simulation results (open circles). The superfluid PSD $\mathcal{D}_s$ (triangles) and quasicondensate PSD $\mathcal{D}_0$ (squares) are determined using the measurements of $\eta(T)$ and the quasicondensate density, respectively; see text.

5.4.2 Density-noise correlation

In addition to the mean density distributions, we can further infer the system properties from individual realisations of fluctuating density distributions after TOF. As described in Section 2.4.3, the fluctuation of density after TOF is dominated by the initial phase fluctuations, as different parts of the cloud interfere during the expansion [70, 71]. In Fig. 5.12 (a), we show the fluctuating density distribution recorded with the density slicing method. Such fluctuation is washed out in a standard imaging method. To characterise the fluctuation of density, we calculated Fourier amplitudes $|\mathcal{F}[n(x)]| = \int dx\ n(x)e^{-ikx}$ of the density distribution after expansion.

In Fig. 5.12 (b), clear peak structures are observed at low temperatures at $k/2\pi \sim 0.18\mu\text{m}^{-1}$, which we observed to be washed out at higher temperatures above the critical point or in the absence of atomic signal. While the peak position remains constant, the peak height depends on the temperature of the gas and the peak height rescaled by the mean density is found to be in a linear relationship with the algebraic exponent η, as predicted in theory [71]. This result is in qualitative

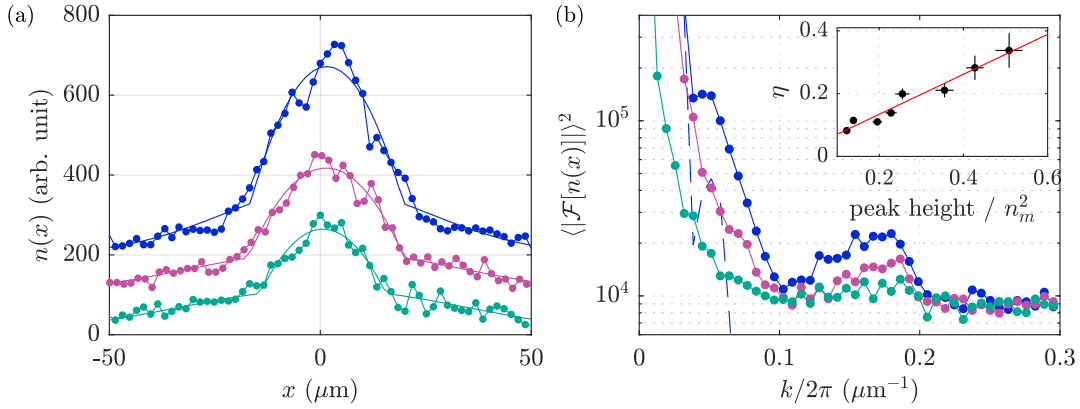

Figure 5.12: Density noise after TOF measured with the density slicing method. (a) Realisations of the density distribution at temperatures $\tilde{T} = 0.41$ (blue), 0.54 (purple) and 0.7 (green). Plots are displaced vertically for clarity. Solid lines are bimodal fit results of each realisation. (b) The averaged spectrum of the density distributions, at varying temperatures. The dashed line in blue is the spectrum of averaged density distribution over 220 realisations. Clear peak structures are observed at $k/2\pi \sim 0.18\mu\text{m}^{-1}$, and we obtain its height by Gaussian fit; we obtain the unitless peak height, rescaled by the mean density n_m, which is plotted in the inset where the red line is the linear fit.

agreement with that predicted in theoretical work Ref. [72] and reported in Ref. [70]; for further quantitative analysis, we need a detailed theoretical investigation to incorporate our specific imaging and analysis procedure.

From the same data, we have also obtained the density-*noise* correlation function,

$$g_2'(\boldsymbol{r}, \boldsymbol{r}') = \frac{\langle \delta n(\boldsymbol{r}) \delta n(\boldsymbol{r}') \rangle}{\langle n_m^2 \rangle}, \tag{5.4.1}$$

where $\delta n(\boldsymbol{r}) = n(\boldsymbol{r}) - n_{\text{bimodal}}(\boldsymbol{r})$ and $n_{\text{bimodal}}(\boldsymbol{r})$ is the fitted bimodal distribution of each density distribution realisations. In this work, we use $\boldsymbol{r} \to x$ since the density slicing method limits us to the measurement of local density at $y = 0$. We show the density-noise correlation function $g_2'(x, x')$ in Fig. 5.13 (a). To obtain 2D density, we have integrated the images after TOF along the z direction. The mean in Eq. (5.4.1) was taken over $N_r = 220$ experimental realisations. We further analyse an averaged form of the correlation function

$$g_2'(r) = \frac{\langle \delta n(x) \delta n(x + r) \rangle}{\langle n^2 \rangle}, \tag{5.4.2}$$

where the mean is taken over experimental realisations and x. We plot g_2' at two temperatures in superfluid regime, in Fig. 5.13 (b). The largest difference between

g_2' and g_2 is that the density noise correlation function g_2' has a long-distance limit of 0, while the standard density correlation function g_2 has 1. From comparison of Fig. 2.9 and Fig. 5.13 (b), we find that the behaviour of experimentally observed g_2' is similar to the theoretically predicted g_2. However, we need further theoretical investigation to make quantitative comparisons.

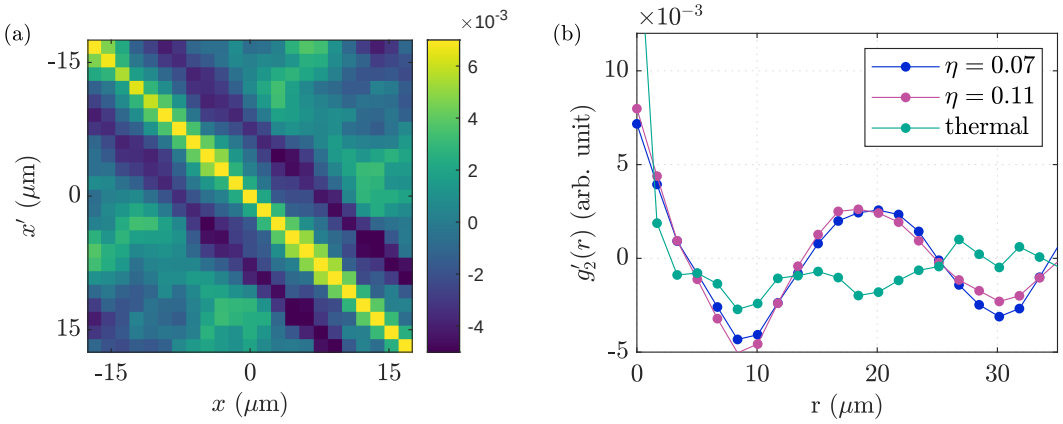

Figure 5.13: Density noise correlation in 2D Bose gases after TOF expansion. (a) Density-noise correlation $g_2'(x, x')$ at temperature $\tilde{T} = 0.44(1)$. (b) Averaged form of the correlation function $g_2'(r)$ at two temperatures deep in the superfluid regime (blue, purple) and the thermal regime. The characteristic oscillation is washed out deep in the thermal regime.

5.5 Vortices

The BKT transition is driven by thermal vortex unbinding, which suppresses the quasi-long-range order above the critical temperature. This underlying mechanism is detected by matter-wave interferometry, where thermally activated free vortices are observed as sharp dislocations in the interference patterns. This enables us to determine the local vortex density using our selective imaging method. In Fig. 5.14 (a), we show examples of matter-wave interference patterns obtained from two independent measurements at $\tilde{T} = 0.55$ and 0.52. The sharp phase dislocations are indicated by red vertical lines, which we count as vortices. We obtain local vortex density $n_v(x)$ by averaging the vortex number over many images at the location x. In Fig. 5.14 (b), we show the vortex density n_v, averaged over the

TF region (see Section 4.5 for details); n_v is small at low temperatures and onset of sharp increase was observed at $\tilde{T} \sim \tilde{T}_c$.

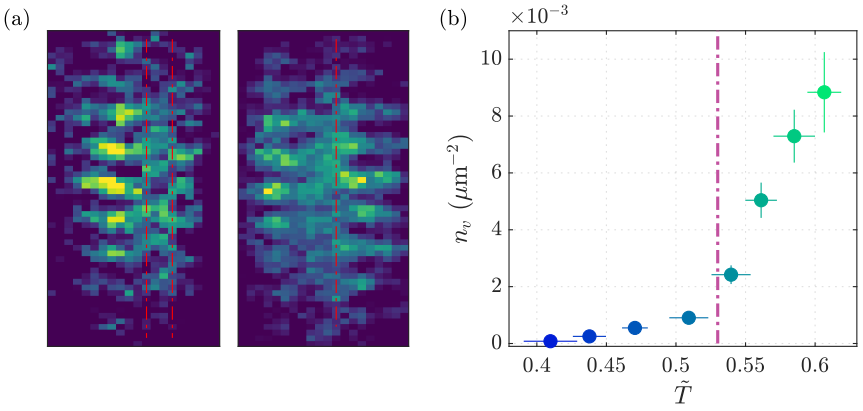

Figure 5.14: Vortex proliferation in 2D Bose gases. (a) Typical interference patterns with phase dislocations (indicated by red vertical lines), which we count as vortices. (b) Mean vortex density n_v as a function of $\tilde{T}$. The error bars for n_v are the statistical uncertainty, given by the square root of the number of detected vortices scaled to the vortex density. Vertical dashed line is the $T_c = 0.53$ obtained by the change in functional form of correlation function, see Fig. 5.6.

In Fig. 5.15, we plot the measured local vortex density $n_v(x)$ against the local PSD $\mathcal{D}_{loc} = n(x)\lambda^2$, where $n(x)$ is the local 2D density at the location x. The measurement results for different temperatures collapse onto a common exponential (continuous line), which is clearly visible in the inset. This demonstrates that the vortex density is only dependent on the local PSD, which indicates the applicability of LDA to vortex nucleation in an inhomogeneous system. In Fig. 5.15 we also present the simulation result of the vortex density, which agrees well with the experimental results.

5.6 Contrast full-counting statistics

In addition to the correlation properties of the gas obtained through the ensemble average, the *full counting statistics* can provide additional insight into the fluctuation of the system across the BKT transition. For the interfering 2D Bose gases, the amplitude of the integrated interference signal is expected to show a characteristic change in its higher moments across the BKT transition [127, 128]. The integrated

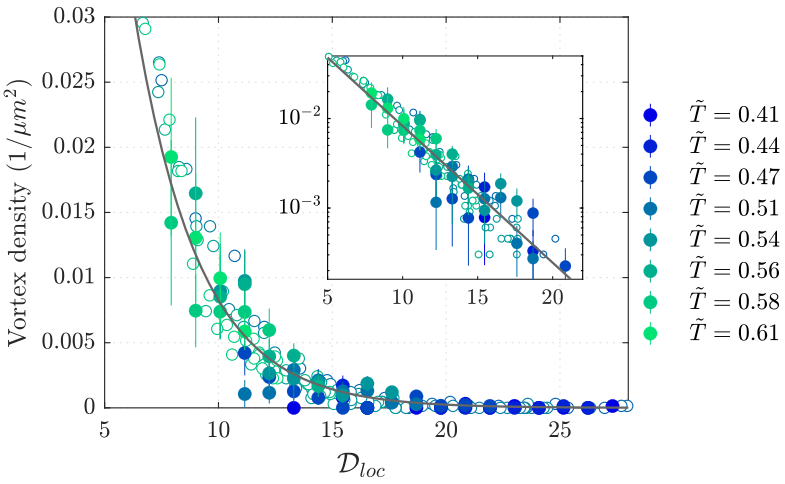

Figure 5.15: Local vortex distribution in a harmonically-trapped 2D Bose gas. Local vortex density $n_v(x)$ is plotted against local PSD $\mathcal{D}_{loc} = n(x)\lambda(T)^2$, where $n(x)$ is the local 2D density at the location x. The measurements (filled circles) and the simulations (open circles) cover a range of temperatures between $\tilde{T} = 0.41$ and 0.61. Experimental datasets with eight different temperatures contribute to this plot, while there are datasets with four temperatures from the simulation. The continuous line is the exponential fit to the data. Inset shows the same results on a log-linear scale to highlight the exponential scaling across the BKT transition. Error bars are statistical, and the datapoints for each temperature were binned into local PSDs for clarity.

interference signal is characterised by the Fourier transform of the integrated density distribution, defined by the operator

$$\hat{A} = \int_{\Omega} d^3\boldsymbol{x}\ \hat{n}(\boldsymbol{x}) e^{-ikz}, \tag{5.6.1}$$

where $\hat{n}(\boldsymbol{x})$ is the three-dimensional density distribution after expansion, Ω is the 3D integration volume and $k = md/\hbar t_{\mathrm{TOF}}$ is the fringe wavenumber. The eigenvalues α of the Hermitian operator $\hat{A}$, which are the experimentally observed values according to standard quantum mechanics, take any value between 0 and the half of atom number $N_\Omega/2$ within the integration volume[1][128]. In the laboratory, the measurement of $\hat{A}$ corresponds to the Fourier amplitudes at wavenumber $k_q = md/\hbar t_{\mathrm{TOF}}$. For simplicity, we scale the interference amplitude by the atom number in the integration volume to obtain[2] the probability distribution of $\mathcal{V} = \frac{2\alpha}{N_\Omega}$.

The integration volume has a large extent along z to cover the entire density

[1]The absolute limit of the α is N_Ω, but with the density bounded to be positive the limit becomes $N_\Omega/2$. $\alpha = N_\Omega/2$ corresponds to the interference contrast of unity.

[2]We numerically confirmed that the rescaled fringe amplitude $\mathcal{V}$ corresponds to the fringe contrast. We used FFT rather than the fitting with Eq. (4.2.4) to obtain $\mathcal{V}$.

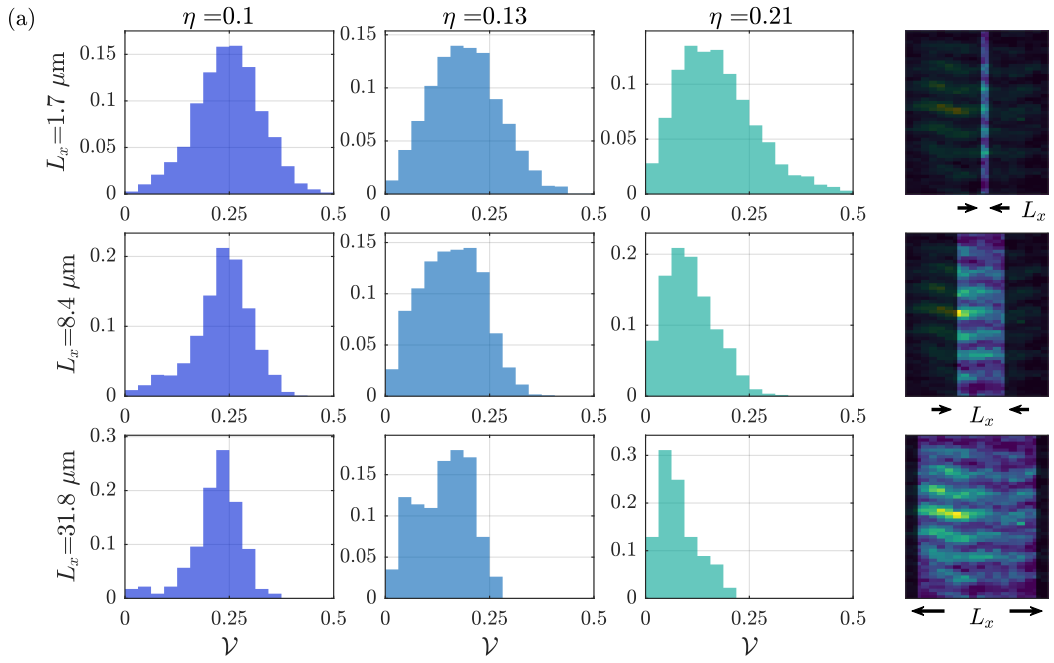

Figure 5.16: Full counting statistics of matter-wave interference contrast $\mathcal{V}$. The histogram of $\mathcal{V}$, scaled to show relative probability, is plotted for different integration lengths in the image L_x and the temperature of the system. 2D systems at non-zero temperatures have phase fluctuations so the measured values of $\mathcal{V}$ are always less than 1. Up to 3000 data points contribute to each histogram.

distribution while integration along y over a length equal to the thickness of the sheet $L_y = 5\,\mu\text{m}$. The integration along the x direction is controllable, by choosing the number of pixels to be integrated over. Fig. 5.16 shows histograms of $\mathcal{V}$ at three temperatures across the BKT transition, for three different values of the integration length L_x. At low temperature with $\eta = 0.1$, these histograms have a similar form independent of L_x. At high temperature, however, the distribution of $\mathcal{V}$ has a strong dependence on the length scale L_x, as a result of strong short-range phase fluctuations, $r_0 \ll L_x$.

In Fig. 5.17 (a), we plot the full counting statistics of the squared contrast $\mathcal{V}^2$ obtained with $L_x = 15\,\mu\text{m}$. The probability distribution undergoes strong shape modification as the temperature is changed across the BKT critical point, as predicted by theory [127, 128]. We also show a theory comparison with one of the distribution functions deep in the superfluid regime in Fig. 5.17 (b). Further quantitative comparison with the theory requires the incorporation of the finite

imaging resolution into the theoretical prediction.

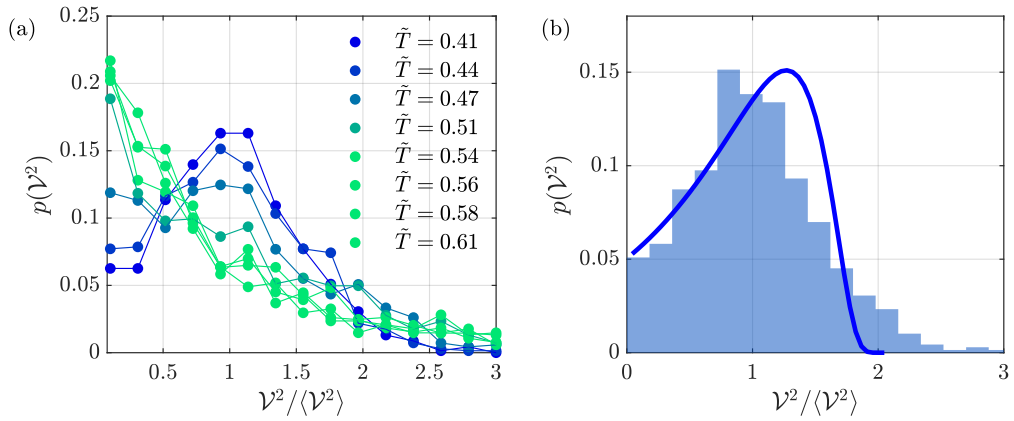

Figure 5.17: Temperature dependence of squared contrast distribution. (a) The temperature dependence of the probability distributions $p(\mathcal{V}^2)$. Points were obtained from the histogram of $\mathcal{V}^2/\langle\mathcal{V}^2\rangle$ which were rescaled so that the height corresponds to probability density. Colour indicates the temperature of the system, from $\tilde{T} = 0.41$ (blue) to $\tilde{T} = 0.61$ (green). (b) Comparison of experimental results deep in the superfluid regime to the theoretical prediction for anisotropic, homogeneous 2D gas in Ref. [128]. The anisotropy of the detection region is $9\ell_p/L_y \sim 3$ for the experimental data. The theoretical prediction (solid line) was rescaled to match the scale of relative probability distribution used for the experimental result, which is dependent on the bin size.

5.7 Conclusion

In conclusion, we have measured the local phase fluctuations of 2D Bose gases via matter-wave interferometry. Our measurements of the phase correlation function and the vortex density provide a comprehensive understanding of the BKT transition in 2D Bose gases. We have mapped out the temperature dependence of the algebraic exponent η and identified the transition by the change in the functional form of the correlation function. The critical temperature was confirmed by the vortex density of the system. We have shown that the local vortex density in inhomogeneous 2D systems follows an exponential scaling as a function of the local PSD, which is temperature independent. Our observation of the density noise correlation function and full counting statistics of interference contrast provides a way to deepen our understanding of 2D Bose gases in and out of equilibrium. Our experimental observations are supported by Monte-Carlo simulations.

6

Quench dynamics across the BKT transition

Contents

The study of non-equilibrium critical dynamics in 2D systems remains a challenge despite significant experimental and theoretical effort. On the theory side, the analytical treatment of BKT critical behaviour is particularly hard because of the presence of vortex excitations. In experiments, it is typically difficult to fully characterise transient states. As we have seen in the last chapter, the interferometric method with selective imaging of 2D Bose gases allows us to understand the properties of 2D system in great detail, in ways that were not possible previously. This experimental advancement, as well as the precise determination of the critical point in Chapter 5 presents an opportunity to study the non-equilibrium critical

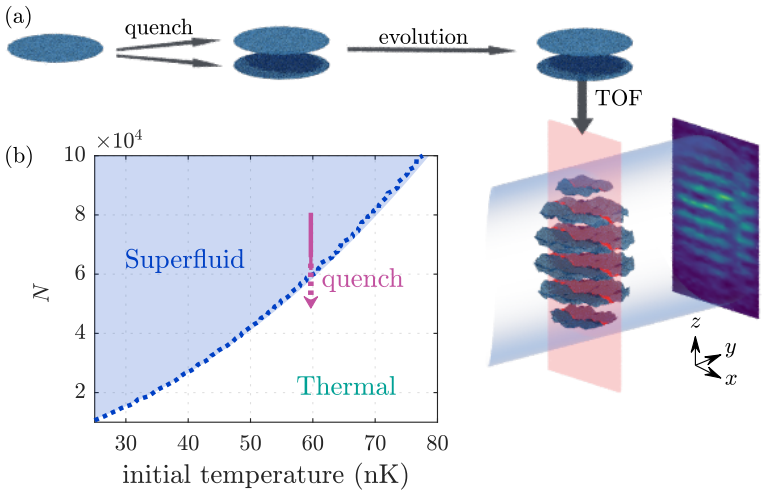

Figure 6.1: Coherent splitting as a quench across the BKT critical point. (a) The schematics of the experimental procedure. A 2D Bose gas is prepared in its superfluid state, and we quench the system by splitting into two daughter clouds. The quench suddenly brings the system parameters to those corresponding to a vortex-proliferated thermal phase as indicated by the arrow in (b), and we monitor the relaxation dynamics towards equilibrium using matter-wave interferometry. (b) The phase digram of harmonically-trapped 2D Bose gases, similar to Fig. 2.7. In the quench the atom number changes from N to $N/2$ non-adiabatically, thereby traversing the critical point for initial temperatures within the range of $50\,\mathrm{nK} \lesssim T \lesssim 75\,\mathrm{nK}$ for an initial atom number $N = 9 \times 10^4$.

dynamics in a 2D system.

We observe the dynamics after a sudden quench of a 2D quantum gas across the BKT transition. In particular, we are interested in the relaxation dynamics of a 2D system after a sudden quench from quasi-ordered to disordered state. The non-equilibrium initial state is prepared by *coherent splitting*, which quenches the system by a sudden reduction of density to approximately a half of its initial value. This is schematically illustrated by the red arrow going from $N = 9 \times 10^4$ to $N/2$ on the phase diagram in Fig. 6.1. The critical point in the equilibrium system was measured in Chapter 5, providing a reference point for this experiment. In addition, the initial *relative* phase is spatially uniform at the time of quench $t = 0$ regardless of the state of the gas before splitting. This ensures well-defined initial conditions and allows for precise characterisation of the dynamics towards thermal equilibrium.

In this chapter, we first report the experimental realisation of sudden quench using the MRF-dressed potential. The quench requires a splitting that is fast enough

to be non-adiabatic while avoiding excitation of collective modes, and we have made careful improvements to the splitting sequence presented in Fig. 3.15 to satisfy these requirements. We benchmark our measurements by numerical simulations, and report a comparison to the real-time renormalisation group theory [46].

6.1 Experimental realisation of fast splitting

The prerequisite to probe non-equilibrium dynamics is the non-adiabatic change in the system Hamiltonian. For two-dimensional Bose gases across the BKT critical point, the properties of the system that can be changed are temperature and density. Naively, a sudden change in temperature of ultracold gases can be achieved simply via parametric vibration or photon scattering. However, such straightforward heating requires the addition of significant energy to the system. Furthermore, the initial states that are created are often not well-defined because of the randomness of the process, which makes precise characterisation of the relaxation dynamics difficult. In comparison, the coherent splitting of a single 2D system into two is a much cleaner method to prepare the system in a non-equilibrium initial state. While the system is isolated from the environment such that the temperature and total atom number remain unchanged, we can non-adiabatically change the density of the cloud to cross the critical point in the quench. The antisymmetric phase mode $\theta(x)$ after the coherent splitting has no fluctuation at $t = 0$, as demonstrated in our lab recently [94], and the dynamics towards thermal equilibrium can be tracked from a well-defined initial state.

To realise a sudden quench experimentally, we perform a similar splitting to that used for the investigation of the equilibrium 2D system but with much shorter duration of 12 ms. The splitting was performed over 220 ms for the experiments in Chapter 5 to prepare the equilibrium system by an adiabatic ramp of potential (see Fig. 3.15). The splitting duration of 12 ms is adiabatic for the vertical degrees of freedom with tight confinement $\omega_z/2\pi = 1$ kHz, but rapid enough to realise a non-adiabatic change in the Hamiltonian for the radial dynamics on a characteristic timescale of $2\pi/\omega_r \sim 100$ ms.

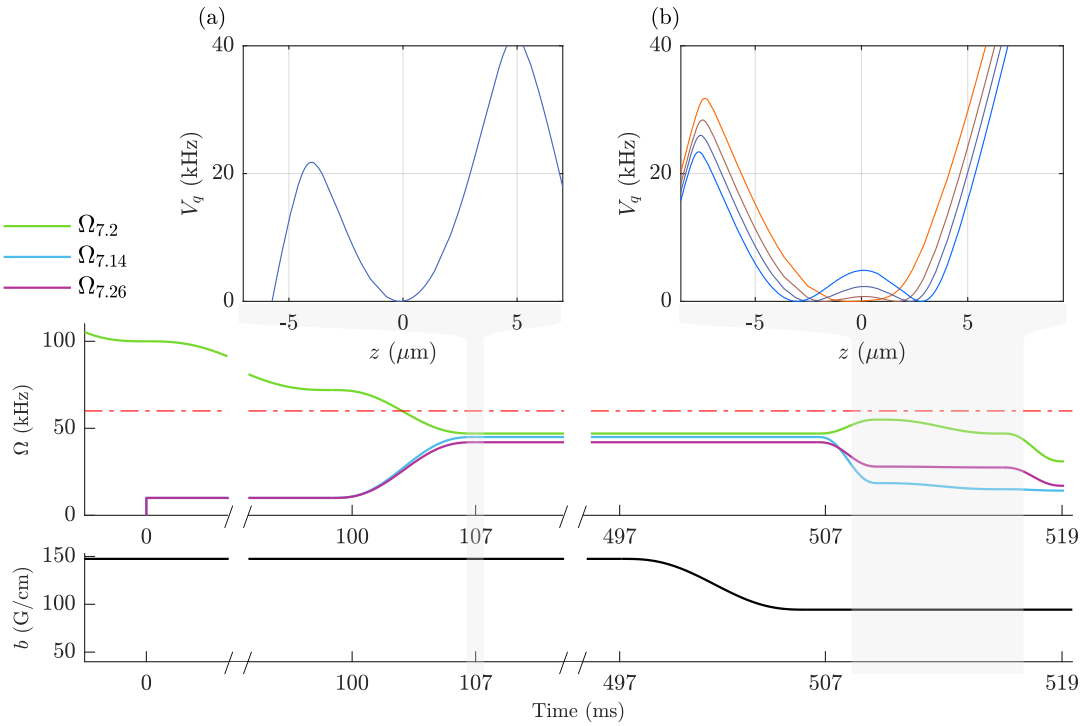

Figure 6.2: MRF loading and fast splitting procedure. The time evolution of RF amplitudes Ω and quadrupole gradient (bottom) is shown with corresponding trapping potentials (MRF-dressed eigenenergies, V_q) at selected times. The MRF loading ramp up to 107 ms is similar to the one shown in Fig. 3.15: we initially turn on $\Omega_{7.14}$ and $\Omega_{7.26}$ at small amplitude to avoid the perturbation to the atoms, and subsequently ramp quickly to satisfy $\Omega < \omega_f$ (red dashed line, see Fig. 3.15) for all RF components. After the fast ramp from 100 to 107 ms, atoms are confined in an MRF-dressed 2D single-well potential as shown in panel (a) The change in the potential up to this stage are performed adiabatically with minimum perturbation to the atoms, and the system is considered to be close to an equilibrium. Additionally, we hold the atoms for 400 ms to equilibrate the system further. At the end of the hold period, we quickly ramp the quadrupole field gradient for 10ms to change the radial confinement ω_r, in order to avoid the collective motion of atoms after the splitting. Finally, we start the splitting at 507 ms for 12 ms, realising a double-well potential.

The experimental procedure of fast splitting is shown in Fig. 6.2. We first prepare a single 2D cloud trapped in a MRF-dressed potential by adiabatically transforming from single-RF dressed potential to multiple-RF dressed potential, in the same way as described in Chapter 3. We then let the system equilibrate further by waiting for 400 ms while keeping the atoms in the single 2D trap. Before commencing the splitting, we quickly ramp the quadrupole magnetic field gradient b down by 50%, to reduce the radial confinement. This additional stage was found

to be necessary to avoid the excitation of the monopole mode after the splitting. The duration of the ramp is 10 ms; this is long enough to satisfy the adiabatic condition for the vertical degrees of freedom while being short enough for the in-plane dynamics. As such, this can be considered a part of the quench. Finally, we perform the coherent splitting over 12 ms as depicted in Fig. 6.2 (b).

After the splitting, the potential is closely matched to that used for the investigation of the equilibrium 2D system reported in Chapter 5, in which the confinement for both potential wells are $\omega_z/2\pi = 1$ kHz, $\omega_r/2\pi = 11$ Hz and double-well separation is $d = 7\,\mu$m. This allows us to use the precise measurement of the critical point in Chapter 5 as a reference point, as well as to compare the critical scaling both in and out of equilibrium.

6.2 Monte-Carlo simulation

As in Chapter 5, we benchmark our experimental results with the Monte Carlo simulation, performed specifically for our case by Dr. V. Singh (Hamburg University). In that numerical work the sudden splitting of the gas is treated using a classical-field simulation of two-component gas in a single harmonic trap, with each species having the same mass and intra-species interaction strength $g = g_{11} = g_{22}$. Each component 1 and 2 correspond to the separate wells in the experiment, and a decoupled double-well is realised by setting the inter-species interaction g_{12} as well as tunnel coupling J to zero. The total Hamiltonian is

$$\hat{H} = \sum_j \int \mathrm{d}\mathbf{r}\Big[\frac{\hbar^2}{2m}\nabla\hat{\psi}_j{}^{\dagger}(\mathbf{r})\cdot\nabla\hat{\psi}_j(\mathbf{r}) + \frac{g}{2}\hat{\psi}_j^{\dagger}(\mathbf{r})\hat{\psi}_j^{\dagger}(\mathbf{r})\hat{\psi}_j(\mathbf{r})\hat{\psi}_j(\mathbf{r}) + V(\mathbf{r})\hat{\psi}_j^{\dagger}(\mathbf{r})\hat{\psi}_j(\mathbf{r})\Big] + g_{12}\int \mathrm{d}\mathbf{r}\hat{\psi}_1^{\dagger}(\mathbf{r})\hat{\psi}_2^{\dagger}(\mathbf{r})\hat{\psi}_2(\mathbf{r})\hat{\psi}_1(\mathbf{r}) + J\int \mathrm{d}\mathbf{r}\Big[\hat{\psi}_1^{\dagger}(\mathbf{r})\hat{\psi}_2(\mathbf{r}) + \hat{\psi}_2^{\dagger}(\mathbf{r})\hat{\psi}_1(\mathbf{r})\Big], \quad (6.2.1)$$

where $j = 1, 2$ and the term with g_{12} is the inter-species interaction and the tunneling term with J couples two clouds. The discretisation length for these simulations is 0.5 µm, as for the simulation performed in Chapter 5.

The coherent splitting in the simulation is implemented by suddenly turning the g_{12} value from g to zero; this corresponds to the spatial density overlap between

the two clouds being suddenly reduced to zero in the experiment. Additionally, the coupling J is turned on at the time of splitting and ramped down exponentially with time constant $\tau_e = 60$ ms. This is motivated by the transient coupling of the two wells in the experiment during the splitting sequence, as well as the weak excitation of the vertical motion of atoms which is damped out over duration $\sim \tau_e$.

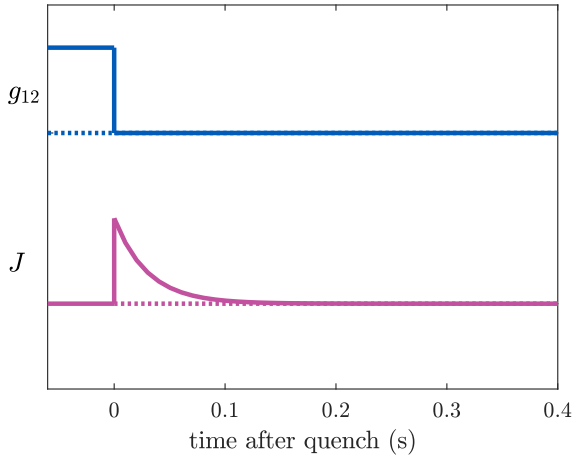

Figure 6.3: Illustration of the MC simulation scheme; the values of g_{12} and J are plotted against time. The y axis is shifted for each quantities for clarity (dotted lines in corresponding colours denote zero energy). Initially, the interaction terms g_{12} have the same finite values corresponding to the experimental values, $g = g_{12} \sim \hbar^2\tilde{g}/m$. At t=0, we suddenly turn g_{12} to zero and turn on the inter-layer coupling J, while g stays constant throughout. The peak value of J is chosen to be the same as g. This is the simplification of the transient state after the splitting where residual coupling between layers exists during and soon after the splitting.

We plot in Fig. 6.3 the parameters used for the MC simulation. At time $t = 0$, g_{12} jumps down to zero, J jumps up to a finite value corresponding to the energy scale equivalent to the interaction energy scale. The coupling J is introduced to reproduce the transient phenomena due to finite excitation of the system after the splitting; the value of J is quickly ramped down to 0 within tens of ms. As we see later, the BKT critical dynamics is much slower, on the order of hundreds of ms, such that this transient effect does not significantly affect the observation of BKT phenomena at long time.

As we describe later, there is a slow linear heating of the system in the MRF-dressed trap and we add heating in the simulation at a rate comparable to the

experimental value, by the addition of stochastic noise at each timestep. Since the energy input into the system by the heating is small over the experimental timescale, it does not significantly alter the relaxation dynamics; but it was important for the quantitative comparison of experiment and simulation.

6.3 Observation of the decoherence dynamics

Once the cloud is split, we vary the holdtime after the quench and probe the system by observing the matter-wave interference in the same way as presented in Chapters 4 and 5. By performing the correlation and vortex analysis, we obtain the correlation function $C(\overline{x})$ at each time, from which we calculate the algebraic exponent η, correlation length r_0 as well as averaged vortex density n_v. The number of experimental repeats at each time was $N_r = 60$, about four times smaller than the dataset used in Chapter 5. To have enough statistics to obtain the correlation function, we modified the evaluation of correlation function (Eq. (4.2.7)) to

$$C(\overline{x}) = \frac{1}{N_{\overline{x}}} \sum_{x=-L/2}^{L/2-\overline{x}} \mathrm{Re}\left[C(x, x+\overline{x})\right], \tag{6.3.1}$$

where L is 80% of the Thomas-Fermi diameter and $N_{\overline{x}}$ is the number of pixels within $[-L/2, L/2-\overline{x}]$. This procedure introduces only a small differences to the mean correlation function[1], and the fitted values of η and r_0.

We have performed the experiments with a range of initial temperatures covering the BKT critical regime while keeping the total atom number at $N \sim 9 \times 10^4$. The 'strength' of the quench is thus determined by how deep in the thermal regime the system is quenched to, which can be characterised by the rescaled temperature $\tilde{T} = T/T_0 \propto T/\sqrt{N}$ where T is the temperature before the quench and T_0 is obtained from the atom number following the quench.

In Fig. 6.4, we plot the correlation functions $C(x)$ obtained after the quench with two different initial temperatures. While the correlation function after the

[1]This was confirmed quantitatively using the dataset for the equilibrium system shown in Chapter 5 where $N_r = 220$. The estimation of errors on $C(\overline{x})$ is slightly modified by using Eq. (4.2.7), due to varying number of datapoints $N_{\overline{x}}$ contributing to $C(\overline{x})$ depending on the distance $\overline{x}$. As such, the χ^2 statistic is difficult to compare between different datasets and we use squared fit residuals to select the preferred fit model (f_{SF} or f_{Exp}) at each time, see Fig. 6.6.

quench is similar for both temperatures (blue, t=0.04 s), the temporal decay is much faster at higher temperature. The functional form of $C(x)$ crosses over from algebraic to exponential, as we discuss later in Section 6.4.

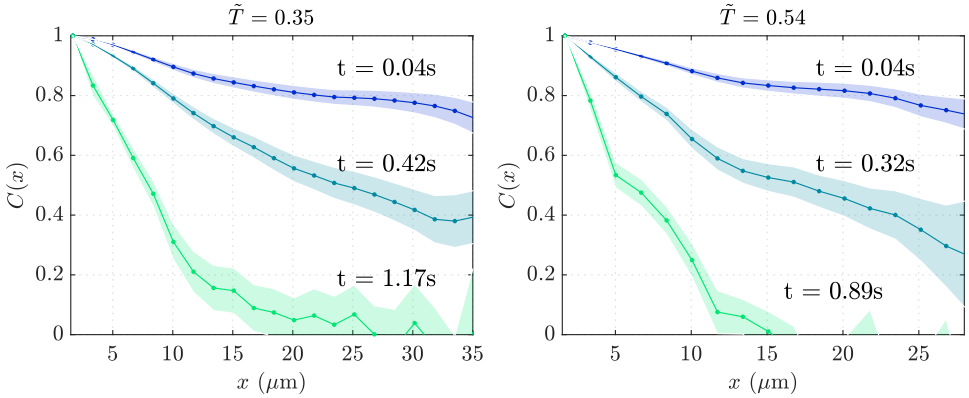

Figure 6.4: Time evolution of the correlation functions following a quench. The temperature shown above each panel is the rescaled temperature after the quench. The shaded region denotes the standard error obtained from bootstrapping resampling method [125, 129].

In Fig. 6.5, we illustrate the measured decoherence dynamics. Fig. 6.5 (b) shows the time evolution of squared interference contrast ${c_0}^2$ of integrated interference patterns (purple), which takes the value of 1 for a completely phase-coherent system and 0 without any coherence over long distances. In the experiment, the presence of a finite thermal component and the effect of finite imaging resolution reduces the maximum contrast to ~ 0.5 as observed in equilibrium (see Fig. 5.16). We indicate the 'critical time' t_c by the green vertical line, which we obtain by the change in functional form of the correlation function, as we discuss later in Section 6.4. While the initial rapid decay of ${c_0}^2$ before the t_c does not accompany any vortex excitations, the following slow decay after t_c is associated with exponential growth of vortex density n_v (blue). This indicates the two-step relaxation of a quench-heated 2D system, as discussed in Section 1.4.

Finite heating in the trap

Before proceeding to the detailed analysis of the time evolution, we first report on the intrinsic heating of atoms in our MRF-dressed trap. The heating effect comes

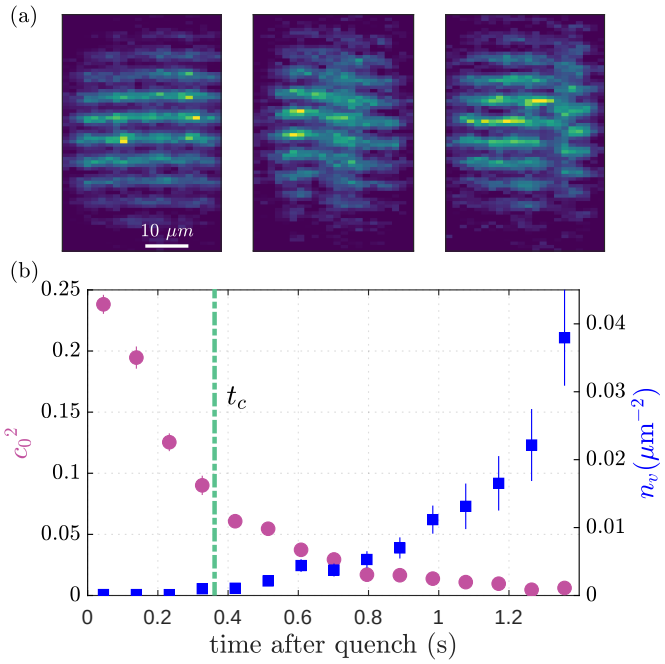

Figure 6.5: Illustration of the observed relaxation dynamics. (a) Examples of images showing observed matter-wave interference patterns. (left) typical image taken immediately after the quench, with only small fluctuation in phase. (middle) At short times, smooth variation of the phases indicate the phonon excitations. (right) At longer times, sudden phase jumps were observed, indicating the nucleation of vortices. (b) Illustration of thermalisation dynamics. The average squared contrast ${c_0}^2$ and vortex density n_v are plotted as a function of time after the quench. The vertical dashed line is the critical time at which the correlation function changes from algebraic to exponential; see Fig. 6.6. The contrast ${c_0}^2$ is obtained from the integrated image over entire slice region, and this value indicates the overall coherence of the system. The uncertainty in vortex density is statistical and the uncertainty in ${c_0}^2$ is the standard error. The temperature after the quench was $\tilde{T} = 0.54$ after the quench.

from the unidentified noise in the experimental apparatus which perturbs the atoms causing heating at a rate of 4 nK/s. This very low value shows that RF-dressed trapping is a very good method, nevertheless the intrinsic heating causes the system to drift towards the thermal state, but the change in $\tilde{T}$ is slow enough that the BKT critical phenomena still dominate the relaxation dynamics.

6.4 Time evolution of the algebraic exponent η

In Fig. 6.6, we show the time evolution of χ^2 values from exponential and algebraic fitting of correlation functions, as well as the algebraic exponent η. The values

of χ^2 show a clear crossover at a few hundred ms after the quench, indicating a transition from algebraic order to short-range correlations. η starts near 0 after the quench, and increases linearly in time. Using this linear relation, we obtain the critical exponent $\eta_c = 0.14(2)$ which is close to the value obtained in equilibrium. This value of the critical exponent is smaller than the universal value $\eta_{\mathrm{BKT}} = 0.25$ because of the finite-size effect (see Eq. (2.1.6)). We show the value of η even after the system enters the exponential regime because even in the thermal regime η is useful as a measure of phase fluctuation.

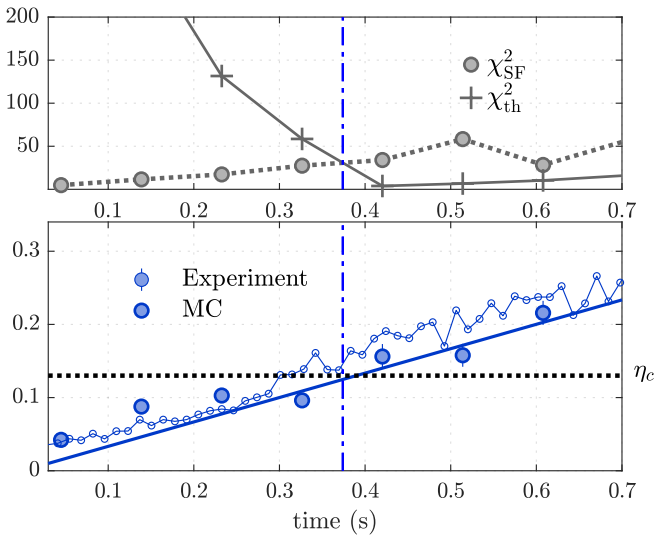

Figure 6.6: Determination of the dynamical critical exponent η_c. (top) The χ^2 statistic of the algebraic and exponential fits. Vertical line indicates the critical time t_c at which the functional form of the correlation function change to exponential. (bottom) The time evolution of η after the quench. The exponent η was obtained by fitting the phase correlation functions with algebraic model with LCA, Eq. (4.4.3). From t_c, we obtain the critical exponent $\eta_c = 0.14(2)$ (horizontal dotted line). Open connected markers denote η obtained from the MC simulation. The solid purple line is a linear fit to the experimental data.

In Fig. 6.7, we show the time evolution of η and the ratio of χ^2 values for algebraic and exponential fits, $\chi^2_{\mathrm{SF}}/\chi^2_{\mathrm{th}}$, at different initial temperatures: $\chi^2_{\mathrm{SF}}/\chi^2_{\mathrm{th}} > 1$ indicates the algebraic scaling, while $\chi^2_{\mathrm{SF}}/\chi^2_{\mathrm{th}} < 1$ for the exponential regime. We obtain the temperature-dependent critical time t_c by looking for $\chi^2_{\mathrm{SF}}/\chi^2_{\mathrm{th}} = 1$, which is marked as the vertical dash-dotted lines in Fig. 6.7. We find linear temporal evolution

of the algebraic exponent η with temperature-dependent slope, as expected from the real-time RG theory described in Section 2.6.2.

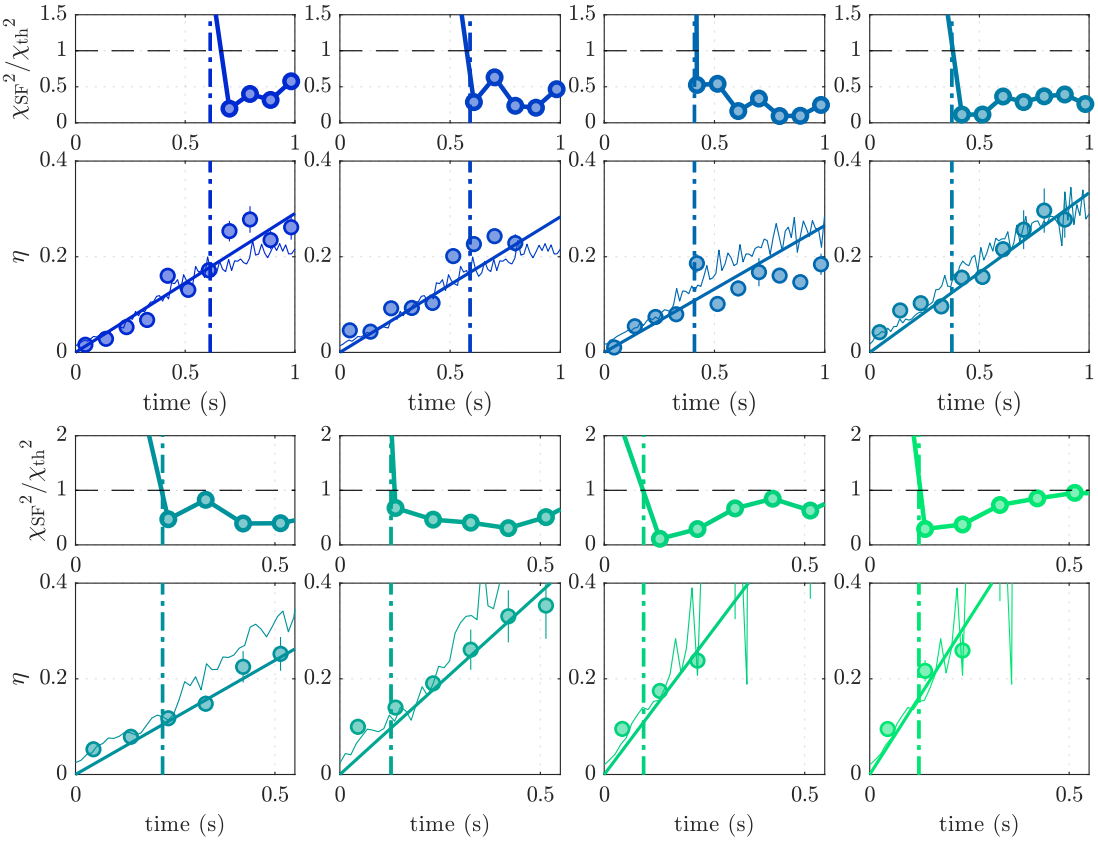

Figure 6.7: The time evolution of the algebraic exponent η after the splitting. Each panel corresponds to different initial temperature of the system, at $\tilde{T}$ =0.37, 0.42, 0.52, 0.54, 0.62, 0.67, 0.68 and 0.75, from top left (blue) to bottom right (green) panel. The ratio of χ^2 values for the algebraic and exponential fit is below 1 for the thermal regime and above 1 in quasi-ordered state. At relatively high temperature and at long time ($\sim$ 500 ms), the fluctuation of the phase is large so that the χ^2 is dominated by the fluctuation of the datapoints, resulting in the ratio $\chi^2_{\rm SF}/\chi^2_{\rm th}$ to approach unity at long time. Straight line is the linear fit to the experimental data (point) while fluctuating line is the numerical simulation result at corresponding temperature. The vertical line denotes the critical time t_c at which the correlation function change from algebraic to exponential scaling. We obtain the critical exponent η_c for each dataset by the measured t_c and the result of linear fit to the $\eta(t)$.

In Fig. 6.8, we show the temperature dependence of observed critical exponent η_c and critical time t_c. We obtain the mean critical exponent $\eta_c = 0.16(3)$, which is in agreement with the value obtained in equilibrium within uncertainties.

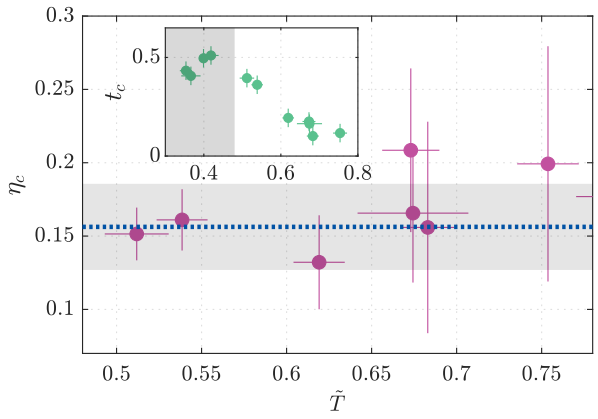

Figure 6.8: The critical exponents obtained from the results shown in Fig. 6.7. The horizontal dotted line is $\eta_c = 0.16(3)$ obtained by averaging the critical exponents measured at different temperatures and the shaded region denotes the standard deviation. Inset shows the critical time t_c against the temperature of the system. The shaded region in inset denotes $\tilde{T} < 0.5$ where the critical point is not crossed by the quench. The error bars in t_c are half of the separation of datapoints in the experiment $dt/2 = 48$ ms, and the uncertainties in each critical exponent datapoint are based on the uncertainty in t_c.

6.4.1 Arrhenius law

As we have seen in Fig. 6.4, the relaxation dynamics after the quench shows strong dependence on the initial temperature, $\tilde{T}$. In our experiment, the range of temperature after the splitting ranges from $\tilde{T} = 0.35$ to $\tilde{T} = 0.8$, corresponding to the rescaled temperature before the splitting from $\tilde{T}_i = 0.25$ to $\tilde{T}_i = 0.58$. Since the observed critical point in equilibrium was $\tilde{T}_c \sim 0.53$ (see Chapter 5), datasets with temperature after splitting $0.53 \lesssim \tilde{T}$, are expected to show the critical behaviour.

In Fig. 6.9, we show the temperature dependence of the slope of $\eta(t)$ obtained by fitting the time evolution of η at each temperature with $f(t) = t\kappa$. While there is a clear dependence on the temperatures above $\tilde{T} \gtrsim 0.5$, the data flattens out at lower temperatures. At low temperatures, since the critical point is not crossed by the quench, the time evolution of η is mainly driven by the intrinsic heating in the trap, at the rate of 4 nK/s.

In the following, we compare the data with the Arrhenius equation

$$\kappa(T) = A \exp\left(-\frac{E_a}{k_B T}\right) + \kappa_0, \tag{6.4.1}$$

where A, E_a and κ_0 are the free parameters. The Arrhenius law characterises the temperature dependence of chemical reaction rates, and can be used to obtain the activation energy E_a of the reaction. We have added a phenomenological offset term κ_0 to the usual Arrhenius equation, to account for the heating in the trap. In our situation, the energy barrier E_a is expected to be the finite energy associated with the nucleation of vortices, as discussed in a simplified argument in Section 2.1. We plot the fit results for experimental and MC datapoints in Fig. 6.9 as solid and dotted lines. The results of fitting to the experimental data are $E_a = 4.4(6) \times k_B T_0$ and $\kappa_0 = 2.8(8)$ s^{-1}. As a comparison, this activation energy E_a corresponds to the energy of a single vortex[2] placed in a circularly-shaped 2D superfluid of density $n_s = 10\,\mu\text{m}^{-2}$, with the healing length $\xi = 1\,\mu\text{m}$ and a system radius $R = 15\,\mu\text{m}$. The healing length and the system size are the same as the experimental value. Since the typical peak density of the atoms in experiments is $40\,\mu\text{m}^{-2}$, this result is consistent with a superfluid fraction of around 0.25, which is comparable to the number observed in equilibrium (see Fig. 5.10 and Fig. 5.11). Furthermore, the constant heating term κ_0 corresponds to a heating rate of 3.0(8) nK/s, which is in close agreement with the independently observed heating rate in the MRF-dressed trap.

6.4.2 Superheated superfluid

The presence of superfluid in interacting Bose gases is related to the emergence of non-zero 'macroscopic wavefunction' $\langle\hat{\Psi}\rangle$, which remains finite only with long-range coherence in the system[3] and is equivalent to the Penrose-Onsager criterion for BEC, $\lim_{r\to\infty} g_1(r) > 0$ [130][4].

[2]This is calculated using Eq. (2.1.3), with the short-range cutoff replaced by the healing length for an atomic system.

[3]In the 2D Bose gases in quasicondensate regime, $\langle\hat{\Psi}\rangle$ is finite only if there is a long-range phase coherence; this is easily seen by considering density-phase representation $\Psi = \sqrt{n}e^{i\phi}$ with no density fluctuation. With completely random phase, $\langle\hat{\Psi}\rangle$ becomes zero while with broken symmetry $\langle\hat{\Psi}\rangle$ becomes finite.

[4]This condition should be modified to $\lim_{r\to L} g_1(r) > 0$ for finite-size systems, where L is the system size.

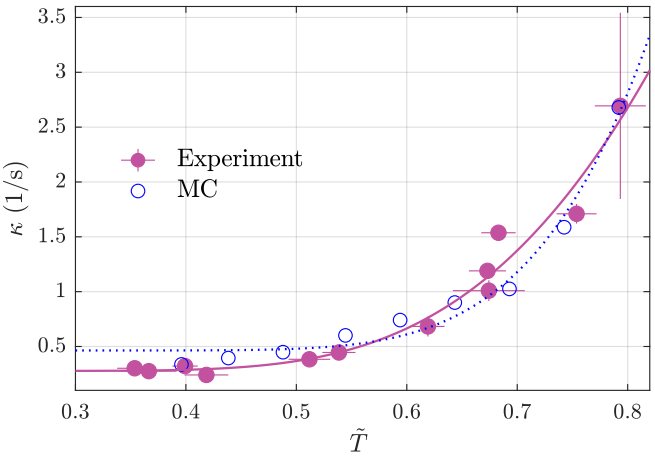

Figure 6.9: Temperature dependence of the time evolution of algebraic exponent η. The slope of $\eta(t)$ observed in the experimental data (Purple, filled) is plotted against the temperature after splitting $\tilde{T}(t = 0)$. Solid line is fit with Eq. (6.4.1). The result from the MC simulation is shown in blue (open markers), with a dashed line that is the fit with Eq. (6.4.1).

To characterise the superfluidity of the transient state where $\eta(t) < \eta_c$, we need to obtain the first-order correlation function of the system $g_1(r)$. The characterisation of $g_1(r)$ using the relative phase correlation as performed in Chapter 5, needs to be treated with care in the non-equilibrium setting in this chapter since there is strong correlation between two clouds soon after the splitting, when the two clouds have the same phase profile. Rapid loss of correlation between the two wells, and the approach of the relative phase correlation function towards the normalised g_1 function, is expected to occur in 2D systems since they are not integrable, in contrast to 1D systems where the symmetric and antisymmetric modes remain out of equilibrium for extended period of time [30]. In 2D, theoretical results suggest that all symmetric and antisymmetric phase and density modes quickly equilibrate into a single temperature, supporting the observation of g_1 function in the transient state by relative phases [45, 46]. Indeed, in the numerical simulation of the quench dynamics, we observe that the symmetric and antisymmetric phase fluctuations converge to having the same correlation functions within a few hundred milliseconds.

6.5 Dynamical vortex unbinding

The direct observation of vortices further elucidates the character of the observed non-equilibrium state and the dynamics towards a vortex-proliferated thermal phase. We detect vortices in the non-equilibrium systems within 90% of the TF region, using the technique described in Section 4.5. In Fig. 6.10, we show the time evolution of averaged vortex density n_v following a quench. We find that the proliferation of vortices follows an exponential scaling, as expected from the real-time RG theory shown in Section 2.6.2. The vortex density is fitted well with an exponential model $f(t) = n_c e^{(t-t_0)/\gamma}$, plotted as solid lines in Fig. 6.10. We have used the critical vortex density $n_c = 2 \times 10^{-3}$ μm^{-2} from the result in equilibrium (see Fig. 5.14), to find the characteristic timescale for the vortex unbinding.

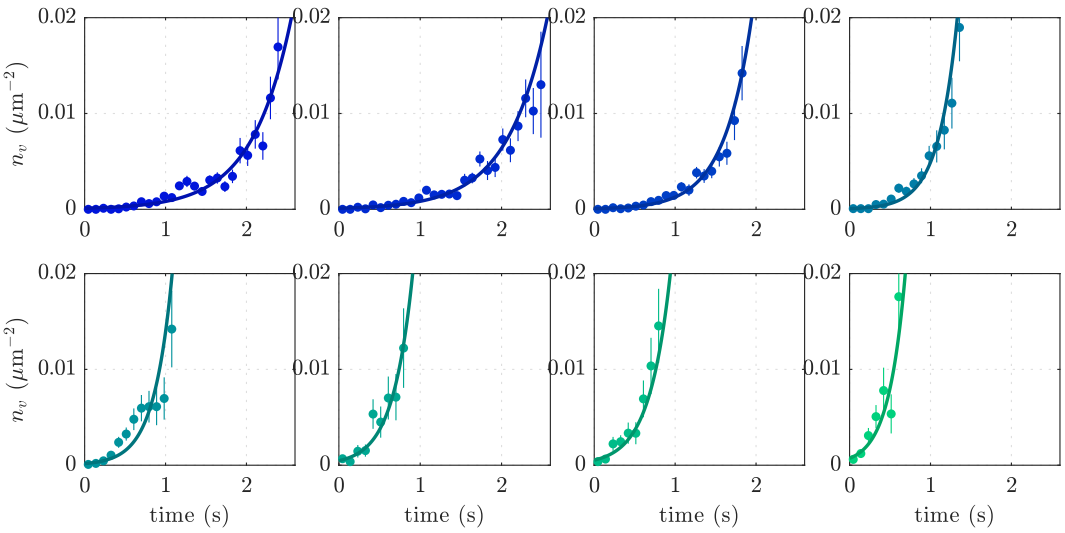

Figure 6.10: Time evolution of the vortex density n_v. Each panel corresponds to different initial temperature of the system, at $\tilde{T}$ =0.35, 0.37, 0.39, 0.54, 0.62, 0.67, 0.68 and 0.75, from top left (blue) to bottom right (green) panel. Solid lines are the fitted exponential model $f(t) = n_c e^{(t-t_0)/\gamma}$

The result of the exponential fitting is shown in Fig. 6.11. For the range of initial temperature at which the critical point is crossed by the quench $0.5 \lesssim \tilde{T}$, the γ is almost constant and t_0 scales linearly. This is in qualitative agreement with the results of real-time RG discussed in Section 2.6.2, where we observed linear dependence of t_0 and only a small dependence of γ on the initial temperature.

However, at $\tilde{T} \lesssim 0.5$, the dynamics is driven by slow heating of the system and the obtained γ and t_0 show a different behaviour to the ones in $\tilde{T} > 0.5$.

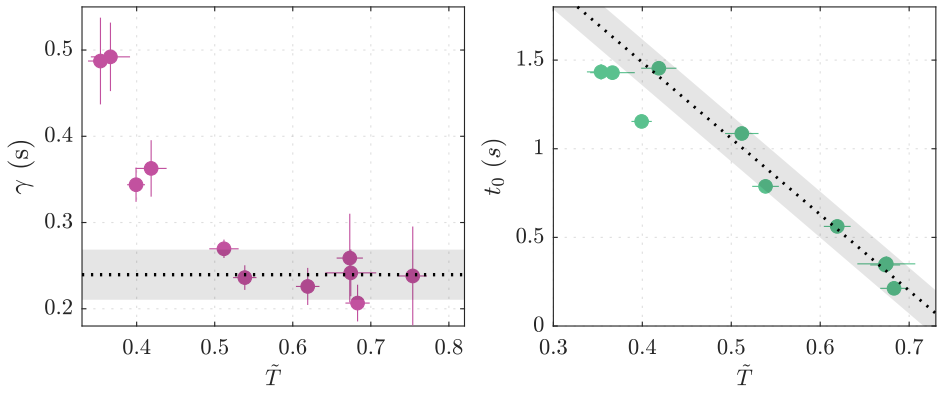

Figure 6.11: The best-fit parameters of the exponential fits in Fig. 6.10. Left panel shows the scaling factor γ for varying temperatures. Dotted line is the mean value within the region $0.5 < \tilde{T}$ and grey shading is the standard deviation. Right panel shows the characteristic vortex unbinding timescale t_0. Dotted line is the linear fit to datapoints that are $\tilde{T} > 0.5$. Shaded region is a guide to the eye. The error in γ and t_0 are the 1σ uncertainties from bootstrapping.

6.6 Real-time RG comparison

To understand the dynamics of vortices, we compare the experimental results with real-time RG theory introduced in Section 2.6.2. The RG flow equations Eq. (2.6.2) predicts the time evolution of $g(t)$ and $\eta(t)$, given an initial condition $\eta_0(t_0), g_0(t_0)$ at time t_0. To incorporate the heating in the MRF-dressed trap from unidentified electrical noise, we have added a phenomenological heating term ζ fixed at 10^{-4}, corresponding to the value in experiment for the time t in the RG equations scaled to milliseconds. The modified RG equation is

$$\begin{aligned} \frac{dg(t)}{dt} &= \left(2 - \frac{1}{2\eta(t)}\right)\frac{g(t)}{t}, \\ \frac{d\eta(t)}{dt} &= \frac{4\pi^2 g^2}{\eta(t)t} + \zeta. \end{aligned} \tag{6.6.1}$$

To directly compare the experimental results with the flow equation, we transform the parameters into $x = 1/2\eta - 2$ and $y = \sqrt{2\pi} g_v$, and plot in Fig. 6.12. We have obtained the g_v from the MF relation of the vortex fugacity and vortex density,

Eq. (2.6.3). The initial condition of the experiment immediately after the quench is $\eta \sim 0, g_v \sim 0$, which is equivalent to $x \to \infty, y = 0$. Following the quench, the phonon thermalisation drives the system towards smaller x (larger η), and eventually cross the critical point. Since the critical point in our (finite-size) system is $\eta_c = 0.16$, we observe the onset of increase in y near $x_c = 1/2\eta_c - 2 = 1.1$, which is different from the universal value x_{BKT}=0. Once the critical point is crossed, the y values increase rapidly, closely following the RG flow. As such, the RG equation Eq. (6.6.1) partially describes the observed vortex unbinding dynamics at late times. A quantitative RG description of the experimentally observed dynamics in the crossover regime $x \sim 1$ where there are finite-size effects requires further theoretical work.

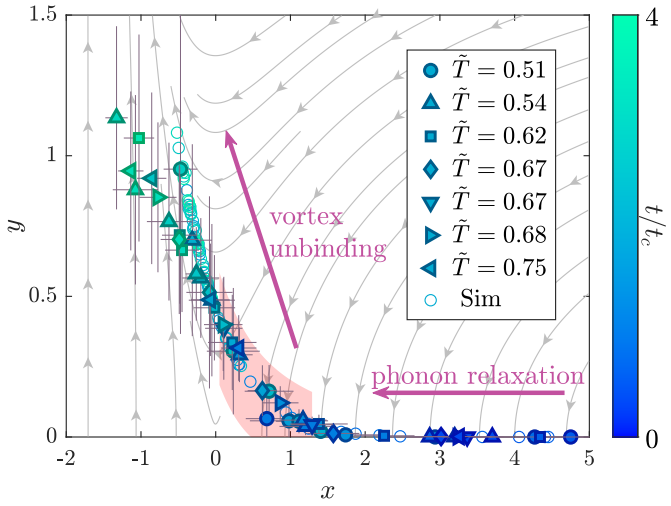

Figure 6.12: Comparison of the experimental results and the real-time RG flow Eq. (6.6.1). Experimental data at different initial conditions are plotted using the variables: $x = 1/2\eta - 2$ and $y = \sqrt{2\pi} g_v$. The vortex fugacity is obtained from the MF relation of the vortex fugacity and vortex density, Eq. (2.6.3). The experimentally observed dynamics was from bottom right ($x \to \infty, y = 0$) towards the top left region, as indicated by the blue arrow.

6.7 Conclusion

In this chapter, we have explored the relaxation dynamics of a 2D system following a quench from superfluid to thermal regime. The quench was realised using coherent splitting, which prepares the system in a well-defined, highly non-equilibrium initial

state. The relaxation dynamics exhibits two regimes: quick phonon thermalisation and the slow vortex nucleation. We found the temporal scaling of the algebraic exponent η and vortex density, which are in qualitative agreement with the predictions of real-time RG theory. We have further compared the observed dynamics on RG flow diagram.

7

Dynamics of coupled 2D Bose gases

Contents

In this chapter, we present the experimental work towards the observation of Josephson oscillation in tunnel-coupled bilayer 2D superfluids. We have realised a double-well potential with $\sim 1\,\mu$m well separation while keeping the quasi-2D condition, and observed the dynamics of phase-imbalanced bilayer 2D gases. In contrast to the previous chapters where the coupling between two layers was kept to a negligible value, here we investigate the non-equilibrium dynamics of bilayer 2D system with finite inter-layer coupling. In this investigation we are interested mainly in the *global* phase difference of two clouds and its time evolution, instead of the spatial correlation of local phases. As such, we prepare the 2D cloud deep in the superfluid regime to reduce the thermal effects that would affect the visibility

of the dynamics. The system of two superfluids with weak tunnel-coupling has similarities with a superconducting Josephson junction [131–134]. The atomic system realisations are called *bosonic Josephson junctions* (BJJ) and have been studied extensively [78, 135–141]. In this chapter, we will first describe the simplified model of Bose gases in a double-well potential using the two-mode approximation and analyse the expected dynamics. We then discuss the experimental investigation with coupled 2D Bose gases, in which we suddenly introduce a coupling between two phase-imbalanced 2D gases and monitor the subsequent dynamics. This investigation is a crucial step towards the understanding of the physics of coupled bilayer 2D Bose gases, such as the novel phase of 2D gases associated with the proliferation of half-vortices [77] and the dynamical control of conductivity for the quantum simulation of the light-induced superconductivity [142]. The realisation of controlled tunnelling in a MRF-dressed potential is also an important ingredient to realise conditional spin squeezing using the non-destructive imaging method, as described in Appendix A as well as our recent preprint [143]. We note that the Josephson junction dynamics of 2D gases separated by a weak link *within the same plane* was recently realised elsewhere [144, 145], and this is an active topic of research.

7.1 Two-mode model

In this section, we introduce the theoretical tools used to understand the observed dynamics. We introduce the two-mode approximation of Bose gases in a double-well potential, which simplifies the description of the systems and allows us to make a prediction of the dynamics. A comprehensive review of this topic can be found in Refs. [146, 147].

For simplicity, we consider 1D dynamics of atoms confined in double-well potentials, which corresponds to the dynamics in the tightly-confined z direction in our experiment.

The full Hamiltonian of a Bose gas in a double-well potential $V(r)$ with contact interactions is

$$\hat{H} = \int dr[-\hat{\Psi}^\dagger(r)\frac{\hbar^2}{2m}\nabla^2\hat{\Psi}(r) + \frac{g}{2}\hat{\Psi}^\dagger(r)\hat{\Psi}^\dagger(r)\hat{\Psi}(r)\hat{\Psi}(r) + \hat{\Psi}^\dagger(r)V(r)\hat{\Psi}(r)]. \tag{7.1.1}$$

In the double-well potential, the two lowest energy eigenstates are symmetric and antisymmetric respectively with small separation of their energies, as illustrated in Fig. 7.1. The two-mode approximation amounts to limiting the wavefunction of the system to these two spatial modes, which we label as ψ_g and ψ_e which is valid provided all the energy of the system is lower than the energy of even higher excited states. We define *left* and *right* modes as the combinations

$$\psi_L = \frac{\psi_e + \psi_g}{\sqrt{2}}, \ \psi_R = \frac{\psi_e - \psi_g}{\sqrt{2}}, \tag{7.1.2}$$

corresponding to localised modes in either left or right wells. We then rewrite the

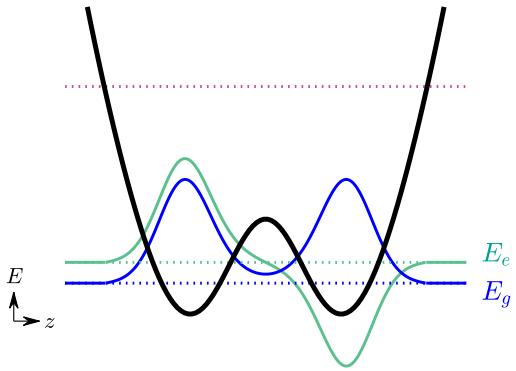

Figure 7.1: Illustration of energy level structure in double-well potential. Two lowest energy eigenstates ψ_g (blue) and ψ_e (green) are shown. At sufficiently low temperature and interaction energy, these two states are macroscopically occupied and higher levels (purple, dotted) can be ignored. This is the two-mode approximation that we use.

wavefunction $\Psi(r)$ with linear superposition of left and right modes,

$$\hat{\Psi} = \psi_L\hat{a}_L + \psi_R\hat{a}_R, \tag{7.1.3}$$

where $\hat{a}_L^\dagger, \hat{a}_R^\dagger$ ($\hat{a}_L, \hat{a}_R$) are the creation (annihilation) operators for particles in the left and right localised modes. The two-mode approximation leads to a two-site

Bose-Hubbard Hamiltonian [146–148],

$$\hat{H}_{BH} = -J(\hat{a}_L^\dagger \hat{a}_R + \hat{a}_R^\dagger \hat{a}_L) + \frac{\Delta}{2}(\hat{n}_R - \hat{n}_L) + \frac{U}{2}\left[\hat{n}_L(\hat{n}_L - 1) + \hat{n}_R(\hat{n}_R - 1)\right], \tag{7.1.4}$$

where the number operators are $\hat{n}_R = \hat{a}_R^\dagger \hat{a}_R$, $\hat{n}_L = \hat{a}_L^\dagger \hat{a}_L$, U is the interaction energy of atoms in same well and Δ is the small potential energy difference between the two wells, as illustrated in Fig. 7.2.

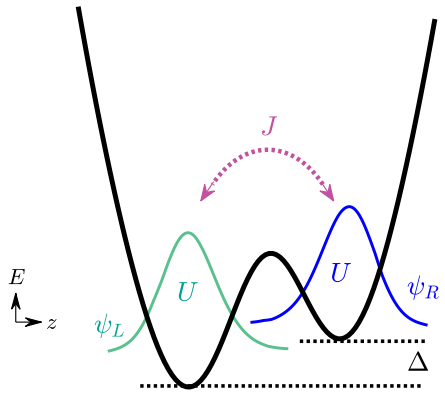

Figure 7.2: Illustration of the parameters in the Hamiltonian Eq. (7.1.4). The left and right localised modes ψ_L and ψ_R are shown in green and blue, with associated interaction energies U which are assumed to be the same for each modes. The amplitude J gives tunnelling between the two wells. Δ describes the asymmetry of the potential.

The coupling strength J is given by [149]

$$J = -\int dr \left(\frac{\hbar^2}{2m}\nabla\psi_L \nabla\psi_R + \psi_L V(r)\psi_R\right). \tag{7.1.5}$$

This quantity can be estimated from the spatial distribution of localised modes ψ_L, ψ_R in the double-well potential. To estimate the magnitude of J, we approximate the double-well potential by two harmonic potentials $V_{L,R}(r) = \frac{1}{2}m\omega_z^2(r \pm d/2)^2$ at distances $\pm d/2$ from the centre. Further, we assume non-interacting gases and take Gaussian ground states in each harmonic potential as the left and right localised modes, characterised by the harmonic oscillator length ℓ_0. The integration in Eq. (7.1.5) can then be performed to obtain [132, 148]

$$J = \frac{\hbar\omega_z}{2}\left(\frac{d^2}{4{\ell_0}^2} - 1\right) e^{-d^2/4{\ell_0}^2}. \tag{7.1.6}$$

From Eq. (7.1.6), we see that the coupling strongly depends on the ratio d/ℓ_0, and sharply increases as d approaches the size of the wavefunction $d \sim \ell_0$ from above. We note that the prediction Eq. (7.1.6) is only to be used for the qualitative understanding of the dependence of J on d/ℓ_0; for example, the value of J also depends strongly on the number of atoms and their interaction strength, through various contributions such as the deformation of wavefunctions [148].

To gain insight into the dynamics under Eq. (7.1.4), we approximate further by applying a mean-field approach [149, 150], which amounts to replacing the annihilation operators by amplitudes that depend of their mean values: we replace the annihilation operators in left and right modes by

$$\begin{aligned} \hat{a}_L &\to \sqrt{n_L} e^{i\phi_L}, \\ \hat{a}_R &\to \sqrt{n_R} e^{i\phi_R}, \end{aligned} \tag{7.1.7}$$

where $n_L, n_R, \phi_L, \phi_R \in \mathbb{R}$. Using this approximation turns Eq. (7.1.4) into a classical Hamiltonian and the time evolution can be expressed in terms of the total atom number $N = n_L + n_R$, fractional population difference $n = (n_L - n_R)/N$ and phase difference $\theta = \phi_R - \phi_L$ [150]

$$\begin{aligned} \dot{n} &= -\frac{JN^2}{\hbar}\sqrt{1-n^2}\sin\theta, \\ \dot{\theta} &= -\frac{\Delta}{\hbar} + \frac{UN}{\hbar}n + \frac{JN^2}{\hbar}\frac{n}{\sqrt{1-n^2}}\cos\theta. \end{aligned} \tag{7.1.8}$$

We plot in Fig. 7.3 the time evolution of θ and n for $\Delta = 0$ and $U/J = 20/N$, and with two different initial conditions of n and θ. Assuming small phase and population differences, we find Josephson oscillation of two quantities (green plot in Fig. 7.3); but for larger population difference, a qualitatively different dynamics emerges which is called self-trapping [139, 146]. We notice that with the condition $n = 0$ and any θ under the conditions of $\Delta = 0$ and $U/J = 20/N$, no self-trapping is expected.

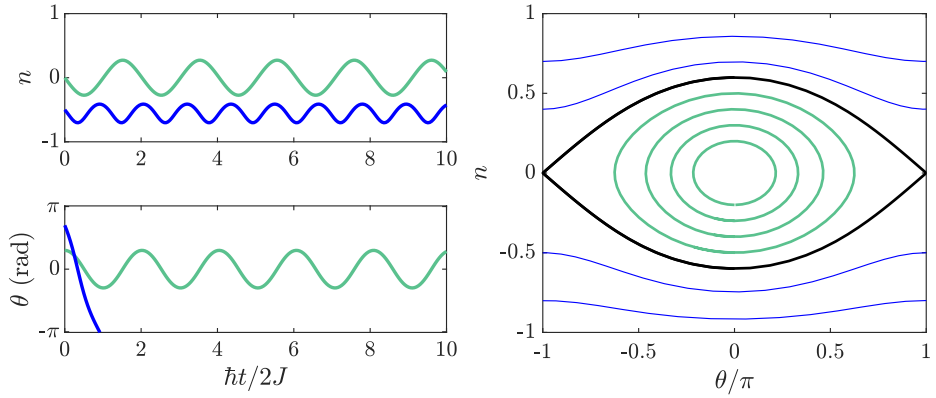

Figure 7.3: The time evolution of the phase difference θ and population imbalance n in the two-mode approximation with $\Delta = 0$ and $U/J = 20/N$. Left panels show the time evolution of n and θ at two selected initial conditions, $\theta(0) = 0.3\pi, n(0) = 0$ (green) and $\theta(0) = 0.7\pi, n(0) = -0.5$ (blue). The θ monotonically decreases for the initial condition $\theta(0) = 0.7\pi, n(0) = -0.5$ (blue). Right panel shows the trajectories in the phase space. The green lines follows a behaviour similar to Josephson oscillations, while the dynamics following blue lines is the so-called self-trapping, with the black line separating the two regimes.

7.2 Coupled MRF-dressed double-well potentials

From Eq. (7.1.6), we find that realisation of a coupled system requires the distance between the two clouds to be small on the order of the spatial extent of wavefunctions. The spatial extent of the gas in the double-well is typically $\ell_0 \lesssim 1\,\mu\text{m}$, and thus we require a comparable spatial separation of the two wells. Utilising the excellent controllability of MRF-dressed double-well potentials, we can achieve precise control of double-well separations, as illustrated in Fig. 7.4. For the experiments reported in this chapter, we used narrow separations of the dressing RF frequencies [7.17, 7.2, 7.23] MHz and a higher quadrupole field gradient of $b = 140$ G/cm compared to the experimental conditions used in Chapters 5 and 6. These values give a separation of $\sim 1.5\,\mu\text{m}$ for which we expect a tunnelling rate of hundreds of Hz.

7.2.1 Experimental procedure

We illustrate our experimental procedure in Fig. 7.5. To observe the Josephson oscillation, we prepare a pair of phase-imbalanced 2D gases and suddenly introduce coupling to initiate the time evolution, in a similar manner to the experiment in 1D

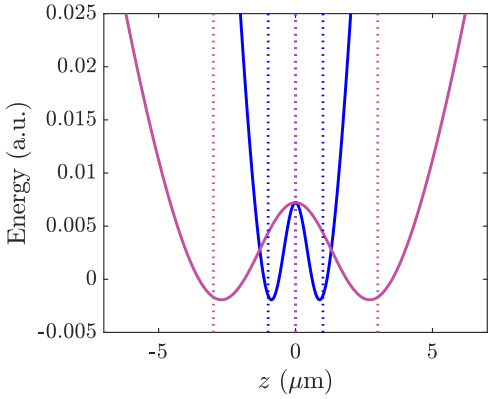

Figure 7.4: Controllability of the double-well separation in a MRF-dressed potential. A wide range of well separations can be chosen by appropriate choice of RF frequency combinations and quadrupole field gradient b. The double-well potential created by a RF frequency combinations of [7.14, 7.2, 7.26] MHz and $b = 100$ G/m is plotted in purple, corresponds to the separation of the wells used in Chapter 5. We plot the potential with [7.17, 7.2, 7.23] MHz and b=140 G/m in blue, which are the values used in this chapter. Vertical dotted lines indicate the RF resonance locations in corresponding colours.

Bose gases performed elsewhere [78, 91]. We start by a coherent splitting of a single cloud into two, which prepares a well-defined initial state with $\theta = 0$. We ensure the equal population of two wells $n \sim 0$ by maximizing the observed interference contrast. After the splitting, we keep the energy of the barrier, between the two wells, E_b high such that the two wells are separated with negligible coupling in this particular stage of the experiment. We then imprint the phase difference by introducing asymmetry Δ of the potential, while keeping the two clouds sufficiently decoupled. Finally, we introduce coupling of the two clouds by reducing the spatial separation of the two wells and lowering the barrier. We observe the dynamics of the relative phase θ using matter-wave interferometry, as described in the following section.

7.3 Experimental results

We start with a cloud of $N \sim 4 \times 10^4$ atoms in a MRF dressed trap, with a temperature around 20 nK such that the system is deep in the superfluid regime. Typical trap frequencies are $\omega_r/2\pi = 13$ Hz and $\omega_z/2\pi = 1.5$ kHz, and the quasi-2D conditions $k_B T, \mu \lesssim \hbar\omega_z$ are satisfied for each well. We perform a coherent splitting over 6 ms into a symmetric double-well with a high energy barrier $E_b/h = 5$ kHz.

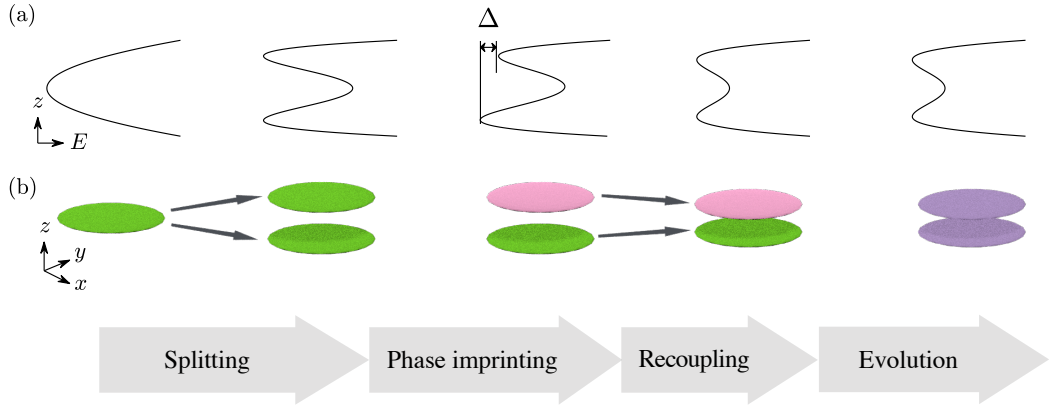

Figure 7.5: Illustration of the experimental sequence. (a), upper row, shows the vertical trapping potential. (b), middle row, shows the state of the 2D clouds during the sequence. The first stage consists of the coherent splitting of a single 2D clouds into two, resulting in a two clouds with the same global phase. We ensure that the coupling of the two wells is negligible immediately after the splitting. After the splitting, we imprint the global phase difference $\theta = t\Delta/h$ by applying energy difference between the two wells, while keeping small coupling. The phase difference is indicated as the different colours of two layers, and we are interested in the phases after the recoupling (indicated by purple). Once the desired phase difference is achieved, we change the potential to introduce the coupling between wells and observe the dynamics.

Immediately after the splitting, we introduce an asymmetry Δ/h =1 kHz between the two wells and wait for a variable time to imprint a phase difference. Finally, we ramp down the energy barrier to $E_b/h = 1$ kHz in order to increase the coupling J, while eliminating the asymmetry; this was performed over a duration of 2 ms, during which the spatial separation of the wells reduces to $d = 1.5\,\mu$m.

We show typical matter-wave interference patterns in Fig. 7.6 obtained after $t_{\mathrm{TOF}} = 10$ ms TOF expansion. Interference fringes at wavenumber $k = md/\hbar t_{\mathrm{TOF}}$ are observed along the z direction. To obtain the phase θ, we have analysed the interference patterns at 20 individual pixel columns within the interfering part of the cloud using FFT (see Fig. 4.3).

7.3.1 Phase accumulation

In Fig. 7.7 , we show the histogram of the phase obtained from the measurements at a few selected times during the phase imprinting stage. The double-well trap

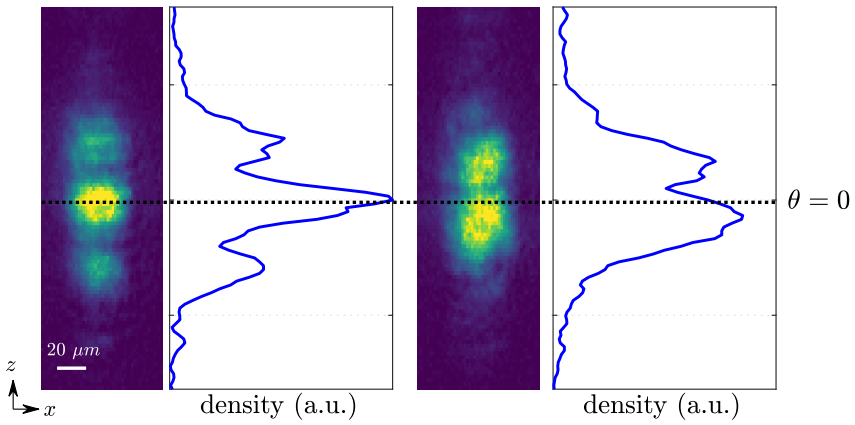

Figure 7.6: Typical matter-wave interference patterns observed after the recoupling quench. Relatively long fringe separation is observed compared to the results in Chapters 5 and 6, because of the small separation of the wells. The horizontal dotted line indicates the centre of mass of the cloud in vertical direction, and having the interference peak at the line indicates zero relative phase between two clouds, $\theta = 0$.

was configured to be asymmetric with $|\Delta|/h = 1$ kHz, with a high energy barrier $E_b/h \sim 5$ kHz and well distance $d \gtrsim 2\,\mu$m such that the coupling J is negligible for the duration of phase accumulation of a few ms. Each column of the bottom panel in Fig. 7.7 corresponds to a single histogram (selected histograms are shown in top panels); 120 datapoints contribute towards each histogram, which are obtained from 6 images taken at each time. We observe the linear increase of phase at a rate corresponding to the value of Δ/h, as expected from Eq. (7.1.8) with $J = 0$ and $U = 0$.

7.3.2 Phase oscillation after recoupling

Once we have the desired phase difference θ, we introduce coupling between the two 2D clouds and observe the dynamics. We transform the potential such that the asymmetry Δ is eliminated and the energy barrier between the wells E_b/h is reduced to 1 kHz. The separation of the wells is reduced to $d = 1.5\,\mu$m to obtain a large value of J. In Fig. 7.8, we plot the time evolution of the phases θ following the recoupling. We have chosen a phase accumulation time of 300 µs, corresponding to an initial phase difference of $\theta(t = 0) \sim \pi/2$. The observed dynamics of θ

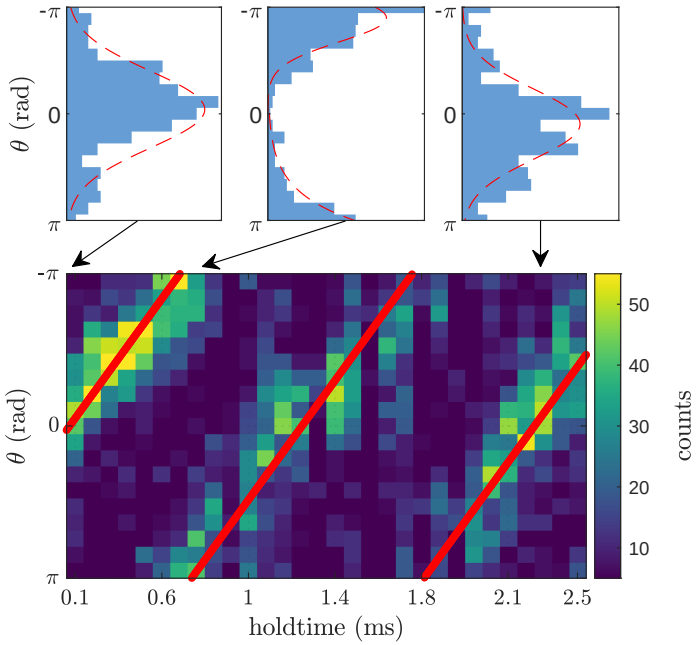

Figure 7.7: Time evolution of the relative phase θ in a decoupled asymmetric double-well. (Top) Histogram of observed relative phases at a few selected times after the splitting and deformation of the double-well (see Fig. 7.5). Red dashed lines are Gaussian fits to the distributions. (Bottom) The time evolution of the relative phase in a imbalanced double-well. Each pixel column corresponds to a single histogram, obtained from images taken at a given time. Red line is a guide to the eye.

show oscillations of around 1 ms period. We fitted the phase dynamics with a sinusoidal, shown as the red line. The best-fit value of the oscillation frequency is f =850(30) Hz. This value of f is on the same order as the value of 300 Hz obtained from the GPE simulation for similar parameters and potential [105]. The large deviation between these two values may arise because of the miscalibration of the atom number; this work on Josephson oscillation was done before the atom number measurement was properly calibrated using the method described in Section 3.5.4. We also note that the slight difference of the confinements of the two wells in the experiment was not taken into account in the GPE simulation.

We have further observed the phase dynamics with different trap configurations. Different trap geometry can be achieved by changing the RF amplitude of the 7.2 MHz component, $\Omega_{7.2}$, which controls the barrier height between the wells. The range of the values of $\Omega_{7.2}/h$ are 19.5, 20, 20.5, 21 and 21.25 kHz, which corresponds to E_b/h = 1.2, 1, 0.8, 0.5 and 0.25 kHz and the double-well spatial separation

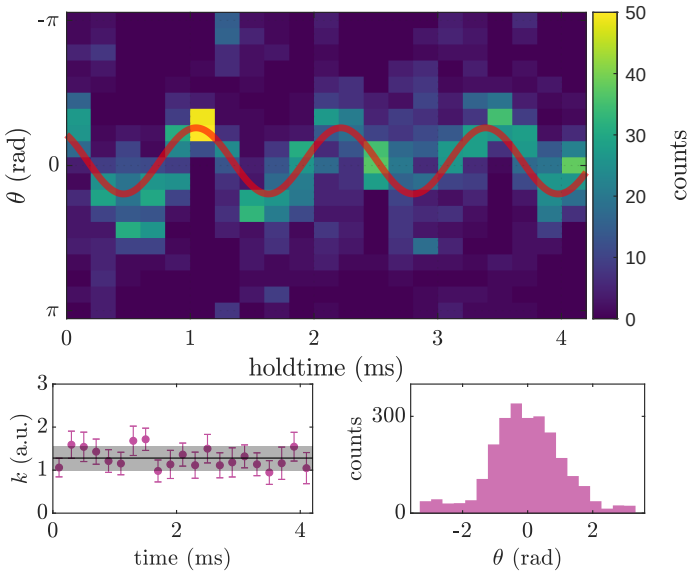

Figure 7.8: The phase oscillation following the recoupling. (top) The time evolution of the phase difference θ following quench. 100 datapoints contribute to the histogram at each time from 5 images. The red line is the sinusoidal fit. (bottom, left) Time evolution of the fringe wavenumber, obtained by fitting the interference patterns with Eq. (4.2.4). Black horizontal line and the shaded region denotes the mean and standard deviation of k. (bottom, right) Histogram of the observed phase, integrated over whole duration shown in top panel.

$d = 1.6$, 1.5, 1.4, 1.2 and 0.9 µm. Higher E_b/h (and larger d) leads to smaller coupling strength J, and we expect to observe a smaller phase oscillation frequencies. Indeed, as we see in Fig. 7.9 bottom right panel, the observed oscillation frequencies strongly depend on the value of E_b.

7.4 Conclusion and future plans

In conclusion, we have presented the experimental method used to achieve small separations of the wells $d \sim 1\,\mu$m and observed the phase oscillation dynamics following a recoupling quench. The high controllability of the MRF-dressed potential allows a wide range of spatial well separation to be realised, resulting in a good controllability of the coupling strength. Using the MRF-dressed potential, we have prepared a phase-imbalanced pair of 2D superfluids and observed the oscillation of the relative phase following a recoupling quench. The observed sinusoidal oscillation of the relative phases and their frequencies are consistent with that of tunnel-

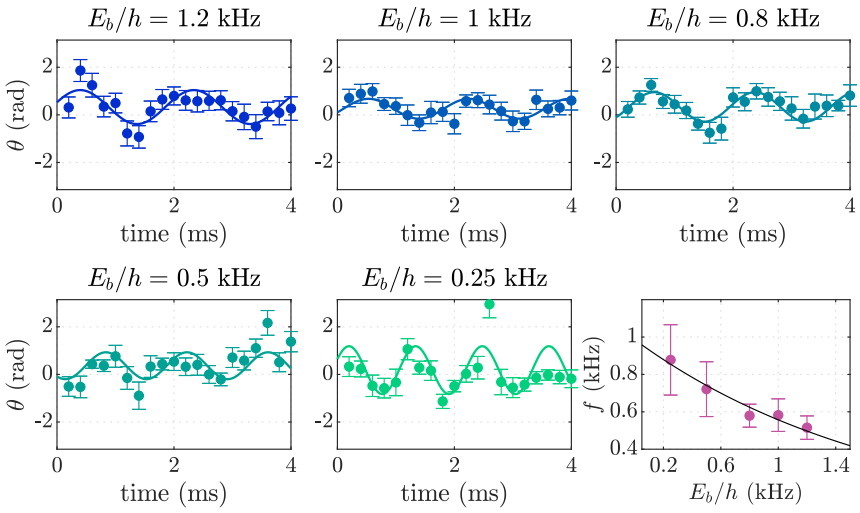

Figure 7.9: Time evolution of the relative phase θ in a coupled double-well for different barrier energies and double-well separations, with $E_b/h = 1.2$, 1, 0.8, 0.5 and 0.25 kHz from top left panel to middle bottom panel. Solid lines are the sinusoidal fit. The corresponding well separations d are 1.6, 1.5, 1.4, 1.2 and 0.9 µm. Solid lines are the sinusoidal fit and uncertainties of datapoints denote standard error from experimental repeats. Bottom right panel shows the observed frequency from the sinusoidal fit against the energy barrier E_b/h. Solid line is the fit to the frequency data with an exponential as a guide to the eye. The value of the E_b is determined from the measured RF amplitudes, based on the Floquet numerical simulation of the MRF-dressed potential [107].

coupled systems. However, our current experimental technique does not allow the measurement of population imbalance between the two wells, which is required to confirm the Josephson dynamics; see Section 7.4.1. Furthermore, the time range that was observed is not enough to determine the long-time limit of the dynamics and to investigate whether the dynamics damps, and if so, at what timescale. One of the main limiting factors was the monopole oscillation of the cloud following the splitting, which prevents the observation of clear interference patterns at long time A straightforward way to overcome the limitations is the slow loading scheme as used in Chapter 5 which was developed after the work reported in this chapter. Further experimental investigation is required to fully understand the dynamics.

7.4.1 Population difference measurement

To fully explore the dynamical regime of the two-mode model, it is necessary to observe the population difference n between the two wells. This is also essential to precisely identify the initial state of the system. The intrinsic difficulty of

measuring the population difference when there is tight 2D confinement of the atoms arise because the atoms expand quickly during the timescale of less than 1 ms along the direction of the double-well. As such, it is not easy to count the number of atoms separately. The small distance between the two wells is comparable to the imaging resolution, so that *in situ* measurement of individual wells is also difficult. A promising method for population counting is the well-selective horizontal momentum kick, which can be implemented by an additional RF field in the z direction. Alternatively, a non-destructive dispersive measurement in a MRF-dressed potential can be used to continuously monitor the evolution of atom number difference, see Appendix A.

7.4.2 Effect of in-plane phase fluctuations and the BKT transition

The two-mode model was derived with the assumption that the two lowest energy eigenstates are macroscopically occupied. The measurements reported in this chapter used a low temperature of 20 nK (deep in the superfluid regime), but it is possible to work at higher temperature while keeping the validity of the two-mode approximation in the z direction (as well as satisfying the quasi-2D condition for each double-well minima). The observation of clear phase oscillation serves as a further confirmation of the coherence in 2D Bose gases, in a similar manner to [144]. In bilayer 2D Bose gas, strong tunnel coupling modifies the phase diagram, and may exhibit novel phases [75, 77]. We have observed strong density dips and vortices in coupled 2D Bose gases, as shown in Fig. 7.10. The density fluctuations after the TOF are associated with the spatial fluctuation in symmetric phases [73], and provides alternative observable to understand the Josephson dynamics of phase-fluctuating 2D gases. The presence of vortices in coupled bilayer 2D gases and their interaction along the z direction is of theoretical interest [77].

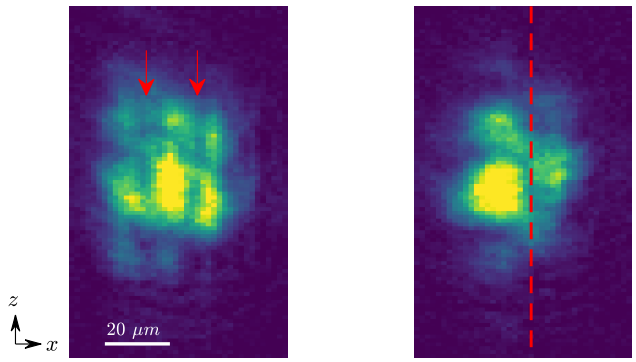

Figure 7.10: Matter-wave interference patterns of coupled 2D gases showing density dips and vortices. The images were taken with double-well separation of $d = 1.5\,\mu\text{m}$, where the two clouds are considered to be coupled. The left panel shows the image with sharp density dips in the x direction (indicated by red arrows), and the right panel shows an image with vortex (red dashed line). Both images were taken with the density slicing method.

8

Conclusion and outlook

Contents

8.1 Conclusion

This thesis describes experimental work to probe the properties of 2D Bose gases in and out of equilibrium. Using the MRF-dressed potential, we create a highly controllable double-well potential for 2D systems, and observe the matter-wave interference. An essential technical aspect is the density slicing method, which allows the direct computation of the phase correlation function. Using this technique, the BKT transition was observed in equilibrium 2D Bose gases. The critical point was identified by the sudden change in the functional form of the correlation function, and we obtained the critical exponent $\eta_c = 0.17(3)$ in a harmonically-trapped, finite-size system. Our experimental technique allows the observation of a wide range of

properties in 2D Bose gases across the critical point, such as local vortex density, density-noise correlation, full counting statistics and the local algebraic exponent.

Based on the detailed understanding of the equilibrium system from extensive experimental measurements, we investigated a non-equilibrium 2D system quenched across the BKT critical point. The quench was performed by coherently splitting a single 2D cloud into two daughter clouds, which suddenly brings the system from superfluid to thermal phase. The subsequent relaxation exhibits two-step dynamics involving the phonon excitations and vortex nucleation. The analysis of phonon excitation dynamics using the algebraic exponent η suggests that the finite energy associated with the nucleation of vortices slowed down the dynamics. We further compared the observed dynamics with the real-time RG theory.

2D gases in a MRF-dressed double-well potential can be trapped with a narrow spatial separation $d \sim 1\,\mu\mathrm{m}$, where quantum tunneling between the two systems are expected. We have achieved this by making a double-well potential with a small frequency separation of the dressing RFs. The high controllability of the MRF-dressed potential allows us to prepare two 2D Bose gases with an arbitrary phase difference, with which a phase oscillation can be initiated by the recoupling quench. The observed phase oscillation dynamics is consistent with that of a Bose gas in a tunnel-coupled double-well, however further extensive measurements are required to fully understand the behaviour.

The major improvements made to the experimental apparatus over the course of the work reported in this thesis allowed stable operation of the tens of thousands of sequences over the duration of weeks, without additional recalibrations. The fluctuations of the RF field amplitudes were kept to the 0.1 % level, which was crucial to gather very large data sets and hence observe effects that would otherwise by obscured by statistical uncertainty. The stability and the reliability of the experiment is illustrated by the fact that the majority of the final data presented in this thesis was taken while the experiment was operated remotely from Tokyo for three months; with only brief twice-a-week *in situ* adjustments of lasers during that period.

8.2 Future experiments

The experimental and theoretical tools that have been developed during the work for this thesis can be used for a variety of exciting future investigations. I conclude this chapter by listing a few of these prospects.

8.2.1 Short-range physics

Currently, the sensitivity of the imaging limits our investigations to the superfluid and crossover regime (and hence cannot access deep in thermal regime). The detection capability of the imaging system sets the lowest density of the cloud that can be imaged with sufficiently high signal-to-noise ratio, and with the density slicing technique we only image a fraction of the total cloud so the observation of interference patterns require a certain threshold 2D density. By improving the detection capability such as with the improvement of imaging system, we could extend the temperature range that can be probed, e.g. to include the vortex-dominated phase. This may enable observation of the 'superfluid jump' [23] by the divergence of η. The improved detection method would also allow for more detailed investigation of short-range physics such as vortex pair correlations in a non-equilibrium system, and would allow us to further map the phase diagram of 2D Bose gases.

8.2.2 Coupled bilayer XY model

The pair of 2D gases in a MRF-dressed potential can be coupled via quantum tunneling. The tunneling induces not only the dynamical effect as presented in Chapter 7; in equilibrium, the phase-locking effect [75, 77] can complete with the thermal fluctuations leading to a novel phase transition which lies in a *mixed universality class* [77]. The investigation of such a system requires an alternative observable such as the symmetric phase mode and direct vortex imaging, which is possible with existing experimental capabilities and theoretical tools described in this thesis.

8.2.3 Controlled tunneling and driven 2D Josephson junction

The MRF-dressed double-well potential allows individual control of each well on a microsecond timescale by the modulation of RF amplitudes. This makes it an unique platform to investigate dynamical control of Josephson dynamics which can be applied to realise a quantum simulation of light-induced superconductivity, as proposed theoretically in Ref. [142].

8.2.4 Arbitrary potentials

The DMD installed in this work for the selective imaging can also be used to shape the laser light to form an arbitrary dipole potential on the atoms (using light that is far detuned from the atomic resonance). The combination of MRF-dressed potential and arbitrary optical potential allows a wide range of investigations. An example is the uniform potential, which can be created by placing a repulsive ring-shaped potential centred on the cloud in the dressed potential. An uniform system allows precise comparison with theory, and a wide variety of novel dynamical phenomena can be probed without being affected by the collective excitations intrinsic in the harmonic trap, such as monopole and dipole mode.

8.2.5 Many-body localization

Most physical systems reach thermal equilibrium over time, losing their memory of the initial state. It generally requires inherent symmetry of the Hamiltonian or lack of interaction to avoid, or slow down, the thermalisation process. One intriguing exception is systems subject to strong disorder, which retain local memory even in the presence of interaction. The phenomenon is known as many-body localization (MBL) and is the subject of active research [151–154]

Using the 2D double-well potential and an additional optical disorder potential, we can study the MBL phase with our novel initial state preparation method and detection scheme, namely the coherently split two-dimensional (2D) quantum gas subject to disorder, probed using matter-wave interferometry. This method

will allow the detailed observation of MBL phases in a continuous 2D system as predicted theoretically [155]. The matter-wave interferometry method allows detailed study of how the system retains its initial memory, such as through higher-order correlations [30, 38]. The competition of quasi-order and the localisation is also of great interest [155].

So far, detailed experimental studies of disordered quantum gases in 2D have been difficult because the low percolation threshold results in classical trapping even at low temperatures. Recently, in 2020, it was shown elsewhere that the point-like disorder method is effective to probe Anderson localisation in 2D Bose gases without being affected by classical trapping [115, 156]. This approach can be directly applied to the investigation of MBL in 2D quantum gases thus providing an excellent opportunity for future investigation.

Appendices

A

Non-destructive imaging and conditional spin squeezing in MRF-dressed potentials

Contents

Here, we describe theoretical and preliminary experimental work towards the realisation of non-destructive measurement of atoms in the MRF-dressed double-well potential, as well as the realisation of conditional spin squeezing. In principle, this approach can detect the atoms in each of the well independent of the spatial separation of the wells and thus this method is not limited by the resolution of any optical system, i.e. it is not diffraction limited. Utilising the complex dynamics of internal states of atoms in the MRF-dressed potential, we show that the dispersive monitoring of the spin constitutes non-destructive imaging of the spatial atomic distribution in the MRF-dressed trap. We show preliminary experimental results for this imaging technique, and propose a method using it to produce conditionally number-squeezed states in a two-mode BEC. We note

that the dispersive measurement of single-RF dressed atomic vapour was recently reported elsewhere [157].

A.1 Position-dependent spin dynamics

We consider an atom in a hyperfine state $\boldsymbol{F}$, trapped in a MRF-dressed potential. The RF fields are linearly polarised AC magnetic fields with n different angular frequencies ω_j and amplitudes B_j. The Hamiltonian describing the dynamics of atoms is

$$\hat{H}_0 = \omega_0(z)\hat{F}_z + \frac{g_F\mu_B}{\hbar}\sum_{j=0}^{n}\hat{\boldsymbol{F}}\cdot\boldsymbol{e_x}B_j\sin(\omega_j t), \tag{A.1.1}$$

where ω_0 is the angular Larmor frequency at position z. In the quadrupole magnetic field $\boldsymbol{B}(r) = b(x\boldsymbol{e_x} + y\boldsymbol{e_y} - 2z\boldsymbol{e_z})$; limiting the region of interest to $x = y = 0$ and $z < 0$ as in the experiment, the Larmor frequency can be expressed as

$$\omega_0(z) = 2g_F\mu_B bz/\hbar. \tag{A.1.2}$$

The first term of Eq (A.1.1) makes the dynamics of spins position-dependent, with resonances where $\delta_j(z) = \omega_j - \omega_0(z) = 0$. Figure A.1 shows numerically calculated, spatially-dependent spectral power of time evolution of $\langle F_x(t)\rangle$. The dressing RF frequencies are $2\pi\times$(3.57, 3.6, 3.63) MHz and $b = 150$ G/cm, resulting in the separation of the wells $d = 1.2\,\mu$m.

A.2 Dispersive measurement of spin dynamics

The position-dependent dynamics of spins shown in Fig. A.1 can be probed by coupling the atomic spin to the polarisation modes of coherent light. Such coupling is induced by circular or linear birefringence of the atomic medium [157–159], Faraday or Voigt effect. We propose to probe the spin dynamics in a MRF-dressed potential with Voigt effect, using far detuned light. In particular, this approach determines the spatial distribution of the atoms in a double-well potential by the spectrum of the signal. In Fig. A.2, we show the schematics of experimental setup. A linearly polarised laser beam propagates along the direction of a static

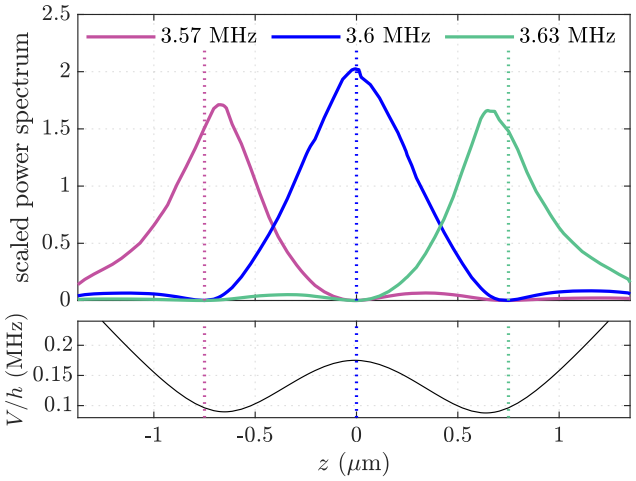

Figure A.1: (Top) Numerically calculated posititon-dependent power spectrum of single-spin dynamics $\langle F_z(t)\rangle$. The dressing RFs are at frequencies (3.57, 3.6, 3.63) MHz with field amplitudes (0.57, 0.71, 0.57) Gauss. The resonance condition for each frequency component $\delta_j(z) = 0$ are indicated by vertical dotted lines. (Bottom) The MRF-dressed double-well potential.

magnetic field z, and detect the time-varying, polarisation-dependent phase shift using polarimetry consisting of Wollaston prism and a balanced photodetector. The probe beam is initially linearly polarised, and we monitor the time evolution of power difference in circular polarisations; see below.

To describe the atom-light interaction, we now introduce the polarisability Hamiltonian which describes the coupling of single spin and the polarisation of optical modes. A comprehensive review of this topic can be found in Ref. [160].

In the following, we use Stokes operators to describe the photon flux of different polarisations of light propagating along z:

$$\begin{aligned}
\hat{S}_0 &= \frac{1}{2}\left(\hat{a}_+^\dagger \hat{a}_+ + \hat{a}_-^\dagger \hat{a}_-\right), \\
\hat{S}_x &= \frac{1}{2}\left(\hat{a}_+^\dagger \hat{a}_- + \hat{a}_-^\dagger \hat{a}_+\right) = \frac{1}{2}\left(\hat{a}_x^\dagger \hat{a}_x - \hat{a}_y^\dagger \hat{a}_y\right), \\
\hat{S}_y &= \frac{i}{2}\left(\hat{a}_-^\dagger \hat{a}_+ - \hat{a}_+^\dagger \hat{a}_-\right) = \frac{1}{2}\left(\hat{a}_{+45}^\dagger \hat{a}_{+45} - \hat{a}_{-45}^\dagger \hat{a}_{-45}\right), \\
\hat{S}_z &= \frac{1}{2}\left(\hat{a}_+^\dagger \hat{a}_+ - \hat{a}_-^\dagger \hat{a}_-\right),
\end{aligned} \tag{A.2.1}$$

where $\hat{a}_\pm^\dagger(\hat{a}_\pm)$ are the creation (annihilation) operators for the right and left circular polarisations, $\hat{a}_{\pm 45}^\dagger(\hat{a}_{\pm 45})$ is with the linear polarisation in $\pm$ 45 degrees between x and y axes and $\hat{a}_{x,y}^\dagger(\hat{a}_{x,y})$ along x and y axes.

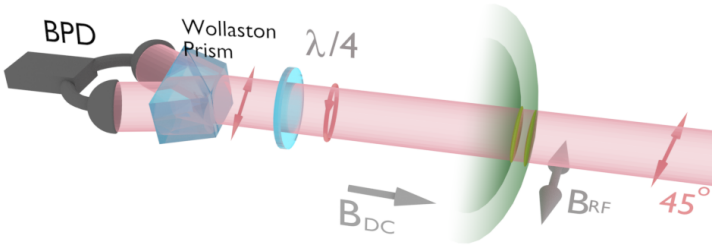

Figure A.2: Experimental setup for the dispersive detection of MRF-dressed atoms. Atoms are trapped at the bottom of double-well 'shell' traps (green transparent half-spheroids). We probe the distribution of atoms in the double-well by a polarised laser beam frequency-locked far from resonance (red semi-transparent beam, propagating from right to left). The time-dependent scattering of light into a different polarisation mode in the atomic medium results in the modulation of the polarisation, which we monitor with a polarimeter consisting of a quarter-waveplate ($\lambda/4$), a Wollaston prism and a balanced photodetector (BPD). The direction of gravity is the same direction as B_{DC} shown in the figure.

For the interaction of atoms with an off-resonant light field at angular frequency ω_L, the dipole Hamiltonian can be approximated into the polarisability form [160], which can be decomposed into irreducible spherical tensor components $\boldsymbol{\alpha}$ [160, 161]:

$$\begin{aligned}\hat{H}_{\mathrm{int}} &= \sum_{k=0,1,2} \hat{\boldsymbol{E}}^{(-)} \frac{\hat{\boldsymbol{\alpha}}^{(k)}}{\hbar\Delta} \hat{\boldsymbol{E}}^{(+)} \\ &= g\frac{2\alpha^{(0)}}{3\Delta}\hat{S}_0\hat{\mathbb{1}} + g\frac{\alpha^{(1)}}{\Delta}\hat{S}_z\hat{F}_z \\ &+ g\frac{\alpha^{(2)}}{\Delta}\left\{\hat{S}_x(\hat{F}_x^2-\hat{F}_y^2) + \hat{S}_y(\hat{F}_x\hat{F}_y+\hat{F}_y\hat{F}_x) + \hat{S}_0\left[3\hat{F}_z^2 - f(f+1)\hat{\mathbb{1}}\right]/3\right\},\end{aligned} \tag{A.2.2}$$

where $g = \omega_L/(2\varepsilon_0 N_{\mathrm{a}})$, ε_0 is the vacuum permittivity, Δ is the detuning of the probe light from atomic transition and $\mathbb{1}$ is the identity operator in the atomic subspace; $\alpha^{(k)} \in \mathbb{R}$ with $k = 0, 1, 2$ for the scalar, vector and tensor polarisabilities.

Using the Eq. (A.2.2) and Eq. (A.1.1), we can study the time evolution of coupled atom-light system. Assuming small values of $\alpha^{(k)}$ (corresponding to large frequency detuning of the laser) such that the dynamics of atomic spin is unaffected by the interaction, we can first obtain the time evolution of atomic spins $\hat{F}$, from which we obtain the equation of motion for the Stokes operators. Using the

initial probe light polarisation of $\hat{S}_y$, we find the Stokes operators $\hat{S}_j(t)$ after time evolution under Eq. (A.2.2) are [157]

$$\hat{S}_x(t) = \frac{2g^2\alpha^{(1)}}{c\hbar^2}\hat{S}_y \sum_i \hat{F}_{z,i}(t) \tag{A.2.3}$$

$$\hat{S}_y(t) = \hat{S}_y, \tag{A.2.4}$$

$$\hat{S}_z(t) = \frac{2g^2\alpha^{(2)}}{c\hbar^2}\hat{S}_y \sum_i \left(\hat{F}^2_{x,i}(t) - \hat{F}^2_{y,i}(t)\right), \tag{A.2.5}$$

where the interaction time is assumed to be short enough such that the change in the input polarisation $\hat{S}_y$ is negligible. The sum over indices i in Eq. (A.2.3) and Eq. (A.2.5) are performed over all atoms in the trap. From Eq. (A.2.5) and the definition of $\hat{S}_z$ in Eq. (A.2.1), we see that the differential measurement of photon flux in right- and left-handed circular polarisation gives the measure of $\sum_i \left(\hat{F}^2_{x,i}(t) - \hat{F}^2_{y,i}(t)\right)$. Equivalently, the measurement of linear polarisation components gives the measure of $\sum_i \hat{F}_{z,i}$.

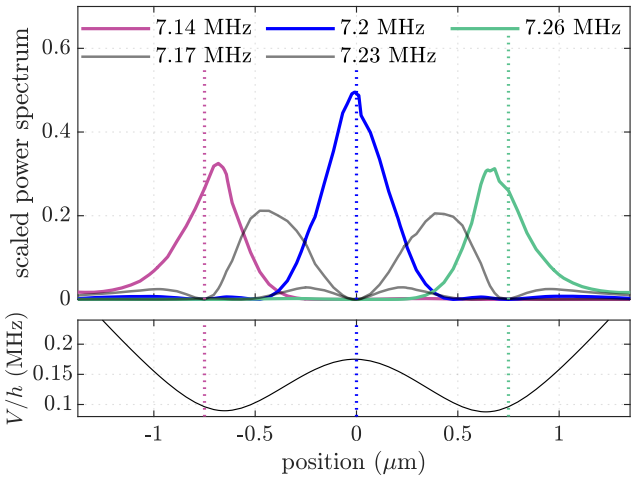

Figure A.3: (Top) Position-dependent power spectrum of single-spin dynamics $\langle \hat{F}^2_x(t) - \hat{F}^2_y(t)\rangle$, with dressing RF frequencies $2\pi\times$(3.57, 3.6, 3.63) MHz and amplitudes (0.57, 0.71, 0.57) Gauss. (Bottom) the potential energy of dressed eigenstates we consider for the calculation shown in the top figure.

To predict the measurement, in Fig. A.3 we show the numerically calculated power spectrum of the single-spin dynamics $\langle \hat{F}^2_x(t) - \hat{F}^2_y(t)\rangle$ under Eq. (A.1.1). We observe clear resonance structure in a similar manner to Fig. A.1, but the signal is at twice the frequency of the dressing RF. From this result and Eq. (A.2.5), we find that

the measurement of $\hat{S}_z$ through the polarimeter at twice the dressing RF frequency constitutes measurement of atoms at the RF resonance positions (equivalently, to within a small offset, at the positions of each well). The position selectivity of this process allows the *in situ* determination of population difference in a double-well potential, independent of spatial separation of the wells. This is a significant advantage over the optical imaging method, which is fundamentally limited by the diffraction limit of the imaging setup which is on the order of micrometres and usually worse due to imperfections of the experiments and refraction of probe light in the dense atomic medium.

A.2.1 Backaction of the measurement

In quantum mechanics the measurement process affects the atomic dynamics. If engineered correctly, backaction can be utilised to produce a correlated state of atoms, such as spin squeezed states [162, 163]. However, in most cases, the backaction results in dephasing of the atomic dynamics and the reduction of signals.

In this section, we describe one of the possible dephasing mechanisms caused by the measurement process. For illustration purpose, we use the term proportional to $\alpha^{(1)}$ in Eq. (A.2.2) as the interaction Hamiltonian $\hat{H}_{\rm int}$. The initial state of the atomic spin in Schrödinger picture is $|\psi_a\rangle_0 = |F, m\rangle$, and the system of light can is described by the product of coherent states in x and y polarised modes, $|\psi_L\rangle_0 = |\beta_x\rangle \otimes |\beta_y\rangle$. Since the flux of photons that passes through the cloud in a small timestep dt, the atom-light interaction at a given time occurs only for a small fraction of the light beam. As such, we expand the coherent states $|\beta\rangle$ in a Fock basis [164, 165],

$$|\psi_L\rangle \simeq |0_x\rangle|0_y\rangle + \beta_x|1_x\rangle|0_y\rangle + \beta_y|0_x\rangle|1_y\rangle. \tag{A.2.6}$$

Furthermore, we expand the propagator to the second-order of the duration of interaction a photon, dt.

$$U = \exp\left(-\frac{i\hat{H}_{\rm int}dt}{\hbar}\right) \simeq 1 - \frac{i\hat{H}_{\rm int}dt}{\hbar} - \frac{\hat{H}^2_{\rm int}dt^2}{2\hbar^2}. \tag{A.2.7}$$

From above results, we can explicitly compute the propagator for atoms $U|\psi_L\rangle$,

$$U|\psi_L\rangle \simeq |\psi_L\rangle + \gamma\hat{F}_z(\beta_x|0_x\rangle|1_y\rangle + \beta_y|1_x\rangle|0_y\rangle) + \gamma^2\hat{F}_z^2\left(\beta_x|1_x\rangle|0_y\rangle + \beta_y|0_x\rangle|1_y\rangle\right), \tag{A.2.8}$$

where $\gamma = g\alpha^{(1)}/(\hbar\Delta)$.

In the following, we express the time evolution of atomic states using density matrix for atomic states $\rho_a = |\psi_a\rangle\langle\psi_a| = |m\rangle\langle m|$ and light fields $\rho_L = |\psi_L\rangle\langle\psi_L|$. The atomic state after the interaction can be calculated by applying propagator U to atom-light state $\rho_a \otimes \rho_L$ and taking the partial trace over the probe field Tr_L:

$$\rho_a(t+dt) = \mathrm{Tr}_L\left[U\rho_a \otimes \rho_L U^\dagger\right] = \sum_{n,m}\langle n_x|\langle m_y|U\rho_a U^\dagger|n_x\rangle|m_y\rangle \tag{A.2.9}$$

$$= \rho_a + \gamma^2(\beta_x^2+\beta_y^2)\left(\rho_a\hat{F}_z\rho_a - \{\hat{F}_z^2,\rho_a\}\right) \tag{A.2.10}$$

$$= \rho_a + \gamma^2 S\left(\rho_a\hat{F}_z\rho_a - \{\hat{F}_z^2,\rho_a\}\right)dt, \tag{A.2.11}$$

where we defined the total photon flux $S = (\beta_x^2+\beta_y^2)/dt$ in Eq (A.2.11).

We add the unitary evolution under Eq (A.1.1) to obtain the Lindblad master equation [166]

$$\rho_a(t+dt) = \rho_a - i[\hat{H}_0,\rho_a]dt + \gamma^2 S\left(\rho_a\hat{F}_z\rho_a - \{\hat{F}_z^2,\rho_a\}\right)dt, \tag{A.2.12}$$

We note that this is the ensemble-averaged result over realisations of measurement results at the polarimeter, and numerical simulation of individual trajectory is possible with the stochastic version of the master equation [166].

In Fig. A.4, we show the power spectrum of spin dynamics $\langle F_z(z)\rangle$, numerically calculated using Eq (A.2.12). The backaction causes the dephasing of the spin dynamics and thus can contribute to a finite decay of the signal. This can be evaded by directly applying the stroboscopic measurement technique in Ref. [159].

A.3 Preliminary experimental results

In this section, we present preliminary experimental results demonstrating the non-destructive Voigt measurement method. We prepared 3×10^6 thermal ^{87}Rb atoms in a three-RF dressed potentials, and probed the system using a linearly polarised light

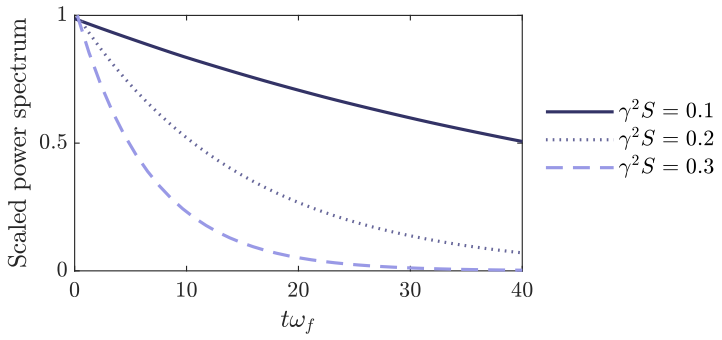

Figure A.4: Time evolution of the power spectum of $\langle F_z(z)\rangle$ at the RF resonance frequency, which linearly affect the non-destructive measurement signal strength. The time evolution was numerically calculated using the master equation Eq. (A.2.12) and plotted against the number of periods of the RF.

detuned from the atomic transition. The RF frequency components were (3.47, 3.6, 3.63) MHz with amplitudes (0.42, 1.81, 0.42) Gauss. This forms a three-RF single-well potential, resulting in atoms localising around the 3.6 MHz magnetic resonance. The probe beam was sent in the direction of static magnetic field, 246 MHz blue detuned from $F = 1 \rightarrow F' = 2$ transition. From the discussion above, we expect to observe the effect from the $\alpha^{(2)}$ term, which measures $\sum_i \left(\hat{F}^2_{x,i}(t) - \hat{F}^2_{y,i}(t)\right)$. We plot the recorded signal in Fig. A.5 left panels.

We further analyse the signal using spectrogram, as shown in Fig. A.5 right. As expected from Fig. A.3 and our choice of dressing frequencies, we observe the signal at 7.17, 7.2 and 7.23 MHz. Since the atoms are localised around the 3.6 MHz magnetic resonance, we did not observe strong peaks at 7.14 and 7.26 MHz.

We observe rapid decay of signals once the probe beam is applied; We found that a significant fraction of atoms is repumped into $F = 2$ state during the measurement process. In a future experiment, much larger detuning from the atomic transition is desired.

A.4 Conclusion and outlook

We have presented theoretical and experimental results towards the non-destructive measurement of atomic distribution in a MRF-dressed potential. The experimental

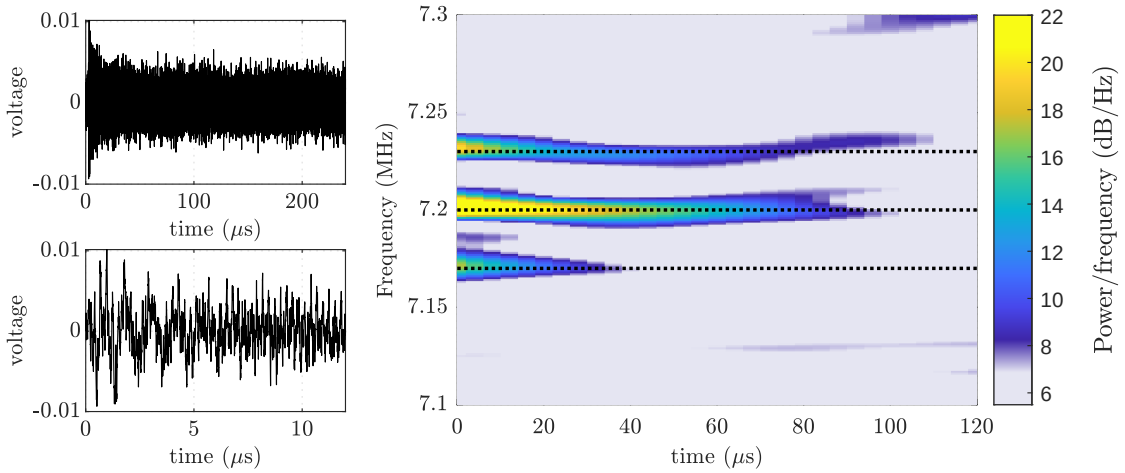

Figure A.5: (Top, left) The balanced photodetector output signal with probe beam coupled to thermal atoms in MRF-dressed potential. The bottom panel shows the first 10 µs. Dressing RF combinations were (3.47, 3.6, 3.63) MHz and amplitudes (0.42, 1.81, 0.42) Gauss. (Right) Spectrogram of the signal plotted on the left. Clear peaks at 7.17, 7.2 and 7.23 MHz (indicated by black dotted lines) are observed.

result suggests the validity of the measurement setup, however significant improvements are required to utilise this method for the non-destructive measurement of BEC trapped in double-well potentials.

A.4.1 Spin squeezing in a double-well potential

The theoretical results in our recent preprint Ref. [143] show that the continuous non-destructive measurement of the spatial two-mode BECs result in quantum correlated states, such as spin squeezed state and macroscopic cat state. The experimental technique presented in this Appendix is a way of directly implementing the scheme described in Ref. [143].

Bibliography

[1] T. W. B. Kibble, "Topology of cosmic domains and strings", J. Phys. A: Math. Gen. **9**, 1387–1398 (1976) 10.1088/0305-4470/9/8/029.

[2] J. Beugnon and N. Navon, "Exploring the kibble–zurek mechanism with homogeneous bose gases", J. Phys. B: At. Mol. Opt. Phys. **50**, 022002 (2017) 10.1088/1361-6455/50/2/022002.

[3] J. Berges, A. Rothkopf, and J. Schmidt, "Nonthermal fixed points: effective weak coupling for strongly correlated systems far from equilibrium", Phys. Rev. Lett. **101**, 041603 (2008) 10.1103/PhysRevLett.101.041603.

[4] N. D. Mermin and H. Wagner, "Absence of ferromagnetism or antiferromagnetism in one- or two-dimensional isotropic heisenberg models", Phys. Rev. Lett. **17**, 1307–1307 (1966) 10.1103/PhysRevLett.17.1307.

[5] P. C. Hohenberg, "Existence of long-range order in one and two dimensions", Phys. Rev. **158**, 383–386 (1967) 10.1103/PhysRev.158.383.

[6] V. Berezinskiĭ, "Destruction of Long-range Order in One-dimensional and Two-dimensional Systems Possessing a Continuous Symmetry Group. II. Quantum Systems", Sov. J. Exp. Theor. Phys. **34**, 610 (1972).

[7] J. M. Kosterlitz and D. J. Thouless, "Ordering, metastability and phase transitions in two-dimensional systems", J. Phys. C Solid State Phys. **6**, 1181–1203 (1973) 10.1088/0022-3719/6/7/010.

[8] C. Gross and I. Bloch, "Quantum simulations with ultracold atoms in optical lattices", Science **357**, 995–1001 (2017) 10.1126/science.aal3837.

[9] F. Schäfer, T. Fukuhara, S. Sugawa, Y. Takasu, and Y. Takahashi, "Tools for quantum simulation with ultracold atoms in optical lattices", Nat. Phys. **2**, 411–425 (2020) 10.1038/s42254-020-0195-3.

[10] M. Prüfer, P. Kunkel, H. Strobel, S. Lannig, D. Linnemann, C.-M. Schmied, J. Berges, T. Gasenzer, and M. K. Oberthaler, "Observation of universal dynamics in a spinor Bose gas far from equilibrium", Nat. 2018 5637730 **563**, 217–220 (2018) 10.1038/s41586-018-0659-0.

[11] J. A. Glidden, C. Eigen, L. H. Dogra, T. A. Hilker, R. P. Smith, and Z. Hadzibabic, "Bidirectional dynamic scaling in an isolated Bose gas far from equilibrium", Nat. Phys. **17**, 457–461 (2021) 10.1038/s41567-020-01114-x.

[12] S. Erne, R. Buecker, T. Gasenzer, J. Berges, and J. Schmiedmayer, "Observation of universal dynamics in an isolated one-dimensional Bose gas far from equilibrium", Nature, 10.1038/s41586-018-0659-0 (2018) 10.1038/s41586-018-0659-0.

[13] L. Chomaz, L. Corman, T. Bienaimé, R. Desbuquois, C. Weitenberg, S. Nascimbène, J. Beugnon, and J. Dalibard, "Emergence of coherence via transverse condensation in a uniform quasi-two-dimensional Bose gas", Nature Communications **6**, 10.1038/ncomms7162 (2015) 10.1038/ncomms7162.

[14] Z. Hadzibabic, P. Krüger, M. Cheneau, B. Battelier, and J. Dalibard, "Berezinskii-Kosterlitz-Thouless crossover in a trapped atomic gas", Nature **441**, 1118–1121 (2006) 10.1038/nature04851.

[15] A. Görlitz, J. M. Vogels, A. E. Leanhardt, C. Raman, et al., "Realization of bose-einstein condensates in lower dimensions", Phys. Rev. Lett. **87**, 130402 (2001) 10.1103/PhysRevLett.87.130402.

[16] D. S. Petrov, M. Holzmann, and G. V. Shlyapnikov, "Bose-einstein condensation in quasi-2d trapped gases", Phys. Rev. Lett. **84**, 2551–2555 (2000) 10.1103/PhysRevLett.84.2551.

[17] N. Prokof'ev, O. Ruebenacker, and B. Svistunov, "Critical point of a weakly interacting two-dimensional bose gas", Phys. Rev. Lett. **87**, 270402 (2001) 10.1103/PhysRevLett.87.270402.

[18] N. Prokof'ev and B. Svistunov, "Two-dimensional weakly interacting Bose gas in the fluctuation region", Physical Review A - Atomic, Molecular, and Optical Physics **66**, 7 (2002) 10.1103/PhysRevA.66.043608.

[19] M. H. Anderson, J. R. Ensher, M. R. Matthews, C. E. Wieman, and E. A. Cornell, "Observation of Bose-Einstein Condensation in a Dilute Atomic Vapor", Science **269**, 198–201 (1995) 10.1126/science.269.5221.198.

[20] K. B. Davis, M. .-. Mewes, M. R. Andrews, N. J. van Druten, D. S. Durfee, D. M. Kurn, and W. Ketterle, "Bose-einstein condensation in a gas of sodium atoms", Phys. Rev. Lett. **75**, 3969–3973 (1995) 10.1103/PhysRevLett.75.3969.

[21] C. D. Rossi, R. Dubessy, K. Merloti, M. de Goër de Herve, T. Badr, A. Perrin, L. Longchambon, and H. Perrin, "The scissors oscillation of a quasi two-dimensional bose gas as a local signature of superfluidity", Journal of Physics: Conference Series **793**, 012023 (2017) 10.1088/1742-6596/793/1/012023.

[22] R. Desbuquois, L. Chomaz, T. Yefsah, J. Léonard, J. Beugnon, C. Weitenberg, and J. Dalibard, "Superfluid behaviour of a two-dimensional Bose gas", Nat. Phys. **8**, 645–648 (2012) 10.1038/nphys2378.

[23] P. Christodoulou, M. Gałka, N. Dogra, R. Lopes, J. Schmitt, and Z. Hadzibabic, "Observation of first and second sound in a BKT superfluid", Nat. 2021 5947862 **594**, 191–194 (2021) 10.1038/s41586-021-03537-9.

[24] R. J. Fletcher, M. Robert-de-Saint-Vincent, J. Man, N. Navon, R. P. Smith, K. G. H. Viebahn, and Z. Hadzibabic, "Connecting berezinskii-kosterlitz-thouless and bec phase transitions by tuning interactions in a trapped gas", Phys. Rev. Lett. **114**, 255302 (2015) 10.1103/PhysRevLett.114.255302.

[25] P. A. Murthy, I. Boettcher, L. Bayha, M. Holzmann, D. Kedar, M. Neidig, M. G. Ries, A. N. Wenz, G. Zürn, and S. Jochim, "Observation of the berezinskii-kosterlitz-thouless phase transition in an ultracold fermi gas", Phys. Rev. Lett. **115**, 010401 (2015) 10.1103/PhysRevLett.115.010401.

[26] I. Boettcher and M. Holzmann, "Quasi-long-range order in trapped two-dimensional bose gases", Phys. Rev. A **94**, 011602 (2016) 10.1103/PhysRevA.94.011602.

[27] M. R. Andrews, C. G. Townsend, H.-J. Miesner, D. S. Durfee, D. M. Kurn, and W. Ketterle, "Observation of interference between two bose condensates", Science **275**, 637–641 (1997) 10.1126/science.275.5300.637.

[28] L. Badurina, E. Bentine, D. Blas, K. Bongs, et al., "AION: an atom interferometer observatory and network", Journal of Cosmology and Astroparticle Physics **2020**, 011–011 (2020) 10.1088/1475-7516/2020/05/011.

[29] J. Coleman, *Magis-100 at fermilab*, 2018, arXiv:1812.00482 [physics.ins-det].

[30] T. Langen, S. Erne, R. Geiger, B. Rauer, T. Schweigler, M. Kuhnert, W. Rohringer, I. E. Mazets, T. Gasenzer, and J. Schmiedmayer, "Experimental observation of a generalized Gibbs ensemble", Science **348**, 207–211 (2015) 10.1126/science.1257026.

[31] M. Gring, M. Kuhnert, T. Langen, T. Kitagawa, B. Rauer, M. Schreitl, I. Mazets, D. A. Smith, E. Demler, and J. Schmiedmayer, "Relaxation and prethermalization in an isolated quantum system", Science **337**, 1318–1322 (2012) 10.1126/science.1224953.

[32] T. Langen, R. Geiger, M. Kuhnert, B. Rauer, and J. Schmiedmayer, "Local emergence of thermal correlations in an isolated quantum many-body system", Nature Physics **9**, 640–643 (2013) 10.1038/nphys2739.

[33] S. Hofferberth, I. Lesanovsky, B. Fischer, T. Schumm, and J. Schmiedmayer, "Non-equilibrium coherence dynamics in one-dimensional Bose gases", Nature **449**, 324–327 (2007) 10.1038/nature06149.

[34] S. Sunami, V. P. Singh, D. Garrick, A. Beregi, A. J. Barker, K. Luksch, E. Bentine, L. Mathey, and C. J. Foot, "Observation of the bkt transition in a 2d bose gas via matter-wave interferometry", (2021), arXiv:2108.08840 [cond-mat.quant-gas].

[35] P. Kunkel, M. Prüfer, S. Lannig, R. Rosa-Medina, A. Bonnin, M. Gärttner, H. Strobel, and M. K. Oberthaler, "Simultaneous readout of noncommuting collective spin observables beyond the standard quantum limit", Phys. Rev. Lett. **123**, 063603 (2019) 10.1103/PhysRevLett.123.063603.

[36] M. Prüfer, T. V. Zache, P. Kunkel, S. Lannig, A. Bonnin, H. Strobel, J. Berges, and M. K. Oberthaler, "Experimental extraction of the quantum effective action for a non-equilibrium many-body system", Nat. Phys. 2020 1610 **16**, 1012–1016 (2020) 10.1038/s41567-020-0933-6.

[37] T. Kinoshita, T. Wenger, and D. S. Weiss, "A quantum Newton's cradle", Nature **440**, 900–903 (2006) 10.1038/nature04693.

[38] T. Schweigler, V. Kasper, S. Erne, I. Mazets, B. Rauer, F. Cataldini, T. Langen, T. Gasenzer, J. Berges, and J. Schmiedmayer, "Experimental characterization of a quantum many-body system via higher-order correlations", Nature **545**, 323–326 (2017) 10.1038/nature22310.

[39] B. Damski and W. H. Zurek, "How to fix a broken symmetry: quantum dynamics of symmetry restoration in a ferromagnetic bose–einstein condensate", **10**, 045023 (2008) 10.1088/1367-2630/10/4/045023.

[40] N. Navon, A. L. Gaunt, R. P. Smith, and Z. Hadzibabic, "Critical dynamics of spontaneous symmetry breaking in a homogeneous bose gas", Science **347**, 167–170 (2015) 10.1126/science.1258676.

[41] C. Eigen, J. A. P. Glidden, R. Lopes, N. Navon, Z. Hadzibabic, and R. P. Smith, "Universal scaling laws in the dynamics of a homogeneous unitary bose gas", Phys. Rev. Lett. **119**, 250404 (2017) 10.1103/PhysRevLett.119.250404.

[42] W. H. Zurek, "Cosmological experiments in superfluid helium?", Nature **317**, 505 (1985) 10.1038/317505a0.

[43] W. Cai, J. Han, F. Mei, Y. Xu, et al., "Observation of topological magnon insulator states in a superconducting circuit", Phys. Rev. Lett. **123**, 080501 (2019) 10.1103/PhysRevLett.123.080501.

[44] S. Nakajima, T. Tomita, S. Taie, T. Ichinose, H. Ozawa, L. Wang, M. Troyer, and Y. Takahashi, "Topological Thouless pumping of ultracold fermions", Nature Physics **12**, 296–300 (2016) 10.1038/nphys3622.

[45] L. Mathey and A. Polkovnikov, "Light cone dynamics and reverse Kibble-Zurek mechanism in two-dimensional superfluids following a quantum quench", Phys. Rev. A **81**, 1–13 (2010) 10.1103/PhysRevA.81.033605.

[46] L. Mathey, K. J. Günter, J. Dalibard, and A. Polkovnikov, "Dynamic Kosterlitz-Thouless transition in two-dimensional Bose mixtures of ultracold atoms", Phys. Rev. A **95**, 10.1103/PhysRevA.95.053630 (2017) 10.1103/PhysRevA.95.053630.

[47] A. L. Gaunt, R. J. Fletcher, R. P. Smith, and Z. Hadzibabic, "A superheated Bose-condensed gas", Nature Physics **9**, 271–274 (2013) 10.1038/nphys2587.

[48] R. P. Smith, S. Beattie, S. Moulder, R. L. D. Campbell, and Z. Hadzibabic, "Condensation dynamics in a quantum-quenched bose gas", Phys. Rev. Lett. **109**, 105301 (2012) 10.1103/PhysRevLett.109.105301.

[49] J. V. José, *40 years of Berezinskii-Kosterlitz-Thouless theory* (World Scientific, 2013), pp. 1–351, ISBN: 9789814417648, 10.1142/8572.

[50] J. M. Kosterlitz, "The critical properties of the two-dimensional xy model", Journal of Physics C: Solid State Physics **7**, 1046–1060 (1974) 10.1088/0022-3719/7/6/005.

[51] D. J. Bishop and J. D. Reppy, "Study of the superfluid transition in two-dimensional ^{4}He films", Phys. Rev. Lett. **40**, 1727–1730 (1978) 10.1103/PhysRevLett.40.1727.

[52] H. Weber and P. Minnhagen, "Monte carlo determination of the critical temperature for the two-dimensional xy model", Phys. Rev. B **37**, 5986–5989 (1988) 10.1103/PhysRevB.37.5986.

[53] Y.-D. Hsieh, Y.-J. Kao, and A. W. Sandvik, "Finite-size scaling method for the berezinskii–kosterlitz–thouless transition", **2013**, P09001 (2013) 10.1088/1742-5468/2013/09/p09001.

[54] K. Epstein, A. M. Goldman, and A. M. Kadin, "Vortex-antivortex pair dissociation in two-dimensional superconductors", Phys. Rev. Lett. **47**, 534–537 (1981) 10.1103/PhysRevLett.47.534.

[55] D. J. Resnick, J. C. Garland, J. T. Boyd, S. Shoemaker, and R. S. Newrock, "Kosterlitz-thouless transition in proximity-coupled superconducting arrays", Phys. Rev. Lett. **47**, 1542–1545 (1981) 10.1103/PhysRevLett.47.1542.

[56] D. Caputo, D. Ballarini, G. Dagvadorj, C. S. Muñoz, et al., "Topological order and thermal equilibrium in polariton condensates", Nature Materials **17**, 145–151 (2018) 10.1038/NMAT5039.

[57] M. Holzmann, M. Chevallier, and W. Krauth, "Semiclassical theory of the quasi–two-dimensional trapped Bose gas", Eur. Phys. Lett. **82**, 30001 (2008) 10.1209/0295-5075/82/30001.

[58] Y. Eto, M. Takahashi, M. Kunimi, H. Saito, and T. Hirano, "Nonequilibrium dynamics induced by miscible–immiscible transition in binary bose–einstein condensates", New J. Phys. **18**, 073029 (2016) 10.1088/1367-2630/18/7/073029.

[59] M. Holzmann and W. Krauth, "Kosterlitz-thouless transition of the quasi-two-dimensional trapped bose gas", Phys. Rev. Lett. **100**, 190402 (2008) 10.1103/PhysRevLett.100.190402.

[60] D. R. Nelson and J. M. Kosterlitz, "Universal jump in the superfluid density of two-dimensional superfluids", Phys. Rev. Lett. **39**, 1201–1205 (1977) 10.1103/PhysRevLett.39.1201.

[61] L. P. Pitaevskii and A. Rosch, "Breathing modes and hidden symmetry of trapped atoms in two dimensions", Phys. Rev. A **55**, R853–R856 (1997) 10.1103/PhysRevA.55.R853.

[62] C. L. Hung, X. Zhang, N. Gemelke, and C. Chin, "Observation of scale invariance and universality in two-dimensional Bose gases", Nature **470**, 236–240 (2011) 10.1038/nature09722.

[63] R. Desbuquois, T. Yefsah, L. Chomaz, C. Weitenberg, L. Corman, S. Nascimbène, and J. Dalibard, "Determination of scale-invariant equations of state without fitting parameters: application to the two-dimensional bose gas across the berezinskii-kosterlitz-thouless transition", Phys. Rev. Lett. **113**, 020404 (2014) 10.1103/PhysRevLett.113.020404.

[64] T. Yefsah, R. Desbuquois, L. Chomaz, K. J. Günter, and J. Dalibard, "Exploring the thermodynamics of a two-dimensional bose gas", Phys. Rev. Lett. **107**, 130401 (2011) 10.1103/PhysRevLett.107.130401.

[65] Z. Hadzibabic, P. Krüger, M. Cheneau, S. P. Rath, and J. Dalibard, "The trapped two-dimensional bose gas: from bose–einstein condensation to berezinskii–kosterlitz–thouless physics", New J. Phys. **10**, 045006 (2008) 10.1088/1367-2630/10/4/045006.

[66] P. Cladé, C. Ryu, A. Ramanathan, K. Helmerson, and W. D. Phillips, "Observation of a 2d bose gas: from thermal to quasicondensate to superfluid", Phys. Rev. Lett. **102**, 170401 (2009) 10.1103/PhysRevLett.102.170401.

[67] C. J. Pethick and H. Smith, *Bose–Einstein condensation in dilute gases* (Cambridge University Press, Cambridge, 2008), ISBN: 9780511802850, 10.1017/CBO9780511802850.

[68] M. Holzmann, M. Chevallier, and W. Krauth, "Universal correlations and coherence in quasi-two-dimensional trapped bose gases", Phys. Rev. A **81**, 043622 (2010) 10.1103/PhysRevA.81.043622.

[69] A. Polkovnikov, E. Altman, and E. Demler, "Interference between independent fluctuating condensates", Proceedings of the National Academy of Sciences **103**, 6125–6129 (2006) 10.1073/pnas.0510276103.

[70] J.-y. Choi, S. W. Seo, W. J. Kwon, and Y.-i. Shin, "Probing phase fluctuations in a 2d degenerate bose gas by free expansion", Phys. Rev. Lett. **109**, 125301 (2012) 10.1103/PhysRevLett.109.125301.

[71] V. P. Singh and L. Mathey, "Noise correlations of two-dimensional bose gases", Phys. Rev. A **89**, 053612 (2014) 10.1103/PhysRevA.89.053612.

[72] A. Imambekov, I. E. Mazets, D. S. Petrov, V. Gritsev, S. Manz, S. Hofferberth, T. Schumm, E. Demler, and J. Schmiedmayer, "Density ripples in expanding low-dimensional gases as a probe of correlations", Phys. Rev. A **80**, 033604 (2009) 10.1103/PhysRevA.80.033604.

[73] T. Schweigler, "Correlations and dynamics of tunnel-coupled one-dimensional Bose gases", PhD thesis (Technical University of Wien, 2019).

[74] I. E. Mazets, "Two-dimensional dynamics of expansion of a degenerate bose gas", Phys. Rev. A **86**, 055603 (2012) 10.1103/PhysRevA.86.055603.

[75] L. Mathey, A. Polkovnikov, and A. H. C. Neto, "Phase-locking transition of coupled low-dimensional superfluids", Eur. Phys. Lett. **81**, 10008 (2007) 10.1209/0295-5075/81/10008.

[76] G. Bighin, N. Defenu, I. Nándori, L. Salasnich, and A. Trombettoni, "Berezinskii-kosterlitz-thouless paired phase in coupled XY models", Phys. Rev. Lett. **123**, 100601 (2019) 10.1103/PhysRevLett.123.100601.

[77] F.-F. Song and G.-M. Zhang, "Hybrid Berezinskii-Kosterlitz-Thouless and Ising topological phase transition in the generalized two-dimensional XY model using tensor networks", Phys. Rev. B **103**, 024518 (2021) 10.1103/PhysRevB.103.024518.

[78] M. Pigneur, T. Berrada, M. Bonneau, T. Schumm, E. Demler, and J. Schmiedmayer, "Relaxation to a phase-locked equilibrium state in a one-dimensional bosonic josephson junction", Phys. Rev. Lett. **120**, 173601 (2018) 10.1103/PhysRevLett.120.173601.

[79] D. Stefanatos and E. Paspalakis, "Relaxation dynamics in a stochastic bosonic josephson junction", Physics Letters A **383**, 2370–2375 (2019) https://doi.org/10.1016/j.physleta.2019.04.054.

[80] Y. D. van Nieuwkerk, J. Schmiedmayer, and F. H. Essler, "Josephson oscillations in split one-dimensional Bose gases", SciPost Phys. **10**, 90 (2021) 10.21468/SciPostPhys.10.4.090.

[81] A. A. Burkov, M. D. Lukin, and E. Demler, "Decoherence dynamics in low-dimensional cold atom interferometers", Phys. Rev. Lett. **98**, 200404 (2007) 10.1103/PhysRevLett.98.200404.

[82] M. Scheffer, J. Bascompte, W. A. Brock, V. Brovkin, S. R. Carpenter, V. Dakos, H. Held, E. H. Van Nes, M. Rietkerk, and G. Sugihara, "Early-warning signals for critical transitions", Nature **461**, 53–59 (2009) 10.1038/nature08227.

[83] K. G. Wilson and J. Kogut, "The renormalization group and the ϵ expansion", Physics Reports **12**, 75–199 (1974) https://doi.org/10.1016/0370-1573(74)90023-4.

[84] K. G. Wilson, "Renormalization group and critical phenomena. ii. phase-space cell analysis of critical behavior", Phys. Rev. B **4**, 3184–3205 (1971) 10.1103/PhysRevB.4.3184.

[85] H. Schoeller, J. König, F. Kuczera, and G. Schön, "Real-Time Renormalization Group: Charge Fluctuations in Metallic Islands and Quantum Dots", Journal of Low Temperature Physics **118**, 409–419 (2000) 10.1023/A:1004650202717.

[86] H. Schoeller and F. Reininghaus, "Real-time renormalization group in frequency space: a two-loop analysis of the nonequilibrium anisotropic kondo model at finite magnetic field", Phys. Rev. B **80**, 045117 (2009) 10.1103/PhysRevB.80.045117.

[87] X. G. Wen, *Quantum Field Theory of Many-Body Systems: From the Origin of Sound to an Origin of Light and Electrons* (Oxford University Press, 2010), 10.1093/ACPROF:OSO/9780199227259.001.0001.

[88] D. C. Aveline, J. R. Williams, E. R. Elliott, C. Dutenhoffer, et al., "Observation of Bose–Einstein condensates in an Earth-orbiting research lab", Nat. 2020 5827811 **582**, 193–197 (2020) 10.1038/s41586-020-2346-1.

[89] E. R. Elliott, M. C. Krutzik, J. R. Williams, R. J. Thompson, and D. C. Aveline, "NASA's Cold Atom Lab (CAL): system development and ground test status", npj Microgravity 2018 41 **4**, 1–7 (2018) 10.1038/s41526-018-0049-9.

[90] M. F. Riedel, P. Böhi, Y. Li, T. W. Hänsch Signnsch, A. Sinatra, and P. Treutlein, "Atom-chip-based generation of entanglement for quantum metrology", Nature **464**, 1170–1173 (2010) 10.1038/nature08988, eprint: 1003.1651.

[91] T. Berrada, S. van Frank, R. Bücker, T. Schumm, J.-F. Schaff, and J. Schmiedmayer, "Integrated Mach–Zehnder interferometer for Bose–Einstein condensates", Nat. Commun. 2013 41 **4**, 1–8 (2013) 10.1038/ncomms3077.

[92] K. Luksch, E. Bentine, A. J. Barker, S. Sunami, T. L. Harte, B. Yuen, and C. J. Foot, "Probing multiple-frequency atom-photon interactions with ultracold atoms", New J. Phys. **21**, 073067 (2019) 10.1088/1367-2630/ab2f60.

[93] A. J. Barker, S. Sunami, D. Garrick, A. Beregi, K. Luksch, E. Bentine, and C. J. Foot, "Realising a species-selective double well with multiple-radiofrequency-dressed potentials", Journal of Physics B: Atomic, Molecular and Optical Physics **53**, 155001 (2020) 10.1088/1361-6455/ab9152.

[94] A. J. Barker, S. Sunami, D. Garrick, A. Beregi, K. Luksch, E. Bentine, and C. J. Foot, "Coherent splitting of two-dimensional bose gases in magnetic potentials", New Journal of Physics **22**, 103040 (2020) 10.1088/1367-2630/abbced.

[95] A. J. Barker, H. Style, K. Luksch, S. Sunami, D. Garrick, F. Hill, C. J. Foot, and E. Bentine, "Applying machine learning optimization methods to the production of a quantum gas", **1**, 015007 (2020) 10.1088/2632-2153/ab6432.

[96] E. Bentine, A. J. Barker, K. Luksch, S. Sunami, T. L. Harte, B. Yuen, C. J. Foot, D. J. Owens, and J. M. Hutson, "Inelastic collisions in radiofrequency-dressed mixtures of ultracold atoms", Phys. Rev. Research **2**, 033163 (2020) 10.1103/PhysRevResearch.2.033163.

[97] H. Perrin and B. M. Garraway, "Chapter four - trapping atoms with radio frequency adiabatic potentials", Vol. 66, edited by E. Arimondo, C. C. Lin, and S. F. Yelin, Advances In Atomic, Molecular, and Optical Physics (Academic Press, 2017), pp. 181–262, https://doi.org/10.1016/bs.aamop.2017.03.002.

[98] K. A. Burrows, H. Perrin, and B. M. Garraway, "Nonadiabatic losses from radio-frequency-dressed cold-atom traps: beyond the landau-zener model", Phys. Rev. A **96**, 023429 (2017) 10.1103/PhysRevA.96.023429.

[99] K. Merloti, R. Dubessy, L. Longchambon, A. Perrin, P. E. Pottie, V. Lorent, and H. Perrin, "A two-dimensional quantum gas in a magnetic trap", New J. Phys. **15**, 033007 (2013) 10.1088/1367-2630/15/3/033007, eprint: 1303.2474.

[100] T. L. Harte, E. Bentine, K. Luksch, A. J. Barker, D. Trypogeorgos, B. Yuen, and C. J. Foot, "Ultracold atoms in multiple radio-frequency dressed adiabatic potentials", Phys. Rev. A **97**, 1–10 (2018) 10.1103/PhysRevA.97.013616.

[101] G. A. Sinuco-León and B. M. Garraway, "Radio-frequency dressed lattices for ultracold alkali atoms", New J. Phys. **17**, 053037 (2015) 10.1088/1367-2630/17/5/053037.

[102] K. Luksch, "Investigating the spectrum of atoms in multiple-radiofrequency dressed potentials for coherent splitting of quantum gases", PhD thesis (University of Oxford, 2019).

[103] M. Grifoni and P. Hänggi, "Driven quantum tunneling", Physics Reports **304**, 229–354 (1998) https://doi.org/10.1016/S0370-1573(98)00022-2.

[104] O. Morizot, L. Longchambon, R. Kollengode Easwaran, R. Dubessy, E. Knyazchyan, P. E. Pottie, V. Lorent, and H. Perrin, "Influence of the Radio-Frequency source properties on RF-based atom traps", European Physical Journal D **47**, 209–214 (2008) 10.1140/epjd/e2008-00050-2.

[105] D. Garrick, "In preparation", PhD thesis (University of Oxford).

[106] A. Beregi, "In preparation", PhD thesis (University of Oxford).

[107] E. Bentine, "Atomic mixtures in radiofrequency dressed potentials", PhD thesis (University of Oxford, 2018).

[108] T. Harte, "Ultracold atoms in dressed potentials", PhD thesis (University of Oxford, 2017).

[109] A. J. Barker, "Bose gases in double-well potentials", PhD thesis (University of Oxford, 2020).

[110] D. J. McCarron, S. A. King, and S. L. Cornish, "Modulation transfer spectroscopy in atomic rubidium", Measurement Science and Technology **19**, 105601 (2008) 10.1088/0957-0233/19/10/105601.

[111] K. I. Lee, J. A. Kim, H. R. Noh, and W. Jhe, "Single-beam atom trap in a pyramidal and conical hollow mirror", Opt. Lett. **21**, 1177–1179 (1996) 10.1364/OL.21.001177.

[112] K. Hueck, N. Luick, L. Sobirey, J. Siegl, T. Lompe, H. Moritz, L. W. Clark, and C. Chin, "Calibrating high intensity absorption imaging of ultracold atoms", Opt. Express **25**, 8670–8679 (2017) 10.1364/OE.25.008670.

[113] D. A. Steck, *Rubidium 87 D line data*, http://steck.us/alkalidata, 2015.

[114] R. P. Smith, R. L. D. Campbell, N. Tammuz, and Z. Hadzibabic, "Effects of interactions on the critical temperature of a trapped bose gas", Phys. Rev. Lett. **106**, 250403 (2011) 10.1103/PhysRevLett.106.250403.

[115] D. H. White, T. A. Haase, D. J. Brown, M. D. Hoogerland, M. S. Najafabadi, J. L. Helm, C. Gies, D. Schumayer, and D. A. Hutchinson, "Observation of two-dimensional Anderson localisation of ultracold atoms", Nature Communications **11**, 1–8 (2020) 10.1038/s41467-020-18652-w.

[116] A. Mazurenko, C. S. Chiu, G. Ji, M. F. Parsons, M. Kanász-Nagy, R. Schmidt, F. Grusdt, E. Demler, D. Greif, and M. Greiner, "A cold-atom Fermi-Hubbard antiferromagnet", Nature **545**, 462–466 (2017) 10.1038/nature22362.

[117] M. Gildemeister, B. E. Sherlock, and C. J. Foot, "Techniques to cool and rotate bose-einstein condensates in time-averaged adiabatic potentials", Phys. Rev. A **85**, 053401 (2012) 10.1103/PhysRevA.85.053401.

[118] F. Dalfovo, S. Giorgini, L. P. Pitaevskii, and S. Stringari, "Theory of bose-einstein condensation in trapped gases", Rev. Mod. Phys. **71**, 463–512 (1999) 10.1103/RevModPhys.71.463.

[119] P. Krüger, Z. Hadzibabic, and J. Dalibard, "Critical point of an interacting two-dimensional atomic bose gas", Phys. Rev. Lett. **99**, 040402 (2007) 10.1103/PhysRevLett.99.040402.

[120] J.-y. Choi, S. W. Seo, and Y.-i. Shin, "Observation of thermally activated vortex pairs in a quasi-2d bose gas", Phys. Rev. Lett. **110**, 175302 (2013) 10.1103/PhysRevLett.110.175302.

[121] G. Hechenblaikner, J. M. Krueger, and C. J. Foot, "Properties of quasi-two-dimensional condensates in highly anisotropic traps", Phys. Rev. A **71**, 013604 (2005) 10.1103/PhysRevA.71.013604.

[122] C. Mora and Y. Castin, "Extension of Bogoliubov theory to quasicondensates", Phys. Rev. A **67**, 053615 (2003) 10.1103/PhysRevA.67.053615.

[123] C. W. Gardiner, *Stochastic methods*, Fourth, Vol. 13, Springer Series in Synergetics (Springer-Verlag, Berlin, 2009), ISBN: 3-540-70712-7.

[124] V. P. Singh, C. Weitenberg, J. Dalibard, and L. Mathey, "Superfluidity and relaxation dynamics of a laser-stirred two-dimensional bose gas", Phys. Rev. A **95**, 043631 (2017) 10.1103/PhysRevA.95.043631.

[125] I. Hughes and T. Hase, *Measurements and their uncertainties: a practical guide to modern error analysis* (Oxford University Press, Oxford, 2010).

[126] N. J. van Druten and W. Ketterle, "Two-step condensation of the ideal bose gas in highly anisotropic traps", Phys. Rev. Lett. **79**, 549–552 (1997) 10.1103/PhysRevLett.79.549.

[127] A. Imambekov, V. Gritsev, and E. Demler, "Mapping of coulomb gases and sine-gordon models to statistics of random surfaces", Phys. Rev. A **77**, 063606 (2008) 10.1103/PhysRevA.77.063606.

[128] S. P. Rath and W. Zwerger, "Full counting statistics of the interference contrast from independent bose-einstein condensates", Phys. Rev. A **82**, 053622 (2010) 10.1103/PhysRevA.82.053622.

[129] M. Kuhnert, "Thermalization and prethermalization in an ultracold Bose gas", PhD thesis (Vienna University of Technology, 2013).

[130] O. Penrose and L. Onsager, "Bose-einstein condensation and liquid helium", Phys. Rev. **104**, 576–584 (1956) 10.1103/PhysRev.104.576.

[131] J. Javanainen, "Oscillatory exchange of atoms between traps containing Bose condensates", Phys. Rev. Lett. **57**, 3164–3166 (1986) 10.1103/PhysRevLett.57.3164.

[132] G. J. Milburn, J. Corney, E. M. Wright, and D. F. Walls, "Quantum dynamics of an atomic Bose-Einstein condensate in a double-well potential", Phys. Rev. A **55**, 4318–4324 (1997) 10.1103/PhysRevA.55.4318.

[133] I. Zapata, F. Sols, and A. J. Leggett, "Josephson effect between trapped bose-einstein condensates", Phys. Rev. A **57**, R28–R31 (1998) 10.1103/PhysRevA.57.R28.

[134] J. C. Davis and R. E. Packard, "Superfluid ^{3}He josephson weak links", Rev. Mod. Phys. **74**, 741–773 (2002) 10.1103/RevModPhys.74.741.

[135] C. Gross, T. Zibold, E. Nicklas, J. Estève, and M. K. Oberthaler, "Nonlinear atom interferometer surpasses classical precision limit", Nature **464**, 1165–1169 (2010) 10.1038/nature08919.

[136] T. Zibold, E. Nicklas, C. Gross, and M. K. Oberthaler, "Classical bifurcation at the transition from rabi to josephson dynamics", Phys. Rev. Lett. **105**, 204101 (2010) 10.1103/PhysRevLett.105.204101.

[137] J. Estève, C. Gross, A. Weller, S. Giovanazzi, and M. K. Oberthaler, "Squeezing and entanglement in a Bose-Einstein condensate", Nature **455**, 1216–1219 (2008) 10.1038/nature07332.

[138] F. S. Cataliotti, S. Burger, C. Fort, P. Maddaloni, F. Minardi, A. Trombettoni, A. Smerzi, and M. Inguscio, "Josephson Junction Arrays with Bose-Einstein Condensates", Science (80-.). **293**, 843–846 (2001) 10.1126/SCIENCE.1062612.

[139] M. Albiez, R. Gati, J. Fölling, S. Hunsmann, M. Cristiani, and M. K. Oberthaler, "Direct observation of tunneling and nonlinear self-trapping in a single bosonic josephson junction", Phys. Rev. Lett. **95**, 010402 (2005) 10.1103/PhysRevLett.95.010402.

[140] R. Gati, B. Hemmerling, J. Fölling, M. Albiez, and M. K. Oberthaler, "Noise thermometry with two weakly coupled bose-einstein condensates", Phys. Rev. Lett. **96**, 130404 (2006) 10.1103/PhysRevLett.96.130404.

[141] C. Groß, *Spin Squeezing and Non-linear Atom Interferometry with Bose-Einstein Condensates*, Springer Theses (Springer Berlin Heidelberg, Berlin, Heidelberg, 2012), 10.1007/978-3-642-25637-0.

[142] B. Zhu, V. P. Singh, J. Okamoto, and L. Mathey, "Dynamical control of the conductivity of an atomic Josephson junction", Phys. Rev. Research **3**, 013111 (2021) 10.1103/PhysRevResearch.3.013111.

[143] E. O. Ilo-Okeke, S. Sunami, C. J. Foot, and T. Byrnes, "Faraday-imaging-induced squeezing of a double-well bose-einstein condensate", Phys. Rev. A **104**, 053324 (2021) 10.1103/PhysRevA.104.053324.

[144] N. Luick, L. Sobirey, M. Bohlen, V. P. Singh, L. Mathey, T. Lompe, and H. Moritz, "An ideal Josephson junction in an ultracold two-dimensional Fermi gas", Science **369**, 89–91 (2020) 10.1126/science.aaz2342.

[145] V. P. Singh, N. Luick, L. Sobirey, and L. Mathey, "Josephson junction dynamics in a two-dimensional ultracold Bose gas", Phys. Rev. Research **2**, 033298 (2020) 10.1103/PhysRevResearch.2.033298.

[146] R. Gati and M. K. Oberthaler, "A bosonic Josephson junction", J. Phys. B: At. Mol. Opt. Phys. **40**, R61–R89 (2007) 10.1088/0953-4075/40/10/r01.

[147] J. F. Schaff, T. Langen, and J. Schmiedmayer, "Interferometry with atoms", La Rivista del Nuovo Cimento **37**, 509–589 (2014) 10.1393/ncr/i2014-10105-7.

[148] T. Barrada, "interacting Bose-Einstein condensates in a double-well potential", PhD thesis (Technical University of Wien, 2014).

[149] S. Raghavan, A. Smerzi, S. Fantoni, and S. R. Shenoy, "Coherent oscillations between two weakly coupled bose-einstein condensates: josephson effects, π oscillations, and macroscopic quantum self-trapping", Phys. Rev. A **59**, 620–633 (1999) 10.1103/PhysRevA.59.620.

[150] A. Smerzi, S. Fantoni, S. Giovanazzi, and S. R. Shenoy, "Quantum coherent atomic tunneling between two trapped bose-einstein condensates", Phys. Rev. Lett. **79**, 4950–4953 (1997) 10.1103/PhysRevLett.79.4950.

[151] D. A. Abanin, E. Altman, I. Bloch, and M. Serbyn, "Colloquium: many-body localization, thermalization, and entanglement", Rev. Mod. Phys. **91**, 021001 (2019) 10.1103/RevModPhys.91.021001.

[152] J.-y. Choi, S. Hild, J. Zeiher, P. Schauß, A. Rubio-Abadal, T. Yefsah, V. Khemani, D. A. Huse, I. Bloch, and C. Gross, "Exploring the many-body localization transition in two dimensions", Science **352**, 1547–1552 (2016) 10.1126/science.aaf8834.

[153] N. Y. Yao, C. R. Laumann, S. Gopalakrishnan, M. Knap, M. Müller, E. A. Demler, and M. D. Lukin, "Many-body localization in dipolar systems", Phys. Rev. Lett. **113**, 243002 (2014) 10.1103/PhysRevLett.113.243002.

[154] V. Khemani, D. N. Sheng, and D. A. Huse, "Two universality classes for the many-body localization transition", Phys. Rev. Lett. **119**, 075702 (2017) 10.1103/PhysRevLett.119.075702.

[155] G. Bertoli, V. P. Michal, B. L. Altshuler, and G. V. Shlyapnikov, "Finite-Temperature Disordered Bosons in Two Dimensions", Phys. Rev. Lett. **121**, 030403 (2018) 10.1103/PhysRevLett.121.030403.

[156] W. Morong and B. DeMarco, "Simulation of anderson localization in two-dimensional ultracold gases for pointlike disorder", Phys. Rev. A **92**, 023625 (2015) 10.1103/PhysRevA.92.023625.

[157] S. Jammi, T. Pyragius, M. G. Bason, H. M. Florez, and T. Fernholz, "Dispersive detection of radio-frequency-dressed states", Phys. Rev. A **97**, 1–13 (2018) 10.1103/PhysRevA.97.043416.

[158] R. Inoue, S.-I.-R. Tanaka, R. Namiki, T. Sagawa, and Y. Takahashi, "Unconditional quantum-noise suppression via measurement-based quantum feedback", Phys. Rev. Lett. **110**, 163602 (2013) 10.1103/PhysRevLett.110.163602.

[159] G. Vasilakis, H. Shen, K. Jensen, M. Balabas, D. Salart, B. Chen, and E. S. Polzik, "Generation of a squeezed state of an oscillator by stroboscopic back-action-evading measurement", Nat. Phys. 2014 115 **11**, 389–392 (2015) 10.1038/nphys3280.

[160] K. Hammerer, A. S. Sørensen, and E. S. Polzik, "Quantum interface between light and atomic ensembles", Rev. Mod. Phys. **82**, 1041–1093 (2010) 10.1103/RevModPhys.82.1041.

[161] J. M. Geremia, J. K. Stockton, and H. Mabuchi, "Tensor polarizability and dispersive quantum measurement of multilevel atoms", Phys. Rev. A - At. Mol. Opt. Phys. **73**, 1–14 (2006) 10.1103/PhysRevA.73.042112.

[162] J. Ma, X. Wang, C. Sun, and F. Nori, "Quantum spin squeezing", Physics Reports **509**, 89–165 (2011) https://doi.org/10.1016/j.physrep.2011.08.003.

[163] M. Kitagawa and M. Ueda, "Squeezed spin states", Phys. Rev. A **47**, 5138–5143 (1993) 10.1103/PhysRevA.47.5138.

[164] J. K. Stockton, "Continuous Quantum Measurement of Cold Alkali-Atom Spins", PhD thesis (California Institute of Technology, 2007).

[165] G. A. Smith, S. Chaudhury, A. Silberfarb, I. H. Deutsch, and P. S. Jessen, "Continuous weak measurement and nonlinear dynamics in a cold spin ensemble", Phys. Rev. Lett. **93**, 1–4 (2004) 10.1103/PhysRevLett.93.163602.

[166] C. Gardiner and P. Zoller, *Quantum Noise: A Handbook of Markovian and Non-Markovian Quantum Stochastic Methods with Applications to Quantum Optics* (Springer, 2004), ISBN: 978-3540223016.